Probabilistic Design of Thin-Walled Fiber Composite Structures

Von der Fakultät für Bauingenieurwesen und Geodäsie

der Gottfried Wilhelm Leibniz Universität Hannover

zur Erlangung des Grades

DOKTOR-INGENIEUR

Dr.–Ing.

genehmigte Dissertation

von

Dipl.-Ing. Benedikt Kriegesmann

geboren am 04.11.1982, in Münster

2012

"… it seems absurd to strive for more and more refinement of methods of stress-analysis if in order to determine the dimension of the structural elements, its results are subsequently compared with the so called working stress, derived in a rather crude manner by dividing the values of somewhat dubious material parameters obtained in conventional material tests by still more dubious empirical numbers called safety factors." - Alfred Martin Freudenthal

Abstract

Properties like geometry and material of structures scatter in reality, which causes the load carrying capability of a real structure to be stochastically distributed. A robust and efficient design requires knowledge of the stochastic distribution of the collapse load. If the load carrying capability is limited by multiple criterions as stability and material failure, the joint probability distribution of these values must be considered for the derivation of a design load.

In the framework of the current dissertation, a fast, probabilistic procedure is derived that allows determining the distribution of load carrying capability with respect to stochastically distributed input parameters. Furthermore, methods for efficient design optimization under consideration of scattering input parameters are given.

The derived methods are applied to axially compressed cylindrical shells and stiffened panels made of fiber composite material. Thin-walled cylinders are prone to stability failure and sensitive to manufacturing inaccuracies, which leads to a large scatter of the collapse load. Therefore, cylindrical shells are well suited for validation of probabilistic methods. In the framework of this dissertation the stochastic distribution of a set of cylindrical shells is estimated, which compares well with the experimentally determined distribution. The probabilistically motivated design load appears to be robust and at the same time less conservative than the design load given by frequently used guidelines.

The load carrying capability of stiffened panels is limited by loss of stability and by material failure. Therefore, this type of structure is well suited for the application of probabilistic analyses with respect to multiple failure modes. The probabilistic analyses provide the stochastic justification of recently developed, efficient design rules.

The design of the regarded cylindrical shells and stiffened panels is optimized under consideration of scattering input parameters. Thereby, the additional design parameters provided by the laminate setup of fiber composites are exploited. The results show that considering scattering input parameters leads to a different optimal design than optimizing the perfect structure. Furthermore, optimization using the probabilistic approach yields a higher design load or weight saving, respectively, than optimization using conventional safety factor design.

Keywords: *probabilistic design; buckling of composite structures; design optimization*

Kurzfassung

Eigenschaften wie Geometrie und Materialparameter realer Strukturen sind Schwankungen unterworfen, die bewirken, dass die Traglast einer realen Struktur stochastisch streut. Um eine Struktur sicher und wirtschaftlich bemessen zu können, muss die stochastische Verteilung der Traglast bekannt sein. Ist die Traglast durch mehrere Kriterien begrenzt, beispielsweise durch Material- und Stabilitätsversagen, muss die gemeinsame Verteilung zur Bestimmung der Bemessungslast betrachtet werde.

Im Rahmen der vorliegenden Dissertation wird ein schnelles, probabilistisches Verfahren vorgestellt, mit dem sich auf Grundlage stochastisch verteilter Eingangsgrößen die Verteilung der Traglast bestimmen lässt. Darüber hinaus werden Methoden zur effizienten Entwurfsoptimierung unter Berücksichtigung streuender Eingangsparameter zur Verfügung gestellt.

Die entwickelten Methoden werden auf axial belastete Kreiszylinderschalen und versteifte Paneele aus Faserverbundmaterial angewandt. Dünnwandige Kreiszylinderschalen versagen durch Stabilitätsverlust und sind besonders sensitiv gegenüber Fertigungsungenauigkeiten. Dies führt zu einer großen Streuung der Traglast, weshalb sich Kreiszylinderschalen besonders zur Validierung probabilistischer Verfahren eigenen. Die im Rahmen der Dissertation vorhergesagte Verteilung der Traglast der untersuchten Kreiszylinderschalen stimmt mit der experimentell bestimmten Verteilung gut überein. Die probabilistisch motivierte Bemessungslast stellt sich als sicher und zugleich weniger konservativ als die Bemessungslast nach gängigen Entwurfsrichtlinien heraus.

Die Tragfähigkeit versteifter Paneele ist durch Material- und Stabilitätsversagen begrenzt, weshalb sich diese Strukturen besonders zur Anwendung probabilistischer Analysen unter Berücksichtigung mehrerer Versagensarten eignen. Die probabilistische Analyse liefert die stochastische Absicherung eines jüngst entwickelten, wirtschaftlichen Bemessungsverfahrens.

Der Entwurf der betrachteten Kreiszylinderschalen und versteiften Paneele wird unter Berücksichtigung streuender Eingangsparameter optimiert, wobei auch der bei Faserverbundmaterialien als zusätzlicher Entwurfsparameter zur Verfügung stehende Laminataufbau ausgenutzt wird. Dabei zeigt sich, dass die Berücksichtigung streuender Parameter zu einem anderen optimalen Entwurf führt als die Betrachtung der perfekten Struktur. Außerdem führt der probabilistische Ansatz in der Optimierung zu einer höheren Bemessungslast bzw. Gewichtsreduktion als die Bemessung mittels konventioneller Abminderungsfaktoren.

Schlagworte: *probabilistische Bemessung; Beulen von Faserverbundstrukturen; Entwurfsoptimierung*

Contents

1   Introduction

The need for design methods that allow a further exploitation of the load carrying capabilities of composite structures is the motivation for the work performed and methods developed within the context of this thesis. In the current chapter, the state of the art in the relevant fields is summarized and the resulting need for further research is formulated as objective of this thesis.

1.1   Motivation

Fiber composite components are increasingly broadly used in aerospace structures. Examples are the Airbus A350 and the Boeing 787 Dreamliner, for which the fuselages are primarily made of carbon fiber composite. Due to their high specific strength and stiffness, composite structures provide a large weight saving potential.

Since fiber composite parts are mostly thin-walled structures, stability failure is often decisive for design. Stability failure occurs, if a thin-walled structure is loaded in plane under compression. As the load exceeds a certain level, deflections perpendicular to the loading plane occur, accompanied by a significant loss of stiffness. Since for shell structures the pattern of lateral deflections usually consists of multiple buckles, this phenomenon is denoted as buckling. For bars and strait shells under compression the load can be further increased after buckling has occurred. In difference to that, circular shells lose their capability to carry the applied load when buckling occurs. Hence, cylindrical shells collapse suddenly when their load carrying capability is exceeded. The load carrying capability of circular shells however depends on the deviations from the ideal structure, where it cannot be stated that for a better manufacturing accuracy the buckling load is necessarily higher. Moreover, the pattern of the imperfections plays an important role.

The sensitivity of circular shell is a problem when designing such a structure, since size and pattern of imperfections are unknown in the design phase. Actually, all measures of a real, manufactured structure deviate from the ideal structure, since all parameters are subjected to a certain scatter. Hence, also the structural response, the load carrying capability of a structure is of random nature. In order to design a structure as lightweight as possible and at the same time as reliable as necessary, the stochastic distribution of the load carrying capability must be known. This requires the application of probabilistic methods.

In this context, two structural components are regarded in this thesis. Unstiffened cylindrical composite shells, which occur as parts of rocket boosters, show a high imperfection sensitivity, which leads to a large stochastic scatter of buckling load. Stiffened composite panels, as a part of an aircraft fuselage, are generally less sensitive to imperfections, but show a more complex buckling behavior. Here, the load carrying capability is not only limited by the buckling load, but also by material failure. Depending on the design, material degradation and stability failure can even interact. This causes additional challenges for the probabilistic method.

Probabilistic analyses of composite structures on the one hand provide information about the reliability of components, and on the other hand offer possibilities to even further exploit the load carrying capability of the structure and therefore save weight.

1.2   State of the Art

This section gives an overview of developments in buckling analyses of stiffened and unstiffened cylindrical shells and curved panels, where due to the historical development metallic structures are considered as well as structures made of composite material. For a comprehensive overview of the history of shell buckling the reader should refer to [1] or [2]. Furthermore, different probabilistic and deterministic design philosophies that have been developed are discussed. The focus of this thesis is on probabilistically motivated design approaches, which is why besides probabilistic analyses of thin-walled shells also probabilistic analyses of composite material in general are summarized. Finally, an overview is given of the probabilistic methods and tools that are used for probabilistic analyses in general.

1.2.1   Buckling of Unstiffened Cylindrical Shells

In the beginning of the 20th century, Lorenz [3], Timoshenko [4] and Southwell [5] in parallel derived the equation for the buckling load of a perfect, isotropic cylindrical shell, assuming a purely membrane stress state for the prebuckling range.

$$P_{cl} = \frac{2\pi E t^2}{\sqrt{3(1-v^2)}} \tag{1.1}$$

In first experimental tests by Lundquist [6] and Donnell [7] it turned out that there is a large discrepancy between test results and analytic solution, which could not be explained at that time. Taking into account all experimental data available at that time, Weingarten et al. [8] showed that for an increasing slenderness R/t, the discrepancy between analytical solution and test results increases and the ratio of experimentally buckling load P and classical buckling load $P_{cl} = 2\pi E t^2 C$ decreases, respectively (see Figure 1-1). In Figure 1-1 the Poisson's ration $v = 0.3$ has been chosen, which yields a maximum buckling coefficient of $C = \sqrt{3(1-v^2)}^{-1} \approx 0.6$.
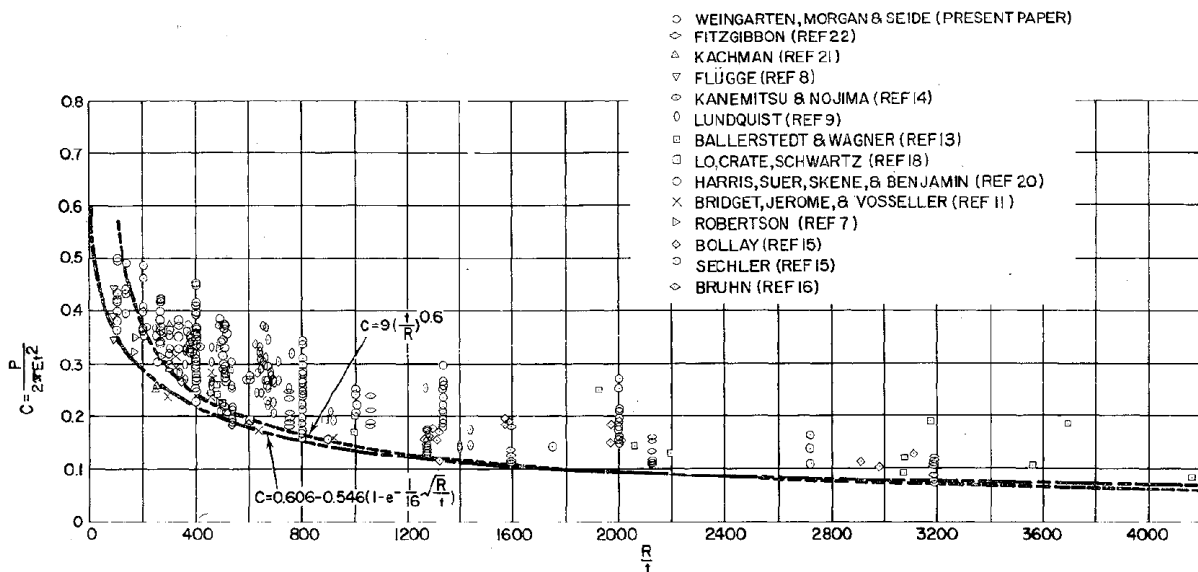
Figure 1-1: Normalized buckling coefficient *C* over slenderness, lower bound proposed by Weingarten et al. and test results (black spots), from Weingarten et al. [8] (Reprinted with permission of the American Institute of Aeronautics and Astronautics.)

Koiter [9] showed that initial geometric imperfections significantly reduce the buckling load and hence, are one reason for the difference of the classical buckling load and test results. In order to describe the postbuckling behavior Koiter used an asymptotic approach at the bifurcation point.

$$\lambda / \lambda_c = 1 + a\xi + b\xi^2 + \dots \tag{1.2}$$

Here, λ/λ_c is the normalized buckling load expanded in ξ. For symmetric buckling problems, the factor a equals zero. The factor b describes the curvature of the load displacement at the bifurcation point and hence, can be used as a measure for the sensitivity of a shell to imperfections. Donnell and Wang [10] showed that even small imperfection amplitudes can decrease the buckling load significantly compared to the buckling load of a perfect shell, whereas Arbocz [11] demonstrated that in the deep postbuckling range the postbuckling paths of imperfect and perfect shells approach each other.

Ohira [12] investigated the influence of boundary conditions and found that even small changes of the boundary conditions lead to significantly different buckling loads. While Ohira considered a perfect shell with linear, membrane prebuckling behavior, Almroth [13] determined buckling loads for eight combinations of boundary conditions with rigorous solution of prebuckling problem. His results show that not only the boundary conditions, but also nonlinear prebuckling behavior has a strong influence on the buckling load. However, the influence of these effects alone is not strong enough to explain the gap between experimentally obtained buckling loads and the classical buckling load.

Donnell [7] gave the basic equations to solve the postbuckling problem for an infinitely long cylindrical shell. Using Ritz technique, von Kármánn and Tsien [14] found in their first postbuckling analyses that several equilibrium configurations exist for one load level. Several works followed taking more and more coefficients into account within the Ritz approach, until Hoff et al. [15] showed that the postbuckling load tends towards zero as the number of coefficients increases.

Thielemann and Esslinger [16] demonstrated theoretically and experimentally that the buckling load of cylinders decreases with increasing length. They consequently concluded that realistic postbuckling loads can only be achieved by taking into account the finite length, which leads to a locally concentrated buckling pattern.

Using high speed camera systems, Almroth et al. [17] and Esslinger [18] captured the highly dynamic buckling of cylindrical shells in experimental tests. They found that buckling is initiated by a single dimple, from where buckles spread over the cylinder surface and build an unstable mode, which then changes again until the stable postbuckling mode is reached.

1.2.2   Buckling of Isotropic Stiffened Cylindrical Shells

In 1963, Baruch and Singer [19] developed a theory to "smeared out" stiffeners for shell stability analyses, which turned out to be satisfactory for closely stiffened (cylindrical) shells that fail by general instability. Hutchinson and Amazigo [20] showed that for stringer-stiffened cylindrical shells the effect of boundary conditions differs significantly from isotropic and ring-stiffened shells. Weller [21] furthermore stated that in difference to isotropic cylinders the effect of boundary conditions is predominant for stiffened shells.

Byskov and Hutchinson [22] stated that in general the buckling load of axially stiffened cylindrical shells is always sensitive to initial imperfections, whereas the effect of interaction between local and general instability is to increase the sensitivity. Weller and Singer [23] showed that the imperfection sensitivity of stiffened cylinders depends on the geometry of

stiffeners and on the ration $A_s/(b\,t)$, respectively, where A_s is cross-section area of the stringer, b the circumferential distance between stringers, and t the wall thickness of the shell.

1.2.3   Buckling of Composite Cylindrical Shells

Hilburger and Starnes [24] analyzed and tested a set of composite cylindrical shells to investigate the imperfection sensitivity. They raised the problem, that the existing test results for isotropic shells did not comprise any information about the structural behavior and the characteristic imperfections of composite shells. Zimmermann [25] earlier showed that the buckling load of composite shells can significantly be influenced by fiber orientations and stacking sequence. Geier et al. [26] demonstrated that the buckling load of composite cylinders can even be doubled by only changing the stacking sequence.

Hühne et al. [27] showed experimentally and numerically that Esslinger's observations concerning the highly dynamic buckling behavior can also be confirmed for composite shells. They furthermore showed that not only the buckling load, but also the imperfection sensitivity is significantly influenced by the laminate layup.

Further, works on composite cylindrical shells have been performed on the framework of new design criteria and will therefore be discussed in sections 1.2.5 and 1.2.6.

1.2.4   Knockdown Factor Design of Cylindrical Shells

Weingarten et al. [8] proposed a lower bound of buckling load with respect to the ratio of radius R and wall thickness t (see Figure 1-1). This lower bound has been adopted by NASA in 1968 in the guideline NASA SP-8007 [28], which is still widely used. The knockdown factor γ is given by

$$\gamma = 1 - 0.901\left(1 - e^{-\phi}\right) \quad \text{with} \quad \phi = \frac{1}{16}\sqrt{\frac{R}{t}} \tag{1.3}$$

(In difference to the equation in Figure 1-1, not the buckling coefficient C, but the actual ration of experimental buckling load and ideal buckling load is considered as γ.) NASA SP-8007 also gives a lower bound for orthotropic shells, where only the exponent ϕ is modified.

$$\phi = \frac{1}{29.8}\sqrt{\frac{R}{t^*}} \quad \text{with} \quad t^* = \sqrt[4]{\frac{\overline{D}_x\,\overline{D}_y}{\overline{E}_x\,\overline{E}_y}} \tag{1.4}$$

This lower bound can also be used for composite shells by inserting the entries of the ABD matrix.

$$\phi = \frac{1}{29.8}\sqrt{\frac{R}{t^*}} \quad \text{with} \quad t^* = \sqrt[4]{\frac{D_{11}\,D_{22}}{A_{11}\,A_{22}}} \tag{1.5}$$

In his PhD thesis deVries [29] used the unified formulation

$$\phi = \frac{1}{29.8}\sqrt{\frac{R}{t^*}} = \frac{1}{16}\sqrt{\frac{R}{t^*\sqrt{12}}} = \frac{1}{16}\sqrt{\frac{R}{t^+}} \quad \text{with} \quad t^+ = \sqrt{12}\sqrt[4]{\frac{D_{11}\,D_{22}}{A_{11}\,A_{22}}} \tag{1.6}$$

This way, the isotropic shell is a special case of the orthotropic shell. Still, the coupling of bending and membrane stresses that occurs for nonsymmetrical laminates is neglected.

An alternative knockdown factor for metal shells is given by ECCS 56 [30]. Here, the KDF for a shell with small imperfections is given by

$$\gamma = \frac{0.83}{\sqrt{1+0.01\frac{R}{t}}} \quad \text{for} \quad \frac{R}{t} < 212$$

$$\gamma = \frac{0.70}{\sqrt{1+0.01\frac{R}{t}}} \quad \text{for} \quad \frac{R}{t} > 212$$

(1.7)

for $L/R \le 0.95\sqrt{R/t}$. The ECCS 56 also gives additional safety factors depending on the manufacturing accuracy. The same holds for the guidelines for steel shells Eurocode 3 [31] and the old German guideline DIN 18800 – Teil 4 [32]. Both guidelines propose to distinguish shells by the deepest initial dimple.
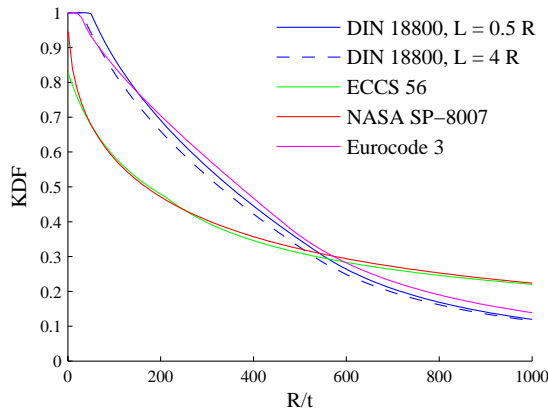
Figure 1-2: Knockdown factor, assuming negligibly small imperfections
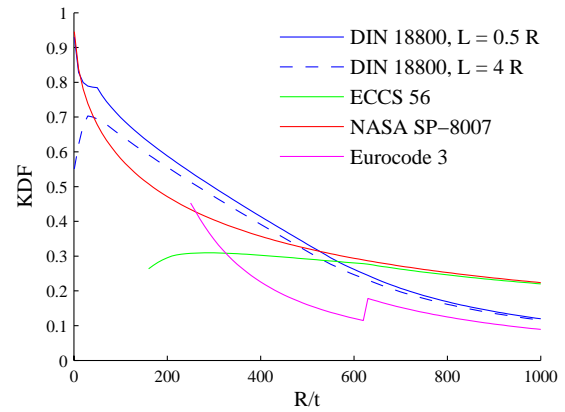
Figure 1-3: Knockdown factors for an imperfection amplitude of *t*

The KDFs delivered by the guidelines mentioned are plotted in Figure 1-2 and Figure 1-3 as functions of *R/t*. For Figure 1-2 the maximum depth of initial dimples was assumed to be zero, while for Figure 1-3 the maximum dimple depth was assumed to equal the wall thickness. The material properties of common steel are used for Eurocode 3 and DIN 18800. Within Eurocode 3 shells are subdivided into three categories depending on their deepest initial dimple and the KDF is determined with respect to the category. For the example considered, the category changes for a ratio $R/t \approx 600$, which explains the jump in the KDF curve of Eurocode 3 in Figure 1-3.

1.2.5   *Probabilistic Design of Cylindrical Shells*

After it was found that geometric imperfections play an important role in the buckling of cylindrical shells, Bolotin [33] concluded that the buckling load must be analyzed probabilistically, since imperfections are of random nature. Bolotin [33] developed an imperfection sensitivity concept combined with probabilistic treatment of imperfections, using a simplified model for the imperfection.

In various works Elishakoff and Arbocz (see e.g. [34] and [35]) performed probabilistic analyses of the buckling load of axially compressed cylindrical shells. Geometric imperfections have been described by buckling modes or Fourier series and the amplitudes or the Fourier coefficients have been regarded as random parameters, respectively. They proposed the first-order second-moment (FOSM) method for analyzing the stochastic distribution of shells and validated the analyses with Monte Carlo simulations. The buckling load calculations within the probabilistic procedures have mostly been performed with analytic and semi-analytic software tools. Arbocz [36] showed that Fourier series are well

applicable to describe the manufacturing signature of shells. In order to have an accurate description of the imperfection pattern, many Fourier coefficients have to be taken into account. The computational cost of the FOSM method increases with the number of random parameters. Hence, in most of their publication Elishakoff and Arbocz reduced the number of imperfection modes taken into account. Most investigations were based on imperfection measurements taken of cylinders with different dimension and types of stiffening. Hence, it was not possible to compare the estimated distribution of buckling load with an experimentally obtained distribution. In order to validate the probabilistic procedure, 30 beer cans have been measured and tested at TU Delft [37]. However, the deterministic model for the determination of buckling loads did not capture all types of imperfection and therefore, the estimated distribution of buckling load did not compare well with the experimentally obtained distribution.

A different approach has been followed by Chryssanthopoulos [38], who analyzed geometric imperfection measurements statistically in order to determine a representative imperfection pattern for a type of shell. With this method the distribution of buckling load and hence, the probability of failure cannot be determined.

In 2002 Arbocz and Hilburger [39] proposed a simple probabilistic design procedure for preliminary design purposes and applied it to a set of composite shells. There, the geometric imperfections are represented by two imperfection modes and the associated amplitudes are determined from the root mean square of the imperfection patterns. This very simplified method does not deliver the real distribution of buckling load and it has been shown that the method in some cases lead to a non-conservative and in some cases to an overly conservative design [40].

Biagi and Del Medico [41] proposed the Equivalent Imperfection Amplitude Concept. Its idea is to substitute the geometric imperfection in the simulation by a single mode and to determine the amplitude that leads to the same buckling load as the experimentally obtained one. This way, a collection of amplitudes is obtained that are somehow related to the tests and that can be used for a probabilistic simulation. Within this method all effects that occur for all types of shells are mixed and captured by one scalar value, the representative amplitude. Hence, also this procedure does not deliver a realistic distribution of buckling load and no statement about the reliability or probability of failure, respectively, can be made.

Degenhardt et al. [42] preformed experimental tests of ten nominally identical composite cylindrical shells and hence, obtained a distribution that allows a validation of a probabilistic procedure. However, Degenhardt et al. did not attempt to estimate the distribution of buckling load, but derived less conservative KDFs from the tests. In their simulation only parameters that could not be measured for each test sample have been treated probabilistically. For material parameters that have been determined from coupon tests, the distribution was given, for a loading imperfection and the scatter of fiber orientation the stochastic parameters have been assumed.

After performing Monte Carlo type simulations of static and dynamic buckling of composite cylindrical shells, Chamis and Abumeri [43] compared the stochastic distributions of the static and the dynamic buckling load. Furthermore, they determined and compared the probabilistic sensitivity of both buckling loads with respect to ply thickness, the fiber volume ratio and the fiber longitudinal modulus. However, geometric imperfections have not been considered by Chamis and Abumeri and comparisons with experimentally obtained distributions was not possible.

Broggi et al. [44] used the measurements of Degenhardt et al. [42] to estimate the distribution of buckling load by performing a Monte Carlo simulation. In difference to Degenhardt et al.,

Broggi et al. considered also geometric imperfections as randomly distributed and approximated the empiric distribution of buckling load very well. Broggi et al. used the results for an assessment of KDF, but did not propose a probabilistic design procedure.

Kriegesmann et al. [45] performed Monte Carlo based probabilistic analyses of the shells investigated by Hühne et al. [27], considering geometric imperfections as well as boundary imperfections as random parameters. The probabilistically derived lower bounds turned out to be less conservative than NASA SP-8007 and undercut the experimental test results. However, due to the small sample size, the estimated distributions of buckling load could not be validated.

In [29] and [46] Kriegesmann et al. applied an extension of the semi-analytic procedure proposed by Elishakoff and Arbocz (see e.g. [34] and [35]) to the set of shells investigated by Degenhardt et al. [42]. The stochastic distribution of buckling load was approximated well by both, the semi-analytic approach as well as a Monte Carlo simulation. The methodology of Kriegesmann et al. [46] is discussed in detail and further extended within this thesis.

1.2.6 Deterministic Design Approaches for Cylindrical Shells

In 2006 a deterministic design procedure has been proposed by Hühne et al. [27,47], which captures the imperfection sensitivity of axially compressed cylindrical shells, but does not require measurement data. Following many works that dealt with the influence of a single dimple or perturbation loads on the buckling load of shells (e.g. [48] and [49]), Hühne et al. derived a simple and promising design procedure, which is referred to as Single Buckle Approach (SBA) or single dimple approach or single perturbation load approach in the literature. For this concept, a single perturbation load is applied to the shell perpendicular to the cylinder axis in the simulation (see Figure 1-4, left). The buckling load is determined for different values of the perturbation load. From a certain value of the perturbation load on, the buckling load hardly decreases any further (see Figure 1-4, right). This value of the perturbation load is assigned to as P_1 and the associated buckling load N_1 is defined as design load. Steinmüller et al. [50] derived an empiric formulation to determine the approximate value of P_1 from the laminate setup, which can decrease the required number of buckling analyses significantly. Hühne et al. [27] applied the procedure to a set of composite shells, where for one shell the design load exceeded the experimentally determined buckling load. Kriegesmann et al. [45] concluded that the single buckle approach is very promising, but further investigations are required to determine for which type of shell the approach is applicable.
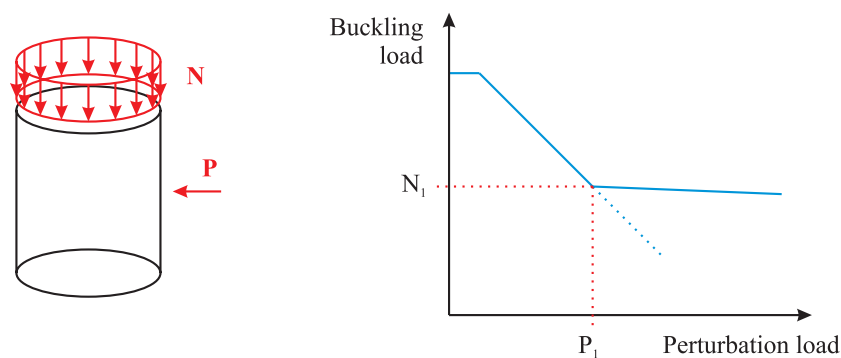
Figure 1-4: Concept of the single buckle approach

Ben-Haim and Elishakoff proposed the convex anti-optimization to account for uncertainties in structural analyses [51]. For this method, the space of input parameters is enclosed by a hyper ellipsoid, based on measurements. Then, the worst case combination of input parameters is determined within the enclosing hyper ellipsoid to obtain the worst case response of the structure. The method has been applied to buckling of shells using measured imperfection data by van den Nieuwendijk [52]. Elishakoff et al. [53] performed a convex anti-optimization of the composite cylindrical shells, which have been tested by Degenhardt et al. [42] and analyzed probabilistically by Kriegesmann et al. [46]. Elishakoff et al. [53] showed that for this set of composite cylinders the convex anti-optimization approach yields similar results as the probabilistic approach. Though convex anti-optimization requires measurement data to account for the scatter of input parameters, the method does not consider stochastic distributions, levels of reliability or other probabilistic aspects. Nevertheless, the method leads to a similar equation for the design load, which is shown in section 8.2.

1.2.7   Buckling and Design of Stiffened Composite Panels

In general, stiffened panels are curved or straight plates, referred to as skin, which are reinforced with stiffeners. Depending on the skin stiffness and the spacing and stiffness of the stringers, under in plane compression the skin can buckle between the stringers, while the stringers do not deflect laterally. This type of buckling is referred to as skin buckling or local buckling. Buckling of the whole panel is therefore referred to as global buckling or overall buckling. The interaction of local and global buckling has already been investigated by Koiter and Pignataro [54] for metallic panels. Stiffened panels as a part of an aircraft fuselage are exposed to axial compression when located at the center bottom, close to the wing box see (e.g. [55,56]). With the increasing application of composites in aircrafts (see e.g. [57]), buckling of stiffened composite panels has been addressed in several projects over the last decade. Within the EDAVCOS (*Efficient Design and Verification of Composite Structures*) "a key aspect was the development of predictive models for post-buckled stiffened structures and verification of these models" [58]. With the POSICOSS (*Improved Postbuckling Simulation for Design of Fibre Composite Stiffened Fuselage Structures*) and COCOMAT (*Improved Material Exploitation of Composite Airframe Structures by Accurate Simulation of Postbuckling and Collapse*) project, the mechanical response of stiffened composite panels was investigated with the goal to exploit the load carrying capability of these structures (see [59] and [60]). The POSICOSS project focused on the development of fast analysis tools. Within COCOMAT the postbuckling behavior including material degradation has been investigated and design rules for stiffened panels have been developed. In many investigations special attention has been paid to skin-stringer debonding (see e.g. [58,61–63]).

The new design guidelines developed within the COCMAT project are summarized in [64]. There, the limit load or design load λ_{LL} is defined as the global buckling load λ_{GB}, divided by a safety factor γ. It furthermore must be ensured that the onset of degradation λ_{OD} is beyond the limit load, while local buckling of the skin is allowed (see Figure 1-5). Mathematically this is expressed by

$$\lambda_d = \min\left(\lambda_{GB}/\gamma, \lambda_{OD}\right) \tag{1.8}$$

Ghilai et al. [64] proposed to use 80% to 90% of the global buckling load as design load, in order to account for uncertainties, which equals a safety factor γ of 1.11 to 1.25.

In the framework of the COCOMAT project Lee et al. [65,66] developed a robustness index for structures with scattering input parameters and applied his method to stiffened panels. It allows determining the influence of a certain input parameter on the scatter of the structural response. To overcome the problem of a small data base, Kelly et al. [67] presented a method

to estimate the scatter of geometric imperfections by simulating the curing process. However, the stochastic distribution of load carrying capability has not been determined and therefore, no safety factors have been derived from their investigations.
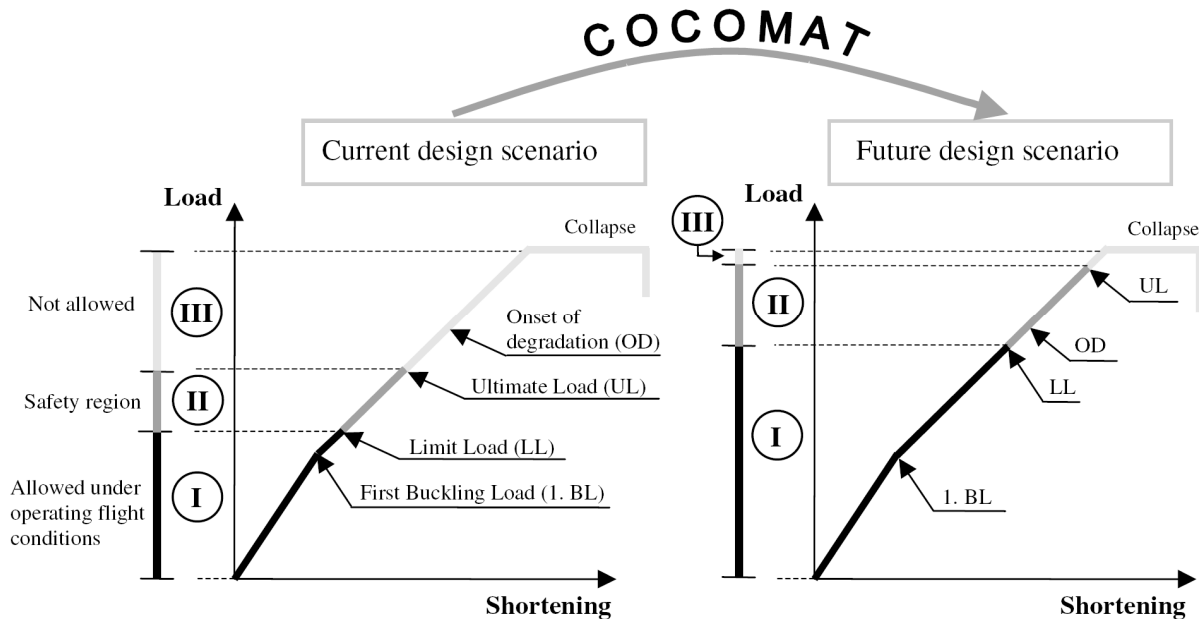
Figure 1-5: Objective of the COCOMAT project - Current and future design scenarios for typical stringer stiffened composite panel, from [60]

An optimization of a curved stiffened panel has been performed by Seibel et al. [68]. However, Seibel et al. considered the first buckling as load carrying capability and hence, did not allow local buckling, as it is proposed in the COCOMAT guidelines.

When stiffened panels are mentioned in the literature, this term often refers to a strait plate that is reinforced with stiffeners (see e.g. [58] or [69]). Within this thesis the focus is on curved stiffened panels, as they are part of an aircraft fuselage. The buckling behavior of these type of panels has been studied for instance by Zimmermann et al. [70].

1.2.8   *Probabilistic Material Failure Analysis of Composite Structures*

A multitude of failure criteria for unidirectional (UD) plies of fiber composite structures has been developed over the last decades. The most often used criterion is the one proposed by Tsai and Wu in 1971 [71]. A more advanced criterion, which, for the first time, differed between fiber failure and inter fiber failure, has been given by Puck and Schneider [72] and later has been enhanced by Hashin [73]. In 2004, Puck and Schürmann [74] developed a criterion that differs between different failure modes of inter fiber failure, for which the applicability has been proven in the World Wide Failure Exercise [75]. However, Puck's criterion requires the iterative determination of the fracture angle of inter fiber failure and is therefore computationally costly. Furthermore, it requires material properties that are not given for composite material by default (see section 3.3). Vogler et al. [76] proposed an Invariant based Quadratic Criterion (IQC), which does not require the determination of the fracture plane and which is defined by fewer material parameters that have to be determined from experiments. Ernst et al. [77] used the material model proposed by Vogler et al. in the framework of a multi scale analysis and predicted the material failure of a textile composite structure on the macro scale based on the material properties of fiber and matrix.

No matter which failure criterion is used, parameters that describe the material resistance scatter in reality and therefore lead to scattering strength of composite structures. Starting at the micro scale, the stiffness and strength parameters of fiber and matrix are of random nature. Also the position of fiber in the matrix and their interface properties are stochastic. Furthermore, fiber waviness and void inclusions can occur randomly. All these effects cause the material parameters of unidirectional plies to be stochastically distributed. When determining the stochastic distribution of the stiffness and strength parameters from experiments, as for instance done by Camanho et al. [78], all these effects are covered. However, when regarding the properties of a whole laminate, void inclusions at the ply interfaces and inaccuracies of the fiber angle lead to additional scatter of structural response.

Summarized, the material characteristics of fiber composite structures scatter on each scale and each scale again influences the distribution on the next higher scale. Several works analyzed the properties of composites on different scales probabilistically in order to estimate the scatter on the next scale. Engelstad and Reddy [79] used stochastic distributions of material characteristics of the UD ply in order to estimate the scatter in the structural response of a certain laminate for a metal matrix composite. Gurvich and Pipes [80,81] considered the properties of a sublaminate (e.g. in the form of [0,±Θ,90]) as randomly distributed in order to estimate the strength distribution of a laminate that consist of the sublaminates considered. They validated their results with bending tests of a $[0]_{14}$ laminate and tensile tests of a $[0,±45,90]_4$ laminate. Philippidis and Lekou [82] performed reliability analysis of a UD ply for given distribution of material strength parameters. Instead of providing stochasitc measures for the analysis on the next scale, they provided semi-analytical and numerical approaches that allow for determining the probability of failure of the single UD ply.

A simple approach to probabilistically analyze the microscopic behavior of fiber composites has been proposed by Wu and Robinson [83]. They considered the tension strength of a single fiber section as random parameter to determine the stochastic distribution of the tensile strength of fiber bundles. A more advanced approach on the micro-scale is given by Ernst [84], who used a Monte Carlo type simulation to determine the stochastic distribution of homogenized material properties in the context of a multi-scale approach. Ernst regarded the fiber positions in a unit cell as randomly distributed and obtained distributions of stiffness and strength of the homogenized material, which then were utilized to analyze a textile composite structure. A full probabilistic multi-scale approach has been demonstrated by Chamis [85]. On the micro level, the stochastic distributions of matrix and fiber properties are used to determine the distributions of material parameters of the UD ply. These again are used as random input parameters for a probabilistic analysis of macro-scale structure. However, the scatters of global properties like geometric imperfections are neglected in this analysis. Shaw et al. [86] performed a probabilistic analysis of UD plies, considering fiber and matrix material properties as well as the void volume fraction as randomly distributed and showed that the estimated distribution is in good agreement with experimentally obtained results. As in other works, the consideration of void inclusions is kept rather simple. Investigations that focus on the effect of voids and their influence on the scatter of material properties are given by Czichon et al. [87]. Here, the actual void morphology is approximated by shape functions and included in finite element models. Thereby, Czichon et al. determined the stochastic distribution of stiffness and strength parameters due to realistically distributed voids.

1.2.9 Probabilistic Analysis Methodologies

The focus of this thesis is on the development of a probabilistic design approach, where existing simulation techniques will be utilized, if possible. Therefore, not the latest state of the art is given here, but an overview of well established methods that have already been applied

in engineering science. An overview of the methods presented in the following can for instance be found in [88–90].
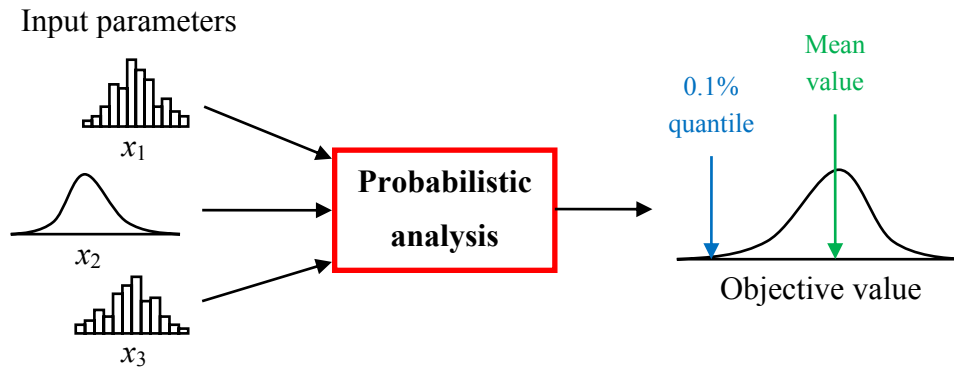
Figure 1-6: General function of a probabilistic analysis

The general objective of probabilistic analyses is to determine the stochastic distribution (or certain characteristics, like mean value and quantiles) of an objective function, which is dependent on scattering input parameters (see Figure 1-6). Since this problem cannot be solved exactly in most cases, a wide range of probabilistic analysis methods is given in the literature, which significantly differ in accuracy and computational cost. In general there is the tendency depicted in Figure 1-7, meaning that the more efficient a method is, the less accurate it is (though there are cases in which accuracy and efficiency are improved at the same time under certain conditions).
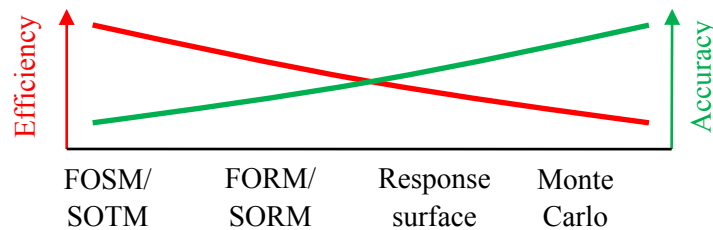
Figure 1-7: Efficiency versus accuracy of different probabilistic methods

The method that requires the fewest evaluations of the objective function is the first-order second-moment (FOSM) method. Within this method, the objective function is approximated by a Taylor expansion at the mean values of all input parameters. This approximation of the objective function is then used to determine mean value and variance of the objective function. While for the FOSM method only linear terms of the Taylor expansion are considered, the second-order third-moment (SOTM) method also considers the quadratic terms of the Taylor series. The basic approach however is the same.

For first and second order reliability methods (FORM/SORM) the limit state function is approximated at the most probable point (MPP). The limit state function is the function that divides the random space into a save region and a failure region. The MPP is the point on the limit state function with the highest probability density and with the smallest distance to the mean values of all input parameters. For the FORM and SORM the MPP is searched in a first step. Then, the limit state function is approximated at the MPP by a linear function (FORM) or a quadratic function (SORM) and the probability of failure of the problem considered is determined. The MPP is found using optimization techniques, which makes the FORM and

SORM more computationally costly than FOSM approach. However, the probability of failure can be determined more accurately.

For the Monte Carlo method, samples of the random parameters are generated based on the stochastic distributions of these parameters. Then, the objective function is evaluated for all generated samples. Doing so, most generated samples accumulate around the mean values. For reliability analyses however, values that are close to the limit state function and which usually occur with low probability are of higher interest. Therefore, Monte Carlo simulations are often improved by importance sampling. Here, samples are not generated based on their distribution function, but on some arbitrary function and then weighted with their probability. For instance, sampling techniques like Latin hypercube sampling can be used in order to ensure that the whole random space is captured. In difference to that, directional sampling (or line sampling) is used to generate samples e.g. around the limit state function. Adaptive sampling methods allow modifying the areas in which most samples are generated during the sampling procedure. No matter which type of sampling technique is used, the objective function must be evaluated a multitude of times for a Monte Carlo simulation. If a very large number of random parameters is considered, Monte Carlo simulations can be more efficient than methods like FOSM or FORM. However, for the number of parameters considered within this thesis, the Monte Carlo method is always the most costly one.

Response surface (RS) methods can be used to reduce the number of evaluation of the objective function, required for a Monte Carlo simulation. Similar to the use of RS methods for optimization, the response surface of the objective function is approximated by generating a number of samples based on a design of experiments approach. The objective function is evaluated for these samples and the RS is obtained by interpolating between the obtained support values. Given a RS, the samples generated within a Monte Carlo simulation are evaluated by interpolation on the RS instead of actually evaluating the objective function. This increases the efficiency at the expense of accuracy.

When applying a probabilistic method, the balance of accuracy and efficiency has to be found, which always depends on the problem considered. For this purpose, the most accurate as well as the most efficient methods are applied for probabilistic design within this thesis, namely the Monte Carlo method and a further developed FOSM/SOTM type approach. These approaches are discussed in detail in chapter 4.

1.3   Objective and Outline

Though several probabilistic analyses of structures prone to buckling have been performed in the past, almost no work compared the estimated distribution with experimentally obtained empirical distribution (with the exception of [44–46,91], which have been published during the preparation of this thesis and/or are part of this thesis). However, a less conservative but still reliable design load compared to existing guidelines can only be determined, if the distribution of buckling load is predicted accurately and if the probabilistic methods that are used in this context are validated. At the same time, this probabilistic method must be fast, if it is the objective to use it for design purposes. All probabilistic design procedures provided before are either fast but do not determine the real distribution of buckling load, or require too high computational costs to be applicable as a design method.

The objective of the present work is to provide a validated probabilistic methodology that is on the one hand accurate enough to determine the actual stochastic distribution of load carrying capability and on the other hand fast enough to serve as a design tool and can even be applied within design optimization.

For stiffened composite panels, which are less sensitive to imperfections than cylindrical shells, but show a much more complex failure behavior, so far no probabilistic concept has been proposed to determine the probability of failure and the reliability of a design, respectively. Here, the objective of the present work is to probabilistically analyze stiffened composite panels and to furthermore derive a methodology for determining the reliability of stiffened panels under consideration of different failure modes.

In the following chapter, the behavior of axially compressed cylindrical shells and stiffened panels made of composite material is described as it has been detected within experiments. Basis of all probabilistic analyses and other design concepts is a validated numerical model and a robust and accurate solution procedure. Different approaches for determining buckling loads and material failure of composite structures by numerical analyses are given in chapter 3. In chapter 4 the theoretical basics of probabilistic analyses is given and the proposed design procedures are summarized. In chapter 5 a simple example of an objective function is given, for which the stochastic distribution function is determined analytically and which is used to validate the implementation of the probabilistic methods considered. The probabilistic procedure is applied to a set of cylindrical shells in chapter 6 and the reliability of the design loads given by other design procedures is evaluated. The data basis for a probabilistic analysis of stiffened panels is discussed in chapter 7 and the proposed design concept for stiffened panels is applied. In chapter 8 the design of the cylindrical shells is optimized with respect to the probabilistically motivated design load. The optimization is also performed using other design procedures and the influence of the chosen design procedure on the optimal design configuration is determined. Procedures to optimize the design of a stiffened panel are described in chapter 9 and an enhanced design is derived. Chapter 10 summarized major findings, consequential conclusions and open questions, as well as need for further research.

2   Experimental Behavior

The validation of numerical simulation methods always requires the comparison with well defined experimental tests. For the validation of probabilistic methods, the same type of test has to be performed for numerous nominally identical structures. In the current chapter, the experimentally observed structural behavior of composite cylindrical shells and curved, stiffened panels under axial compression is described in general as well as especially for the tests that serve for the validation of the numerical models and probabilistic methods applied in chapter 6 and chapter 7.

2.1   *Unstiffened Cylindrical Composite Shells*

As stated in section 1.2, a multitude of experimental tests of cylindrical shells have been performed in the past. Esslinger [18,92] recorded the highly dynamic buckling process of metallic shells with high speed cameras and explained the mechanical mechanism that leads to the catastrophic collapse. Hühne et al. [27] monitored the buckling behavior of composite cylindrical shells with high speed digital image correlation system and were able to confirm Esslinger's findings for composite shells.

The buckling behavior of axially compressed cylindrical shells can be subdivided into three steps, namely the prebuckling range, the highly dynamic buckling process and the postbuckling range (see Figure 2-1).
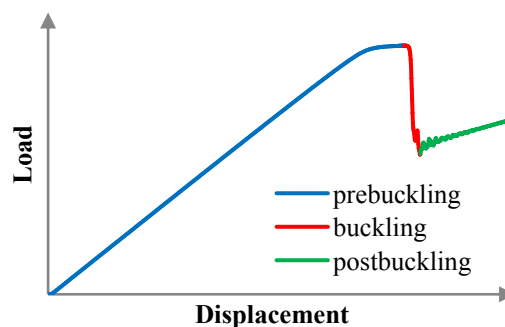
Figure 2-1: Load-displacement curve of an axially compressed composite cylindrical shell

In the prebuckling range, the cylinder cross section widens due the axial compression, which causes tension in circumferential direction. For the classical solution of the buckling load, isotropic material and boundary conditions that only fixes axial translation are assumed, which leads to a pure membrane stress state (see Figure 2-2, left). However, in reality most cylindrical shells are clamped at the edges and a widening is inhibited there (see Figure 2-2, right). Therefore, significant bending stresses occur close to the edges.

Furthermore, in composite shells with unsymmetrical laminate setup bending is induced by in plane forces. These effects can lead to nonlinearities in the prebuckling range. Of course, material nonlinearities can occur additionally. However, the cylindrical shells considered in the following did not show plastic deformations within the tests.

The actual onset of buckling starts with a single buckle. Due to initial imperfections, the shell starts to deflect inwards at a certain location. Therefore, the circumferential tension decreases or even turns into compression. The stabilizing effect of the circumferential stress vanishes and a local loss of stiffness leads to the first initiating buckle. The load redistribution around

this buckle leads to further buckles adjacent to the initiating one. The buckles start to spread over the whole shell and several buckling patterns are passed through until the stable postbuckling pattern occurs. The spread of buckles is attended by a significant decrease of the load the shell is able to carry, which is displayed by a large drop in the load-displacement curve.
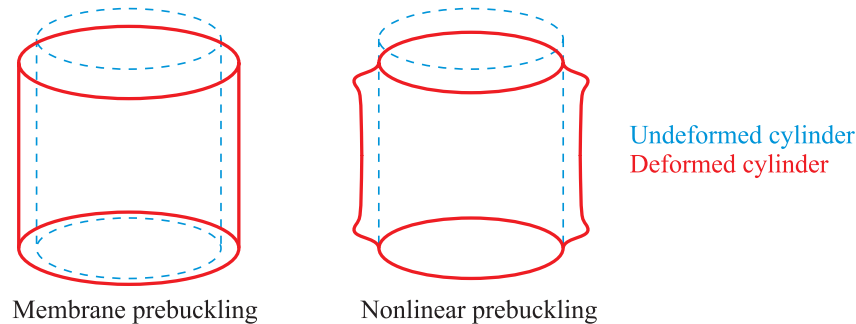
Figure 2-2: Effect of boundary conditions on prebuckling deformation

As the displacement is further increased in the postbuckling region, the oscillation induced by the dynamic buckling process fades away and load can be further increased, where the stiffness is significantly smaller than in the prebuckling range. In the deep postbuckling range, further buckling processes are attended by mode changes. However, since the first global buckling of a cylinder is considered as failure, the deep postbuckling behavior is not of interest within the framework of this thesis.

Because the initiation of buckling is caused by small imperfections, the experimentally determined buckling loads scatter a lot and are much smaller than predicted buckling loads given by perfect shell analyses.

Hühne et al. [27] tested six composite cylindrical shells with four different laminate setups. The experimentally determined buckling loads, the buckling loads given by numerical simulations of the ideal shells and the knockdown, the ration of experimental buckling load and perfect shell analysis, are given in Table 2-1.

Shell	Z07	Z08	Z09	Z10	Z11	Z12
Experiment in kN	21.8	21.9	15.7	15.7	16.7	18.6
Perfect shell analysis in kN	31.8	31.8	17.0	23.0	22.0	22.0
Knockdown	0.686	0.689	0.924	0.683	0.759	0.845

Table 2-1: Buckling loads for Z07-Z12 from [27]

Degenhardt et al. [42] tested ten nominally identical composite cylinders with the same laminate setup as shell Z07, tested by Hühne et al. The perfect shell analysis of Degenhardt et al. delivered a buckling load 38.2 kN, which differs from the analysis of Hühne et al. due to differing material properties. The experimentally determined buckling loads and the associated knockdowns are given in Table 2-2.

In Figure 2-3 the load-displacement curves of the cylinders tested by Degenhardt et al. [42] are depicted. The increasing slope at the beginning of the test is due to the fact that full contact has to be established at the beginning. The actual stiffness of the cylinders in the

prebuckling range is equal for all cylinders. While the deformations in the prebuckling range are influenced by the imperfections and therefore differ slightly for all shells, the postbuckling pattern is the same. An extensive description of the DLR test facilities and the experimental tests of the cylinders of set #2 as well as of the stiffened panels considered in chapter 7 are given in [93].

Shell	Z15	Z17	Z18	Z20	Z21	Z22	Z23	Z24	Z25	Z26
Experiment in kN	23.36	24.63	21.32	23.08	22.63	23.99	25.02	23.62	25.69	22.43
Knockdown	0.612	0.645	0.558	0.604	0.592	0.628	0.655	0.618	0.673	0.587

Table 2-2: Buckling loads for Z15-Z26 from [42]
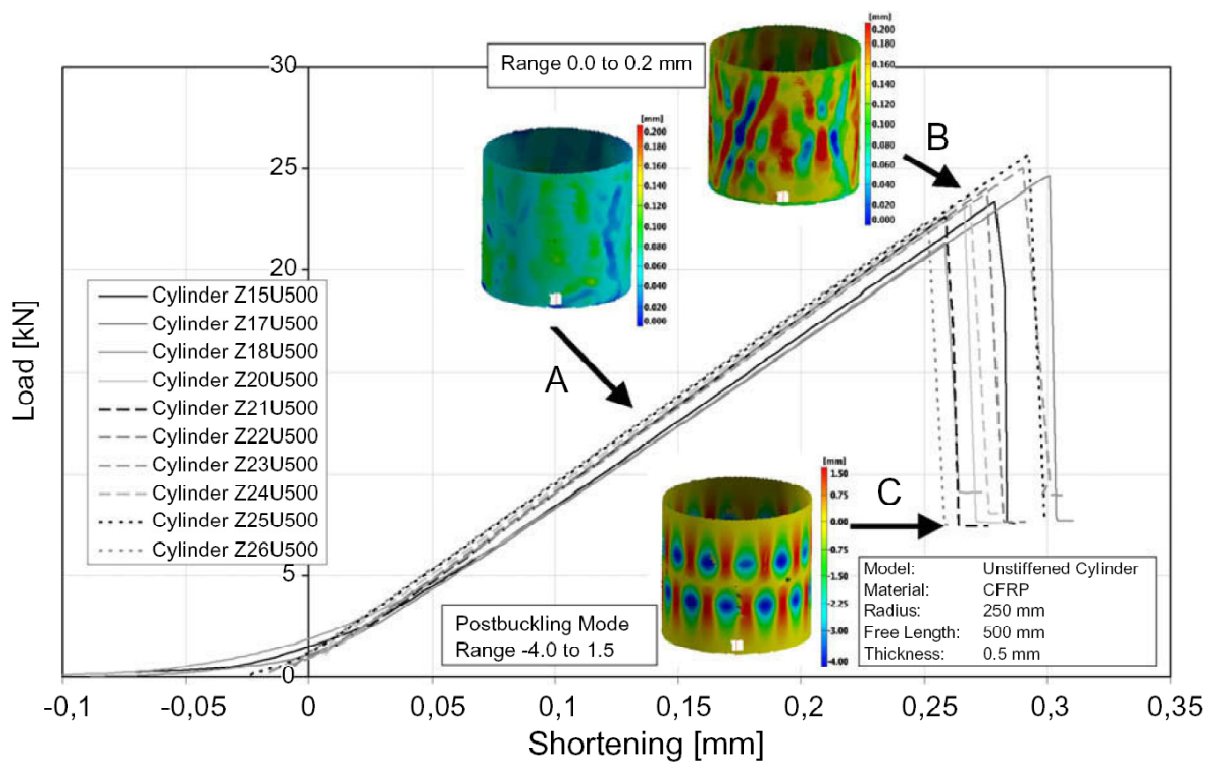
Figure 2-3: Load-displacement curves and displacement patterns for cylinders Z15-Z26 from [42]

Waters [94] and Hilburger [24] tested cylindrical composite shells with different laminate setup, for which the buckling loads are given in Table 2-3. The shell AW-Cyl-5-1 was damaged prior to testing, but tested nevertheless. In [24] the cylinders AW-Cyl-92-01, AW-Cyl-92-02 and AW-Cyl-92-03 are referred to as C1, C2 and C3. The normalized load-displacement curves of these cylinders are shown in Figure 2-4. Unsurprisingly, these cylinders show different prebuckling stiffnesses.

The experimental results show the large scatter of the knockdown for the different designs, but also for nominally identical shells. The shells tested by Hühne et al. [27] and Degenhardt et al. [42] all have the same nominal radius and wall thickness and therefore, the same knockdown factor would be applied using the existing guidelines, though the experimentally determined knockdown ranges from 0.558 for Z18 to 0.924 for Z09. The shells tested by Waters [94] and Hilburger [24] have the same radius, but different wall thickness. Since the

ply-thickness is equal for all shells, the shells AW-Cyl-2-1 to AW-Cyl-5-1 have a twice as thick wall thickness as the rest of the shell. Though it contradicts the guidelines given in section 1.2.4, for two of the thinner shells (AW-Cyl-11-1 and AW-Cyl-92-01) higher knockdown factors (KDFs) have been obtained.

Shell	Laminate	Experiment in kN	Perfect shell analysis in kN	Knockdown
AW-Cyl-1-1	$[\pm 45, 0, 90]_s$	134.2	184.1	0.729
AW-Cyl-2-1	$[\pm 45, \mp 45]_{2s}$	329.2	436.3	0.755
AW-Cyl-3-1	$[\pm 45, 0, 90]_{2s}$	657.5	745.9	0.881
AW-Cyl-4-1	$[\pm 45, 0_4, \mp 45]_s$	558.6	621.4	0.899
AW-Cyl-5-1*	$[\pm 45, 90_4, \mp 45]_s$	407.9	672.7	0.606
AW-Cyl-11-1	$[\pm 45, 0, 90]_{2s}$	676.6	745.9	0.907
AW-Cyl-92-01	$[\pm 45, 0_2]_s$	123.6	133.1	0.929
AW-Cyl-92-02	$[\pm 45, 90_2]_s$	142.0	170.1	0.835
AW-Cyl-92-03	$[\pm 45, 0, 90]_s$	152.0	184.1	0.826

*Cylinder was damaged prior to testing

Table 2-3: Buckling loads for AW-Cylinders from [39]

The observations show the strong influence of the laminate setup on the buckling load as well as on the sensitivity. Therefore, the physical effect of the laminate setup must be taken into account in novel design procedures.
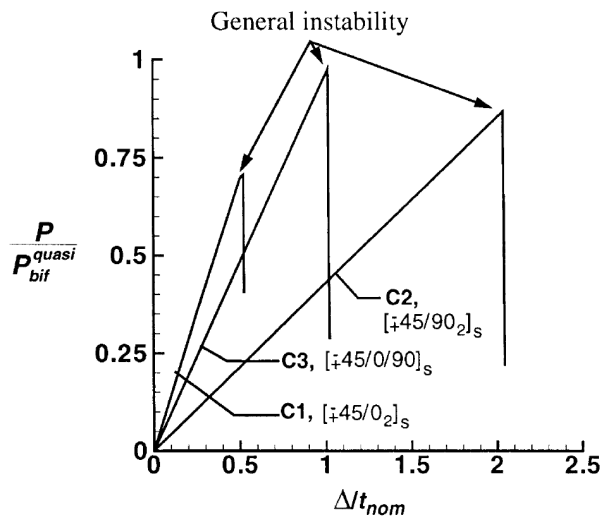
Figure 2-4: Normalized load-displacement curves for AW-Cyl-92-01, AW-Cyl-92-02 and AW-Cyl-92-03 from [24]

2.2   Stiffened Curved Composite Panels

For stiffened composite panels under axial compression the first point of instability is often given by buckling of the skin only. This point is often referred to as local buckling or skin

buckling. Local buckling is usually attended by a slight reduction of global stiffness, but the load can be further increased. As the stringers start to deflect laterally to the loading plane, the panel stiffness decreases significantly. Depending on the design, the global buckling in some cases corresponds to a decrease of the carried load and a drop in the load-displacement curve. When the axial displacement is further increased the load increases until material failure leads to the total collapse of the panel. An idealized, typical load-displacement curve of axially compressed stiffened panels is given in Figure 2-5.

Depending on the panel design, the global buckling load can be lower than the local buckling load. This may be the case if the bending stiffness of the skin is high relative to the bending stiffness of the stringers and/or if the stringers are spaced closely. However, in the context of this thesis only designs are regarded for which local buckling occurs before global buckling.
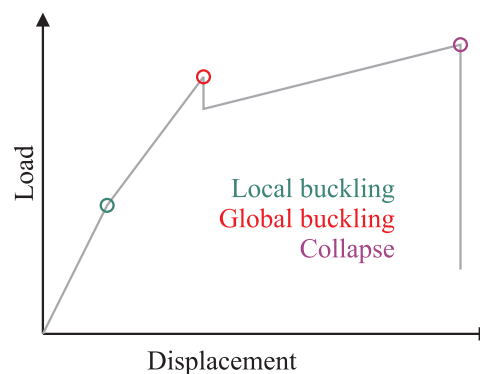
Figure 2-5: Load-displacement curve of a stiffened panel under axial compression

Zimmermann et al. [70] tested eight composite stiffened panels, for which the experimentally determined local buckling load and collapse load are given in Table 2-4. The panels P09-P11 have the same design, so do panels P12-P14 and P15-P16. The panels P12-P14 have one more stiffener and two more ply in the skin than the other panels. Panels P15-P16 have a smaller curvature radius than panels P09-P14.

Shell	P09	P10	P11	P12	P13	P14	P15	P16
Skin buckling load in kN	11.2	9.5	9.6	28.8	29.6	38.9	29.4	23.9
Global buckling load in kN[*]	42	43	42	70	66	72	75	73
Collapse load in kN	56.1	54.3	58.7	87.3	89.4	100.6	75.4	73.3

[*]The global buckling loads are not given explicitly in [70], but have been determined based on load-displacement curves given in [70] and the criterion for global buckling given in section 3.2.6

Table 2-4: Experimentally determined buckling loads for P09-P16 from [70]

The load-displacement curves and the associated displacement fields shown in Figure 2-6 confirm the already described typical behavior of stiffened panels. The prebuckling stiffnesses of the three nominally identical panels P12-14 are almost identical. Also in the postbuckling range the slope of the load-displacement curves compare well. However, the global buckling loads, detectable by the smooth decrease of reaction force in the load-displacement curves, show a noticeable scatter.
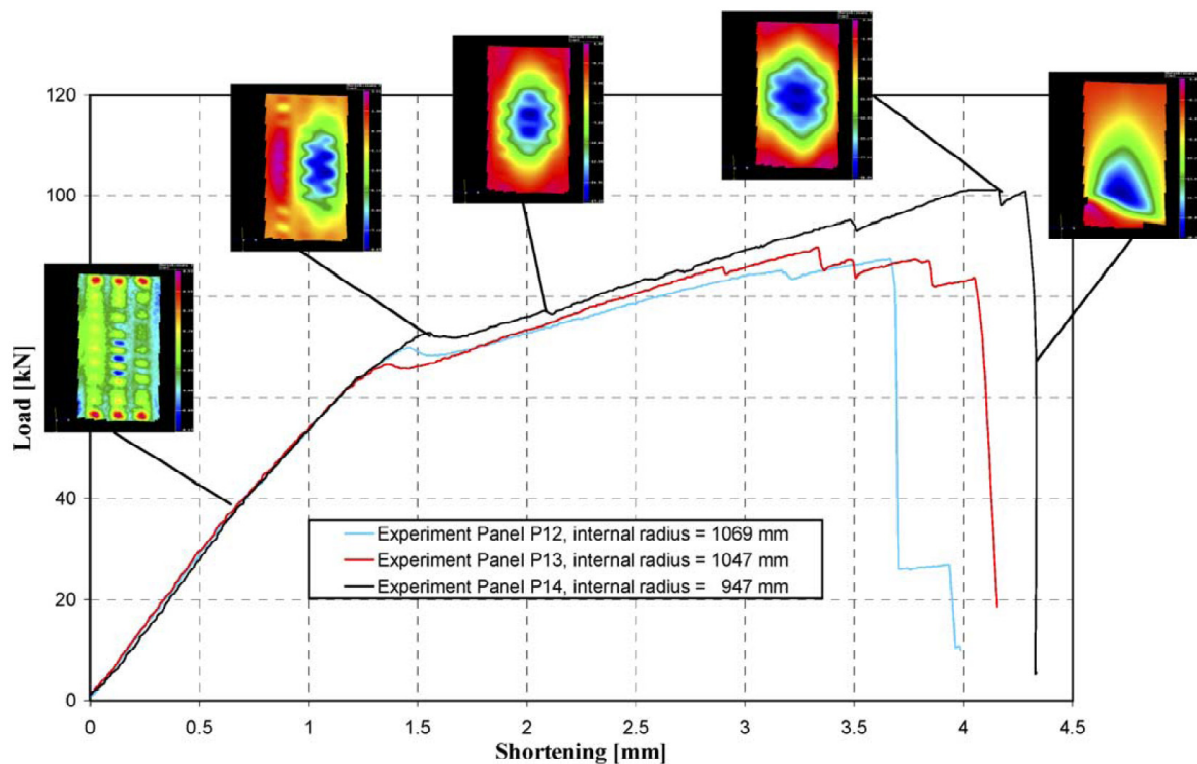
Figure 2-6: Load-displacement curves of panels P12-P14 and deformation patterns of P14 from [70]

A further test result of a panel tested at DLR is given by Orifici et al. [61]. From the load-displacement curve given in Figure 2-7 a global buckling load of 74.4kN and a collapse load of 83.6kN have been determined. Investigations of the failure mechanisms of this panel performed by Degenhardt et al. [62] show that large areas of the skin-stringer connection failed.
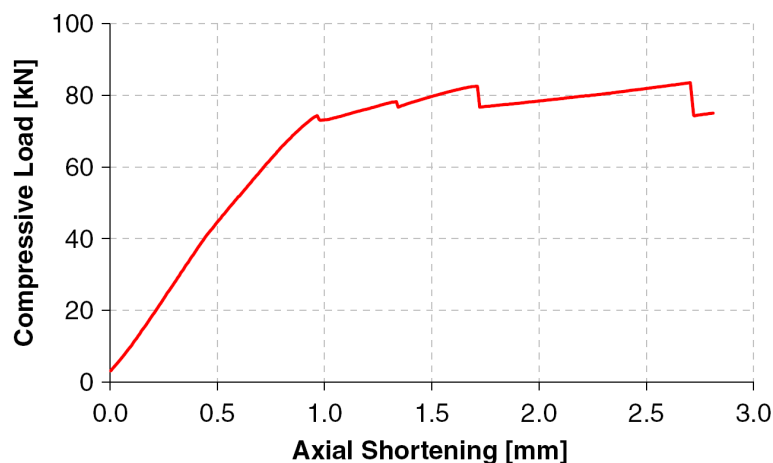
Figure 2-7: Load-displacement curve of stiffened panel from [61]

The results show that the load carrying capability of stiffened panels indeed can be exploited beyond local buckling, accepting small stiffness decreases. The load carrying capability is limited by global buckling and material failure, where both can interact.

3   Numerical Failure Analysis

The fundamental basis for probabilistic analyses, which have the objective to predict the stochastic distribution of load carrying capability, is a reliable deterministic simulation of the structural behavior. In the framework of this thesis, the deterministic analyses are performed using the finite element method. Two failure modes are considered that limit the load carrying capability. On the other hand, a significant loss of structural stiffness and/or a decrease of the carried load due to buckling are considered as structural failure. One the one hand, a structure is considered to fail if material failure occurs somewhere in the structure. The material failures considered occur in combination with buckling and the focus lies on the phenomenon of instability.

In this chapter, definitions of instability and analysis techniques for the numerical simulation of buckling are discussed. Furthermore, failure criteria for detecting the onset of material degradation in composite materials are given.

3.1   Definition of the Instability of Structures

In [95], El Naschie gives an overview of three criteria to define instability: the criterion of non-trivial equilibrium state, the dynamical criterion and the total potential energy criterion.

The most commonly used criterion for instability is the potential energy criterion. The total potential energy Π of a structure equals the sum of the elastic strain energy, stored in the deformed structure, and the potential energy of the applied forces. If the first variation of Π equals zeros, equilibrium is satisfied. A stable equilibrium configuration is given, if the potential energy is a relative minimum and hence, the second variation is positive. If the second variation is negative, an instable configuration is present and hence, the critical state is given, if the second derivative equals zero.

$$
\begin{aligned}
\delta \Pi = 0 & \quad \Rightarrow \quad \text{equilibrium} \\
\delta^2 \Pi > 0 & \quad \Rightarrow \quad \text{stable} \\
\delta^2 \Pi < 0 & \quad \Rightarrow \quad \text{instable} \\
\delta^2 \Pi = 0 & \quad \Rightarrow \quad \text{critical state}
\end{aligned}
\tag{3.1}
$$

Another widely used definition of instability is the criterion of non-trivial equilibrium state. Here, an equilibrium state is considered instable, if there is an adjacent equilibrium state. Mathematically, this is the case is the stability determinate $\det(\mathbf{K})$, derived either from equilibrium condition or the second derivative of the energy function, equals zero.

$$
\begin{aligned}
\det(\mathbf{K}) > 0 & \quad \Rightarrow \quad \text{stable} \\
\det(\mathbf{K}) < 0 & \quad \Rightarrow \quad \text{instable} \\
\det(\mathbf{K}) = 0 & \quad \Rightarrow \quad \text{critical state}
\end{aligned}
\tag{3.2}
$$

The dynamical criterion provides the most general definition of instability. Here, stability is given if a system that is perturbated returns to its initial equilibrium state. In case of instability, the system converges towards a different configuration, which is the case if the frequency determinant vanishes.

For conservative systems, all definitions deliver the same results. Following El Naschie [95], a system is conservative if the work is path independent. Considering no material

nonlinearities, but only geometric nonlinearity, no energy is dissipated and the inherent work is indeed path independent. Therefore, axially compressed cylinders as well as stiffened panels are considered conservative systems, at least until the onset of material failure.

For buckling analyses it is relevant to differ between bifurcation problems and snap through problem. For perfectly straight beams or shells under axial compression there exists a load level where the primary equilibrium path is intersected by a secondary path, while for imperfect structures this is not necessarily the case. The classic example to describe the difference between bifurcation problems and snap through problems is the von Mises truss, depicted in Figure 3-1. Due to the geometry of the problem, there is a local maximum on the load-displacement curve, which is called limit point. Increasing the applied load at this point would lead to a dynamic snap trough of the truss. If the bending stiffness of the two beams is small enough, the beams will buckle before the limit point is reached. However, in a simulation with perfectly straight beams the system will not take the secondary path. To detect the secondary path, which the system would take in an experiment, a small imperfection or perturbation would have to be applied to at least one beam.
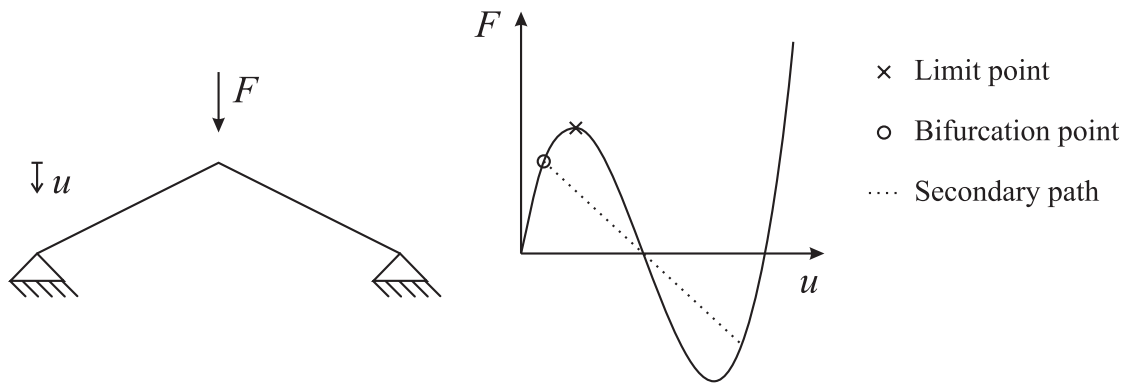
Figure 3-1: Load-displacement curve of von Mises truss

3.2   Buckling Analysis

In the following, commonly used techniques to detect points of instability using the finite element method are described.

3.2.1   Eigenvalue Analysis

Following the total potential energy criterion the second variation of the potential energy of a structure equals zero at points of instability. From this approach the linear eigenvalue problem is derived (see Singer et al. [2] or Wriggers [96]).

$$\left[\mathbf{K}_L + \lambda \left(\mathbf{K}_U + \mathbf{K}_\sigma \right) \right] \phi = \mathbf{0} \tag{3.3}$$

$$\mathbf{K}_T = \mathbf{K}_L + \mathbf{K}_U + \mathbf{K}_\sigma \tag{3.4}$$

$\mathbf{K}_L$ is the linear stiffness matrix, $\mathbf{K}_U$ the stiffness matrix that captures geometrically nonlinear behavior and the influence of initial deformations, respectively, and $\mathbf{K}_\sigma$ is the stiffness matrix that describes the stress depending stiffness. The eigenvalue λ is at the same time the load parameter and the eigenvector ϕ describes the associated buckling mode. The classical eigenvalue problem does not consider the prebuckling deformation and hence, is given by

$$\left[\mathbf{K}_L + \lambda \, \mathbf{K}_\sigma \right] \phi = \mathbf{0} \tag{3.5}$$

This way, points of instability are determined directly and relatively fast. However, due to a nonlinear prebuckling behavior, the direct solution without considering $\mathbf{K}_U$ can lead to inaccurate results. The closer the displacement field is to the real point of instability, the more accurate is the prediction given by the solution of the eigenvalue problem (see Figure 3-2). Figure 3-3 exemplarily shows the first buckling mode of shell Z07 from [27].
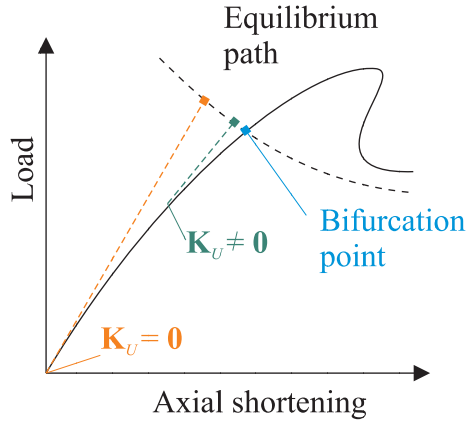
Figure 3-2: Sketch – load shortening curve with eigenvalue estimates
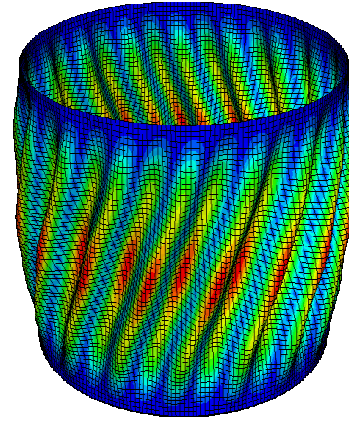
Figure 3-3: First buckling mode of shell Z07

In order to obtain the displacement dependent stiffness matrices $\mathbf{K}_U$ and $\mathbf{K}_\sigma$ for a certain equilibrium state, a geometrically nonlinear simulation must be performed. The fact that the current stiffness matrix $\mathbf{K}_T$ becomes singular if a point of instability is reached can then be used to detect bifurcation and limit points. However, it is still valuable to perform an eigenvalue analysis for the detected equilibrium state in order to determine whether a bifurcation point or a limit point has been detected. If the scalar product of eigenvector and load vector equals zero, a bifurcation point is reached, whereas if the scalar product does not equal zero, the current state equals a limit point.

$$\phi^T \mathbf{P} = 0 \rightarrow \text{bifurcation point}$$
$$\phi^T \mathbf{P} \neq 0 \rightarrow \text{limit point}$$

(3.6)

with the eigenvector ϕ and the load vector $\mathbf{P}$.

3.2.2   Nonlinear Static Analysis

With the criteria given in the previous, points of instability can be detected by "usual" geometrically nonlinear analyses that solve the equilibrium of internal and external force.

$$\mathbf{R}(\mathbf{u}, \lambda) = \mathbf{I}(\mathbf{u}) - \lambda \mathbf{P} = 0$$

(3.7)

$\mathbf{R}$ is the residual vector, $\mathbf{I}$ is the vector of internal forces and a function of the displacements vector $\mathbf{u}$, and $\mathbf{P}$ the vector of external forces that is multiplied by a load parameter λ. Equation (3.7) is usually solved with Newton iteration given by

$$\mathbf{K}_T(\mathbf{u}_i) \Delta \mathbf{u}_{i+1} = -\mathbf{R}(\mathbf{u}_i, \bar{\lambda})$$

(3.8)

The current stiffness matrix $\mathbf{K}_T$ and the residual vector $\mathbf{R}$ are functions of the actual displacement $\mathbf{u}_i$. In each iteration step, the displacement is increased by

$$\mathbf{u}_{i+1} = \mathbf{u}_i + \Delta \mathbf{u}_{i+1}$$

(3.9)

where $\Delta\mathbf{u}_{i+1}$ is obtained from equation (3.8).
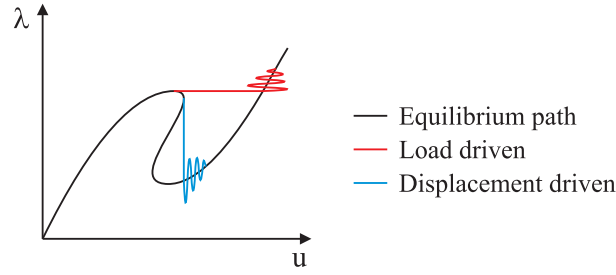
Figure 3-4: Load or displacement driven analysis of snap back problem

If a snap back problem shall be solved, a dynamic process occurs (see Figure 3-4) that only be simulated using artificial damping. For that, viscous forces $c\,\mathbf{M}^*\,\dot{\mathbf{u}}$ are introduced into the system of equations.

$$\mathbf{R}(\mathbf{u},\lambda)=\mathbf{I}(\mathbf{u})-\lambda\,\mathbf{P}+c\,\mathbf{M}^*\,\dot{\mathbf{u}}=\mathbf{0} \tag{3.10}$$

Here, the damping factor c is multiplied by an artificial mass matrix $\mathbf{M}^*$ and the vector of nodal velocities $\dot{\mathbf{u}}$, which is approximated by

$$\dot{\mathbf{u}}=\frac{\Delta\mathbf{u}}{\Delta t} \tag{3.11}$$

Here, the time increment Δt "may or may not have a physical meaning in the context of the problem being solved." [97]

3.2.3   Path Following Algorithms

In order to capture the load displacement curve of snap back problems, path following procedures like arc length methods can be used [96]. The basic idea is to consider the loading parameter λ as an additional degree of freedom and to extend the equation system that describes the equilibrium by a constrain equation $f=0$.

$$\begin{pmatrix}\mathbf{R}(\mathbf{u},\lambda)\\ f(\mathbf{u},\lambda)\end{pmatrix}=\mathbf{0} \tag{3.12}$$

The linearization then reads

$$\begin{pmatrix}\mathbf{K}_T & -\mathbf{P}\\ \nabla f & \dfrac{\partial f}{\partial\lambda}\end{pmatrix}_i\begin{pmatrix}\Delta\mathbf{u}\\ \Delta\lambda\end{pmatrix}_{i+1}=-\begin{pmatrix}\mathbf{R}\\ f\end{pmatrix} \tag{3.13}$$

Riks [98] proposed the following linear constrain equation.

$$f=(\mathbf{u}_0-\overline{\mathbf{u}})^T(\mathbf{u}-\mathbf{u}_0)+(\lambda_0-\overline{\lambda})(\lambda-\lambda_0) \tag{3.14}$$

Here, $\overline{\mathbf{w}}=(\overline{\mathbf{u}},\overline{\lambda})^T$ is the current state and $\mathbf{w}_0=(\mathbf{u}_0,\lambda_0)^T$ is the solution of a prediction step. The constraint equation is a plane perpendicular to the prediction step (see Figure 3-5, left).

Chrisfield proposed the nonlinear constrain equation that describes a hyper sphere around the current state $\overline{\mathbf{w}}=(\overline{\mathbf{u}},\overline{\lambda})^T$ with the radius Δs (see Figure 3-5, right).

$$f=\sqrt{(\mathbf{u}-\overline{\mathbf{u}})^T(\mathbf{u}-\overline{\mathbf{u}})+(\lambda-\overline{\lambda})^2}+\Delta s \tag{3.15}$$

The advantage of this formulation is that always one solution is found, which is not ensured using Riks' equation. The disadvantage is that multiple solutions may occur.
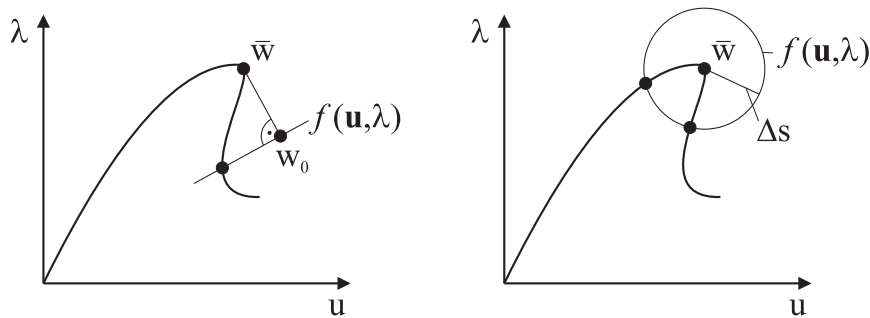
Figure 3-5: Arc length method with Riks (left) and Crisfield (right) constraints equation

The buckling of cylindrical shells is a snap back problem and therefore, arc length methods allow determining the whole equilibrium path. However, especially when regarding the perfect structure, many equilibrium paths, each connected to a certain buckling mode, are close to each other. It turned out that implemented arc length methods do not reliably find the desired equilibrium path.

Wriggers [96] provided a method to directly determine points of instability by utilizing the fact that the stiffness matrix becomes singular for a point of instability as constrained equation.

$$f = \mathbf{K}_T \, \phi = \mathbf{0} \qquad l = \|\phi\| - 1 = 0 \qquad\qquad (3.15)$$

The additional equation l ensures the exclusion of the trivial solution $\phi = 0$. By using (3.6) for the additional constrained equation, this methodology can even be utilized to search only bifurcation points or only limit points. It should be stressed that this methodology is actually not a path following method, but due to the similarities it is mentioned within this context.

If only the buckling load is of interest, the limit point can be determined with a load controlled simulation and the use of an arc length method unnecessarily increases the computation time.

3.2.4   Bisection Procedure

No matter whether "usual" geometrically nonlinear analyses is performed, or path following algorithms are used to capture the buckling behavior of a structure, it is possible that due to a too large increment a bifurcation point is missed. This can be checked by regarding the eigenvalues of the stiffness matrix. If a bifurcation point is missed, the stiffness matrix becomes indefinite and negative eigenvalues occur. By restarting the simulation at the last stable equilibrium state [99], or changing the direction of the path following procedure [96], and reducing the step size, the interval, in which negative eigenvalues occur, is determined (see Figure 3-6).

By introducing imperfections, the buckling of a cylindrical shell changes from a bifurcation problem to a snap through (or snap back) problem, where the limit point defines the buckling load. Therefore, the bisection procedure is required especially for analyses of perfect structures.
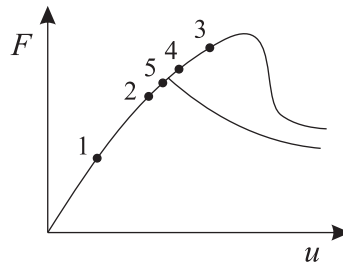
Figure 3-6: Bisection method for determining points of instability

3.2.5   Explicit Time Integration

Given the nonlinear differential equation of the time dependent displacement $\mathbf{u}(t)$

$$\mathbf{M}\,\ddot{\mathbf{u}}(t)+\mathbf{C}\,\dot{\mathbf{u}}(t)+\mathbf{I}\big(\mathbf{u}(t)\big)=\mathbf{P}(t) \tag{3.16}$$

with the mass matrix $\mathbf{M}$, the damping matrix $\mathbf{C}$, the vector of internal forces $\mathbf{I}$ and the vector external forces $\mathbf{P}$. By approximating velocity and acceleration at the time step t_n by central differences

$$\dot{\mathbf{u}}(t_n)=\frac{\mathbf{u}(t_{n+1})-\mathbf{u}(t_{n-1})}{2\,\Delta t}$$

$$\ddot{\mathbf{u}}(t_n)=\frac{\mathbf{u}(t_{n+1})-2\,\mathbf{u}(t_n)+\mathbf{u}(t_{n-1})}{\Delta t^2} \tag{3.17}$$

Equation (3.16) can be transformed to the linear system of equations

$$\left[\mathbf{M}+\tfrac{\Delta t}{2}\mathbf{C}\right]\mathbf{u}(t_{n+1})=\Delta t^2\left[\mathbf{P}(t_n)-\mathbf{I}\big(\mathbf{u}(t_n)\big)\right]+\tfrac{\Delta t}{2}\mathbf{C}\,\mathbf{u}(t_{n-1})+\mathbf{M}\left[2\,\mathbf{u}(t_n)-\mathbf{u}(t_{n-1})\right] \tag{3.18}$$

which can be solved with respect to the displacements $\mathbf{u}$ at the time t_{n+1}. Since the matrices $\mathbf{M}$ and $\mathbf{C}$ are time independent, the left hand side has to be decomposed only once. Because the right hand side is known, the system of equations can be solved very efficiently for each time step. The efficiency of the procedure is limited by the maximum time step Δt. Additional considerations have to be made for the initial conditions. For details the reader should refer to [96].

Concerning the buckling analysis of shells, the explicit time integration appears to be less efficient than implicit algorithms until the onset of buckling. However, in order to capture the highly dynamical buckling process and the postbuckling behavior, the explicit time integration is well suited due to its robustness.

3.2.6   Determination of Global Buckling of Stiffened Panels

In difference to cylindrical shells, for stiffened panel it is often not the first point of instability that limits the load carrying capability. As described in section 2.2, the load still can be increased after the skin of a stiffened panel has buckled. The skin buckling can be detected for instance by the procedure given in section 3.2.1. The global buckling load however appears in the post buckling range and can only be captured using one of the methods described in section 3.2.2-3.2.5. The problem in identifying global buckling of stiffened panels is that due to imperfections or design it can appear that neither a bifurcation point nor a limit point occurs at the onset of global buckling. Hence, none of the definitions given in 3.1 applies. Nevertheless, large displacements lateral to the loading direction go along with significant

stiffness reduction and an upper bound must be defined for this phenomenon. For the identification of the global buckling load, three criteria are discussed in the following, for which an overview is given in Table 3-1.

The most intuitive definition of global buckling is the onset of radial displacement of one of the stringers. However, if an imperfect structure is considered there is a small radial displacement of the stringers from the beginning of the simulation. The solution is to define an upper bound for the radial displacement of stringers. This upper bound is hard to justify and can significantly influence the value obtained for the global buckling load.

Another technique for identifying global buckling, which is also used in experiments, is to monitor the axial strains on the stringer foot and below the skin at the same position of the shell. From the difference of the strains, the onset of bending of stringers can be detected. However, the same disadvantages as mentioned before are valid for this technique.

Criterion	Advantage	Disadvantage
Radial deformation of stringer / bending strains	Close to the general understanding of global buckling	In practice, an upper bound for lateral displacement/bending must be chosen, which does not necessarily coincide with drop in load-displacement curve
Drop in load-displacement curve	Well defined point in the load-displacement curve	Not applicable, if no drop occurs (e.g. due to imperfections)
Global in-plane stiffness reduction	Describes the actual problem of global buckling; captures drops in the load-displacement curve	Lower bound for stiffness reduction must be chosen

Table 3-1: Advantages and disadvantages of different criteria for identifying global buckling

A well defined point that indicates global buckling is a drop in the load-displacement curve, as it appears for many curved panels. However, not for every design this drop appears and even for panels, for which the simulation of the ideal panel delivers a drop in the load-displacement curve, this drop can vanish as imperfections are introduced. The last criterion considered is given by the reduction of in-plane stiffness, which is obtained from the load-displacement curve. Then, global buckling is defined as the state where the current stiffness is, say 50%, of the initial stiffness. If there is a drop in the load-displacement curve, the global buckling load is detected close to the drop. If no drop occurs, the global buckling load is detected at a state, where the buckling of the stringers leads to a significant stiffness reduction. Thus, the stringer deformation criterion as well as the drop criterion are captured by the global stiffness criterion. Furthermore, the last criterion is based on the actual technical problem of global buckling, because the significant reduction is the failure mode that shall be avoided when designing stiffened panels. The obvious disadvantage of this criterion is the fact that the percentage of allowed stiffness reduction must be chosen more or less arbitrarily.

Figure 3-7 depicts the described criteria and the results they yield for a panel with a significant drop in the load-displacement curve (design A) and for a panel without drop in the load-displacement curve (design B). If the lateral deflection of stringers or the bending strains are monitored and a certain upper bound defines global buckling, there is the risk that

the obtained global buckling load does not coincide with the drop in the load-displacement curve of design A (Figure 3-7, right). If however the global stiffness is monitored, the global buckling load will always be found close to the drop (Figure 3-7, left).
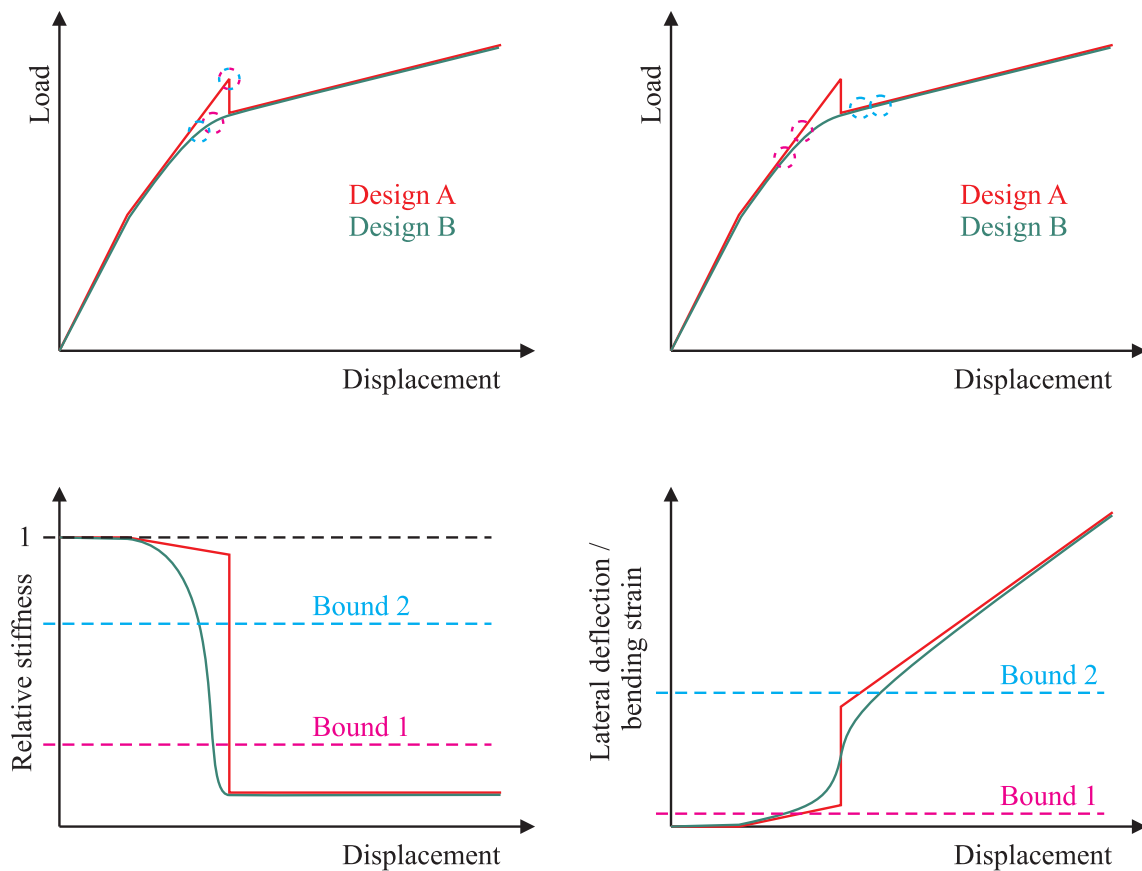
Figure 3-7: Different criteria for global buckling

3.3   *Material failure analysis*

In axially compressed stiffened panels material failure can occur before or after global buckling, and can even interact with stability failure. The panels that are considered in section 7 are designed such that material failure occurs after global buckling. Hence, no material degradation needs to be considered within the buckling analysis. However, the onset of degradation is relevant for design and therefore, criteria to detect material failure in fiber composites and in the skin-stringer connection are given in the following. Furthermore, only composite materials with unidirectional plies are considered. The failure criteria given in section 3.3.2 and 3.3.3 are applicable to these types of laminates with transversally isotropic plies, but e.g. not to textile composites.

While the skin stringer connection will be modeled with cohesive elements, standard shell elements are used in the simulation for the skin and the stringers themselves (see section 7.2). Hence, no stresses in thickness direction occur ($\sigma_{33} = 0$). Due to this simplification, no delaminations can be detected in the laminate. To capture the influence of the stresses in thickness direction a multi scale approach as suggested in [67] and [100] could be used.

3.3.1   Cohesive Zone Failure

In order to capture the onset of skin-stringer separation, cohesive elements are used to connect stringer foot and skin, and the quadratic nominal stress damage criterion [97] is used to detect the onset of separation.

$$\left(\frac{\langle t_n \rangle}{t_n^0}\right)^2 + \left(\frac{t_s}{t_s^0}\right)^2 + \left(\frac{t_t}{t_t^0}\right)^2 = 1 \tag{3.19}$$

Here, t_n is the normal stress perpendicular to the cohesive zone, t_s and t_t are the shear stresses in the cohesive zone and t_n^0, t_s^0 and t_t^0 are the maximum allowable stresses. Cohesive elements allow defining the thickness of the cohesive zone to be smaller than the element thickness. The element thickness is given by the distance of the center plane of the skin and the center plane of the stringer foot, but the cohesive zone equals the thickness of the adhesive layer, which is much smaller (see also section 7.2).

3.3.2   Hashin Criterion for Intra Lamina Failure

For detecting the onset of material failure in the plies, the Hashin criterion [73] can be used. Hashin's criterion for fiber fracture is given by

$$\frac{\sigma_{11}^2}{X_t^2} + \frac{\tau_{12}^2 + \tau_{13}^2}{S_{\perp\parallel}^2} > 1 \quad \text{for } \sigma_{11} > 0 \quad \text{and} \quad \frac{\sigma_{11}^2}{X_c^2} > 1 \quad \text{for } \sigma_{11} < 0 \tag{3.20}$$

With the simplification that $\sigma_{33} = 0$, the criteria for matrix cracking can be written as

$$\frac{\sigma_{22}^2}{Y_t^2} + \frac{\tau_{23}^2}{S_{\perp\perp}^2} + \frac{\tau_{12}^2 + \tau_{13}^2}{S_{\perp\parallel}^2} > 1 \quad \text{for } \sigma_{22} > 0 \tag{3.21}$$

and

$$\frac{\sigma_{22}^2}{4 S_{\perp\perp}^2} + \frac{\sigma_{22}}{Y_c}\left[\left(\frac{Y_c}{2 S_{\perp\perp}}\right)^2 - 1\right] + \frac{\tau_{12}^2 + \tau_{13}^2}{S_{\perp\parallel}^2} + \frac{\tau_{23}^2}{S_{\perp\perp}^2} > 1 \quad \text{for } \sigma_{22} < 0 \tag{3.22}$$

While the criterion for fiber failure turned out to be sufficiently accurate, other failure criteria provide more satisfying results for inter fiber failure [75].

3.3.3   Puck Criterion for Inter Fiber Failure

While Hashin's criteria for failure in fiber direction (3.20) perform well, the criteria (3.21) and (3.22) for inter fiber failure showed potential for improvement. A more advanced inter fiber fracture criterion that allows differing between certain fracture modes has been proposed by Puck [74]. Puck formulated his criterion with respect to the stresses in the fracture plane σ_n, τ_{nt} and τ_{n1}. (see Figure 3-8)

The criteria for inter fiber fracture are given by

$$f_E(\theta) = \sqrt{\left[\left(\frac{1}{R_\perp^{(+)A}} - \frac{p_{\perp\psi}^{(+)}}{R_{\perp\psi}^A}\right)\sigma_n\right]^2 + \left(\frac{\tau_{nt}}{R_{\perp\perp}^A}\right)^2 + \left(\frac{\tau_{n1}}{R_{\perp\parallel}^A}\right)^2} + \frac{p_{\perp\psi}^{(+)}}{R_{\perp\psi}^A}\sigma_n \quad \text{for } \sigma_n(\theta) \geq 0 \tag{3.23}$$

and

$$f_E(\theta) = \sqrt{\left(\frac{\tau_{nt}}{R_{\perp\perp}^A}\right)^2 + \left(\frac{\tau_{n1}}{R_{\perp\parallel}^A}\right)^2 + \left[\frac{p_{\perp\psi}^{(-)}}{R_{\perp\psi}^A}\sigma_n\right]^2} + \frac{p_{\perp\psi}^{(+)}}{R_{\perp\psi}^A}\sigma_n \quad \text{for } \sigma_n(\theta) < 0 \qquad (3.24)$$

with

$$R_{\perp}^{(+)A} = Y_t \quad , \quad R_{\perp\parallel}^A = S_{\perp\parallel} \quad , \quad R_{\perp\perp}^A = \frac{Y_c}{2\left(1 + p_{\perp\perp}^{(-)}\right)} \quad ,$$

$$\frac{p_{\perp\psi}^{(+)}}{R_{\perp\psi}^A} = \frac{p_{\perp\perp}^{(+)}}{R_{\perp\perp}^A}\cos^2\psi + \frac{p_{\perp\parallel}^{(+)}}{R_{\perp\parallel}^A}\sin^2\psi \quad \text{and} \quad \frac{p_{\perp\psi}^{(-)}}{R_{\perp\psi}^A} = \frac{p_{\perp\perp}^{(-)}}{R_{\perp\perp}^A}\cos^2\psi + \frac{p_{\perp\parallel}^{(-)}}{R_{\perp\parallel}^A}\sin^2\psi$$

$$(3.25)$$
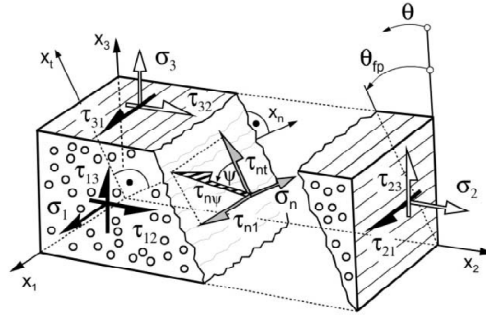
Figure 3-8: Fracture plane in Puck's inter fiber fracture criterion, from [101]

Beside the strength parameters, the parameters $p_{\perp\perp}^{(+)}$ and $p_{\perp\perp}^{(-)}$, which describe the slope of the failure surface at the transition from fiber lateral compression to tension (see Figure 3-9), have to be determined experimentally as described in [101].
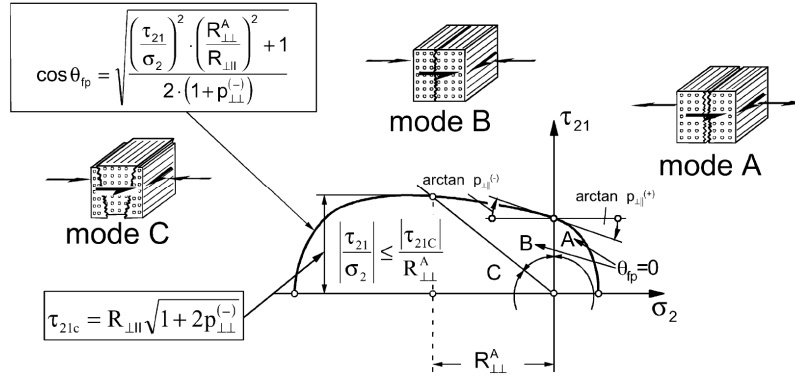
Figure 3-9: Analytical solutions for the plane stress state of Puck's inter fiber fracture criterion, from [101]

As depicted in Figure 3-9, Puck's criterion differs between three failure modes of inter fiber failure. If the stresses perpendicular to the fiber direction are positive, mode A failure is present and the failure criterion is given by (3.23). In case the UD ply is under compression perpendicular to the fiber direction, the criterion is given by (3.24) and a mode B or mode C failure is present. Depending on the fraction of shear stresses and normal stress, the fracture plane can be perpendicular to the normal stresses and parallel to the shear stresses, which is assigned as mode B. In case of a high fraction of compressive normal stresses, the fracture plane is inclined and a wedge like piece of the laminate is pushed out perpendicular to the normal stress and fiber direction (see Figure 3-9, left), which is called mode C failure.

In order to find the decisive fracture plane, which is described by the angle θ, the failure criteria are evaluated for several angles and the decisive plane is determined iteratively. Therefore, the evaluation of the criterion is time consuming.

3.3.4   Invariant Base Quadratic Criterion for Inter Fiber Failure

Vogler et al. [76] proposed a failure criterion for inter fiber fracture that is based on the invariants of the stress tensor, which is referred to as Invariant base Quadratic Criterion (IQC, see also [102]). The IQC is given by

$$\beta_1 I_1 + \beta_2 I_2 + \beta_3 I_3 + \beta_{32} I_3^2 = 1 \tag{3.26}$$

where following invariants of the stress tensor are used by Vogler et al.

$$
\begin{aligned}
I_1 &= \tfrac{1}{2}\operatorname{tr}\left(\boldsymbol{\sigma}^{\text{pind}}\right)^2 - \mathbf{a}^T\left(\boldsymbol{\sigma}^{\text{pind}}\right)^2 \mathbf{a} \\
I_2 &= \mathbf{a}^T\left(\boldsymbol{\sigma}^{\text{pind}}\right)^2 \mathbf{a} \\
I_3 &= \operatorname{tr}\left(\boldsymbol{\sigma}\right) - \mathbf{a}^T \boldsymbol{\sigma}\,\mathbf{a}
\end{aligned}
\tag{3.27}
$$

The vector $\mathbf{a}$ describes the fiber direction and $\boldsymbol{\sigma}^{\text{pind}}$ is the extra stress tensor, given by

$$\boldsymbol{\sigma}^{\text{pind}} = \boldsymbol{\sigma} - \tfrac{1}{2}\left[\operatorname{tr}\left(\boldsymbol{\sigma}\right) - \mathbf{a}^T \boldsymbol{\sigma}\,\mathbf{a}\right]\mathbf{1} + \tfrac{1}{2}\left[\operatorname{tr}\left(\boldsymbol{\sigma}\right) - 3\mathbf{a}^T \boldsymbol{\sigma}\,\mathbf{a}\right]\mathbf{A} \tag{3.28}$$

with $\mathbf{A} = \mathbf{a}\,\mathbf{a}^T$ being the structural tensor of $\mathbf{a}$. In case the fiber direction is given by $\mathbf{a} = (1,0,0)^T$ and stress in thickness direction equals zero ($\sigma_{33} = 0$), the invariants are given by

$$
\begin{aligned}
I_1 &= \tfrac{1}{4}\sigma_{22}^2 + \tau_{23}^2 \\
I_2 &= \tau_{12}^2 + \tau_{13}^2 \\
I_3 &= \sigma_{22}
\end{aligned}
\tag{3.29}
$$

The parameters β_1, β_2, β_3 and β_{32} in (3.26) are depending on the strength parameters of the lamina.

$$
\begin{aligned}
\beta_1 &= 1/S_{\perp\perp}^2 \\
\beta_2 &= 1/S_{\perp\parallel}^2 \\
\beta_{32} &= \frac{Y_t^{-1} - Y_c^{-1} - \tfrac{1}{4}\beta_1\left(Y_t - Y_c\right)}{Y_t - Y_c} \\
\beta_3 &= Y_t^{-1} - \tfrac{1}{4}\beta_1 Y_t - \beta_{32} Y_t
\end{aligned}
\tag{3.30}
$$

Inserting (3.29) and (3.30) into (3.26) yields the simplified formulation of the IQC given by

$$\frac{\tau_{23}^2}{S_{\perp\perp}^2} + \frac{\tau_{12}^2}{S_{\perp\parallel}^2} + \frac{\tau_{13}^2}{S_{\perp\parallel}^2} + \left[\frac{Y_t - Y_c}{Y_t} + \frac{Y_t}{Y_c} - 1\right]\frac{\sigma_{22}}{Y_t - Y_c} + \left[\frac{1}{Y_t} - \frac{1}{Y_c}\right]\frac{\sigma_{22}^2}{Y_t - Y_c} = 1 \tag{3.30}$$

Figure 3-10 shows the interaction of transverse shear and compression perpendicular to the fiber as taken into account by the invariant based quadratic criterion. The material law that Vogler et al. [76] proposed along with IQC turned out to give accurate results even for complex stress states, as occurring in ultra thick laminates [103]. Compared to Puck's criteria, the IQC is relatively fast, since it does not require the determination of the fracture plane. Furthermore, IQC requires fewer parameters, which have to be determined from experiments. For a detailed comparison the reader should refer to [84].
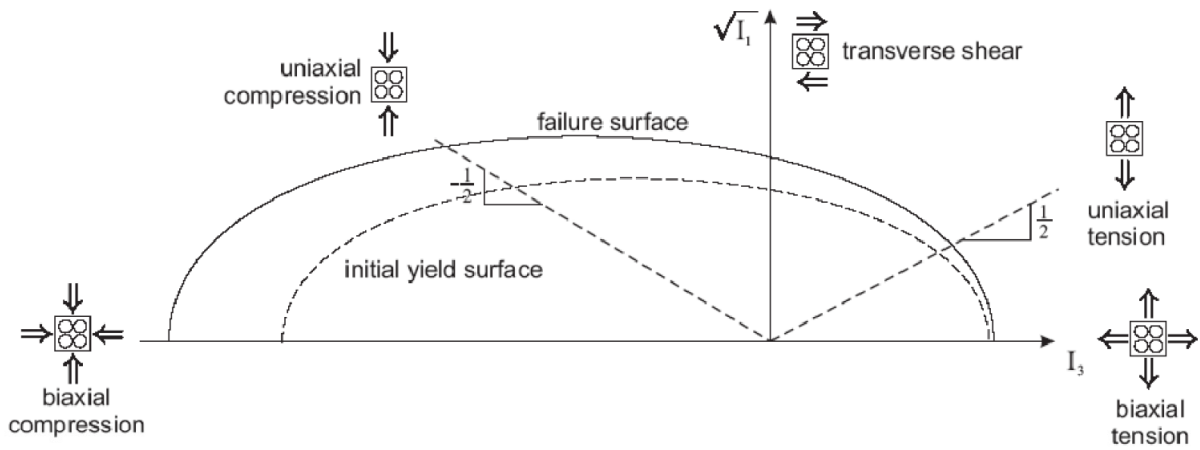
Figure 3-10: Yield and failure surface of the transversely-isotropic material model of Vogler et al., from [76]

4   Probabilistic Design Method

The probabilistic methods that are the basis for the proposed design procedure are described in this chapter. This includes the modeling and reduction techniques for scattering input parameters, especially geometric imperfections. The probabilistic design approach itself is presented including a summarizing flow chart. Therefore, the current chapter can be regarded as the core of this thesis. Furthermore, the basic concept of the convex anti-optimization is given and the derivatives of the design loads according to the probabilistic approach and convex anti-optimization are derived, which can be used for design optimization.

4.1   *Representation of Geometric Imperfections*

The geometric imperfection of a shell $\overline{W}(x, y)$ is a two-dimensional random field. As shown in Figure 4-1, the geometric imperfections are defined inward positive, the coordinate x refers to the axial direction and the coordinate y refers to the circumferential direction on the surface of the ideal cylinder.

For probabilistic analyses, this field must be parameterized in order to capture the characteristics of this field by a random vector. Furthermore, it is desirable to have as few as possible random parameters, since the number of parameters determines the computational cost of the introduced probabilistic procedures.
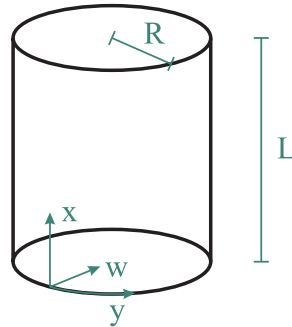
Figure 4-1: Sign convention for geometric imperfections

4.1.1   *Fourier Series*

In general, the double Fourier series approximation f_F of a periodic function f is given by

$$
\begin{aligned}
f(x, y) \approx f_F(x, y) = \sum_{k=0}^{n_x} \sum_{l=0}^{n_y} \Bigg(& A_{kl} \cos\frac{k\pi x}{a} \cos\frac{l\pi y}{b} + B_{kl} \cos\frac{k\pi x}{a} \sin\frac{l\pi y}{b} \\
& + C_{kl} \sin\frac{k\pi x}{a} \cos\frac{l\pi y}{b} + D_{kl} \sin\frac{k\pi x}{a} \sin\frac{l\pi y}{b} \Bigg)
\end{aligned}
\tag{4.1}
$$

The derivation from the product of two one-dimensional Fourier series is given in Appendix A. Here, a is the period in the x-direction, and b is the period in the y-direction. A_{kl}, B_{kl}, C_{kl} and D_{kl} are the Fourier coefficients. Theoretically, the Fourier series describes a function exact, if the number of coefficients considered is infinite. In practice the number of coefficients considered is limited by the bounds of the sums n_x and n_y.

Elishakoff and Arbocz [34] proposed to describe the geometric imperfection field of cylindrical shells by double Fourier series. Since the imperfection pattern is a periodic

function only in the circumferential direction, the Fourier series approximation leads to inaccuracies at the boundaries (see Appendix A). Hence, two different series are proposed in the literature, the half wave cosine (4.2) and the half wave sine approach (4.3).

$$\bar{W}(x,y) = 2t \sum_{k=0}^{n_1} \sum_{l=0}^{n_2} \cos\frac{k\pi x}{L}\left(A_{kl}\cos\frac{ly}{R} + B_{kl}\sin\frac{ly}{R}\right) \tag{4.2}$$

$$\bar{W}(x,y) = 2t \sum_{k=1}^{n_1} \sum_{l=0}^{n_2} \sin\frac{k\pi x}{L}\left(C_{kl}\cos\frac{ly}{R} + D_{kl}\sin\frac{ly}{R}\right) \tag{4.3}$$

L, R and t are length, radius and wall thickness of the shell. x and y are the coordinate on the shell surface in axial and circumferential direction. L is assumed to equal the half period in x-direction and the index k equals the number of axial half waves. The period in y-direction equals $2R\pi$, which is why π disappears in the y-terms, and the index l equals the number of circumferential full waves. For the characterization of imperfections, the Fourier coefficients are normalized with the wall thickness t and hence, the series must be multiplied with t.

Note that in the literature concerning buckling of cylinders, the factor two in (4.2) and (4.3) does not appear. Then, the Fourier coefficients as defined in Appendix A simply have to be doubled. In the framework of this thesis the Fourier series approximation will also be used for the imperfections of stiffened panels and hence, the more general double Fourier series (4.1) is the starting point and the Fourier coefficients are defined according to the general approach.

Using the half wave sine approach, no imperfections are captured at the boundaries of the shell, because

$$\sin\frac{k\pi x}{L} = 0 \quad\text{for}\quad x = 0 \text{ and } x = L \tag{4.4}$$

Thus, the half wave cosine approach leads to a more accurate approximation of measured geometric imperfections in most cases. The half wave cosine approach can also be represented by

$$\bar{W}(x,y) = 2t \sum_{k=0}^{n_1} \sum_{l=0}^{n_2} \bar{\xi}_{kl} \cos\frac{k\pi x}{L}\cos\left(\frac{ly}{R} - \bar{\varphi}_{kl}\right) \tag{4.5}$$

with $\bar{\xi}_{kl} = \sqrt{A_{kl}^2 + B_{kl}^2}$ and

$$\tan(\bar{\varphi}_{kl}) = \frac{B_{kl}}{A_{kl}} \quad\text{for}\quad A_{kl} > 0$$

$$\tan(\bar{\varphi}_{kl} - \pi) = \frac{A_{kl}}{B_{kl}} \quad\text{for}\quad A_{kl} < 0 \tag{4.6}$$

$$\bar{\varphi}_{kl} = \text{sgn}(B_{kl})\frac{\pi}{2} \quad\text{for}\quad A_{kl} = 0$$

The representation (4.5) will be referred to as phase shift representation. Here, the Fourier coefficients are substituted by the amplitude $\bar{\xi}_{kl}$ and the circumferential phase shift $\bar{\varphi}_{kl}$. This way, a circumferential phase shift that is caused by the position of the cylinder during the measurements can be eliminated (see [45]).

Why it is important to consider the circumferential shift is depicted by the following example. Consider one and the same imperfection pattern as two realizations, but with different circumferential shifting, as depicted in Figure 4-2, top. If the mean imperfection is determined from these patterns, in the obtained mean pattern the real imperfections are smeared out

(Figure 4-2, top right). If however the imperfection patterns are shifted in the way that the ovalization mode has a circumferential shift of zero, the original pattern is obtained when determining the mean pattern (Figure 4-2, bottom).
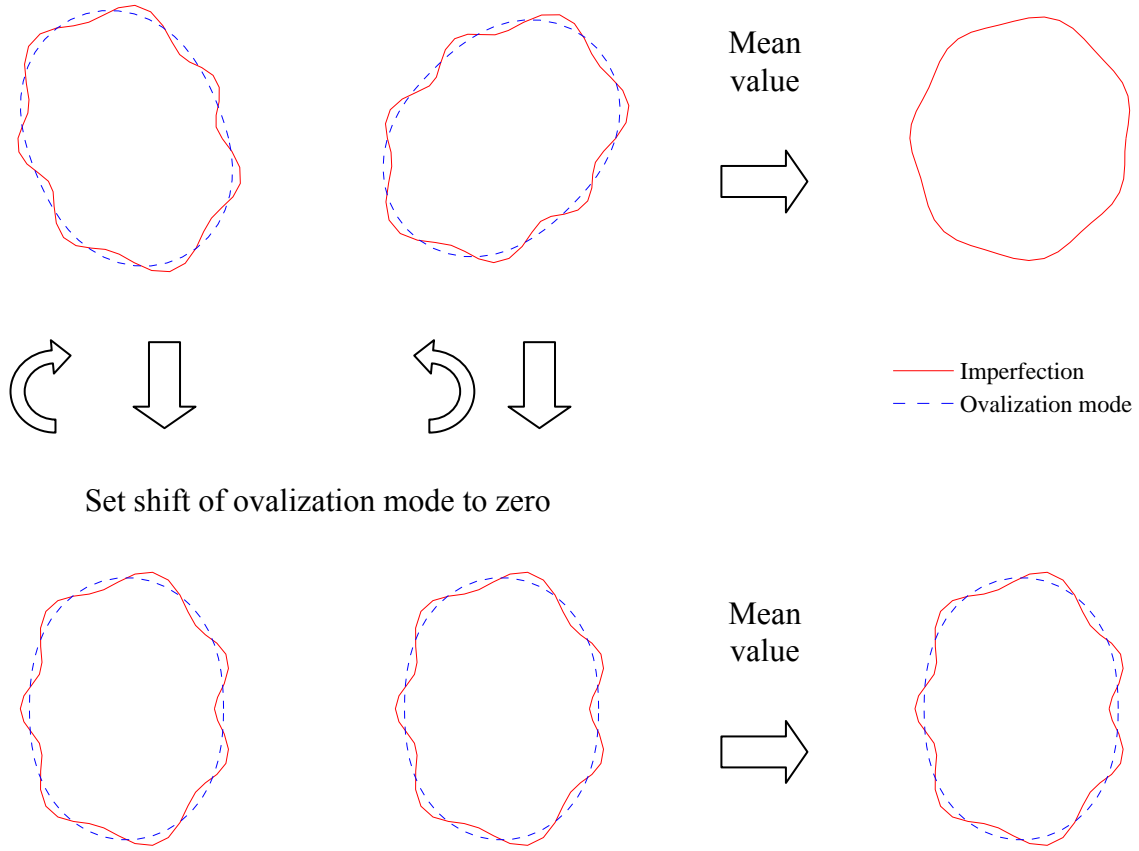
Figure 4-2: Influence of referring the circumferential shift of imperfection patterns to the ovalization mode on the obtained mean imperfection

Mathematically, this shifting is expressed as follows. The term in (4.5) that includes the phase shift can be written as

$$\cos\left(\frac{l\,y}{R} - \bar{\varphi}_{kl}\right) = \cos\left(\frac{l\left(y - \bar{y}_{kl}\right)}{R}\right) \tag{4.7}$$

where the relation of the phase shift angle $\bar{\varphi}_{kl}$ and the corresponding coordinate shift $\bar{y}_{kl}$ is given by

$$\bar{\varphi}_{kl} = \frac{l\,\bar{y}_{kl}}{R} \quad \Leftrightarrow \quad \bar{y}_{kl} = \frac{R\,\bar{\varphi}_{kl}}{l} \tag{4.8}$$

If now the phase shift angles shall be substituted by their relative shift with respect to e.g. the ovalization mode ($k = 0$ and $l = 2$), the imperfection function must be shifted in circumferential direction and the new coordinate shift $\bar{y}_{kl}^{\text{mod}}$ is given by

$$\bar{y}_{kl}^{\text{mod}} = \bar{y}_{kl} - \bar{y}_{02} \tag{4.9}$$

In terms of phase shift angles, the relation (4.9) is given by

$$\frac{R\,\overline{\varphi}_{kl}^{\mathrm{mod}}}{l} = \frac{R\,\overline{\varphi}_{kl}}{l} - \frac{R\,\overline{\varphi}_{02}}{2}$$

$$\Leftrightarrow \tag{4.10}$$

$$\overline{\varphi}_{kl}^{\mathrm{mod}} = \overline{\varphi}_{kl} - \tfrac{1}{2}l\,\overline{\varphi}_{02}$$

Note that here the ovalization mode only serves as an example. In general, any imperfection mode that is dominant can be used as the reference mode, where those imperfection modes are preferable, which describe a more or less global imperfection shape. If the geometric imperfection function shall be expressed relative to some dominant mode with the phase shift $\overline{\varphi}_{mn}^{\mathrm{ref}}$, the modified phase shift angles $\overline{\varphi}_{kl}^{\mathrm{mod}}$ are given by

$$\overline{\varphi}_{kl}^{\mathrm{mod}} = \overline{\varphi}_{kl} - \frac{l}{n}\overline{\varphi}_{mn}^{\mathrm{ref}} \tag{4.11}$$

Of course, Fourier series are not the only possibility to parameterize the random field of geometric imperfections. Furthermore, the Fourier representation leads to inaccuracies at the boundaries where no periodicity is given. However, the Fourier series provide several advantages. Firstly, using a Fourier series for describing the imperfection pattern delivers the manufacturing signature of the shell. It furthermore provides a mesh independent representation of the imperfection measurement. A side effect is the fact that by using a Fourier series measurement noise is smoothed out. For cylindrical shell the representation (4.5) furthermore enables the elimination of circumferential phase shift.

4.1.2   Multi Mode Imperfection Model

For structures like columns, which are not sensitive to imperfections, it is common pratice to apply the eigenmode or buckling mode associated with the lowest eigenvalue in order to trigger buckling in numeric simulations. This is also possible for cylindrical shells, but the chosen amplitude decisively determines the buckling load. Depending on the boundary conditions and whether axisymmetry is assumed or not, the eigenmodes of cylindrical shells following the classical approach are given by

	Axisymmetric	Asymmetric	
Simply supported	$W(x,y) = \xi \sin\dfrac{i\pi x}{L}$	$W(x,y) = \xi \sin\dfrac{i\pi x}{L} \cdot \cos\dfrac{j\,y}{R}$	(4.12)
Clamped	$W(x,y) = \xi \cos\dfrac{i\pi x}{L}$	$W(x,y) = \xi \cos\dfrac{i\pi x}{L} \cdot \cos\dfrac{j\,y}{R}$	(4.13)

When choosing an eigenmode as initial imperfection pattern, the initial imperfection field $\overline{W}(x,y)$ is given e.g. by

$$\frac{\overline{W}(x,y)}{t} = \overline{\xi} \sin\frac{k\pi x}{L} \cdot \cos\frac{l\,y}{R} \tag{4.14}$$

with the initial imperfection amplitude $\overline{\xi}$. Koiter [9] used an axisymmetric single imperfection mode for his derivation of the imperfection sensitivity of shells. Within the design concept proposed by Biagi [41] a single mode imperfection model is used and the amplitude $\overline{\xi}$ is treated as random parameter. Arbocz and Hilburger [39] chose a two-mode approach for the initial imperfection.

$$\frac{\overline{W}(x,y)}{t} = -\Delta_{axi}\cos\frac{i\pi x}{L} + \Delta_{asy}\sin\frac{k\pi x}{L}\cdot\cos\frac{ly}{R} \tag{4.15}$$

The two mode imperfection is a superposition of an asymmetric and an axisymmetric mode. If the lowest eigenvalue corresponds to an asymmetric mode, the number of axial half waves of the axisymmetric mode i is determined from Koiter's coupling condition $i = 2k$. If the lowest eigenvalue is an axisymmetric mode, k is determined from the coupling condition and l is the number of circumferential full waves of the eigenmode with the smallest eigenvalue and with k axial half waves. For the amplitudes, Arbocz and Hilburger [39] used the root mean square value (rms-value), which is a measure that quantifies the averaged imperfections. If the rms-value is determined with the Fourier representation, it can be divided into an axisymmetric Δ_{axi} and an asymmetric part Δ_{asy} (for details see [40]).

With a single mode as well as with the two mode approach the attempt is made to model the imperfection pattern as simple as possible and to capture the randomness of the buckling load by only one or two parameters that are somehow related to measurements. Such approaches include significantly simplifying assumptions and cannot be used for determining the real distribution of buckling load.

In [104], Arbocz and Starnes modeled the imperfection patterns with the multimode approach (4.16), which is superposition of selected modes of the Fourier series.

$$\frac{\overline{W}}{t} = A_{2,0}\cos\frac{2\pi x}{L} - \sin\frac{\pi x}{L}\left(\overline{\xi}_{1,2}\cos\frac{2y}{R} + \overline{\xi}_{1,9}\cos\frac{9y}{R} + \overline{\xi}_{1,10}\cos\frac{10y}{R}\right.$$
$$\left. + \overline{\xi}_{1,11}\cos\frac{11y}{R} + \overline{\xi}_{1,19}\cos\frac{19y}{R} + \overline{\xi}_{1,21}\cos\frac{21y}{R}\right) \tag{4.16}$$

This approach leads to a more realistic representation of the imperfections patterns than single or two mode approaches. However, the negligence of phase shift leads to an accumulation of the imperfection mode amplitudes in one place, as it has been showed by Kriegesmann et al. [45]. The multimode approach delivers a conservative model and allows a probabilistic analysis with almost realistic imperfections, requiring a relatively small number of random parameters. Nevertheless, the real distribution of buckling load cannot be determined with this approach. Furthermore, it requires a selection of decisive modes, which again requires an intensive study of imperfections and eigenvalues in order to determine, which modes are dominant in the measured pattern and at the same time associated with small eigenvalues.

4.1.3   Transformation to Uncorrelated Parameters and Parameter Reduction

In order to reduce the number of random parameters, a variant of the Mahalanobis transformation is used, that has similarities with the principle component analysis. Note that in the following random parameters and random vectors are symbolized with capital letters, while the realizations are symbolized by lowercase letters.

In general, the Mahalanobis transformation [105] is given by

$$\mathbf{x} = \mathbf{\Sigma}^{\frac{1}{2}}\mathbf{z} + \boldsymbol{\mu} \quad\text{and}\quad \mathbf{z} = \mathbf{\Sigma}^{-\frac{1}{2}}(\mathbf{x} - \boldsymbol{\mu}) \tag{4.17}$$

Considering for instance geometric imperfections, the random vector $\mathbf{X}$ contains all Fourier coefficients.

$$\mathbf{X} = \left(\xi_{00}, \varphi_{00}, \xi_{10}, \varphi_{10}, \ldots, \xi_{n_x n_y}, \varphi_{n_x n_y}\right)^T \tag{4.18}$$

In practice, the mean vector $\boldsymbol{\mu}$ and the covariance matrix $\boldsymbol{\Sigma}$ of $\mathbf{X}$ are estimated from measurements according to

$$\boldsymbol{\mu} \simeq \frac{1}{m}\sum_{i=1}^{m}\mathbf{x}^{(i)} \quad \text{and} \quad \boldsymbol{\Sigma} \simeq \frac{1}{m-1}\sum_{i=1}^{m}\left(\mathbf{x}^{(i)}-\boldsymbol{\mu}\right)\left(\mathbf{x}^{(i)}-\boldsymbol{\mu}\right)^{T}. \tag{4.19}$$

The entries of the random vector $\mathbf{Z}$ are uncorrelated with a standard deviation of one and a mean value of zero.

As proven in Appendix B.2, the estimated covariance matrix $\boldsymbol{\Sigma}$ is singular, if the number of measurements m is smaller than the number of random parameters n. in this case, the root of $\boldsymbol{\Sigma}$ cannot be determined from Choleski decomposition, as proposed in [34], but it can be determined from the spectral decomposition of $\boldsymbol{\Sigma}$. The matrix $\mathbf{B}$ is defined as

$$\mathbf{B} = \mathbf{Q}\,\mathbf{D}^{\frac{1}{2}} = \left(\mathbf{q}_1,\ldots,\mathbf{q}_r\right)diag\left(\sigma_1,\ldots,\sigma_r\right) \tag{4.20}$$

The columns of matrix $\mathbf{Q}$ are the eigenvectors of $\boldsymbol{\Sigma}$ and the diagonal elements of the matrix $\mathbf{D}$ are the eigenvalues σ_i^2 of $\boldsymbol{\Sigma}$. As shown in Appendix B.3, the matrix $\mathbf{B}$ is a root of $\boldsymbol{\Sigma}$. The rank r of $\boldsymbol{\Sigma}$ is smaller than the number of measurements m. When using the matrix $\mathbf{B}$ for the Mahalanobis transformation, the vector $\mathbf{z}$ must have the length r, since $\mathbf{B}\in\mathbb{R}^{n\times r}$.

$$\mathbf{x} = \mathbf{B}\,\mathbf{z}+\boldsymbol{\mu} \quad \text{and} \quad \mathbf{z} = \mathbf{B}^{-1}\left(\mathbf{x}-\boldsymbol{\mu}\right) \tag{4.21}$$

Hence, if the number of measurements m is smaller than the number of origin random parameters n, the number of random parameters can be reduced to r by using (4.21). It is worth mentioning that by using (4.20) to determine the root of $\boldsymbol{\Sigma}$, the Mahalanobis transformation is almost equal to the principal component analysis (4.22) or discrete Karhunen-Loève transformation.

$$\mathbf{y} = \mathbf{Q}^{T}\left(\mathbf{x}-\boldsymbol{\mu}\right) \tag{4.22}$$

In difference to the Mahalanobis transformation the Karhunen-Loève transformation does not normalize the standard deviations to one. For a detailed discussion on the relation of Mahalanobis transformation and principal component analysis see Appendix B.4.

4.2   *Representation of Non-traditional Imperfections*

After Koiter discovered that geometric imperfections explain the gap between experimentally determined buckling loads and analytical results, a multitude of investigations focused on the influence on geometric imperfections (see section 1.2.1). Later, also other types of imperfections started to be considered. Therefore, the term "traditional" imperfections has been established for geometric imperfections, while the term "non-traditional" imperfections is used for all other types of deviations from the ideal structure (see e.g. [24,104]). Non-traditional imperfections that can occur in circular shell structures are imperfect boundary conditions or load applications, wall thickness deviations, residual stresses and scattering material properties. For fiber composite structures, deviations of the fiber angles or fiber waviness and void inclusions can occur additionally.

If, for instance, the wall-thickness or a material property is considered as a random field in the sense that it can have a different value at each location of the shell, this random field can be described by double Fourier series, as it is done for geometric imperfection in the previous section. Often it is difficult to get samples of such random fields for non-traditional imperfections. For the cylinders considered in chapter 6 the wall thickness has been measured at each point for each shell. However, it has been shown in [106] that it is sufficient to only

consider the mean wall thickness of a shell as random parameter for the shells considered in chapter 6.

The material properties of the unidirectional ply are not determined for the actually build structure, but from coupon test. Therefore, each material parameter is described by a single scalar; however, the material parameters are correlated in general. In such cases, the Mahalanobis transformation must be used to transform the set of parameters to a set of uncorrelated parameters, as described in section 4.1.3.

If an imperfection can be described by a single random parameter, which is independent from all other random parameters, the treatment in the probabilistic analysis is quite straight forward. Examples are the fiber angle of a certain ply, a global inclination angle as discussed in section 6.3.4, or the mean wall thickness.

4.3   Probabilistic Analysis Methodology

In case the arguments of a mathematical function $g(\mathbf{x})$, which is called objective function in the following, are randomly distributed and the stochastic distribution of this function g is to be determined, probabilistic analysis methods must be conducted. The scattering arguments are represented by the random vector $\mathbf{X}$, where realizations of $\mathbf{X}$ are denoted as $\mathbf{x}$. Within the probabilistic analysis of structures, the objective function $g(\mathbf{x})$ is the load carrying capability, given by buckling or material failure, and the entries of the random vector $\mathbf{X}$ are the scattering parameters of the structure.

In this section, the most straight forward numerical simulation technique to solve this problem is given. For a faster analysis, the objective of the probabilistic analysis can be restricted to only determine the stochastic moments of the objective function. Here, the existing second-order third-moment approach is extended in the sense that the complete second order approach for determining stochastic moments is given. Furthermore, the same type of approach is used to determine the covariance of two objective functions.

4.3.1   General Problem Description of Probabilistic Design

The objective of probabilistic design is to find the value of the objective function g_d, which is exceeded with a certain probability R, referred to as the level of reliability given by

$$R = 1 - P\big(g_d \leq g(\mathbf{x})\big) \tag{4.23}$$

For determining the probability that a certain value $\overline{g}$ of the objective function takes a value less than or equal to $g(\mathbf{x})$, the cumulative distribution function F_g must be determined, which is given by the multidimensional integral (4.24).

$$P\big(\overline{g} \leq g(\mathbf{x})\big) = F_g\big(g(\mathbf{x})\big) = \int\limits_{\mathbf{x}: g(\mathbf{x}) \leq \overline{g}} f_{\mathbf{X}}(\mathbf{x}) d\mathbf{x} \tag{4.24}$$

While the probability density function $f_{\mathbf{X}}(\mathbf{x})$ of the random vector $\mathbf{X}$ can be estimated from measurements, the objective function $g(\mathbf{x})$ is often not given analytically in practice. Then, (4.24) must be solved numerically or approximated with analytic or semi-analytic approaches.

4.3.2   Numerical Analysis - the Monte Carlo Method

The Monte Carlo method is the most straight forward and numerically most intensive procedure to estimate the distribution of the objective function. Within this thesis, the Monte Carlo method is used to validate the semi-analytical, probabilistic procedures.

A Monte Carlo simulation basically consists of the following steps [107]. First, a large amount of realizations **x** is generated with respect to the distribution $f_{\mathbf{X}}(\mathbf{x})$. Descriptively spoken, a large number of virtual test specimens is created. Then, for each realization **x** the objective function is evaluated and the discrete cumulative distribution function of the objective function is obtained. Because the required number of realizations **x** is not known initially, a convergence study is recommended with respect to the parameters of interest.

The generation of random samples of course requires that the distribution $f_{\mathbf{X}}(\mathbf{x})$ of the random vector is known, which is typically not the case in practice. In order to evaluate which type of distribution fits the real scatter best, a statistical test methods like the χ^2 test or Kolmogorov-Smirnov test (K-S test) can be used [88]. Compared to other tests, the K-S test has the advantage that it is applicable even if only a small number of samples is given, and it also allows comparing two empiric distributions. The K-S test is described in detail in Appendix C. For the generation of a single random number, a random number u, which is uniformly distributed in the interval [0,1], is generated by common mathematic software. Given a distribution function $F_X(x)$, a random number x can be generated by

$$x = F_X^{-1}(u) \tag{4.25}$$

For those distributions functions, for which it is not possible to find the inverse of F_X, the acceptance-rejection method can be used [90].

Because the random parameters X_i are transformed to uncorrelated variables Z_i, the entries of the random vector **Z** can be generated individually with respect to the assumed distribution function. Then, each generated vector **z** is transformed to a vector **x** using (4.21).

4.3.3   Stochastic Moment Approximation

For the semi-analytic approach described in the following, the objective function is approximated by a Taylor expansion at the mean vector of input parameters.

$$g(\mathbf{x}) = g(\boldsymbol{\mu}) + \sum_{i=1}^{n} \frac{\partial g(\boldsymbol{\mu})}{\partial x_i}(x_i - \mu_i) + \frac{1}{2}\sum_{i=1}^{n}\sum_{j=1}^{n} \frac{\partial^2 g(\boldsymbol{\mu})}{\partial x_i \, \partial x_j}(x_i - \mu_i)(x_j - \mu_j) + \ldots \tag{4.26}$$

Instead of determining the cumulative distribution function F_g the idea of the Taylor series based approach is to determine the characteristic stochastic moments of the objective function, namely the mean value (first moment), the variance (second central moment) and the skewness (determined from the third central moment). Then, a type of distribution is assumed with respect to the stochastic moments.

The mean value μ_g of the objective function is given by

$$\mu_g = E\big(g(\mathbf{X})\big) = \int\limits_{-\infty}^{\infty} g(\mathbf{x})\, f_{\mathbf{X}}(\mathbf{x})\, d\mathbf{x} \tag{4.27}$$

Inserting the second order Taylor approximation (4.26) into (4.27) leads to the approximation of the mean value approximation (4.28). For the complete derivation see Appendix D.1.

$$\mu_g \approx g(\boldsymbol{\mu}) + \frac{1}{2}\sum_{i=1}^{n}\sum_{j=1}^{n} \frac{\partial^2 g(\boldsymbol{\mu})}{\partial x_i \, \partial x_j}\, \mathrm{cov}(X_i, X_j) \tag{4.28}$$

For the mean value approximation (4.28) neither the objective function $g(\mathbf{x})$ nor the probability density function $f_{\mathbf{X}}(\mathbf{x})$ needs to be given analytically. Hence, in difference to Monte Carlo simulations, no assumptions are required concerning the type of distribution of **X**. Instead, the derivatives of the objective functions at the mean vector must be determined

and the stochastic moments of the input parameters must be known. The derivatives can be determined numerically (see section 4.5) and the stochastic moments are determined from measurements using the estimators to (4.73), (4.75) etc.

When assuming independence of the random variables, the covariance of the input parameters equals zero and the approximation of μ_g is given by

$$\mu_g \approx g(\boldsymbol{\mu}) + \frac{1}{2} \sum_{i=1}^{n} \frac{\partial^2 g(\boldsymbol{\mu})}{\partial z_i^2} \operatorname{var}(Z_i) \tag{4.29}$$

The variance of the objective function is given by

$$\sigma_g^2 = var\big(g(\mathbf{x})\big) = \int_{-\infty}^{\infty} \big(g(\mathbf{x}) - \mu_g\big)^2 f_{\mathbf{X}}(\mathbf{x}) \, d\mathbf{x} \tag{4.30}$$

For reasons of simplicity, the following abbreviations are introduced.

$$g(\boldsymbol{\mu}) = g_{\boldsymbol{\mu}} \quad , \quad \frac{\partial g(\boldsymbol{\mu})}{\partial z_i} = g_{,i} \quad , \quad \frac{\partial^2 g(\boldsymbol{\mu})}{\partial z_i \, \partial z_j} = g_{,ij} \tag{4.31}$$

Assuming again independent random parameters, the second order approximation of the variance σ_g^2 is given by

$$\sigma_g^2 \approx g_{\boldsymbol{\mu}}^2 + \sum_{i=1}^{n} g_{,i}^2 \, \mu_{i,2} + \frac{1}{4} \sum_{i=1}^{n} g_{,ii}^2 \, \mu_{i,4} + g_{\boldsymbol{\mu}} \sum_{i=1}^{n} g_{,ii} \, \mu_{i,2} + \sum_{i=1}^{n} g_{,i} \, g_{,ii} \, \mu_{i,3}$$
$$+ \frac{1}{2} \sum_{i=1}^{n} \sum_{j=i+1}^{n} g_{,ii} \, g_{,jj} \, \mu_{i,2} \, \mu_{j,2} + \sum_{i=1}^{n} \sum_{j=i+1}^{n} g_{,ij}^2 \, \mu_{i,2} \, \mu_{j,2} - \mu_g^2 \tag{4.32}$$

For the complete derivation see Appendix D.2., The third central moment of the objective function is approximated in the same manner as mean value and variance.

$$\mu_{g,3} = E\Big(\big[g(\mathbf{x}) - \mu_g\big]^3\Big) = \int_{-\infty}^{\infty} \big(g(\mathbf{x}) - \mu_g\big)^3 f_{\mathbf{X}}(\mathbf{x}) \, d\mathbf{x} \tag{4.33}$$

The second order approximation of $\mu_{g,3}$ and its derivation are given in Appendix D.4. From the third central moment $\mu_{g,3}$ the skewness of the distribution is calculated by

$$v_g = \frac{\mu_{g,3}}{\sigma_g^3} \tag{4.34}$$

Considering only the linear terms of the Taylor series, the approximations of mean value, variance and third central moment of the objective function are given by

$$\mu_g \approx g(\boldsymbol{\mu}) \tag{4.35}$$

$$\sigma_g^2 \approx \sum_{i=1}^{n} g_{,i}^2 \, \mu_{i,2} \tag{4.36}$$

$$\mu_{g,3} \approx \sum_{i=1}^{n} g_{,i}^3 \, \mu_{i,3} \tag{4.37}$$

If only linear terms of the Taylor expansion are considered and only stochastic moments of second order are considered, the method is referred to as first-order second-moment (FOSM) method (see e.g. [35]). If also the quadratic terms of the Taylor expansion and stochastic moments of third order are taken into account, the method is referred to as second-order third-

moment (SOTM) method (see [108]). Since the highest moments that occur when using the quadratic Taylor expansion are of sixth order, the full second order approach is referred to as second-order sixth-moment (SOSM) approach. As it will be discussed in section 4.5.1, it is reasonable to consider the SOSM approach, but neglect the terms with partial derivatives with respect to different variables. This approach will be referred to as incomplete second order approach (ISOA) in the following.

4.3.4   Approximation of Covariance and Correlation

In case different failure modes limit the load carrying capability of a structure, the joint distribution function of these failure modes must be considered. The stochastic moment that captures the characteristics of a joint distribution is the covariance. Therefore, two objective functions $g(\mathbf{x})$ and $h(\mathbf{x})$ are considered in the following. Their mean values and standard deviations can be estimated with the approximations given in section 4.3.3. The covariance Σ_{gh} of the objective functions is defined as

$$\Sigma_{gh} = \text{cov}\big(g(\mathbf{x}), h(\mathbf{x})\big) = \int_{-\infty}^{\infty} \big(g(\mathbf{x}) - \mu_g\big)\big(h(\mathbf{x}) - \mu_h\big) f_{\mathbf{X}}(\mathbf{x}) \, d\mathbf{x} \tag{4.38}$$

Inserting the second order Taylor approximation of both objective functions into (4.38) and assuming independence of the entries of the random vector $\mathbf{X}$ leads to the second order approximation of the covariance.

$$\begin{aligned}
\Sigma_{gh} \approx{}& g_{\boldsymbol{\mu}}\, h_{\boldsymbol{\mu}} - g_{\boldsymbol{\mu}}\, \mu_h - \mu_g\, h_{\boldsymbol{\mu}} + \mu_g \mu_h + \sum_{i=1}^{n} g_{,i}\, h_{,i}\, \mu_{i,2} + \frac{1}{2} g_{\boldsymbol{\mu}} \sum_{i=1}^{n} h_{,ii}\, \mu_{i,2} + \frac{1}{2} h_{\boldsymbol{\mu}} \sum_{i=1}^{n} g_{,ii}\, \mu_{i,2} \\
&- \mu_g \frac{1}{2} \sum_{i=1}^{n} h_{,ii}\, \mu_{i,2} - \mu_h \frac{1}{2} \sum_{i=1}^{n} g_{,ii}\, \mu_{i,2} + \frac{1}{2} \sum_{i=1}^{n} g_{,ii}\, h_{,i}\, \mu_{i,3} + \frac{1}{2} \sum_{i=1}^{n} g_{,i}\, h_{,ii}\, \mu_{i,3} \\
&+ \frac{1}{4} \sum_{i=1}^{n} \sum_{\substack{j=1 \\ j \neq i}}^{n} g_{,ii}\, h_{,jj}\, \mu_{i,2}\, \mu_{j,2} + \frac{1}{2} \sum_{i=1}^{n} \sum_{\substack{j=1 \\ j \neq i}}^{n} g_{,ij}\, h_{,ij}\, \mu_{i,2}\, \mu_{j,2} + \frac{1}{4} \sum_{i=1}^{n} g_{,ii}\, h_{,ii}\, \mu_{i,4}
\end{aligned} \tag{4.39}$$

The first order approximation of the covariance reads

$$\Sigma_{gh} \approx \sum_{i=1}^{n} g_{,i}\, h_{,i}\, \mu_{i,2} \tag{4.40}$$

From the covariance and the standard deviations of each objective function, the coefficient of correlations ρ_{gh} is determined, which is a measure of the linear dependency of g and h.

$$\rho_{gh} = \frac{\Sigma_{gh}}{\sigma_g \, \sigma_h} \tag{4.41}$$

With knowledge of the covariance, an appropriate type of distribution can be chosen to describe the multivariate distribution of g and h.

4.4   Convex Anti-Optimization

An alternative approach to account for uncertainties is the convex anti-optimization method proposed by Ben-Haim and Elishakoff [51]. Though it is not a probabilistic procedure in principle, this approach shows similarities to the proposed concept and therefore, it is discussed in the following.

The basic idea of anti-optimization is to find the combination of input parameters that leads to the lowest load carrying capability, whereas the input parameters scatter in a certain domain. In case only one input parameter is non-deterministic, the parameter scatters in an interval, in

which the lowest buckling load is to be found (see Figure 4-3). One possibility is to determine the minimum buckling load using standard optimization algorithms. Taking into account more scattering input parameters the definition of the domain space becomes difficult and the computational cost of usual optimization algorithms increases dramatically. Obviously, this approach is not useable as a design procedure. The goal of convex anti-optimization is the same: finding the minimum buckling load in the domain of scattering input parameters. However, by making use of some simplifying assumptions, a domain of input parameters is determined based on measurements, as it is discussed in the following section, and a lower bound of buckling load can be found by performing only a small number of buckling analyses.
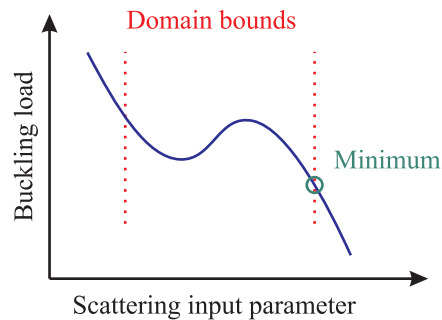
Figure 4-3: Sketch of a one dimensional minimization problem

4.4.1   Minimum Volume Enclosing Hyper Ellipsoid

It is assumed that the domain of input parameters is bounded by a hyper ellipsoid. The position and orientation of the ellipsoid is determined from measurements. Each set of measurements is interpreted as a vector. In Figure 4-4 a two dimensional example with ten pairs of measured values is shown. In order to bound the domain, the ellipse with the smallest area is search that includes all measurement vectors. In the general, higher dimensional case, the measurement vectors are bounded by the hyper ellipsoid with the minimum volume. This domain is referred to as minimum volume enclosing hyper ellipsoid (MVEE) in the following.

Figure 4-4: Minimum area enclosing ellipse

The surface of a hyper ellipsoid with semi-axes a_i parallel to the coordinate system is given by

$$\sum_{i=1}^{n} \frac{\left(x_i - x_{c,i}\right)^2}{a_i^2} = 1 \tag{4.42}$$

By moving the center of the ellipsoid $\mathbf{x}_c$ and by rotating and changing the length of the semi-axes, the hyper ellipsoid is modified so that it captures all measurement vectors. Procedures to find the MVEE are given for instance by Zhu et al. [109] and Elishakoff et al. [53].
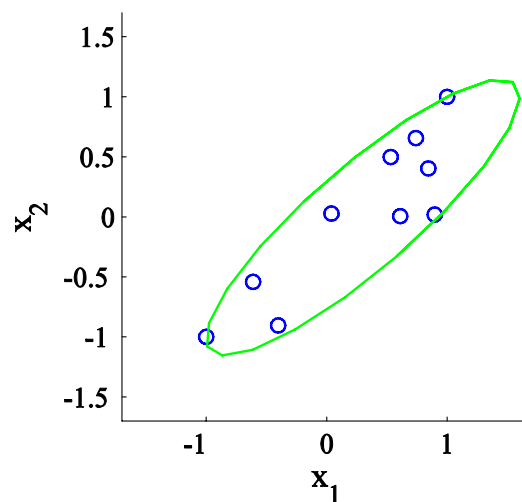
4.4.2   Approximation of Pessimum

For the approximation of the minimum value of the objective function g_{min} within the MVEE, the objective function g is approximated by a Taylor expansion in ζ at the center $\mathbf{x}_c$.

$$g\left(\mathbf{x}_c + \zeta\right) \approx g\left(\mathbf{x}_c\right) + \varphi^T \zeta + \tfrac{1}{2} \zeta^T \Xi \zeta \tag{4.43}$$

with the gradient $\varphi = \nabla g$ and the Hessian $\Xi = \nabla\nabla g$. If the inequality

$$\varphi^T \Xi^{-1} \Omega \Xi^{-1} \varphi < 1 \tag{4.44}$$

holds, the minimum buckling load is found inside the minimum volume enclosing hyper-ellipsoid and is given by the expression

$$g_{\text{min}} = g\left(\mathbf{x}_c\right) - \tfrac{1}{2} \varphi^T \Xi \varphi \tag{4.45}$$

If (4.44) does not hold, the input parameters that lead to the minimum buckling load are on the boundary of the minimum volume enclosing hyper-ellipsoid. Then the second order approximation of the minimum buckling load is given by

$$g_{\text{min}} = g\left(\mathbf{x}_c\right) - \varphi^T \mathbf{M}^{-1} \varphi + \tfrac{1}{2} \varphi^T \mathbf{M}^{-1} \Xi \mathbf{M}^{-1} \varphi \tag{4.46}$$

with

$$\mathbf{M} = \Xi + 2\gamma\Omega \ , \ \gamma^2 = \tfrac{1}{4}\varphi^T \mathbf{G}\varphi \ \text{and} \ \mathbf{G} = \Omega^{-1} = diag\left(a_1^2, \ldots, a_d^2\right) \tag{4.47}$$

Using the first order Taylor expansion the minimum buckling load is given by

$$g_{\text{min}} = g\left(\mathbf{x}_c\right) - \sqrt{\varphi^T \mathbf{G}\varphi} = g\left(\mathbf{x}_c\right) - \sqrt{\sum_{i=1}^{n} a_i^2 \left(\frac{\partial g\left(\mathbf{x}_c\right)}{\partial x_i}\right)^2} \tag{4.48}$$

For more details concerning the anti-optimization procedure, see [51].

As for the probabilistic approach, the derivatives of the objective function have to be estimated numerically, since the objective function is not given explicitly in practice.

4.5   Numerical Derivatives of the Objective Function

Since the approach given in section 4.3.3 and 4.4 are based on the Taylor expansion, the derivatives of the objective function at some point $\hat{\mathbf{x}}$ are required. For the probabilistic approach, this point $\hat{\mathbf{x}}$ equals the mean vector μ, for the convex anti-optimization the partial derivatives have to be estimated at the center of the MVEE $\mathbf{x}_c$. If the objective function is not given explicitly, the derivatives have to be determined numerically.

If only the first derivatives have to be estimated, the fastest way to do so is using the approximation

$$\frac{\partial g\left(\hat{\mathbf{x}}\right)}{\partial x_i} \approx \frac{g\left(\hat{x}_1, \ldots, \hat{x}_i + \Delta x_i, \ldots, \hat{x}_n\right) - g\left(\hat{\mathbf{x}}\right)}{\Delta x_i} \tag{4.49}$$

This approximation is considered "fast" since it requires only $n+1$ evaluations of the objective function to get all partial derivatives; one at $\hat{\mathbf{x}}$ and one for each random variable. A more accurate estimation is given by

$$\frac{\partial g(\hat{\mathbf{x}})}{\partial x_i} \approx \frac{g(\hat{x}_1,\ldots,\hat{x}_i + \Delta x_i,\ldots,\hat{x}_n) - g(\hat{x}_1,\ldots,\hat{x}_i - \Delta x_i,\ldots,\hat{x}_n)}{2\,\Delta x_i} \tag{4.50}$$

This approximation is exact also for quadratic objective function. However, it requires $2\,n+1$ evaluations of the objective function. On the other hand, with the values evaluated for (4.50), the second partial derivatives with respect to one variable can be estimated according to

$$\frac{\partial g^2(\hat{\mathbf{x}})}{\partial x_i^2} \approx \frac{g(\hat{x}_1,\ldots,\hat{x}_i + \Delta x_i,\ldots,\hat{x}_n) - 2\,g(\hat{\mathbf{x}}) + g(\hat{x}_1,\ldots,\hat{x}_i - \Delta x_i,\ldots,\hat{x}_n)}{\Delta x_i^2} \tag{4.51}$$

However, the second derivative with respect to different variables requires additional evaluations of the objective function. Using the approach (4.52), the objective function has to be evaluated $\frac{1}{2}\,(n^2 - n)$ times additionally for each combination of variables.

$$\frac{\partial^2 g(\hat{\mathbf{x}})}{\partial x_i\,\partial x_j} \approx \frac{g(\hat{x}_i + \Delta x_i, \hat{x}_j + \Delta x_j) - g(\hat{x}_i + \Delta x_i,) - g(\hat{x}_i + \Delta x_j) + g(\hat{\mathbf{x}})}{\Delta x_i\,\Delta x_j} \tag{4.52}$$

Hence, for estimating all second derivatives, the $2\,n+1+\frac{1}{2}\,(n^2 - n) = 0.5\,n^2 + 1.5\,n + 1$ evaluations of the objective functions are required. The approximation (4.52) is exact only for bilinear objective functions. A better approximations, that is exact for quadratic functions, is given by using a second order polynomial

$$g(\mathbf{x}) \approx \mathbf{x}^T \mathbf{A}\,\mathbf{x} + \mathbf{b}^T \mathbf{x} + c \tag{4.53}$$

with the coefficients $\mathbf{A} \in \mathbb{R}^{n\times n}\left(\mathbf{A} = \mathbf{A}^T\right)$, $\mathbf{b} \in \mathbb{R}^n$ and $c \in \mathbb{R}$. First and second derivative are then given by

$$\frac{\partial g(\hat{\mathbf{x}})}{\partial x_i} \approx 2\sum_{j=1}^{n} A_{ij}\,\hat{x}_j + b_i \tag{4.54}$$

and

$$\frac{\partial^2 g(\hat{\mathbf{x}})}{\partial x_i\,\partial x_j} \approx 2\,A_{ij} \tag{4.55}$$

For determining the coefficients, the same number of support points is required as needed for the approach (4.52).

4.5.1 Computational Cost of the Probabilistic Approach

The numerical approximations of the derivatives determine the numerical effort or computational cost of the probabilistic method.

In chapter 6 a probabilistic analysis with 15 random parameters is executed. An overview of the required number of evaluations of $g(\mathbf{z})$ in general and for the considered set of 15 uncorrelated random variables is listed in Table 4-1.

When using the complete second order approach, the number of required evaluations of the objective function increases quadratically with the number of random parameters. A more efficient approach is to consider only those terms that do not include derivatives with respect to different variables. The standard deviation is then given by

$$\sigma_g^2 \approx g_\mu^2 - \mu_g^2 + \sum_{i=1}^{n} g_{,i}^2\, \mu_{i,2} + \frac{1}{4}\sum_{i=1}^{n} g_{,ii}^2\, \mu_{i,4} + g_\mu \sum_{i=1}^{n} g_{,ii}\, \mu_{i,2} + \sum_{i=1}^{n} g_{,i}\, g_{,ii}\, \mu_{i,3}$$

$$+ \frac{1}{2}\sum_{i=1}^{n}\sum_{j=i+1}^{n} g_{,ii}\, g_{,jj}\, \mu_{i,2}\, \mu_{j,2} \tag{4.56}$$

where, compared to (4.32), only one term is neglected. The same holds for the approximation of the covariance, given in section 4.3.4. The second order approximation of the third central moment is reduced by the terms G_{ij} in (D.52). Using the second order approximation of the stochastic moment, but neglecting the term with derivatives with respect to different variables, will be referred to as incomplete second order approach (ISOA) in the following.

Approach	Required number of calculations	Required number of calculations for analyses in chapter 6
First order approach, using (4.49)	$n_z + 1$	16
First order approach, using (4.50)	$2\,n_z + 1$	31
Any second order approach, excluding derivatives with respect to different variables	$2\,n_z + 1$	31
Complete second order approach, using (4.52) or (4.55)	$2\,n_z + 1 + \frac{1}{2}\left(n_z^2 - n_z\right)$	136

Table 4-1: Required number of evaluations of the objective function for different Taylor series based approaches

Summarized, this means by neglecting only a small number of terms in the approximations for mean value, variance and third central moment, the computational cost is only linearly dependent of the number of random parameters instead of quadratically. For the example considered in chapter 6, the ISOA approach requires only 31 buckling analyses instead of 136 simulations for the full approach, which equals a reduction of computational costs by 77%. It will be demonstrated in chapter 6 that there is no noticeable loss of accuracy when using the ISOA instead of the full approach, which is why it is strongly recommended to make use of this approach.

4.5.2   Influence of the Step Size

Because the derivatives are estimated numerically, the quality of the Taylor series approximation that is used for the semi-analytic, probabilistic approach (section 4.3.3) as well as for the convex anti-optimization (section 4.4) is influenced by the step size Δx used for the numerical derivative. A small step size is expected to deliver the best approximation of the derivatives at the point considered; however, the best approximation of the objective function in a certain interval of interest is not necessarily given by a small step size.

Figure 4-5 shows the function of buckling load for shell Z07 with respect to different random parameters. The real shape of the functions is approximated by a sensitivity study. Depending on the shape of the function of buckling load, the quality of its quadratic Taylor approximation can significantly depend on the step size chosen for the numerical derivatives.
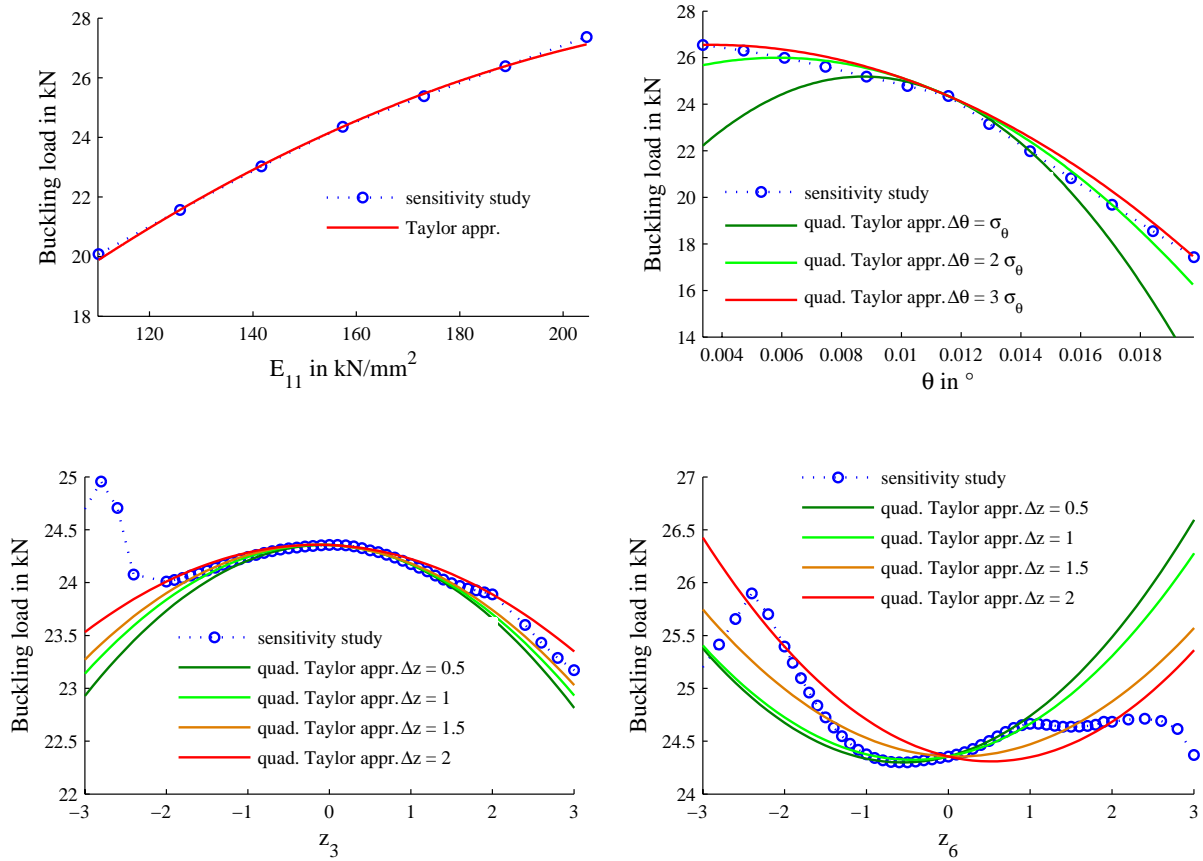
Figure 4-5: Function of buckling load for shell Z07 with respect to different random parameters (see also chapter 6)

The approximations (4.29) and (4.32) implicitly solve the integrals

$$\mu_g = \int_{-\infty}^{\infty} g(\mathbf{z}) f_{\mathbf{Z}}(\mathbf{z}) \, d\mathbf{z} \quad \text{and} \quad \sigma_g^2 = \int_{-\infty}^{\infty} \left(g(\mathbf{z}) - \mu_g \right)^2 f_{\mathbf{Z}}(\mathbf{z}) \, d\mathbf{z} \tag{4.57}$$

where $f_{\mathbf{Z}}(\mathbf{z})$ is the probability density function (PDF) of the transformed random vector $\mathbf{Z}$, with uncorrelated entries. Assuming independence of the entries of $\mathbf{Z}$, the PDF can be written as

$$f_{\mathbf{Z}}(\mathbf{z}) = f_{Z_1}(z_1) \cdot \ldots \cdot f_{Z_n}(z_n) \tag{4.58}$$

and hence, each random parameter can be regarded independently. The objective function $g(\mathbf{z})$ must be approximated well for regions where the PDF $f_{\mathbf{Z}}(\mathbf{z})$ is different from zero. This is the case for values of z_i which are close to the mean value μ_i. Such an interval can be expressed as $[\mu_i - a \cdot \sigma_i, \mu + a \cdot \sigma_i]$, where the choice of the scalar a is depending on the shape of the PDF. E.g. for the random parameter Z_3 of the probabilistic analysis in chapter 6, the logistic distribution is assumed (see Appendix C) and the PDF of Z_3 is significantly different to zero for $-3 < z_3 < 3$ (see Figure 4-6)

In order to find the stepsize Δz for which the discrepancy of Taylor approximation $\tilde{g}$ and real function g is minimal in the interval of interest, the approximation error ε_g is defined as

$$\varepsilon_g(\Delta z_i) = \int_{-\infty}^{\infty} \left| g(z_i) - \tilde{g}(z_i, \Delta z_i) \right| f_{Z_i}(z_i) \, dz_i \tag{4.59}$$
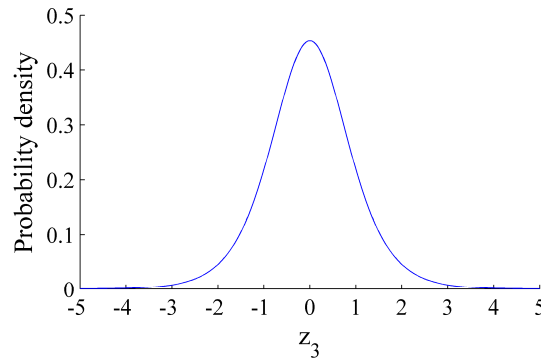
Figure 4-6: Probability density function $f(z_3)$ assuming logistic distribution

The difference of g and $\tilde{g}$ is weighted by the PDF of Z_i and summed up by integrating over z_i. Since the Taylor expansion is a function of z_i and Δz_i, ε_g is a function of Δz_i. The dimension of the approximation error ε_g equals the dimension of the objective function, because the uncorrelated random parameters Z_i are dimensionless. By minimizing ε_g with respect to Δz_i the optimal Δz_i is obtained. Because g is not given analytically, also this problem has to be solved numerically.
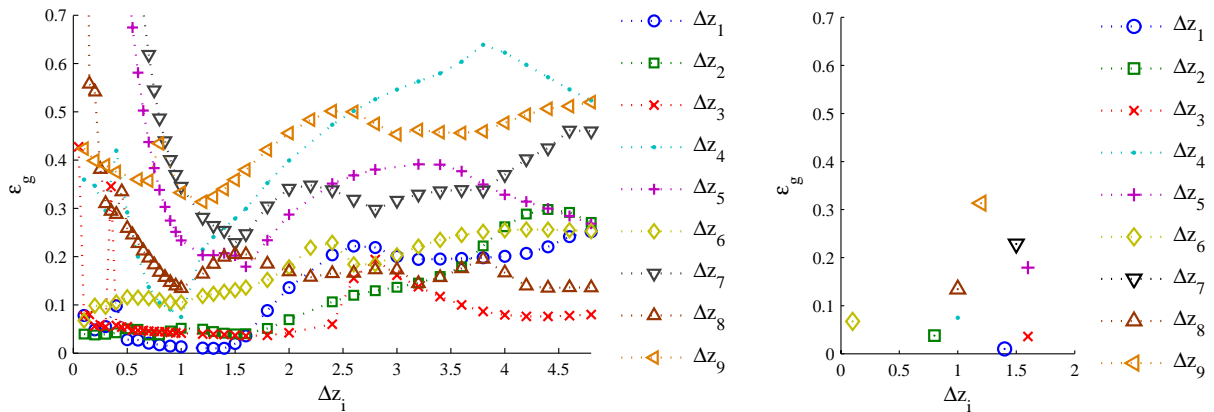

Figure 4-7: Functions of the approximation error ε_g in kN (left) and minimum approximation errors (right) for different step sizes Δz_i for shell Z07

In Figure 4-7 the approximation error ε_g is plotted over Δz_i for all geometry parameters of the case considered in chapter 6. Since the function of buckling load is different for each laminate setup, also ε_g is depending on the laminate setup. However, by minimizing the approximation error ε_g with respect to Δz_i the optimal derivative step size Δz_i has been determined for all parameters and for all different laminate setups. In Figure 4-7 (right) only the minimum approximation errors and the associated optimal step sizes are plotted.

The procedure of optimizing Δz_i shall not be repeated each time the semi-analytical method is applied. Hence, the goal is to find a derivative step size that always delivers good approximations. The mean value of optimal step sizes of all parameters and all laminate setups considered equals $1.31\,\sigma_i$, which could be used as standard step size. For most parameters z_i is has been found that the smaller the step size Δz_i is, the more sensitive is ε_g to the choice of Δz_i (see e.g. $\varepsilon_g(\Delta z_5)$ and $\varepsilon_g(\Delta z_7)$ in Figure 4-7). Thus, $\Delta z_i = 1.5\,\sigma_i$ is chosen as the standard step size. From Figure 4-7 it becomes visible that the approximation errors for

$\Delta z_i = 1.5 \, \sigma_i$ and the minimum approximation errors have the same order of magnitude for all shells considered. This shows that $\Delta z_i = 1.5 \, \sigma_i$ indeed is a step size that can be used as a standard step size. However, it must be noted that this result is based on the considered set of measurements and therefore, it is not valid in general. A general derivation of the optimal step size appears to be impossible, since the approximation error given by (4.59) is dependent on the objective function and the PDFs of the input parameters.

More important than the question how the step size influences the approximation error is the question, how the choice of step size influences the results of the probabilistic analysis. The results of the incomplete second order approach are plotted over the step size in Figure 4-8 for the application considered in chapter 6. It is concluded that for an increasing step size the results of the probabilistic analysis become less sensitive to the choice of Δz_i. Note that the results do not converge to the correct solution, but converge to the solution that is obtained when assuming a constant objective function. The reason is that the objective function in this case has physical upper and lower bounds and therefore the approximation of the objective function flattens as the step size increases.
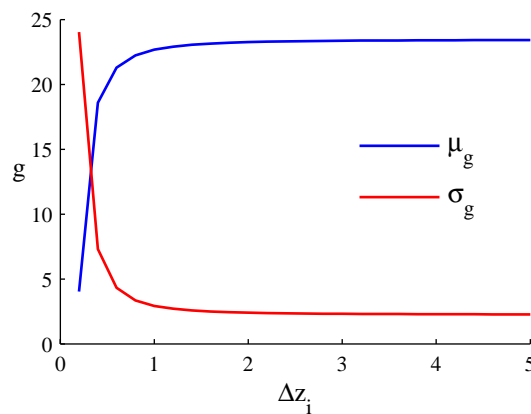

Figure 4-8: Result of the incomplete second order approach with respect to the step size for Z07

It cannot be concluded that a step size of $\Delta z_i = 1.5 \, \sigma_i$ provides good results independently of the given problem, but it seems to be reasonable, since the interval of interest is about $[\mu_i - 3 \, \sigma_i, \, \mu + 3 \, \sigma_i]$ for usual distribution functions. Furthermore, it always has to be assured that the chosen step size is large enough to significantly influence the objective function. E.g. for the material parameters considered the buckling load rarely changes if the parameters are increased by the standard deviation. Hence, the change of bucking load is too small in order to estimate the derivative accurately. Thus, a larger step size should be chosen in these cases.

Summarized, the derivative step size should have an order of magnitude of 1.5 times the standard deviation and it should be large enough to yield a well conditioned estimation of derivatives.

4.6   Probabilistic Design Procedure

In this section the proposed procedure to define the lower bound of load carrying capability are summarized.

4.6.1   Design of Cylindrical Shells

For the design of axially compressed cylindrical shells, the objective function $g(\mathbf{x})$ in the probabilistic analysis is the buckling load $\lambda(\mathbf{x})$. The random vector $\mathbf{X}$ represents all scattering

input parameters, such as geometric imperfections, boundary conditions and load introduction, wall thickness, material properties, fiber orientation, etc. Given the mean value μ_Λ and the standard deviation σ_Λ of buckling load, the design load λ_d can be expressed by

$$\lambda_d = \mu_\Lambda - b\,\sigma_\Lambda \qquad (4.60)$$

The factor b depends on the assumed type of distribution and the chosen level of reliability (see Figure 4-9 and Table 4-2). When assuming normal distribution, the factor b can also be interpreted as the reliability index β with changed sign, which is defined as

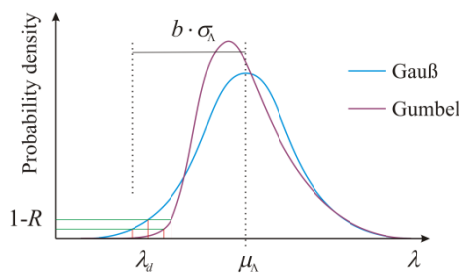$$\beta = \frac{\lambda_d - \mu_\Lambda}{\sigma_\Lambda} = -b \qquad (4.61)$$

Figure 4-9: Influence of the factor b on the design load

Distribution	Reliability		
	0.99	0.999	0.9999
Normal	2.3263	3.0902	3.719
Uniform	1.6974	1.7286	1.7317
Gumbel	1.6408	1.9569	2.1812
Laplace	3.912	6.2146	8.5172
Logistic	4.5951	6.9068	9.2102

Table 4-2: Design factor b for different distributions and levels of reliability

Appropriate mathematical description of input parameters (e.g. Fourier series for geometric imperfections)	$\mathbf{x} = \left(\bar{\bar{\xi}}_{00}, \bar{\varphi}_{00}, \ldots, \bar{\bar{\xi}}_{10\,20}, \bar{\varphi}_{10\,20}, \theta, \omega, E_{11}, \ldots \right)$

Probabilistic method

1. Reducing the number of random parameters by transforming to uncorrelated random parameters

$$\mathbf{x} = \mathbf{B}\,\mathbf{z} + \boldsymbol{\mu}$$

2. Numerical determination of first and second derivative with $\Delta z_i \approx 1.5\,\sigma_i$

$$\lambda_{,ii} \approx \frac{\lambda\left(\mu_i + \Delta z_i\right) - 2\,\lambda\left(\boldsymbol{\mu}\right) + \lambda\left(\mu_i - \Delta z_i\right)}{\Delta z_i^2}$$

3. Semi-analytical first order or incomplete second order approach to determine μ_Λ, σ_Λ and v_Λ

$$\mu_\Lambda \approx \lambda(\boldsymbol{\mu}) + \frac{1}{2}\sum_{i=1}^{n}\lambda_{,ii}\,\mu_{i,2}$$

4. Choice of type of distribution and level of reliability (with respect to v_Λ) to determine b and the hence the design load λ_d

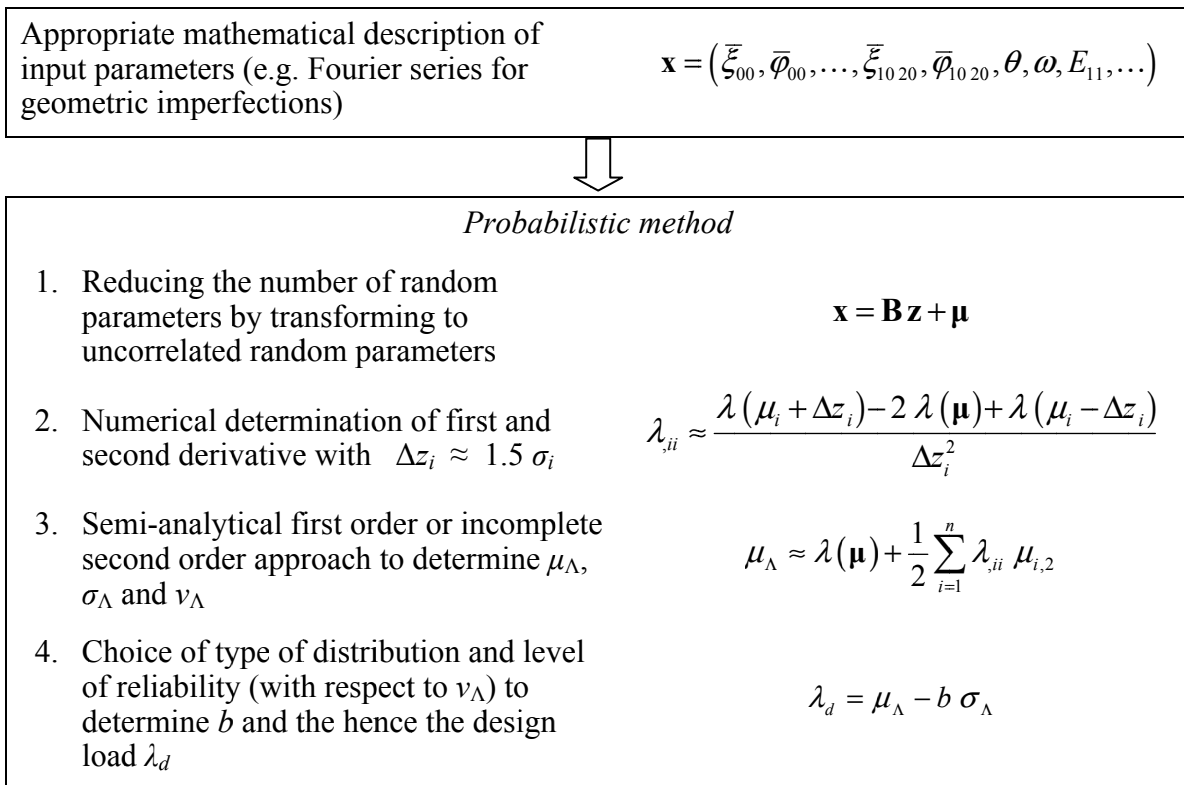$$\lambda_d = \mu_\Lambda - b\,\sigma_\Lambda$$

Figure 4-10: Flow chart of the proposed probabilistic design procedure

It is proposed to estimate the stochastic moments with the incomplete second order approach (ISOA), as reasoned in section 4.5.1. The proposed probabilistic design procedure is summarized in Figure 4-10. Except for the first step, the procedure is applicable to all problems with only one objective functions, for which derivatives can be estimated.

The previously proposed probabilistic design concepts that are discussed in section 1.2.5, simplified the imperfection models in order to reduce the number of random parameters or dealt with very large number of random parameters. The probabilistic design procedure proposed here combines a purely mathematical reduction technique (step 1) with the fast probabilistic method (step 3). This altogether provides a fast analysis tool that does not require simplifying imperfections and therefore allows for a realistic approximation of the stochastic distribution of the load carrying capability and provides a realistic lower bound.

4.6.2   Reliability of Stiffened Panels

For stiffened panels not only the global buckling load is decisive for design; it also must be ensured that no material degradation occurs. Hence, two objective functions and their joint probability density function (see Figure 4-11) have to be considered within the probabilistic analysis. The failure region of a stiffened panel is plotted in Figure 4-12. The design load is a lower bound for the global buckling load as well as for the onset of degradation, which is why the design load is a value on the bisection line. The yellow area equals the failure region in which the global buckling load or the onset of degradation load or both are smaller than the design load.
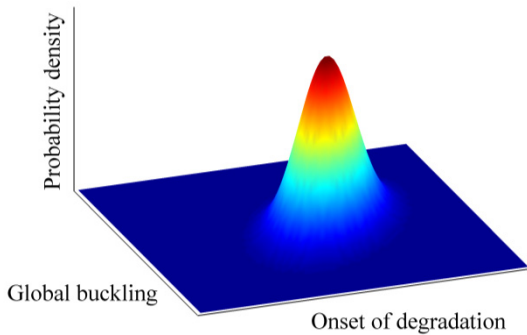

Figure 4-11: Joint probability density function of global buckling and onset of degradation
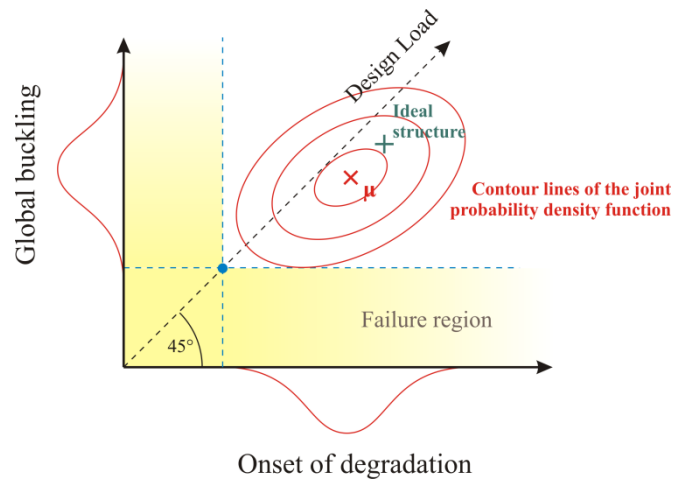

Figure 4-12: Failure region of stiffened panels

Depending on the panel design it is possible that the load level at onset of degradation is smaller than the global buckling load, but the global buckling still occurs first (see Figure 4-13). Hence, for determining the probability of failure (PoF) of a stiffened panel, the displacements should be considered as random output parameters. Then, the PoF of a stiffened panel equals the probability that the displacement at global buckling u_{GB} or the displacement at onset of degradation u_{OD} or both are smaller than the displacement connected to the design load level u_d.

$$PoF = P\left(U_{GB} < u_d \vee U_{OD} < u_d\right)$$
$$= \int_{-\infty}^{\infty} \int_{-\infty}^{u_d} f_{\mathbf{U}}\left(u_{GB}, u_{OD}\right) \ du_{OD} \ du_{GB} + \int_{-\infty}^{u_d} \int_{u_d}^{\infty} f_{\mathbf{U}}\left(u_{GB}, u_{OD}\right) \ du_{OD} \ du_{GB} \tag{4.62}$$
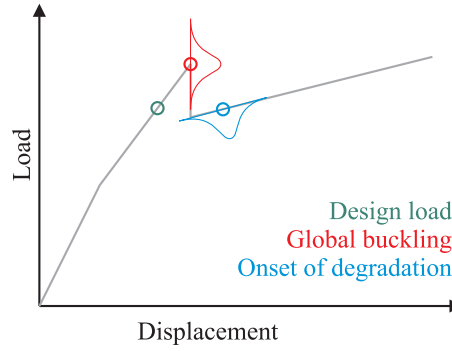
Figure 4-13: Sketch of a load-displacement curve of a stiffened panel with significant dropoff and early onset of degradation

If the critical displacements are assumed to be normally distributed, their joint probability density function is given by

$$f_{\mathbf{U}}\left(u_{GB},u_{OD}\right)=\frac{1}{2\pi\left|\mathbf{\Sigma}_{uGD}\right|^{\frac{1}{2}}}\exp\left(-\frac{1}{2}\left[\begin{pmatrix}u_{GB}\\u_{OD}\end{pmatrix}-\begin{pmatrix}\mu_{uG}\\\mu_{uD}\end{pmatrix}\right]^{T}\mathbf{\Sigma}_{uGD}^{-1}\left[\begin{pmatrix}u_{GB}\\u_{OD}\end{pmatrix}-\begin{pmatrix}\mu_{uG}\\\mu_{uD}\end{pmatrix}\right]\right) \qquad (4.63)$$

where μ_{uG} and μ_{uD} are the mean values of the critical displacements, which are estimated as described in section 4.3.3. The covariance matrix $\mathbf{\Sigma}_{uGD}$ is given by

$$\mathbf{\Sigma}_{uGD}=\begin{pmatrix}\sigma_{uG}&\sigma_{uD}\end{pmatrix}\begin{pmatrix}1&\rho_{uGD}\\\rho_{uGD}&1\end{pmatrix}\begin{pmatrix}\sigma_{uG}\\\sigma_{uD}\end{pmatrix} \qquad (4.64)$$

where σ_{uG} and σ_{uD} are the standard deviations of the displacement at global buckling and onset of degradation, and ρ_{uGD} is the correlation coefficient of the critical displacements, which is determined according to section 4.3.4. With this assumption, the integral (4.62) can be solved numerically.

In general, the joint probability density function $f_{\mathbf{U}}(u_{GB},u_{OD})$ is unknown and can be of any type of distribution. Compared to the one-dimensional case there is a smaller number of types of distributions that describe a multivariate distribution. However, if two random parameters X and Y are independent, their joint PDF $f_{X,Y}(x,y)$ can be written as the product of the PDFs of each random variable.

$$f_{X,Y}\left(x,y\right)=f_{X}\left(x\right)\cdot f_{Y}\left(y\right) \qquad (4.65)$$

Then, the type of distribution can be chosen independently for each random parameter. Hence, it is desirable to transform the objective values u_{GB} and u_{OD} to uncorrelated parameters using the Mahalanobis transformation (4.17) as illustrated in Figure 4-14.

The Mahalanobis transformation of the critical displacements is given by

$$\begin{pmatrix}u_{GB}\\u_{OD}\end{pmatrix}=\mathbf{\Sigma}_{uGD}^{\frac{1}{2}}\begin{pmatrix}v_{1}\\v_{2}\end{pmatrix}+\begin{pmatrix}\mu_{uG}\\\mu_{uD}\end{pmatrix} \qquad (4.66)$$

In the space of v_1 and v_2, the design displacements $v_{d,1}$ and $v_{d,2}$ are given by

$$\mathbf{\Sigma}_{uGD}^{-\frac{1}{2}}\left[\begin{pmatrix}u_{d}\\u_{d}\end{pmatrix}-\begin{pmatrix}\mu_{uG}\\\mu_{uD}\end{pmatrix}\right]=\begin{pmatrix}v_{d,1}\\v_{d,2}\end{pmatrix} \qquad (4.67)$$
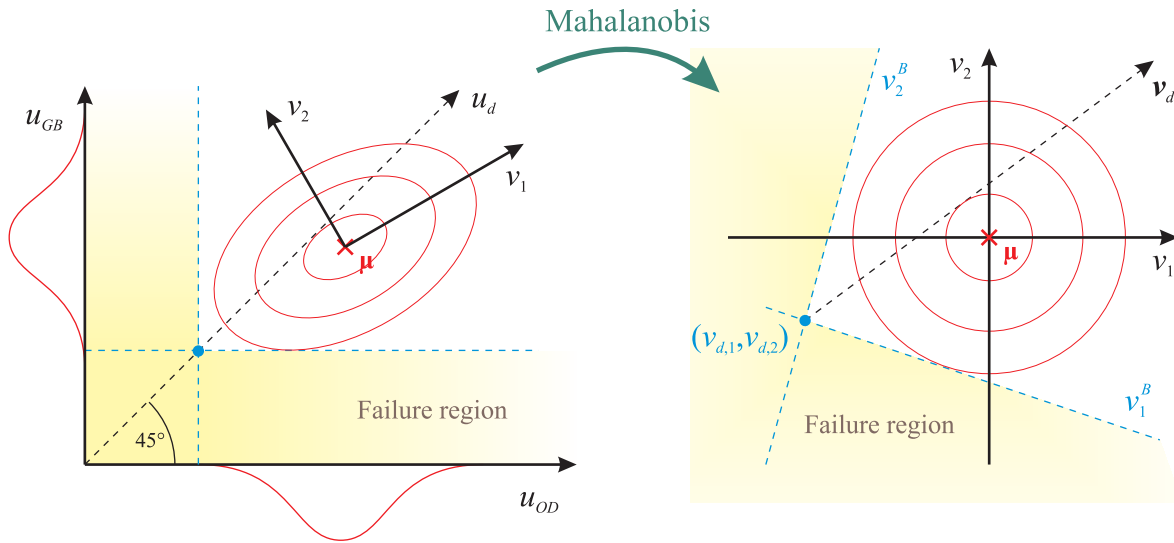
Figure 4-14: Transformation of the failure region to a space of uncorrelated objective values

Assuming independence of the transformed parameters, the probability density function can be written as

$$f_{\mathbf{V}}(v_1, v_2) = f_{V_1}(v_1) \cdot f_{V_2}(v_2) \tag{4.68}$$

Now, the probability density functions of the two design variables can be regarded independently. The probability of failure then is determined from

$$PoF \approx \int_{-\infty}^{v_{d,1}} f_{V_1}(v_1)\, dv_1 \cdot \int_{-\infty}^{v_{d,2}} f_{V_2}(v_2)\, dv_2 + \int_{v_{d,1}}^{\infty} f_{V_1}(v_1) \int_{-\infty}^{v_2^B} f_{V_2}(v_2)\, dv_2\, dv_1$$

$$+ \int_{v_{d,2}}^{\infty} f_{V_2}(v_2) \int_{-\infty}^{v_1^B} f_{V_1}(v_1)\, dv_1\, dv_2 \tag{4.69}$$

Due to the transformation (4.66), the integral bounds change as shown in Figure 4-14. The new integral bounds v_1^B and v_2^B read

$$v_1^B(v_2) = \frac{u_d - \sigma_{12}\, v_2 - \mu_{uG}}{\sigma_{11}} \quad \text{and} \quad v_2^B(v_1) = \frac{u_d - \sigma_{21}\, v_1 - \mu_{uD}}{\sigma_{22}} \tag{4.70}$$

Here, σ_{11}, σ_{12}, σ_{21} and σ_{22} are the entries of the root of the covariance matrix.

$$\begin{pmatrix} \sigma_{11} & \sigma_{12} \\ \sigma_{21} & \sigma_{22} \end{pmatrix} = \mathbf{\Sigma}_{uGD}^{\frac{1}{2}} \tag{4.71}$$

Summarized, it is proposed to estimate the stochastic moments of the displacements with the approximations given in section 4.3.3 and 4.3.4. Then, the PoF is to be determined from (4.69) for a given displacement at design load. The reliability of the associated design load is given by $R = 1 - PoF$.

4.7   Provision for the Sample Size

The mean vector and the covariance matrix of the random vector are determined from a set of samples obtained from measurements. When using the transformation discussed in section

4.1.3, the number of uncorrelated random parameters depends on the number of these samples. In turn, the number of random parameters determines the computational cost of the semi-analytic, probabilistic approach (see section 4.5.1). Hence, the smaller the sample size, the faster is the probabilistic method, which might lead to the conclusion that it is better to have a small data basis. This is of course not the case, because the smaller the sample size is, the less accurate is the estimation of mean values and variances of input parameters and hence, the less accurate is the probabilistic analysis. To make this issue more clear, some introductory remarks on the determination of stochastic moments from measurements are given in the following.

Given a random number X with the probability density function f_X. The exact mean value μ_X of X is given by

$$\mu_X = \int\limits_{-\infty}^{\infty} x\, f_X(x)\, dx \tag{4.72}$$

Given a set of m realization $x^{(i)}$ of X (with $i = 1,\ldots,m$), the mean value can be estimated.

$$\overline{x} = \frac{1}{m}\sum_{i=1}^{m} x^{(i)} \tag{4.73}$$

Note that the estimator $\overline{x}$, which is often referred to as samples mean value or empiric mean value, does not equal the exact mean value μ_X. Moreover, $\overline{x}$ differs for different sets of realizations and is therefore a stochastically distributed variable itself. For $m \to \infty$ the estimator $\overline{x}$ converges towards μ_X and the scatter vanishes.

The same considerations hold for the variance σ_X^2 of X. The exact variance is given by

$$\sigma_X^2 = \int\limits_{-\infty}^{\infty} (x - \mu_X)^2\, f_X(x)\, dx \tag{4.74}$$

and the estimator s^2 of the variance is given by

$$s^2 = \frac{1}{m-1}\sum_{i=1}^{m}\left[x^{(i)} - \overline{x} \right]^2 \tag{4.75}$$

Again, the estimator depends on the given set of realizations and is therefore a random number itself.

Summarized, the smaller the sample size, the more scatter the estimators of mean value and variance and hence, the higher the probability that the estimated mean value and variance are not representative for the random number considered. In the context of probabilistic design this might lead to a non-conservative design, if for instance the variance of one input parameter is underestimated based on the present data. Therefore, the probabilistically motivated design load should be more conservative, the smaller the sample size is. In this section a concept to account for the uncertainties of the estimators is derived.

4.7.1   Distribution of Estimators

The estimator $\overline{x}$ given in (4.73) is now regarded as a random number and will therefore be denoted as $\overline{X}$. Given the realizations $x^{(i)}$ of the random number X are distributed independently, the mean value $E(\overline{X})$ and the variance $\mathrm{var}(\overline{X})$ of the estimator are given by

$$E(\overline{X}) = \mu_X \quad \text{and} \quad \mathrm{var}(\overline{X}) = \frac{\sigma_X^2}{m} \tag{4.76}$$

The assumption that the realizations are distributed independently is valid for the application considered within this thesis. For instance, the wall thickness of a shell is not dependent on the wall thickness of previously manufactured shells (though underlying the same distribution).

The estimator s^2 of the variance, given in (4.75), has a mean value $E(S^2)$ and variance $\text{var}(S^2)$ given by

$$E(S^2) = \sigma_X^2 \quad \text{and} \quad \text{var}(S^2) = \frac{1}{m}\left(\mu_{X,4} - \frac{m-3}{m-1}\sigma_X^4\right) \tag{4.77}$$

where $\mu_{X,4}$ is the fourth central moment of X. For the derivation of mean value and variance of the estimators the reader should refer to section 8.2 in [110].

4.7.2   Procedure to Account for Uncertainties of Estimators

If a more conservative approach shall be used in order to account for the uncertainties, it is suggested to modify the estimator as follows.

$$\overline{x}_{mod} = E(\overline{x}) \pm c \sqrt{\text{var}(\overline{x})} \tag{4.78}$$

$$s_{mod}^2 = E(S^2) \pm c \sqrt{\text{var}(S^2)} \tag{4.79}$$

This way, the estimators are deviated from their mean values about their standard deviation times some factor c. It is suggested to chose the factor $c = 2$. Then, the conservative estimator is exceeded (or undercut, respectively) by 95% of the estimations using the standard estimator. However, it is not always obvious whether increasing or decreasing the estimator leads to a conservative design approach.

According to equation (4.60) a decrease of the mean value of the objective function and an increase of the standard deviation of the objective function lead to a decreasing design load. Using the first-order second-moment approach, mean value and variance of the objective function g are given by

$$\mu_g \approx g(\boldsymbol{\mu}) \tag{4.80}$$

and

$$\sigma_g^2 \approx \sum_{i=1}^{n} g_{,i}^2 \, \mu_{i,2} \tag{4.81}$$

It is obvious that an increase of the variance $\mu_{i,2}$ of an input parameters X_i always increases the variance of the objective function σ_g^2. Therefore, modifying the estimator s_i^2 of the variance such that it overestimates the variance leads to a conservative approach. This conservative estimator is expressed as

$$s_{i,con}^2 = E(S_i^2) + c \sqrt{\text{var}(S_i^2)} \tag{4.82}$$

Since the real variance is unknown, the mean value and the variance of the standard deviation given by (4.77) must be determined using the estimated values. Then, the conservative estimator of the variance reads

$$s_{i,con}^2 = s_i^2 + c \sqrt{\frac{1}{m}\left(\overline{\mu}_{i,4} - \frac{m-3}{m-1}s_i^4\right)} \tag{4.83}$$

where $\overline{\mu}_{i,4}$ is the estimated fourth central moment of X_i.

Whether increasing or decreasing an estimated mean value $\bar{x}$ leads to a higher or lower mean value of the objective function depends on the objective function itself. If increasing a random parameter X_i leads to a higher value of g and according to (4.80) to a higher μ_g, the estimator must be modified such that it decreases $\bar{x}_i$ in order to be conservative. If increasing X_i decreases μ_g, the estimator must be increased. Mathematically, this is expressed as

$$\bar{x}_{i,con} = \begin{cases} E(\bar{x}_i) + c\sqrt{\mathrm{var}(\bar{x}_i)} & \text{if } \dfrac{\partial g(\boldsymbol{\mu})}{\partial x_i} < 0 \\[2ex] E(\bar{x}_i) - c\sqrt{\mathrm{var}(\bar{x}_i)} & \text{if } \dfrac{\partial g(\boldsymbol{\mu})}{\partial x_i} > 0 \end{cases} \tag{4.84}$$

When inserting (4.76), but using the estimated values, (4.84) reads

$$\bar{x}_{i,con} = \begin{cases} \bar{x}_i + c\dfrac{s_i}{\sqrt{m}} & \text{if } \dfrac{\partial g(\bar{\mathbf{x}})}{\partial x_i} < 0 \\[2ex] \bar{x}_i - c\dfrac{s_i}{\sqrt{m}} & \text{if } \dfrac{\partial g(\bar{\mathbf{x}})}{\partial x_i} > 0 \end{cases} \tag{4.85}$$

Using the conservative estimators (4.85) and (4.83), and the FOSM method, the conservative probabilistic design load is given by

$$\lambda_{d,con} = \lambda(\bar{\mathbf{x}}_{con}) - b\sqrt{\sum_{i=1}^{n} g_{,i}^2 \, s_{i,con}^2} \tag{4.86}$$

For a small sample size, this design load is much smaller than the design load λ_d obtained with unchanged estimators. With increasing sample size, the conservative design load $\lambda_{d,con}$ increases and converges against λ_d. An overview of discussed estimators and their mean value, variance and conservative modification is given in Table 4-3.

Estimator	$\bar{x} = \dfrac{1}{m}\sum\limits_{i=1}^{m} x^{(i)}$	$s^2 = \dfrac{1}{m-1}\sum\limits_{i=1}^{m}\left[x^{(i)} - \bar{x}\right]^2$
Mean value of estimator	μ_X	σ_X^2
Variance of estimator	$\dfrac{\sigma_X^2}{m}$	$\dfrac{1}{m}\left(\mu_{X,4} - \dfrac{m-3}{m-1}\sigma_X^4\right)$
Conservative estimator	$\bar{x}_{con} = \bar{x} \pm c\dfrac{s}{\sqrt{m}}$	$s_{con}^2 = s_i^2 + c\sqrt{\dfrac{1}{m}\left(\bar{\mu}_{i,4} - \dfrac{m-3}{m-1}s_i^4\right)}$

Table 4-3: Properties and modifications of estimators for mean value and variance

4.8   Design Optimization

Compared to structures made of isotropic material, fiber composite structures have the fiber orientations of each ply as additional design variable and therefore provide additional design freedom for optimization. Using knockdown or safety factors for the design of composite structures, maximizing the design load is equivalent to maximizing the load carrying capability of the perfect structure. This does not take into account sensitivities to scattering

parameters. Hühne et al. [27] and Kriegesmann et al. [111] showed that for a composite cylinder under axial compression the optimal design changes in presence of an imperfection. Hence, the proposed design methods should be considered for design optimization. For this, the derivatives of the probabilistically motivated design load as well as the derivatives of the lower bound given by convex anti-optimization with respect to design variables are given in this section. This enables the application of gradient based optimization algorithms for design optimization.

4.8.1   Optimization Procedures

A multitude of optimization algorithms are given in the literature (see e.g. [112]). The methods can be divided into gradient based methods, like for instance conjugated gradient methods, and non-gradient based methods, like genetic algorithms. Gradient based methods often converge faster where non-gradient based methods are often more robust. If the design parameters are discrete and it is not possible to determine a gradient, non-gradient based methods must be used. In order to combine the advantages of both strategies, hybrid methods have been developed. There, the optimization may start with a genetic algorithm to avoid the risk that the following gradient based optimization only finds a local minimum and misses the global minimum. In case the design parameters are discrete, but can be regarded in a continuous space, gradient based methods can be used to find a good initial guess for the following genetic algorithm (see e.g. [113]). One example for such a problem is the optimization of a laminate setup, where the ply angles may only take the values 0°, 45°, -45° and 90°.

The design procedures given in section 4.4 and 4.6 require a multitude of buckling analyses. Hence, maximizing the design loads given by these approaches appears to be only possible when using gradient based methods and/or having a relatively small number of design variables.

Three gradient based optimization algorithms are discussed in the following. The goal is to minimize the objective function $f(\mathbf{x})$ with the gradient $\mathbf{g}(\mathbf{x}) = \nabla f(\mathbf{x})$ and the Hessian $\mathbf{H} = \nabla\nabla f$. For each algorithm, a start vector $\mathbf{x}_0$ has to be chosen; the iteration stops when $\|\mathbf{g}_i\| \approx 0$ or $\|\mathbf{g}_i\| \leq \varepsilon$, respectively. A very simple gradient based algorithm is given by

$$\mathbf{x}_{i+1} = \mathbf{x}_i + \mathbf{g}_i \tag{4.87}$$

For quadratic objective functions the Newton method (4.88) offers a more efficient algorithm

$$\mathbf{x}_{i+1} = \mathbf{x}_i - \mathbf{H}_i^{-1}\mathbf{g}_i \tag{4.88}$$

The conjugate gradient method is a gradient based optimization algorithm, which is frequently used to solve large linear systems of equation, since this problem is equivalent to finding the minimum of a quadratic function. In the first iteration step $\mathbf{s}_0 = -\mathbf{g}_0$. Then, according to Jarre and Stoer [112], the conjugate gradient algorithm consists of the following steps.

1. $\lambda_i = \dfrac{-\mathbf{g}_i^T\mathbf{s}_i}{\mathbf{s}_i^T\mathbf{H}_i\mathbf{s}_i}$

2. $\mathbf{x}_{i+1} = \mathbf{x}_i + \lambda_i\mathbf{s}_i$

3. $\mathbf{g}_{i+1} = \mathbf{g}(\mathbf{x}_{i+1})$, $\mathbf{H}_{i+1} = \mathbf{H}(\mathbf{x}_{i+1})$

4. $\gamma_{i+1} = \dfrac{\mathbf{g}_{i+1}^T\mathbf{g}_{i+1}}{\mathbf{g}_i^T\mathbf{g}_i}$

5. $\mathbf{s}_{i+1} = -\mathbf{g}_{i+1} + \gamma_{i+1}\mathbf{s}_i$

The convergence of the conjugate gradient method can be improved by preconditioning the problem. For instance, the Cholesky decomposition $\mathbf{L}\,\mathbf{L}^T = \mathbf{H}$ can be used to optimize in the transformed space of $\mathbf{z}$ with $\mathbf{z} = \mathbf{L}^{-T}\mathbf{x}$ and replace $\mathbf{H}$ by the better conditioned matrix $\mathbf{L}^T\mathbf{H}\,\mathbf{L}^{-T}$ [112]. The resulting modified and more efficient algorithm is for instance given in [114].

In the given form, all algorithms find minima, but they can also be used for maximization problems, since this only requires a change of the algebraic sign.

When maximizing the design load, the simple gradient algorithm has the important advantage that it does not require the determination of the second derivatives. Hence, each iteration step needs significantly less buckling load calculations than the Newton algorithm and the conjugate gradient method.

4.8.2   Gradient of Probabilistically Based Design Load

Considering the buckling load function $\lambda(\mathbf{x},\mathbf{y})$ as a function of random variables, subsumed in the vector $\mathbf{x}$, and design variables, subsumed in the vector $\mathbf{y}$, also the probabilistically motivated design load λ_d is a function of $\mathbf{y}$, which is given by

$$\lambda_d\left(\mathbf{y}\right) = \mu_\Lambda\left(\mathbf{y}\right) - b\sqrt{\sigma_\Lambda^2\left(\mathbf{y}\right)} \tag{4.89}$$

where b depends on the assumed type of distribution and the chosen level of reliability (see section 4.6.1). The first derivative with respect to one design variable y_k equals

$$\frac{\partial \lambda_d\left(\mathbf{y}\right)}{\partial y_k} = \frac{\partial \mu_\Lambda\left(\mathbf{y}\right)}{\partial y_k} - \frac{b}{2\,\sigma_\Lambda}\frac{\partial \sigma_\Lambda^2\left(\mathbf{y}\right)}{\partial y_k} \tag{4.90}$$

As derived in Appendix E, the derivatives of the second order approximations of the mean value and the variance are given by

$$\frac{\partial \mu_\Lambda\left(\mathbf{y}\right)}{\partial y_k} \approx \frac{\partial \lambda\left(\boldsymbol{\mu},\mathbf{y}\right)}{\partial y_k} \tag{4.91}$$

and

$$\frac{\partial \sigma_\Lambda^2\left(\mathbf{y}\right)}{\partial y_k} \approx 2\left(\lambda_\mu - \mu_\Lambda\right)\frac{\partial \lambda}{\partial y_k} + 2\sum_{i=1}^{n}\frac{\partial \lambda}{\partial x_i}\frac{\partial^2 \lambda}{\partial x_i\,\partial y_k}\mu_{i,2} + \frac{\partial \lambda}{\partial y_k}\sum_{i=1}^{n}\frac{\partial^2 \lambda}{\partial x_i^2}\mu_{i,2} + \sum_{i=1}^{n}\frac{\partial^2 \lambda}{\partial x_i^2}\frac{\partial^2 \lambda}{\partial x_i\,\partial y_k}\mu_{i,3} \tag{4.92}$$

If the buckling load function is assumed to be linear, the derivative of the variance vanishes and the gradient of the design load equals the gradient of the mean value. If it is assumed that the objective function is linearly dependent of x, then the derivative of the variance is given by

$$\frac{\partial \sigma_\Lambda^2\left(\mathbf{y}\right)}{\partial y_k} \approx 2\sum_{i=1}^{n}\frac{\partial \lambda}{\partial x_i}\frac{\partial^2 \lambda}{\partial x_i\,\partial y_k}\mu_{i,2} \tag{4.93}$$

When using this approach, it is not necessary to estimate the second derivative of the buckling load with respect to the random parameters. However, this simplification does not decrease the computational costs significantly.

In general, a design parameter can at the same time be a random parameter. This has to be considered by setting the design parameter y_q equal to the random parameter x_p and use equation (4.90)-(4.93) in an unchanged manner. The only difference is that the derivatives with respect to x_p and y_q only have to be determined once, of course. A more challenging case is given if the moments of the input parameters $\mu_{i,k}$ are dependent of design parameter. In this

case, the derivatives of the stochastic moments with respect to the design parameters $\partial \mu_{i,k} / \partial y_q$ must be estimated. This is only possible if either the stochastic moments are known for different values of the design parameters or can be estimated by simulation.

4.8.3   Gradient of Design Load given by Convex Anti-Optimization

Considering the buckling load function $\lambda(\mathbf{x},\mathbf{y})$ as a function of scattering variables, subsumed in the vector $\mathbf{x}$, and design variables, subsumed in the vector $\mathbf{y}$, the minimum buckling load given by convex anti-optimization is a function of $\mathbf{x}$ and $\mathbf{y}$. The first order approach of the minimum buckling load is given by

$$\lambda_{\min}(\mathbf{y}) = \lambda(\mathbf{x}_c, \mathbf{y}) - \sqrt{\varphi^T(\mathbf{y})\mathbf{G}\,\varphi(\mathbf{y})} \tag{4.94}$$

According to the derivation in Appendix F, the first derivative with respect to one design parameter y_j is given by

$$\frac{\partial \lambda_{\min}}{\partial y_j} = \frac{\partial \lambda}{\partial y_j} - \frac{1}{\sqrt{\varphi^T \mathbf{G}\,\varphi}}\,\varphi^T\,\mathbf{G}\,\frac{\partial \varphi}{\partial y_j} \tag{4.95}$$

with the gradient of the buckling load with respect to the uncertainty parameters

$$\varphi = \left(\frac{\partial \lambda}{\partial x_1}, \cdots, \frac{\partial \lambda}{\partial x_d}\right)^T \tag{4.96}$$

and its derivative with respect to one design parameter

$$\frac{\partial \varphi}{\partial y_j} = \left(\frac{\partial^2 \lambda}{\partial x_1\,\partial y_j}, \cdots, \frac{\partial^2 \lambda}{\partial x_d\,\partial y_j}\right)^T \tag{4.97}$$

4.8.4   Number of Buckling Analysis per Iteration Step

Finding the maximum design load given by convex anti-optimization requires the estimation of the following derivatives of buckling load.

$$\frac{\partial \lambda(\hat{\mathbf{x}},\mathbf{y})}{\partial x_i} \quad,\quad \frac{\partial \lambda(\hat{\mathbf{x}},\mathbf{y})}{\partial y_k} \quad \text{and} \quad \frac{\partial^2 \lambda(\hat{\mathbf{x}},\mathbf{y})}{\partial x_i\,\partial y_k} \tag{4.98}$$

The same holds for the maximization of the probabilistic approach, if the simplified approach for the gradient of the variance (4.93) is used. Regarding the probabilistic analysis, $\hat{\mathbf{x}}$ equals the mean vector of random parameters $\boldsymbol{\mu}$, and in case of the convex anti-optimization $\hat{\mathbf{x}}$ is the center point $\mathbf{x}_c$ of the MVEE. The vector $\mathbf{y}$ includes the design variables of the current step.

Using the approximation (4.49) and (4.52) to estimate the derivatives (4.98), the buckling load function λ must be evaluated once at $(\hat{\mathbf{x}},\mathbf{y})$, once for each entry of $\mathbf{x}$, once for each entry of $\mathbf{y}$ and once for each combination of x_i and y_k. Given p random or uncertainty parameters ($p = n_z$ or $p = d$, respectively) and q design parameters, the number of required buckling analyses per iteration step equals $1 + p + q + p\,q$.

When using the full approach for the derivatives of the variance (4.92) within the probabilistic approach, the second derivative of the buckling load with respect to the random parameters must be estimated additionally. Then, p additional buckling load calculations have to be performed in each iteration step, in order to estimate the second derivative according to (4.51). This also allows a more accurate estimation of the first derivative, using (4.50).

	Convex anti-optimization and probabilistic approach, using (4.93)	Probabilistic approach, using (4.92)
Required derivatives	$\dfrac{\partial \lambda(\hat{\mathbf{x}}, \mathbf{y})}{\partial x_i}, \; \dfrac{\partial \lambda(\hat{\mathbf{x}}, \mathbf{y})}{\partial y_k}, \; \dfrac{\partial^2 \lambda(\hat{\mathbf{x}}, \mathbf{y})}{\partial x_i \, \partial y_k}$	additionally $\dfrac{\partial^2 \lambda(\hat{\mathbf{x}}, \mathbf{y})}{\partial x_i^2}$
Buckling load calculations per iteration step	$1 + p + q + p\,q$	$1 + 2\,p + q + p\,q$

Table 4-4: Required derivatives of the buckling load and resulting number of buckling load calculations per iteration step for gradient based design optimization under uncertainty (p: number of random or uncertainty parameters, $p = n_z$ or $p = d$, respectively; q: number of design parameters)

The number of required buckling analyses per iteration step is summarized in Table 4-4 for the different design approaches that consider uncertain input parameters. The most buckling analyses are required for the estimation of the second derivative with respect to one uncertainty parameter x_i and one design variable y_k. Therefore, using the more accurate estimation of the derivative of the variance (4.92) hardly causes additional numerical costs.

5   Verification with Analytical Example

When using numerical methods like the finite element method for evaluating the objective function of a probabilistic analysis, the objective function is never given in an explicit form, which requires the use of approximate methods as given in the previous chapter. However, in order to validate a probabilistic method itself, an example must be considered for which the stochastic distribution function of the objective function and its characteristic moments can be determined exactly.

For this reason, an example function is considered in this chapter for which the stochastic distribution can be determined analytically from solving integral (4.24). By applying the probabilistic methods given in section 4.3 to the example, the methods and their implementations are verified. The example also can be used by other scientist for validating probabilistic methods in the future.

5.1   Verification Example

In the following, a simple distribution function for a random vector **X** and a linear objective function are given, which allow solving the integral (4.24) analytically. Furthermore, a quadratic objective function is considered in order to validate also the second order approach, given in sections 4.3.3 and 4.3.4.

5.1.1   Example Distribution

Given the random parameters X_1 and X_2 with the probability density functions (PDF) f_1 and f_2, given by

$$f_1(x_1) = \begin{cases} -\frac{3}{4}(x_1 - 2)^2 + \frac{3}{4} & \text{for } 1 \leq x_1 \leq 3 \\ 0 & \text{else} \end{cases} \tag{5.1}$$

and

$$f_2(x_2) = \begin{cases} \frac{1}{3}(x_2 - 1) & \text{for } 1 \leq x_2 \leq 3 \\ -\frac{2}{3}(x_2 - 4) & \text{for } 3 \leq x_2 \leq 4 \\ 0 & \text{else} \end{cases} \tag{5.2}$$
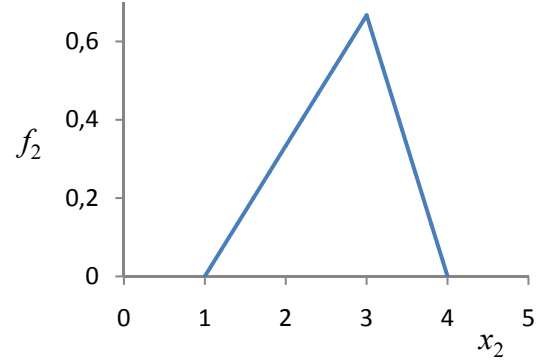
which are plotted in Figure 5-1 and Figure 5-2.

By solving the integral

$$F_X(x) = \int_{-\infty}^{x} f_X(\overline{x}) \, d\overline{x} \tag{5.3}$$

the cumulative distribution functions (CDF) F_1 and F_2 are obtained.

$$F_1(x_1) = \begin{cases} 0 & \text{for } x_1 \leq 1 \\ -\frac{1}{4}x_1^3 + \frac{3}{2}x_1^2 - \frac{9}{4}x_1 + 1 & \text{for } 1 \leq x_1 \leq 3 \\ 1 & \text{for } 3 \leq x_1 \end{cases} \tag{5.4}$$

$$F_2(x_2) = \begin{cases} 0 & \text{for } x_2 \leq 1 \\ \frac{1}{6}x_2^2 - \frac{1}{3}x_2 + \frac{1}{6} & \text{for } 1 \leq x_2 \leq 3 \\ -\frac{1}{3}x_2^2 + \frac{8}{3}x_2 - 4\frac{1}{3} & \text{for } 3 \leq x_2 \leq 4 \\ 1 & \text{for } 4 \leq x_2 \end{cases} \tag{5.5}$$
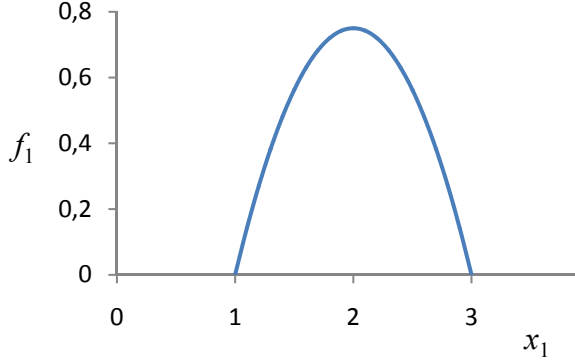
Figure 5-1: Probability density function of X_1   **Figure 5-2: Probability density function of X_2**

Now, the random vector **X** shall be defined as $\mathbf{X} = (X_1, X_2)^T$, and the joint PDF $f_\mathbf{X}$ is chosen to equal

$$f_\mathbf{X}(\mathbf{x}) = f_1(x_1) \cdot f_2(x_2) \tag{5.6}$$

Note that, by definition, two random parameters are independent, if their joint PDF can be written as a product as in (5.6). Then, also the distribution function $F_\mathbf{X}$ is given by the product of CDFs of the independent variables, since

$$F_\mathbf{X}(\mathbf{x}) = \int_{-\infty}^{x_1} \int_{-\infty}^{x_2} f_\mathbf{X}(\overline{\mathbf{x}}) \, d\overline{x}_2 \, d\overline{x}_1 = \int_{-\infty}^{x_1} \int_{-\infty}^{x_2} f_1(x_1) \cdot f_2(x_2) \, d\overline{x}_2 \, d\overline{x}_1$$
$$= \int_{-\infty}^{x_1} f_1(\overline{x}_1) \, d\overline{x}_1 \cdot \int_{-\infty}^{x_2} f_2(\overline{x}_2) \, d\overline{x}_2 = F_1(x_1) \cdot F_2(x_2) \tag{5.7}$$

5.1.2   Characteristic Moments of the Example Distribution

In the following, the characteristic moments of the random parameters are determined. The entries of the mean vector **μ** and the covariance matrix **Σ** are determined by

$$\mu_i = \int_{-\infty}^{\infty} \ldots \int_{-\infty}^{\infty} x_i \, f_\mathbf{X}(\mathbf{x}) \, dx_1 \ldots dx_n \tag{5.8}$$

and

$$\Sigma_{ij} = \int_{-\infty}^{\infty} \int_{-\infty}^{\infty} x_i \, x_j \, f_\mathbf{X}(\mathbf{x}) \, dx_i \, dx_j - \mu_i \mu_j \tag{5.9}$$

For the distributions considered, the mean values yield as follows.

$$\mu_1 = \int_{-\infty}^{\infty} \int_{-\infty}^{\infty} x_1 \, f(x_1, x_2) \, dx_1 \, dx_2 = \int_{-\infty}^{\infty} x_1 f_1 \, dx_1 \cdot \underbrace{\int_{-\infty}^{\infty} f_2 \, dx_2}_{=1} = \int_1^3 x_1 \left[-\tfrac{3}{4}(x_1 - 2)^2 + \tfrac{3}{4} \right] dx_1 = 2 \tag{5.10}$$

$$\mu_2 = \int_1^3 x_2 \tfrac{1}{3}(x_2 - 1) \, dx_2 + \int_3^4 -x_2 \tfrac{2}{3}(x_2 - 4) \, dx_2 = \tfrac{8}{3} \qquad (5.11)$$

The entries of the covariance matrix equal

$$\Sigma_{11} = \int_{-\infty}^{\infty} \int_{-\infty}^{\infty} x_1^2 \, f_{\mathbf{X}}(\mathbf{x}) \, dx_1 \, dx_2 - \mu_1^2$$

$$= \int_1^3 x_1^2 \left[-\tfrac{3}{4}(x_1 - 2)^2 + \tfrac{3}{4} \right] dx_1 - 2^2 = \tfrac{21}{5} - 4 = \tfrac{1}{5} \qquad (5.12)$$

$$\Sigma_{22} = \int_{-\infty}^{\infty} \int_{-\infty}^{\infty} x_2^2 \, f_{\mathbf{X}}(\mathbf{x}) \, dx_1 \, dx_2 - \mu_2^2$$

$$= \int_1^3 x_2^2 \tfrac{1}{3}(x_2 - 1) \, dx_2 + \int_3^4 -x_2^2 \tfrac{2}{3}(x_2 - 4) \, dx_2 - \left(\tfrac{8}{3}\right)^2 = \tfrac{15}{2} - \tfrac{64}{9} = \tfrac{7}{18} \qquad (5.13)$$

and

$$\Sigma_{12} = \int_{-\infty}^{\infty} \int_{-\infty}^{\infty} x_1 \, x_2 \, f_{\mathbf{X}}(\mathbf{x}) \, dx_1 \, dx_2 - \mu_1 \mu_2 = \int_{-\infty}^{\infty} x_1 \, f_1 \, dx_1 \cdot \int_{-\infty}^{\infty} x_2 \, f_2 \, dx_2 - \mu_1 \mu_2 = 0 \qquad (5.14)$$

Summarized, mean vector and covariance matrix of the example joint PDF equal

$$\boldsymbol{\mu} = \begin{pmatrix} 2 \\ \tfrac{8}{3} \end{pmatrix} \qquad \boldsymbol{\Sigma} = \begin{pmatrix} \tfrac{1}{5} & 0 \\ 0 & \tfrac{7}{18} \end{pmatrix} \qquad (5.15)$$

For the semi-analytic, probabilistic approach given in section 4.3.3 and 4.3.4, also higher order moments are required, which are defined as

$$\mu_{i,k} = \int_{-\infty}^{\infty} [x_i - \mu_i]^k \, f_{\mathbf{X}}(\mathbf{x}) \, d\mathbf{x} \qquad (5.16)$$

In Table 5-1, the higher order moments of the example PDF are summarized.

	$\mu_{i,2}$	$\mu_{i,3}$	$\mu_{i,4}$	$\mu_{i,5}$	$\mu_{i,6}$
X_1	1/5	0	3/35	0	1/21
X_2	7/18	-2/27	49/135	-40/243	9661/20412

Table 5-1: Higher order moments of the example distribution

5.1.3   Distribution of a Linear Example Objective Function

Given the linear objective function g as

$$g(\mathbf{x}) = x_1 + 2x_2 \qquad (5.17)$$

with the gradient $\nabla g = (1 \quad 2)^T$. For a fixed value of g the relation of x_1 and x_2 equals

$$x_2 = \tfrac{1}{2}(g - x_1) \qquad (5.18)$$

For the example considered, the integral (4.24) equals

$$F_g(g) = \int\limits_1^3 \int\limits_1^{\frac{1}{2}(g-x_1)} f_{\mathbf{X}}(\mathbf{x}) \, dx_2 \, dx_1 \tag{5.19}$$

since the PDF is only non-equal to zero for $1 \le x_1 \le 3$ and $1 \le x_2 \le 4$. Due to the fact that both PDFs are piecewise functions, also the integral (5.19) has to be solved piecewise, according to the cases depicted in Figure 5-3. The red box represents the integral bounds, the red dashed line represents the change of the definition of $f_2(x_2)$ and the green line is the variable upper integral bound, which is depending on g.
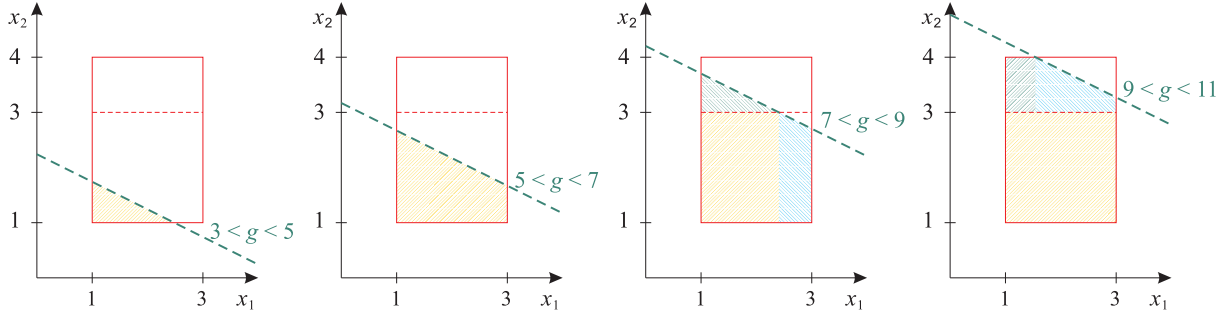
Figure 5-3: Cuts of the objective function g in the domain of the PDF $f_{\mathbf{X}}$ for the example considered

The CDF of g the can be expressed as

$$F_g(g) = \begin{cases} 0 & \text{for } g \le 3 \\ F_{g,1} & \text{for } 3 \le g \le 5 \\ F_{g,2} & \text{for } 5 \le g \le 7 \\ F_{g,3} & \text{for } 7 \le g \le 9 \\ F_{g,4} & \text{for } 9 \le g \le 11 \\ 1 & \text{for } 11 \le g \end{cases} \tag{5.20}$$

with

$$F_{g,1}(g) = \int\limits_1^{g-2} \int\limits_1^{\frac{1}{2}(g-x_1)} f_{\mathbf{X}}(\mathbf{x}) \, dx_2 \, dx_1 = -\tfrac{1}{960} g^5 + \tfrac{1}{48} g^4 - \tfrac{5}{32} g^3 + \tfrac{9}{16} g^2 - \tfrac{63}{64} g + \tfrac{27}{40} \tag{5.21}$$

$$F_{g,2}(g) = \int\limits_1^3 \int\limits_1^{\frac{1}{2}(g-x_1)} f_{\mathbf{X}}(\mathbf{x}) \, dx_2 \, dx_1 = \tfrac{1}{24} g^2 - \tfrac{1}{3} g + \tfrac{27}{40} \tag{5.22}$$

$$F_{g,3}(g) = \int\limits_1^{g-6} \int\limits_1^3 f_{\mathbf{X}}(\mathbf{x}) \, dx_2 \, dx_1 + \int\limits_{g-6}^3 \int\limits_1^{\frac{1}{2}(g-x_1)} f_{\mathbf{X}}(\mathbf{x}) \, dx_2 \, dx_1 + \int\limits_1^{g-6} \int\limits_3^{\frac{1}{2}(g-x_1)} f_{\mathbf{X}}(\mathbf{x}) \, dx_2 \, dx_1$$
$$= \tfrac{1}{320} g^5 - \tfrac{1}{8} g^4 + \tfrac{63}{32} g^3 - \tfrac{733}{48} g^2 + \tfrac{11255}{192} g - \tfrac{7149}{80} \tag{5.23}$$

and

$$F_{g,4}(g) = \int\limits_1^3 \int\limits_1^3 f_{\mathbf{X}}(\mathbf{x}) \, dx_2 \, dx_1 + \int\limits_1^{g-8} \int\limits_3^4 f_{\mathbf{X}}(\mathbf{x}) \, dx_2 \, dx_1 + \int\limits_{g-8}^3 \int\limits_3^{\frac{1}{2}(g-x_1)} f_{\mathbf{X}}(\mathbf{x}) \, dx_2 \, dx_1$$
$$= -\tfrac{1}{480} g^5 + \tfrac{5}{48} g^4 - \tfrac{33}{16} g^3 + \tfrac{121}{6} g^2 - \tfrac{9317}{96} g + \tfrac{14721}{80} \tag{5.24}$$

The PDF of g is the first derivative of the CDF, yielding

$$\frac{\partial F_g(g)}{\partial g} = f_g(g) = \begin{cases} 0 & \text{for } g \leq 3 \text{ and } 11 \leq g \\ -\frac{1}{192}g^4 + \frac{1}{12}g^3 - \frac{15}{32}g^2 + \frac{9}{8}g - \frac{63}{64} & \text{for } 3 \leq g \leq 5 \\ \frac{1}{12}g - \frac{1}{3} & \text{for } 5 \leq g \leq 7 \\ \frac{1}{64}g^4 - \frac{1}{2}g^3 + \frac{189}{32}g^2 - \frac{733}{24}g + \frac{11255}{192} & \text{for } 7 \leq g \leq 9 \\ -\frac{1}{96}g^4 + \frac{5}{12}g^3 - \frac{99}{16}g^2 + \frac{121}{3}g - \frac{9317}{96} & \text{for } 9 \leq g \leq 11 \end{cases} \tag{5.25}$$

The PDF and CDF of g are plotted in Figure 5-4.
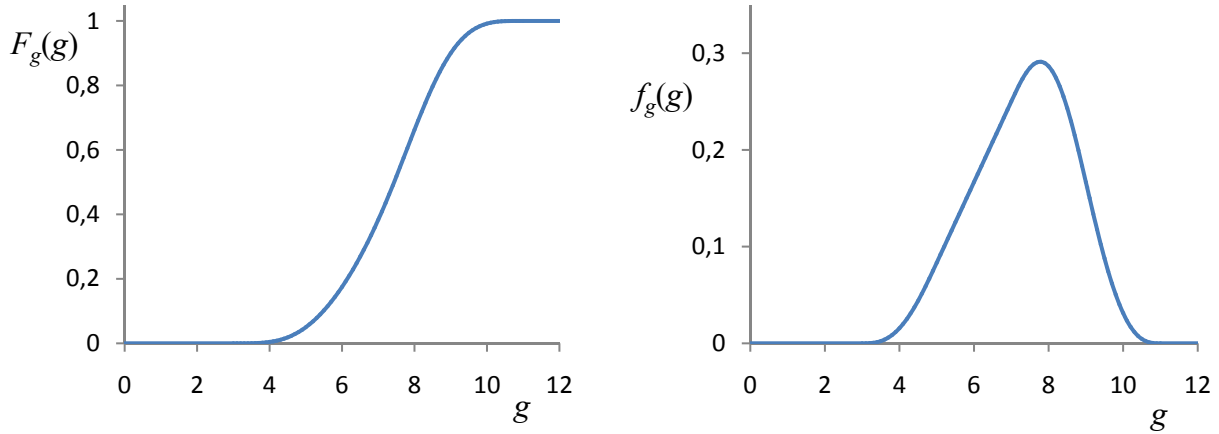
Figure 5-4: CDF (left) and PDF (right) of the objective function *g* for the example considered

The mean value, variance and skewness of the objective function can either be determined based on its PDF according to

$$\mu_g = \int_{-\infty}^{\infty} g\, f_g(g)\, dg \tag{5.26}$$

$$\sigma_g^2 = \int_{-\infty}^{\infty} (g - \mu_g)^2 f_g(g)\, dg = \int_{-\infty}^{\infty} g^2 f_g(g)\, dg - \mu_g^2 \tag{5.27}$$

and

$$v_g = \int_{-\infty}^{\infty} \left[g - \mu_g \right]^3 f_g(g)\, dg \Big/ \sigma_g^3 \tag{5.28}$$

or based on the PDF of random vector **X**.

$$\mu_g = \int_{-\infty}^{\infty} g(\mathbf{x})\, f_{\mathbf{X}}(\mathbf{x})\, d\mathbf{x} \tag{5.29}$$

$$\sigma_g^2 = \int_{-\infty}^{\infty} \left[g(\mathbf{x}) - \mu_g \right]^2 f_{\mathbf{X}}(\mathbf{x})\, d\mathbf{x} = \int_{-\infty}^{\infty} g^2(\mathbf{x})\, f_{\mathbf{X}}(\mathbf{x})\, d\mathbf{x} - \mu_g^2 \tag{5.30}$$

$$v_g = \int_{-\infty}^{\infty} \left[g(\mathbf{x}) - \mu_g \right]^3 f_{\mathbf{X}}(\mathbf{x})\, d\mathbf{x} \Big/ \sigma_g^3 \tag{5.31}$$

For the given examples, the characteristic moments are

$$\mu_g = \tfrac{22}{3}, \; \sigma_g^2 = \tfrac{79}{45} = 1.7\overline{5} \;\; \text{and} \;\; v_g = -\tfrac{16}{27} \Big/ \left(\tfrac{79}{45}\right)^{\frac{3}{2}} \approx -0.25476 \tag{5.32}$$

5.1.4   Stochastic Moments of a Quadratic Example Objective Function

Since the approximation given in section 4.3.3 accounts for quadratic terms, an example of a quadratic objective function is given. The objective function is given by

$$h(\mathbf{x}) = x_2^2 + x_1 x_2 - \tfrac{1}{2} x_1^2 + 2 \tag{5.33}$$

Gradient and Hessian of h equal

$$\nabla h(\mathbf{x}) = \begin{pmatrix} x_2 - x_1 \\ 2 x_2 + x_1 \end{pmatrix} \quad \text{and} \quad \nabla\nabla h = \begin{pmatrix} -1 & 1 \\ 1 & 2 \end{pmatrix} \tag{5.34}$$

At the mean vector $\mathbf{\mu} = \begin{pmatrix} 2 & \tfrac{8}{3} \end{pmatrix}^T$, the gradient is $\nabla h(\mathbf{\mu}) = \begin{pmatrix} \tfrac{2}{3} & \tfrac{22}{3} \end{pmatrix}^T$. Using equations (5.29)-(5.31), the stochastic moments of h are obtained without determining the PDF first.

$$\mu_h = 12.7\overline{3} \qquad \sigma_h^2 = 20.217 \qquad v_h = 0.052 \tag{5.35}$$

The two objective functions g and h are functions of the same random vector $\mathbf{X}$. The covariance Σ_{gh} of the two function considered can therefore be determined by

$$\Sigma_{gh} = \int_{-\infty}^{\infty} \int_{-\infty}^{\infty} (g - \mu_g)(h - \mu_h) f_{gh}(g, h) \, dg \, dh \tag{5.36}$$

which requires knowledge of the joint PDF f_{gh}. The covariance can also be determined by integrating over the space of the random vector.

$$\Sigma_{gh} = \int_{-\infty}^{\infty} \big(g(\mathbf{x}) - \mu_g\big)\big(h(\mathbf{x}) - \mu_h\big) f_{\mathbf{X}}(\mathbf{x}) \, d\mathbf{x} \tag{5.37}$$

For the example considered, the covariance of the objective function equals $\Sigma_{gh} = \tfrac{256}{45} = 5.6\overline{8}$. According to (4.41) this yields a coefficient of correlation of $\rho_{gh} = 0.955$.

5.2   Monte Carlo Simulation of the Linear Example Objective Function

Since the entries of the random vector $\mathbf{X}$ are independent, the realizations used for the Monte Carlo simulation are generated independently. Realization of X_2 are generated using the inverse of F_2, according to (4.25). Since F_1 appears to be difficult to invert, the acceptance rejection method is used to generate realizations of X_1 (see e.g. [90]). The discrete CDF of g equals the number of realizations, for which the objective value g_i is smaller or equal to the value considered, divided by the number of realizations m.

$$F_g(g) = \sum_{i=1}^{g_i \leq g} \frac{1}{m} \tag{5.38}$$

In order to evaluate the influence of the assumed type of distribution of the random vector, two Monte Carlo simulations are executed. For the first simulation the given distributions are considered, and for another one the random parameters are assumed to be normally distributed, but with the correct mean values and variances.

Figure 5-5 shows the resulting CDFs compared to the exact solution. When using the actual distributions of the random parameters, the CDF given by Monte Carlo simulation matches the exact solutions very good, while a significant deviation is detected when assuming normal distribution for the random parameters. This not only shows that the implemented method

works, but also that the accuracy of the Monte Carlo simulation mainly depends on the right choice of distribution of the random parameters.
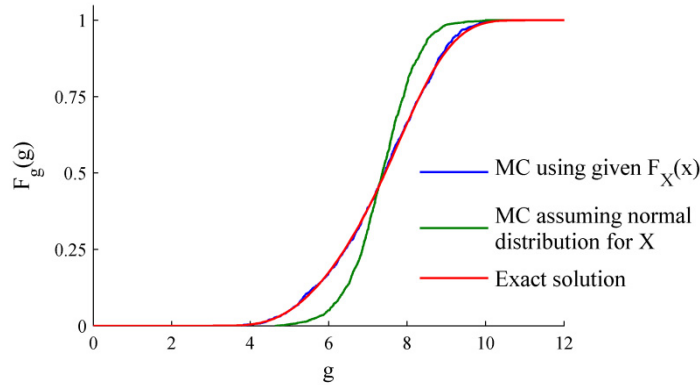

Figure 5-5: CDF of the example objective function, obtained from Monte Carlo simulation

5.3   *Semi-Analytical Analysis of the Linear Example Objective Function*

Using the first order approximations given equations (4.35)-(4.37) to estimate the stochastic moments of the linear objective function g yields

$$\mu_g \approx g(\mathbf{\mu}) = \mu_1 + 2\mu_2 = 2 + 2 \cdot \tfrac{8}{3} = \tfrac{22}{3}$$
$$\sigma_g^2 \approx g_{,1}^2 \, \mu_{1,2} + g_{,2}^2 \, \mu_{2,2} = 1^2 \cdot \tfrac{1}{5} + 2^2 \cdot \tfrac{7}{18} = 1.7\overline{5} \tag{5.39}$$
$$\mu_{g,3} \approx g_{,1}^3 \, \mu_{1,3} + g_{,2}^2 \, \mu_{2,3} = 1^3 \cdot 0 + 2^3 \cdot \left(-\tfrac{2}{27}\right) = -\tfrac{16}{27}$$

Since g is linear, the first order approach matches the exact solution. In order to obtain a distribution function based on the semi-analytic approach, a distribution type has to be chosen. When assuming g to be normally distributed with the obtained mean value and variance, the PDF and CDF plotted in Figure 5-6 are obtained. One could also e.g. choose Gumble distribution for the distribution functions, which is given by

$$f_g(g) = \frac{1}{b} e^{-\frac{g-a}{b}} e^{-e^{-\frac{g-a}{b}}} \quad \text{and} \quad F_g(g) = e^{-e^{-\frac{g-a}{b}}} \tag{5.40}$$
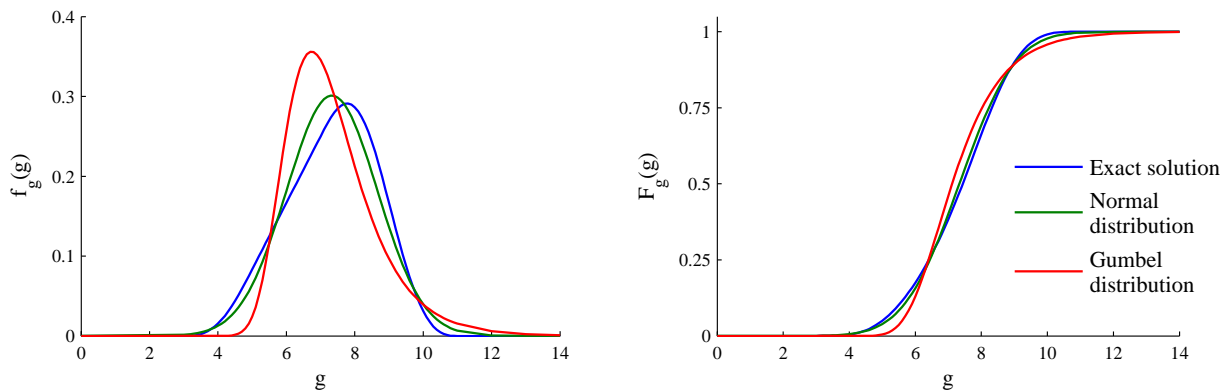
Figure 5-6: Distribution function of *g* given by the semi-analytic approach

The parameters a and b can be determined from mean value and variance according to

$$b = \pi^{-1}\sqrt{6\sigma_g^2} \quad \text{and} \quad a = \mu_g - b \cdot \gamma \tag{5.41}$$

with the Euler–Mascheroni constant $\gamma \approx 0.5772$. The resulting distribution functions are shown in Figure 5-6.

Assuming normal distribution the exact solution is approximated much better than assuming Gumble distribution. This could already be seen when looking at the skewness. The normal distribution has a skewness of zero, which is closer to the actual skewness of -0.255 than the skewness of the Gumble distribution, which always equals 1.14.

5.4   Semi-Analytic Analysis of the Quadratic Example Objective Function

Applying the first order approaches (4.35)-(4.37) to the quadratic objective function h, the approximations of the stochastic moments are given by

$$\mu_{h,FOSM} \approx h(\boldsymbol{\mu}) = \mu_2^2 + \mu_1\,\mu_2 - \tfrac{1}{2}\mu_1^2 + 2 = \left(\tfrac{8}{3}\right)^2 + \tfrac{8}{3}\cdot 2 - \tfrac{1}{2}\cdot 2^2 + 2 = 12,\overline{4} \tag{5.42}$$

$$\sigma_{h,FOSM}^2 \approx h_{,1}^2\,\mu_{1,2} + h_{,2}^2\,\mu_{2,2} = \left(\tfrac{2}{3}\right)^2 \cdot 0.2 + \left(\tfrac{22}{3}\right)^2 \cdot 0.3\overline{8} \approx 21.00 \tag{5.43}$$

$$\mu_{h,3,FOSM} \approx \left(\tfrac{2}{3}\right)^3 \cdot 0 + \left(\tfrac{22}{3}\right)^3 \cdot \left(-\tfrac{2}{27}\right) \approx -29.213 \quad \Rightarrow \quad v_{h,FOSM} = \frac{-29.213}{21.00^{\frac{3}{2}}} \approx -0.304 \tag{5.44}$$

Unsurprisingly, the first order approximations do not equal the exact solutions, where it is noticed that with increasing order of the stochastic moment the deviation from the exact solution increases.

The full second order approaches given in 4.3.3 and Appendix D provide an exact approximation of the stochastic moments of the quadratic objective function h. Following Equation (4.29), the mean value of h is given by

$$\mu_h \approx h_{\boldsymbol{\mu}} + \frac{1}{2}\left(h_{,11}\,\mu_{1,2} + h_{,22}\,\mu_{2,2}\right) = 12.\overline{4} + \frac{1}{2}\left(-1\cdot 0.2 + 2\cdot 0.3\overline{8}\right) = 12.7\overline{3} \tag{5.45}$$

and the second order approach of the variance (4.32) yields

$$\begin{aligned}
\sigma_h^2 \approx\ & 12.\overline{4}^2 + \left[\left(\tfrac{2}{3}\right)^2 \cdot 0.2 + \left(\tfrac{22}{3}\right)^2 \cdot 0.3\overline{8}\right] + 12,\overline{4}\cdot\left[-0.2 + 2\cdot 0.3\overline{8}\right] \\
& + \left[\tfrac{2}{3}\cdot(-1)\cdot 0 + \tfrac{22}{3}\cdot 2\cdot\left(-\tfrac{2}{27}\right)\right] + \tfrac{1}{4}\left[(-1)^2\cdot\tfrac{3}{35} + 2^2\cdot\tfrac{49}{135}\right] \\
& + \frac{1}{2}\cdot(-1)\cdot 2\cdot 0.2\cdot 0.3\overline{8} + 1^2\cdot 0.2\cdot 0.3\overline{8} - 12.7\overline{3}^2 \\
\approx\ & 20.217
\end{aligned} \tag{5.46}$$

The complete second order approach of the third central moment given by Equation (D.52) delivers $\mu_{h,3} = 4.7245$ and hence, the skewness is

$$v_h = \frac{\mu_{h,3}}{\sigma_h^3} = \frac{4.7245}{20.217^{\frac{3}{2}}} \approx 0.0520 \tag{5.47}$$

The first order approximation of the covariance (4.40) of g and h yields

$$\Sigma_{gh} \approx g_{,1}\,h_{,1}\,\mu_{1,2} + g_{,2}\,h_{,2}\,\mu_{2,2} = 1\cdot\tfrac{2}{3}\cdot\tfrac{1}{5} + 2\cdot\tfrac{22}{3}\cdot\tfrac{7}{18} = \tfrac{788}{135} = 5.8\overline{370} \tag{5.48}$$

Since all second derivatives of g equal zero, the second order approach (4.39) simplifies to

$$\Sigma_{gh} \approx g_{\mu}\, h_{\mu} - g_{\mu}\, \mu_{h} - \mu_{g}\, h_{\mu} + \mu_{g}\mu_{h} + \sum_{i=1}^{n} g_{,i}\, h_{,i}\, \mu_{i,2} + \frac{1}{2}\, g_{\mu} \sum_{i=1}^{n} h_{,ii}\, \mu_{i,2}$$
$$- \mu_{g}\, \frac{1}{2} \sum_{i=1}^{n} h_{,ii}\, \mu_{i,2} + \frac{1}{2} \sum_{i=1}^{n} g_{,i}\, h_{,ii}\, \mu_{i,3} \tag{5.49}$$

Again, the second order approach yields the exact solution of $\Sigma_{gh} = 5.6\overline{8}$. Here, the first order approach is close to the exact solutions, because only one of the two objective functions is nonlinear.

In order to evaluate the error that is made by the second-order third-moment (SOTM) method and by the incomplete second order approach (ISOA), the characteristic moments are also determined using these approaches. While the mean value approximation yields the same results as the complete second order approach, the variances given by SOTM and ISOA equal

$$\sigma_{h,SOTM}^{2} \approx \sum_{i=1}^{n} h_{,i}^{2}\, \mu_{i,2} + h_{\mu}^{2} - \mu_{h}^{2} + h_{\mu} \sum_{i=1}^{n} h_{,ii}\, \mu_{i,2} + \sum_{i=1}^{n} h_{,i}\, h_{,ii}\, \mu_{i,3} \approx 19.833 \tag{5.49}$$

and

$$\sigma_{h,ISOA}^{2} = \sigma_{h}^{2} - \sum_{i=1}^{n} \sum_{j=i+1}^{n} h_{,ij}^{2}\, \mu_{i,2}\, \mu_{j,2} \approx 20.139 \tag{5.49}$$

and the approximations of the skewness yield

$$v_{h,SOTM} \approx -0.526 \qquad \text{and} \qquad v_{h,ISOA} \approx 0.030 \tag{5.49}$$

The covariance of g and h is approximated exactly by both approaches due to the linearity of g.

5.5   Overview of Example and Results

For the sake of comprehensibility, an overview of the example considered is given in this section. All information that is required as input for the probabilistic analyses are listed in Tables in section 5.5.1. The results obtained from solving the example analytically are summarized in section 5.5.2.

Random variable	Probability density function (PDF)	Cumulative distribution function (CDF)	
X_1	$f_1(x_1) = \begin{cases} 0 \\ -\frac{3}{4}(x_1-2)^2 + \frac{3}{4} \\ 0 \end{cases}$	$F_1(x_1) = \begin{cases} 0 \\ -\frac{1}{4}x_1^3 + \frac{3}{2}x_1^2 - \frac{9}{4}x_1 + 1 \\ 1 \end{cases}$	for $x_1 \le 1$ for $1 \le x_1 \le 3$ for $3 \le x_1$
X_2	$f_2(x_2) = \begin{cases} 0 \\ \frac{1}{3}(x_2-1) \\ -\frac{2}{3}(x_2-4) \\ 0 \end{cases}$	$F_2(x_2) = \begin{cases} 0 \\ \frac{1}{6}x_2^2 - \frac{1}{3}x_2 + \frac{1}{6} \\ -\frac{1}{3}x_2^2 + \frac{8}{3}x_2 - 4\frac{1}{3} \\ 1 \end{cases}$	for $x_2 \le 1$ for $1 \le x_2 \le 3$ for $3 \le x_2 \le 4$ for $4 \le x_2$

Table 5-2: PDFs and CDFs of the random variables considered in the current example

5.5.1   Input Information of the Example Considered

The PDFs and CDFs of the two random parameters X_1 and X_2 considered in this chapter are summarized in Table 5-2. The mean value and the central stochastic moments of both distributions are given in Table 5-3. The two objective functions considered are given in Table 5-4.

	μ_i	$\mu_{i,2}$	$\mu_{i,3}$	$\mu_{i,4}$	$\mu_{i,5}$	$\mu_{i,6}$
X_1	2	1/5	0	3/35	0	1/21
X_2	8/3	7/18	-2/27	49/135	-40/243	9661/20412

Table 5-3: Stochastic moments of the example distributions

Linear objective function	Quadratic objective function
$g(\mathbf{x}) = x_1 + 2x_2$	$h(\mathbf{x}) = x_2^2 + x_1 x_2 - \frac{1}{2}x_1^2 + 2$

Table 5-4: Objective functions considered in the current example

5.5.2   Results of the Probabilistic Analysis of the Objective Functions Considered

By solving the integral (4.24) analytically for the linear objective function (5.17), the PDF and the CDF of the objective function have been determined, which are given in Table 5-5.

$$f_g(g) = \begin{cases} 0 \quad \text{for } g \leq 3 \text{ and } 11 \leq g \\ -\frac{1}{192}g^4 + \frac{1}{12}g^3 - \frac{15}{32}g^2 + \frac{9}{8}g - \frac{63}{64} \quad \text{for } 3 \leq g \leq 5 \\ \frac{1}{12}g - \frac{1}{3} \quad \text{for } 5 \leq g \leq 7 \\ \frac{1}{64}g^4 - \frac{1}{2}g^3 + \frac{189}{32}g^2 - \frac{733}{24}g + \frac{11255}{192} \quad \text{for } 7 \leq g \leq 9 \\ -\frac{1}{96}g^4 + \frac{5}{12}g^3 - \frac{99}{16}g^2 + \frac{121}{3}g - \frac{9317}{96} \quad \text{for } 9 \leq g \leq 11 \end{cases}$$

$$F_g(g) = \begin{cases} 0 \quad \text{for } g \leq 3 \\ -\frac{1}{960}g^5 + \frac{1}{48}g^4 - \frac{5}{32}g^3 + \frac{9}{16}g^2 - \frac{63}{64}g + \frac{27}{40} \quad \text{for } 3 \leq g \leq 5 \\ \frac{1}{24}g^2 - \frac{1}{3}g + \frac{27}{40} \quad \text{for } 5 \leq g \leq 7 \\ \frac{1}{320}g^5 - \frac{1}{8}g^4 + \frac{63}{32}g^3 - \frac{733}{48}g^2 + \frac{11255}{192}g - \frac{7149}{80} \quad \text{for } 7 \leq g \leq 9 \\ -\frac{1}{480}g^5 + \frac{5}{48}g^4 - \frac{33}{16}g^3 + \frac{121}{6}g^2 - \frac{9317}{96}g + \frac{14721}{80} \quad \text{for } 9 \leq g \leq 11 \\ 1 \quad \text{for } 11 \leq g \end{cases}$$

Table 5-5: PDF and CDF of the linear objective function considered in the current example

The shape of the distribution function has been approximated very well by a Monte Carlo simulation using the given distribution functions for X_1 and X_2. When assuming X_1 and X_2 to be normally distributed, the resulting distribution function deviates significantly from the exact solution (see Figure 5-5). This shows how sensitive the Monte Carlo method is to the choice of the distribution functions of input parameters.

Using the semi-analytic, probabilistic approach requires assuming a type of distribution to obtain a distribution function of the objective function. When assuming Normal distribution, the approximate distribution function matches the exact solution well, where assuming Gumbel distribution leads to a worse approximation (see Figure 5-6). However, even when assuming Gumbel distribution the distribution function is approximated better than by the Monte Carlo simulation under the assumption of normally distributed input parameters. This leads to the conclusion that (at least for the example considered) the results of the semi-analytic approach are less sensitive to the choice of the type of distribution $f_g(g)$ of the objective function than the results of the Monte Carlo method are sensitive to the choice of the type of distribution $f_\mathbf{X}(\mathbf{x})$ of the input variables.

Objective function	Mean value	Variance	Skewness	Covariance
$g(\mathbf{x})$	$\mu_g = 7.\overline{3}$	$\sigma_g^2 = 1.7\overline{5}$	$v_g \approx -0.25476$	
				$\Sigma_{gh} = 5.6\overline{8}$
$h(\mathbf{x})$	$\mu_h = 12.7\overline{3}$	$\sigma_h^2 = 20.217$	$v_h = 0.052$	
FOSM approach for $h(\mathbf{x})$	$\mu_h \approx 12,\overline{4}$	$\sigma_h^2 \approx 21.00$	$v_h \approx -0.304$	$\Sigma_{gh} \approx 5.837$
SOTM approach for $h(\mathbf{x})$	$\mu_h = 12.7\overline{3}$	$\sigma_h^2 \approx 19.833$	$v_h \approx -0.526$	$\Sigma_{gh} = 5.6\overline{8}$
ISOA for $h(\mathbf{x})$	$\mu_h = 12.7\overline{3}$	$\sigma_h^2 \approx 20.139$	$v_h \approx 0.030$	$\Sigma_{gh} = 5.6\overline{8}$

Table 5-6: Stochastic moments of the objective functions considered in the current example

The stochastic moments of the two objective functions considered have been determined directly and are summarized in Table 5-6. Using the full second order semi-analytic approach, the stochastic moments are determined exactly. When using the FOSM approach for the quadratic objective function $h(\mathbf{x})$, still reasonably good approximation of the mean value and the variance of h are obtained (last row of Table 5-6). The deviation of the skewness however is unacceptably large. Unsurprisingly, better approximations are given by the SOTM approach and the ISOA. While both approaches estimate the variance well, the skewness is estimated much better by the ISOA. This leads to the conclusion that the first order approach can be sufficiently accurate for estimating mean value and variance even for a nonlinear objective function and it is therefore expected that the use of a second order approach yields reasonably accurate results even is the objective function is of higher order. This conclusion however cannot be regarded as generally valid, since the accuracy of a lower order approach always depends on the regarded objective function.

6   Probabilistic Design of Composite Cylindrical Shells

In this chapter, the probabilistic design procedure proposed in section 4.6.1 is applied to a set of cylindrical composite shells.

6.1   Properties of the Shells Considered

The shells considered have been manufactured, measured and tested at the German Aerospace Centre in Braunschweig (see Ref. [27] and [42]). All cylindrical shells considered have a nominal radius of 250mm and a laminate consisting of four plies with the nominal ply thickness of 0.125mm. The ratio of radius to wall thickness is hence $R/t = 500$ for all cylindrical shells considered.

	Identifier	Laminate setup
Set #1	Z07, Z08	[±24°, ±41°]
	Z09	[±41°, ±24°]
	Z10, Z11	[24°, ±41°, -24°]
	Z12	[±45°, 0, -79°]
Set #2	Z15, Z17, Z18, Z20-Z26	[±24°, ±41°]

Table 6-1: Laminate setups of the cylinders considered

The shells considered are subdivided into two sets (see Table 6-1). The shells of set #1 have been investigated by Hühne et al. [27]. These shells with the identifiers Z07–Z12 have a free length of 510mm and four different laminate setups. The ten shells of set #2, which have been analyzed by Degenhardt et al. [42], all have the same laminate setup as Z07. Their free length is 500mm and the shells are denominate Z15, Z17, Z18 and Z20-Z26.

	Set #1, Z07-Z12, from [27]	Set #2, Z15-Z26, from [42]
E_{11}	125774MPa	157362MPa
E_{22}	10030MPa	10095MPa
G_{12}	5555MPa	5321MPa
v_{12}	0.271	0.277

Table 6-2: Elastic material properties of the panels considered

As listed in Table 6-2, Hühne et al. and Degenhardt et al. gave different elastic material parameters. For the following probabilistic analyses imperfections measurements of set #2 will be used and hence, the material properties given for this set are used in the following.

6.2   Numerical Model

As a result of a mesh convergence study, a finite element model with 240 nodes in circumferential direction and 61 nodes in axial direction has been chosen, which leads to $240 \cdot 61 \cdot 6 = 87840$ degrees of freedom. For the $240 \cdot 60 = 14400$ elements, linear shell elements with four nodes and reduced integration (S4R elements in ABAQUS) have been used.
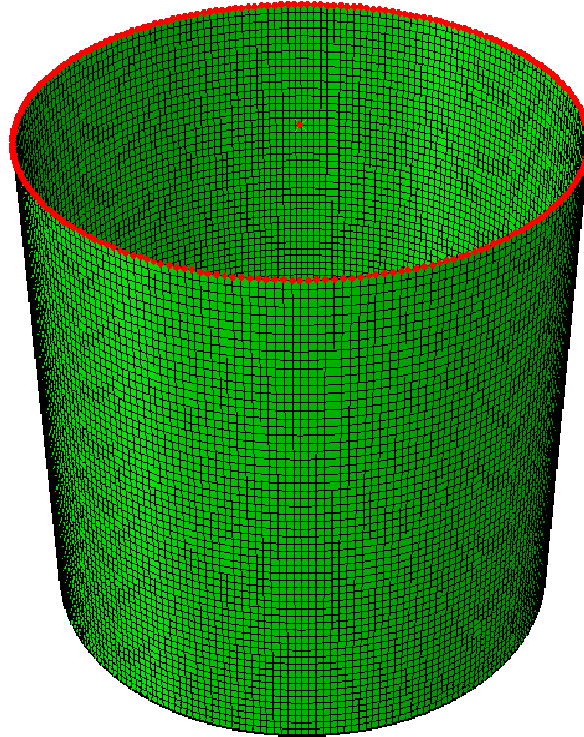
Figure 6-1: Numerical model of cylindrical shell

For the experimental tests the ends of the shells have been potted in epoxy resign in order to realize clamping. Hence, also in the numerical simulations clamped edges are modeled. In order to be able to run load controlled simulations, the clamping has been realized by defining the cylinder edge as a rigid body with a reference node at the center, as it is shown for the upper edge in Figure 6-1. Hence, the boundary conditions at the bottom and the displacement or loading on the top is applied to the reference node. This technique furthermore allows the application of a rotation at one edge, as it is used in section 6.3.4.

In the experiments, no plastic deformation have been detected and repeating buckling tests for one shell always delivered the same buckling load, which indicates that the material behaved fully elastically. Hence, a linear elastic material model is used within the numeric simulations.

For determining buckling loads within probabilistic analyses, load driven, geometrically nonlinear simulations are performed, as described in section 3.2.2, using the finite elemente code ABAQUS.

6.3   Imperfection Measurements

All kinds of deviations from the nominal dimensions are regarded as imperfections. Beside the geometrical imperfections of the shell surface, this includes imperfect boundary conditions or load applications, deviations of the wall thickness or the scattering of material

parameters. Additionally, inaccuracies of the fiber angle, fiber waviness and void inclusions can occur in fiber composite shells.

For both sets of shells, geometric imperfections have been measured. For set #2 furthermore the wall thickness deviations and the standard deviations of the material properties E_{11}, E_{22} and G_{12} are available. Considering further imperfections in the probabilistic analysis would require unfunded assumptions. Only a loading imperfection is considered additionally, since the data could be estimated indirectly (see section 6.3.4).

6.3.1   Geometric Imperfections

The geometric imperfections have been measured with an optically measurement system ATOS [115]. Using the software tool VISTIM (see [47]) the position of the ideal cylinder has been determined with respect to the point cloud given by measurement. This allows determining the deviations from the ideal structure at each position of the cylinder. The 3D-model of shell Z07 with scaled imperfection is shown in Figure 6-2 (left). The unwounded shell surface with the radial geometric imperfections as a two-dimensional function is given in Figure 6-2 (right).
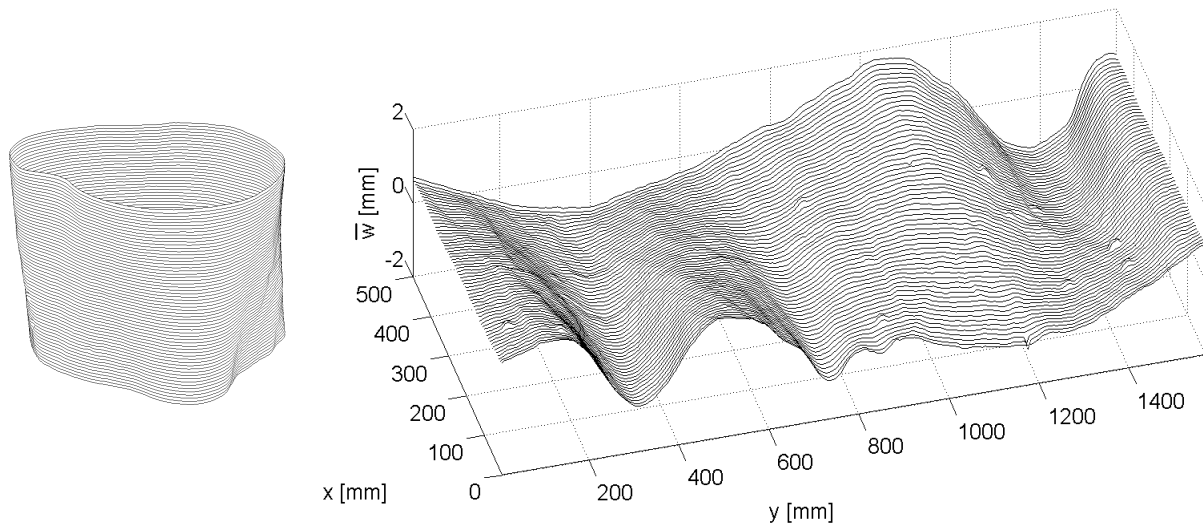
Figure 6-2: 3D-model (left) and unwounded measured imperfection pattern (right) of shell Z07 with scaling factor

As discussed in section 4.1.1 the imperfection pattern is approximated by a double Fourier series. For the shells considered, the measured patterns are approximated sufficiently accurate for $n_1 = 10$ and $n_2 = 20$ and hence, $11 \cdot 21 \cdot 2 = 462$ coefficients are taken into account.

Using the half wave cosine approach (4.2) leads to the approximated imperfection pattern shown in Figure 6-4 shows the recalculated imperfection pattern using the half wave sine approach (4.3). Due to the large imperfections at the edges, the half wave cosine approach describes the measured surface much more accurate than the half wave sine approach (see Figure 6-3). Plotting the Fourier coefficients for different numbers of axial half waves over the number of circumferential full waves, as done in Figure 6-5, gives insight into the manufacturing characteristics of the shells. The imperfection patterns of set #1 are dominated by modes with small numbers of axial and circumferential full waves. The ovalization mode with two circumferential full wave and no axial waves is one of the modes with the biggest amplitude for all shells of set #1. The imperfections of set #2 show significantly smaller

imperfections and hence, modes with shorter wave lengths become more visible in the imperfection pattern and the Fourier spectra.
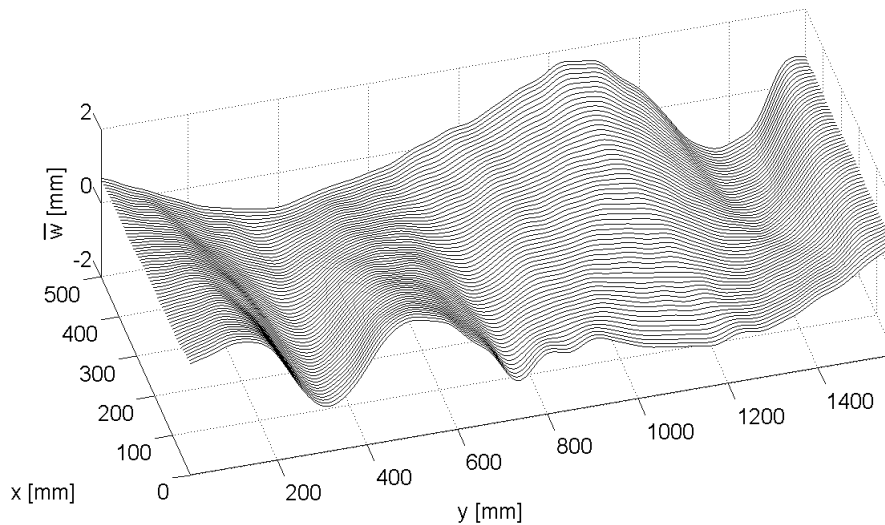
Figure 6-3: Recalculated imperfection shape of Z07 using the half-wave cosine Fourier representation
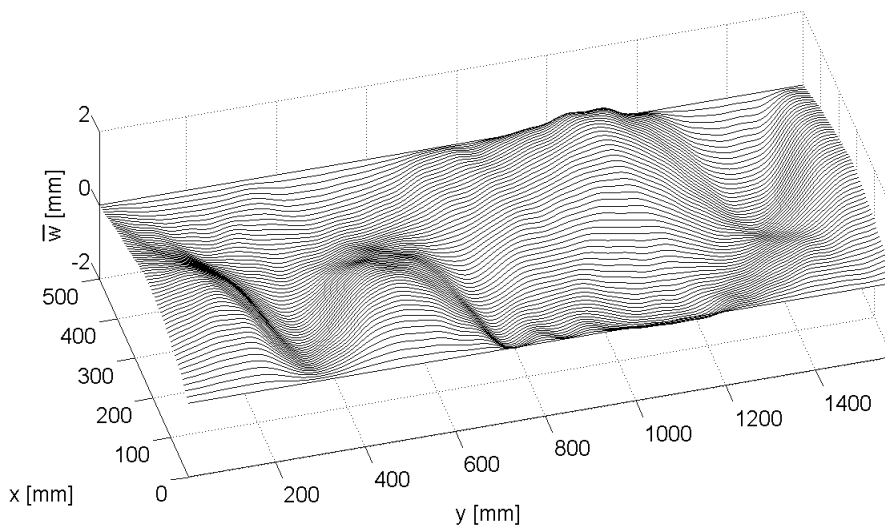
Figure 6-4: Recalculated imperfection shape of Z07 using the half-wave sine Fourier representation

6.3.2   Scattering of Material Parameter

The mean values and standard deviations of the material parameters E_{11}, E_{22} and G_{12} have been determined experimentally from a set of Coupon tests. Due to the test procedure it was not possible to detect correlations between the parameters and hence, material properties are assumed to be uncorrelated even though it seems reasonable that e.g. the shear modulus G_{12} increases at the same time as the Young's modulus E_{22} increases. However, it is shown in section 6.5 that the scattering of material properties has minor influence on the scatter of buckling load. In [42] the mean values and standard deviation of E_{11}, E_{22} and G_{12} are given and the parameters are assumed to be normally distributed.

$$\bar{\xi}_{kl} = \sqrt{A_{kl}^2 + B_{kl}^2}$$
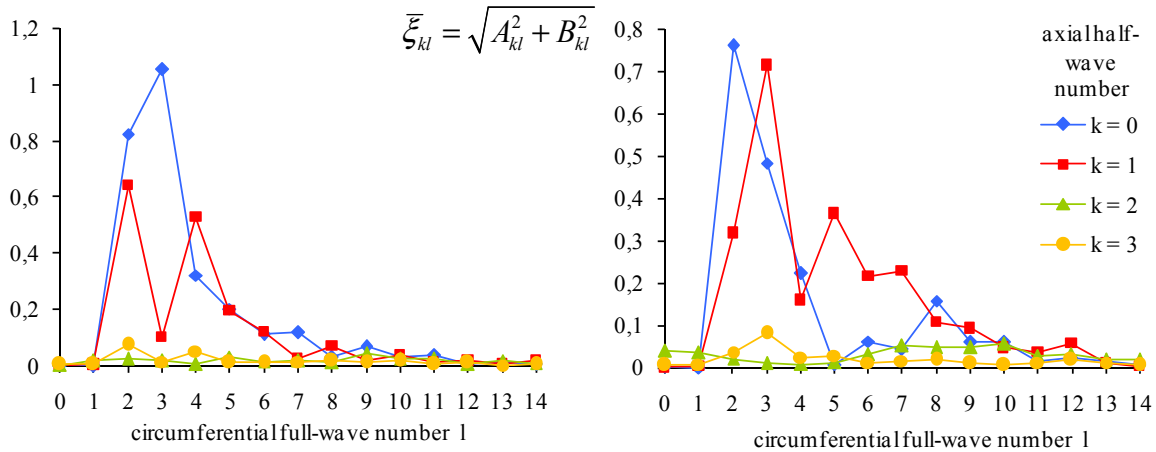
Figure 6-5: Fourier coefficients for the shells Z07 (left) and Z08 (right)

	E_{11}	E_{22}	G_{12}
Mean value in MPa	157362	10095	5321
Standard deviation in MPa	3763	415	59
Coefficient of variation in %	2.4	4.1	1.1

Table 6-3: Stochastic moments of material properties, from [42]

6.3.3   Wall Thickness Deviations

The wall thickness has been measured with ultrasonic measurements [42] and varies for different shells, as well as within the surface of one shell. Orf [106] compared finite element buckling analyses of shells with measured wall thickness patterns and shells with a constant thickness and concluded that there is no significant difference, if the average wall thickness is equal. Thus, a constant wall thickness is regarded as random parameter for which the average wall thickness is the data base. If the distribution of the wall thickness over the shell surface has to be considered, this two dimensional function can be represented by Fourier series as well.

The stochastic moments of the average wall thickness are obtained from the ten measurements of set #2. The mean value equals $\mu_t = 0.479$mm and the standard deviation is $\sigma_t = 0.012$mm.

6.3.4   Loading Imperfection

A small inclination was applied unintentionally to the shells during tests. It was caused by the test setup, but has not been measured. Because of the significant influence of the resulting bending moment on the buckling load, the inclination should be considered and is determined indirectly. As demonstrated in Figure 6-6, in finite elemente simulations the shell is bended with the bending angle θ about an axis, which is described by the circumferential variation angle ω. Within these simulations the measured geometric imperfection pattern, the measured average wall thickness and the mean values of the material properties are applied.

Figure 6-7 shows the numerically determined buckling load of one test shell with respect to the inclination. For the imperfect shell the position of the bending axis has an influence on the buckling load; however the position during test is unknown. In order to approach the applied

bending angle, the mean buckling load for fixed θ and varying ω is fitted to the experimental result. (E.g. for the example in Figure 6-7, a good approximation is given for $\theta = 0.009°$.) This procedure is applied to the ten shells of set #2 and ten bending angles are obtained with mean value $\mu_\theta = 0.01157°$ and standard deviation of $\sigma_\theta = 2.74° \cdot 10^{-3}$.
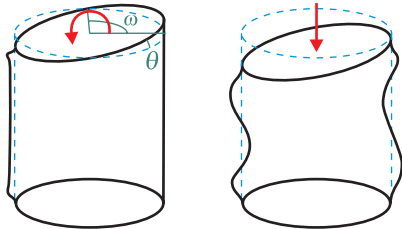
Figure 6-6: Illustration of the FE-simulation for the determination of bending angles
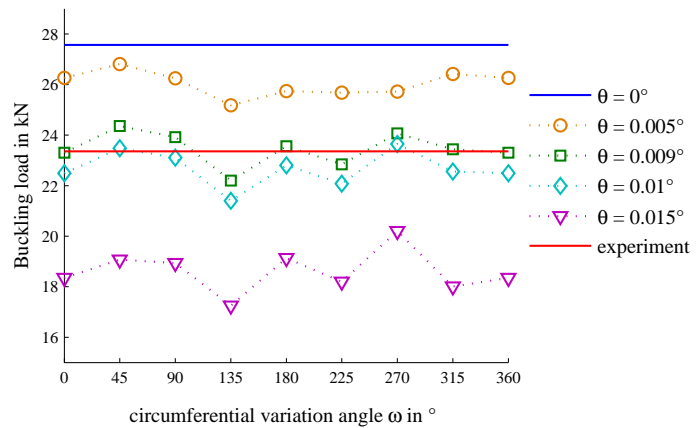
Figure 6-7: Buckling loads for different inclinations of the imperfect shell Z15

Because the value of ω is unknown during the tests, the estimation of θ includes measurable uncertainties. For the example given in Figure 6-7 the estimated bending angle θ equals 0.009°. If the circumferential variation angle ω had a value of 45° during the test, θ must equal 0.01°. If ω was equal 135°, a bending angle of 0.008° would fit the test result. This shows that the estimation of θ has an accuracy of about 0.001°, which equals approximately 10% of the obtained mean value, and which is larger than the estimated standard deviation.

This shows the uncertainty that is included when determining mean value and standard deviation of the inclination angle. Both, mean value and standard deviation are probably overestimated or underestimated. It would be a conservative approach to solve this issue by increasing the standard deviation. However, this comprises the risk to end up with an overly conservative result. Since the objective of the probabilistic design procedure is to estimate the stochastic distribution as accurate as possible without introducing conservative assumptions, the indirectly determined inclination angles serve as measurement data as they are.

6.4   *Influence of Representation of the Geometric Imperfection*

Different representations of geometric imperfections are proposed in the literature, which often introduce simplifications in order to reduce the number of random parameters (see section 4.1). The influence of the representation of geometric imperfections on the result of probabilistic analyses is discussed in this section. For this, a Monte Carlo simulation with a relatively small number of realizations is performed, regarding only geometric imperfections as randomly distributed. The imperfection measurements of set #1 are used as data basis.

According to the multimode approach proposed by Arbocz and Starnes [104], the multi mode representation (6.1) is used to investigate the performance of such a simplified representation of geometric imperfections within probabilistic analyses. It mainly differs from the original Fourier representation by neglecting the circumferential phase shift of each mode. This simplified approach is considered besides the Fourier representation in the following in order to show its influence on the results of a probabilistic analysis.

$$\overline{W}(x,y) = t\sum_{k=0}^{n_1} A_{k0}\cos\frac{2\pi x}{L} + t\sum_{k=1}^{n_1}\sum_{l=0}^{n_2}\sqrt{C_{kl}^2 + D_{kl}^2}\sin\frac{k\pi x}{L}\cos\frac{l y}{R} \qquad (6.1)$$

Figure 6-8 shows two virtually generated imperfection patterns based on the multimode approach. It is conspicuous that the imperfections accumulate in one point near the edge. This phenomenon is caused by neglecting the circumferential phase shift of each mode.
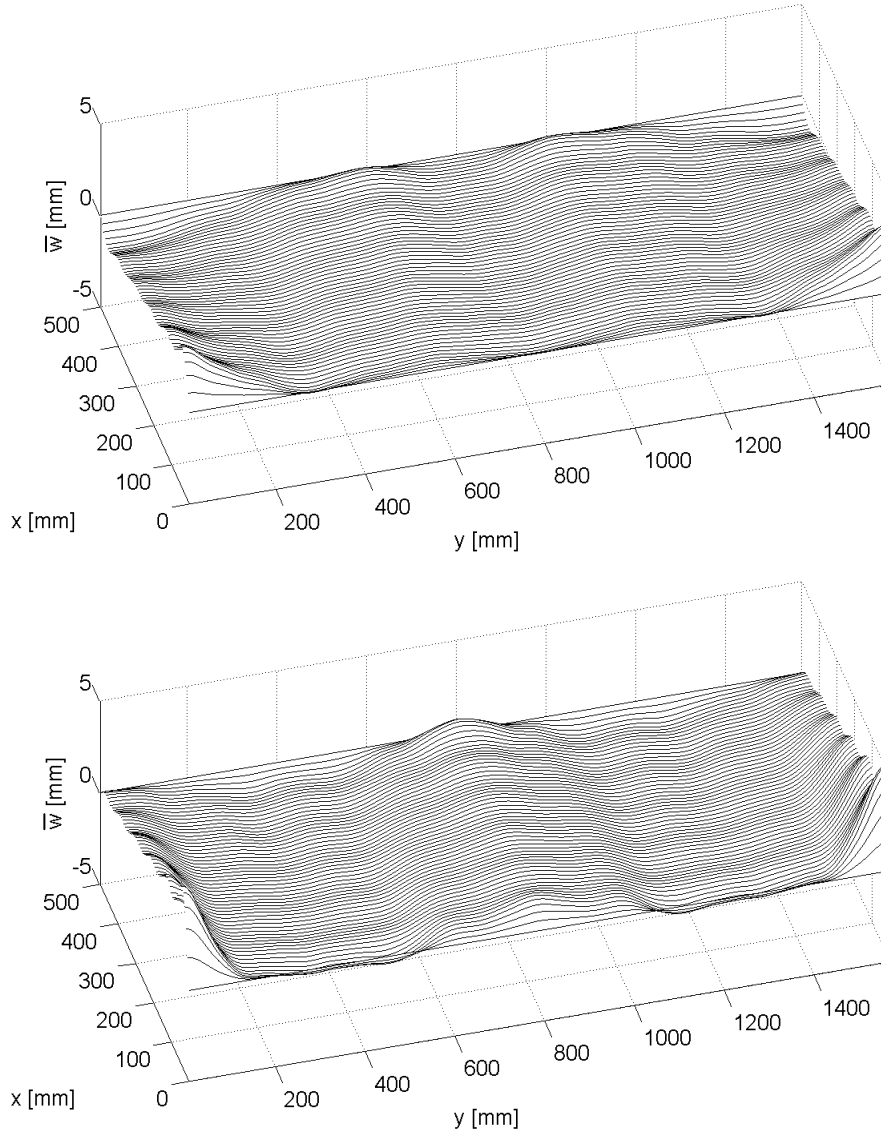
Figure 6-8: Examples of generated imperfection shapes using the multi-mode approach with random amplitudes

Monte Carlo simulations are performed for the buckling load of Z07 using 400 virtual samples. The Fourier coefficients are regarded as random parameters. Besides the multimode approach (6.1), also the half wave cosine approach (4.2) and the phase shift representation (4.5) are used. For the phase shift representation the phase shift angle of the ovalization mode is set to zero and only the relative phase shift of other modes is regarded. This way, the position of the shell during measurement is eliminated as discussed in section 4.1.1.

The histograms in Figure 6-9 obtained from the Monte Carlo simulations show that by using the multi mode approach the buckling loads are underestimated significantly. From the

cumulative distribution functions given in Figure 6-10 it is seen that the obtained standard deviations compare well, but the mean values differ strikingly. Furthermore, it is noticeable that the cumulative distribution obtained using the phase shift representation is much smoother than the one determined with the standard Fourier approach. Obviously, the technique described in section 4.1.1 eliminating positioning of the shell during measurement indeed yields better results than neglecting this effect.
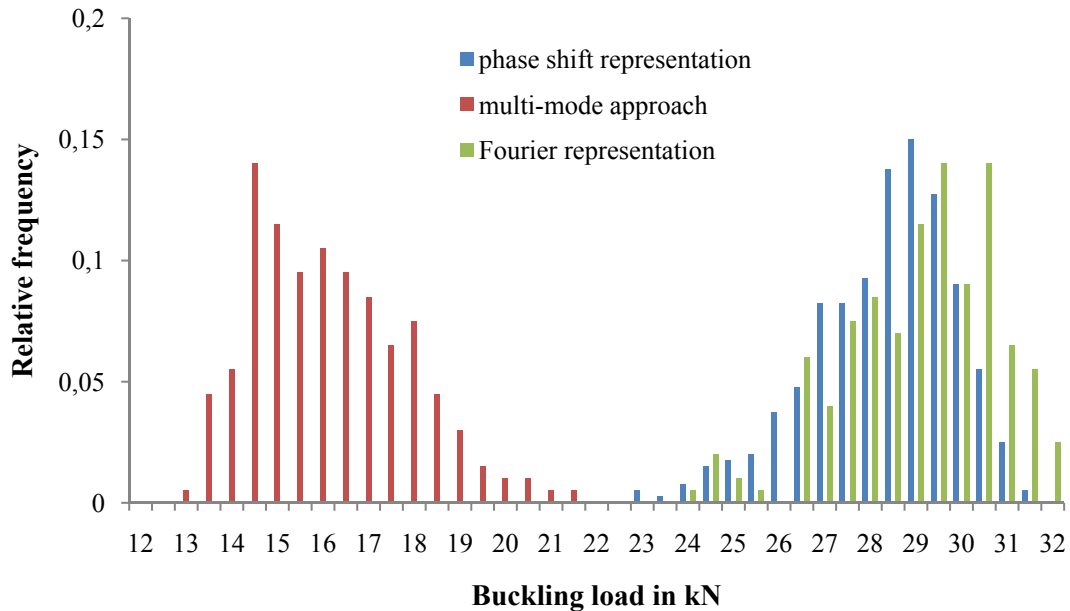
Figure 6-9: Histograms of Monte Carlo simulations with different representations of imperfection patterns for Z07
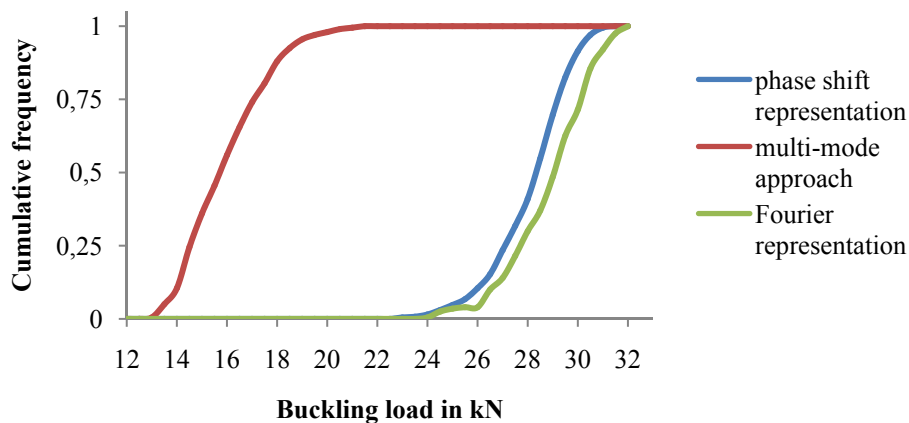
Figure 6-10: Cumulative frequency of Monte Carlo simulations with different representations of imperfection patterns for Z07

The results of Monte Carlo simulations with the laminate setup of Z10 are similar to the results for Z07 (see Appendix G). However, Monte Carlo simulations with the laminate setup of Z09 show a considerable difference not only for the mean value, but also for the standard deviation given by the multimode approach compared to the two other approaches (see Figure 6-11). While the mean value is underestimated, the standard deviation is overestimated heavily. Again, the cumulative distribution function given by the phase shift representation is

smoother than the one obtained with the standard Fourier approach. Monte Carlo simulations with the laminate setup of Z12 deliver similar results as Z09.
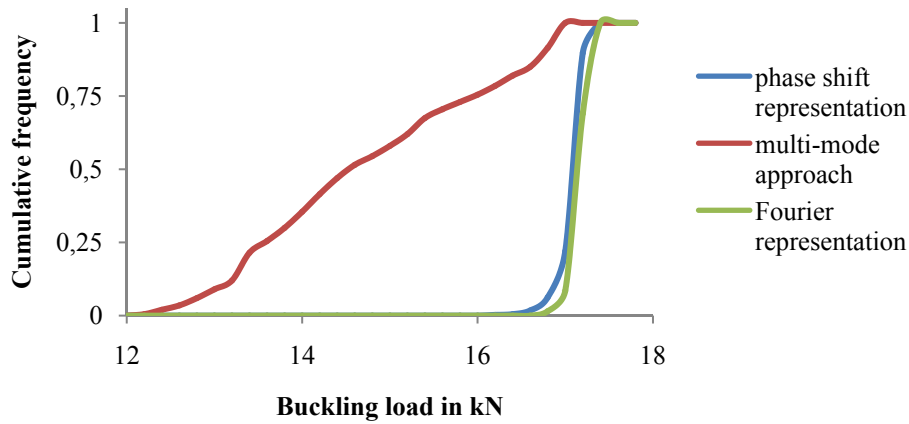
Figure 6-11: Cumulative frequency of Monte Carlo simulations with different representations of imperfection patterns for Z09

An underestimation of the mean value and an overestimation of the standard deviation will always lead to a more conservative approach of the lower bound of buckling load, compared to the accurate representations of imperfection patterns. Hence, it is concluded that the multi mode representation is usable for a conservative approach, but, due to the negligence of the phase shift, it is not appropriate for estimating the distribution of buckling load as accurate as possible.

6.5   Semi-Analytic, Probabilistic Analysis

The semi-analytic, probabilistic approach given in section 4.6.1 is applied to the shells of set #2. For that, the stochastic moments of the buckling load are determined using the approximations given in section 4.3.3.

	μ_Λ in kN	σ_Λ in kN	v_Λ
First order approach, using (4.49)	24.36	2.25	0.012
Second order third moment (SOTM) approach	23.10	2.20	0.469
Incomplete second order approach (ISOA)	23.10	2.53	0.118
Full second order approach (SOSM), using (4.53)-(4.55)	23.10	3.53	0.239
Monte Carlo simulation (see section 6.7)	24.06	2.75	0.228
Empiric distribution	23.58	1.31	-0.019

Table 6-4: Results of the semi-analytic approaches for set #2

The results given in Table 6-4 show that all approaches overestimate the standard deviation and skewness. Even the Monte Carlo simulation overestimates the standard deviation, which will be discussed in the section 6.7. However, the full second order approach, or second-order sixth-moment (SOSM) approach, overestimates the standard deviation significantly more than the all other approaches. The reason is the term that is neglected by the ISOA, the last sum in (4.32), which is taken into account within the full approach. Each of the $\frac{1}{2}\left(n^2 - n\right)$ summands of this term is always positive and hence, approximation errors in the mixed partial derivatives sum up and can have a significant influence compared to other terms, which turned out to be the case in the present study.

In order to obtain a probability function a type of distribution has to be assumed. This choice influences the shape of the probability density function of buckling load. In Figure 6-12 several probability density functions are plotted, which all have the mean value and standard deviation obtained from the incomplete second order approach. The skewness can help to choose an appropriate type of distribution. E.g. the Gumbel distribution always has a skewness of 1.14, but the estimated skewness is close to zero. Unfortunately, the normal, logistic and Laplace distribution all have a skewness of zero. Comparing the resulting cumulative distribution function with the experimentally obtained cumulative distribution does not allow definitely deciding which type of distribution matches best. The normal distribution is the most commonly used distribution. Its prevalence can be partially explained by the central limit theorem (see e.g. [105]). Therefore, normal distribution will be used subsequently, though a K-S test of the empiric distribution with the assumed distributions delivers a slightly better match for Logistic and Laplace distribution.
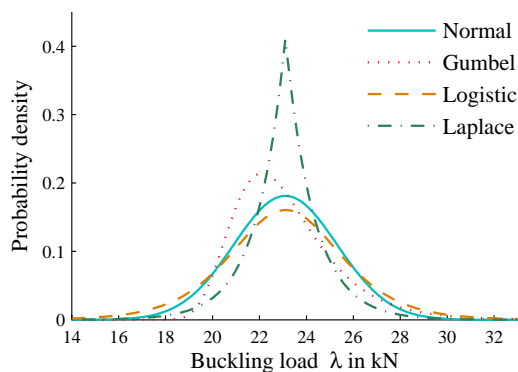
Figure 6-12: Probability density function of buckling load for set #2 assuming different types of distribution
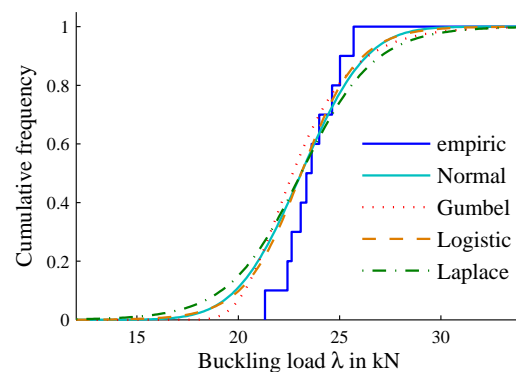
Figure 6-13: Cumulative distribution function of buckling load for set #2assuming different types of distribution

The incomplete second order approach matches the empiric distribution better than the first order approach, as it is seen when comparing the cumulative distribution functions (see Figure 6-14). The reliability function given by $R(\lambda) = 1 - F_\Lambda(\lambda)$ is plotted in Figure 6-15 for the ISOA. Due to the small derivative of the reliability function in the region of high reliabilities, the design load is very sensitive to the chosen level of reliability. However, though the difference of levels of reliability of say 99.9% and 99.99% appears to be very small at first glance, it is equivalent to a change from one failure out of 1000 to one failure out of 10,000. Therefore, a reduction of the design load of about 10% is reasonable when increasing the level of reliability from 99.9% to 99.99%.

As stated before, the design load not only depends on the level of reliability, but also on the chosen type of distribution. From the design loads listed in Table 6-5 it is concluded that the

distribution type can significantly influence the lower bound of buckling load, especially for high levels of reliability.
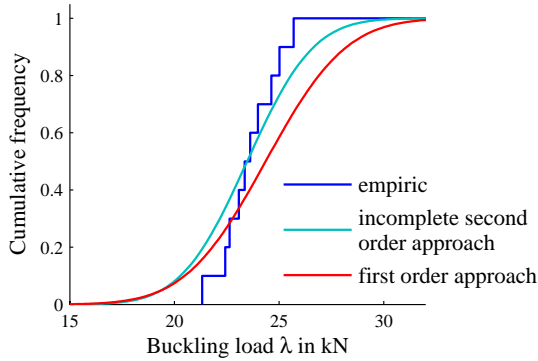
Figure 6-14: Cumulative distribution function of buckling load of set #2 assuming normal distribution
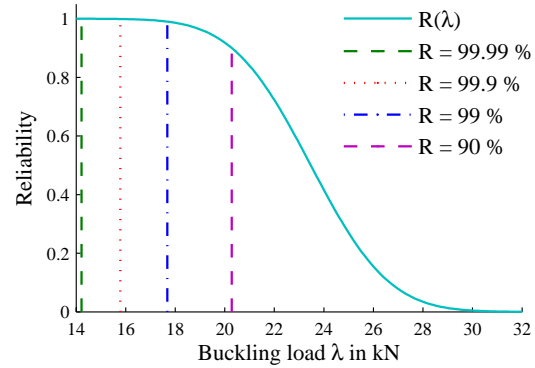
Figure 6-15: Reliability function of buckling load and lower bounds of set #2 given by ISOA assuming normal distribution

Reliability	Assumed distribution		
	Normal	Logistic	Laplace
99.99 %	13.7kN	10.2kN	7.8kN
99.9 %	15.3kN	13.5kN	12.0kN
99 %	17.2kN	16.7kN	16.1kN
90 %	19.9kN	20.0kN	20.2kN

Table 6-5: Probabilistic based design loads for set #2 for different types of distribution

Following the design approach summarized in section 4.6.1, the design load is given by

$$\lambda_d = \mu_\Lambda - b\,\sigma_\Lambda \tag{6.2}$$

In this formulation, the chosen level of reliability as well as the assumed type of distribution are captured by the factor b. Typical values for b and their relation to types of distribution and levels of reliability are listed in Table 4-2.

Assuming normal distribution and choosing a level of reliability of 99.9% equals a factor $b = 3$ and leads to a design load of 15.3kN. If the assumption of normal distribution is wrong and the actual distribution is Laplace or logistic distribution, the real reliability of this design load is between 99% and 99.9% (see Table 6-5). This shows that a wrong assumption for the type of distribution does not lead to an inapplicable lower bound, but only to a different level of reliability than intended. Within the Six Sigma design philosophy [116], this issue is even neglected by expressing the level of reliability always by the factor b (e.g. $b = 4$ provides a higher reliability than $b = 3$). Still, one should always keep in mind that the choice of b implies not only the desired level of reliability, but also an assumed type of distribution.

Without performing additional buckling analyses, the results of the semi-analytic approach can be used to determine the influence of each random parameter or of a group of random parameters on the distribution of buckling load. When treating all parameters as deterministic parameters and only regarding for instance geometric imperfections as randomly distributed,

the resulting standard deviation can be determined. Hence, a very descriptive measure of how the scatter of buckling load is influenced by a certain type of imperfection is given.

Random parameters	First order approach		Incomplete second order approach	
	μ_Λ	σ_Λ	μ_Λ	σ_Λ
Geometry	24.36kN	1.11kN	24.01kN	1.17kN
Material parameters	24.36kN	0.40kN	24.34kN	0.41kN
Wall thickness	24.36kN	1.45kN	24.34kN	1.45kN
Loading imperfection	24.36kN	1.61kN	23.48kN	1.67kN
All	24.36kN	2.25kN	23.10kN	2.53kN

Table 6-6: Semi-analytic approaches considering the random variables individually

In Table 6-6 the mean values and standard deviations of buckling load when regarding only a set of parameters as randomly distributed are given. The results show that the material properties have a minor influence on the scatter of buckling load. The influences of geometric imperfections, wall thickness and loading imperfection have the same order of magnitude.

6.6   *Influence of the Sample Size*

The method for provision of the sample size given in section 4.7 is applied to the shells considered in order to check whether the relatively small sample size of ten has an influence on the accuracy of the semi-analytic method. Furthermore, set #2 is subdivided into two sets of five shells and the probabilistic analysis is repeated using only five samples with and without using the conservative estimators given in Table 4-3. As suggested in section 4.7.2, the factor c is set equal to 2. The results of the FOSM analysis for the complete set and the subset, with and without using the conservative estimators are summarized in Table 6-7. The FOSM approach is used because within this approach it is obvious whether increasing or decreasing an estimator is conservative (see section 4.7.2). For the numerical determination of derivatives the approximation (4.50) is used, instead of (4.49). Therefore, the results differ slightly from the results given in Table 6-4.

The results of the standard approach considering the subset of five samples compare very well with the results considering all samples. Using the conservative estimators for the set of ten samples leads to a slightly more conservative design load λ_d than the standard approach. When considering only five samples, the conservative approach yields higher mean value of buckling load than the standard approach, which should not be the case. Obviously, the partial derivatives are misleading and therefore lead to a modified mean vector for which the buckling load is higher compared to the buckling load of the original mean vector. This effect can occur, if the original mean vector is close to a local minimum (see Figure 6-16) or if the step size of the numerical derivative is too large. However, the conservative approach with five samples still yields a significantly more conservative design load than the standard approach (see last row of Table 6-7).

Shells considered		Complete set #2	Z15, Z17, Z18, Z20, Z21	Z22, Z23, Z24, Z25, Z26
Standard FOSM approach	μ_Λ in kN	24.36	24.26	24.08
	σ_Λ in kN	2.455	2.459	2.339
	$\lambda_d{}^*$ in kN	17.0	16.9	17.1
Approach with conservative estimators	μ_Λ in kN	24.20	24.87	25.08
	σ_Λ in kN	2.461	3.747	3.232
	$\lambda_d{}^*$ in kN	16.8	13.6	15.4

* according to (6.2) with $b = 3$

Table 6-7: Mean value and standard deviation of buckling load given by FOSM approach considering conservative estimators and shell subsets with small sample size
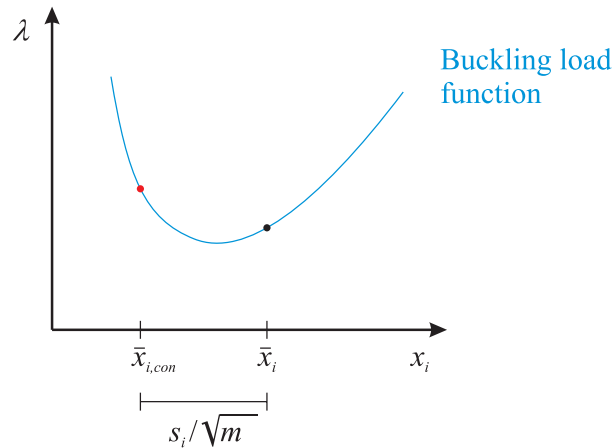
Figure 6-16: Example of an estimated mean value close to a local minimum of the objective function

The analyses with five samples show that using a conservative estimator for the mean values and standard deviations of input parameters indeed leads to a more conservative design load. However, for a sample size of ten the use of conservative estimators has a negligibly small effect on the design load. Hence, for the following considerations the standard approach is used.

6.7   Monte Carlo Simulation

In order to validate the semi-analytical, probabilistic analysis, a Monte Carlo simulation is executed. For determining the required number of virtual samples, the parameters of interest, namely the lower bound given by high levels of reliability, are observed within a convergence study (see Figure 6-17). The simulation convergences for about 1300 samples, however, the results for 2500 samples are used in the following.

The discrete cumulative distribution function obtained by the Monte Carlo method is shown in Figure 6-18. The numerical procedure does not deliver more accurate results than the semi-analytic approach. Both procedures overestimate the variance, which indicates that the deviations from the experimentally obtained distribution are due to uncertainties of the data

basis. The most uncertain data are the values of indirectly determined loading imperfection (see section 6.3.4). It is possible, that the inclination angle was exactly the same for each shell tested, and that the obtained scatter only results from the indirect determination procedure described in section 6.3.4. This would lead to a smaller variance of the buckling load and hence, to a better match with the experimental results. However, there is no way to verify this supposition.
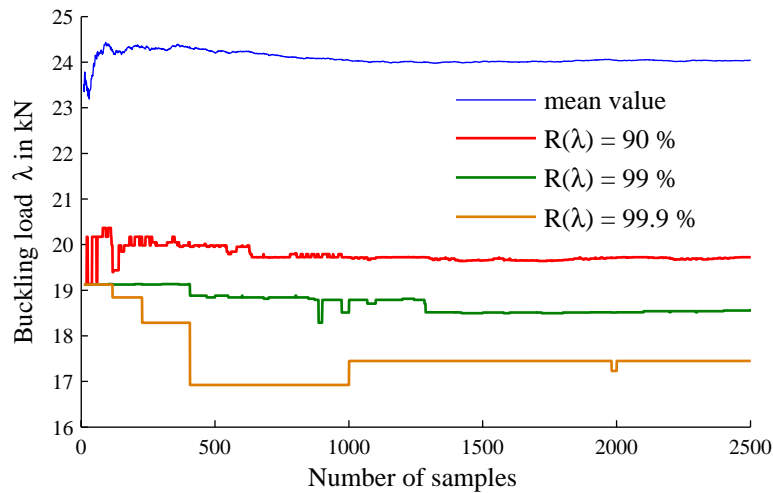
Figure 6-17: Convergence of Monte Carlo simulation for set #2

Since both approaches, the Monte Carlo simulation and the semi-analytic approach, deliver similar results it is concluded that the inaccuracies of the probabilistic approaches are not caused by the methods themselves, but due to the uncertainties in the input parameters, namely the loading imperfection.
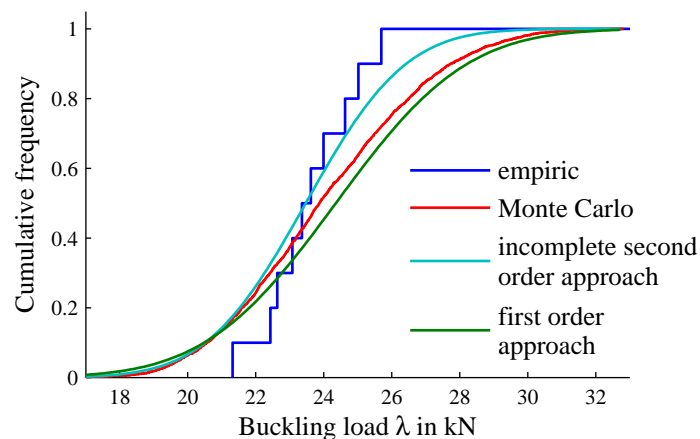
Figure 6-18: Cumulative distribution function of buckling load of set #2

6.8   *Comparison with other Design Procedures for Different Laminate Setups*

The semi-analytic method and the Monte Carlo method are applied to the shells with the laminate setups of set #1. Still, the imperfection measurements of set #2 are used as data basis. This implies the assumption that the imperfections are independent from the laminate setup. Especially for the geometric imperfections, this assumption appears to be invalid at first

glance. However, the Fourier spectra of all measured imperfections indicates that for the shells considered the manufacturing process has a much more important influence on the imperfection pattern than the laminate setup. For all non-traditional imperfections the assumption of independence from the laminate setup appears to be reasonable. However, it is worth mentioning that the material properties of set #2 are used in the following even though they differ slightly from the properties given for set #1 in [27]. This assumption is necessary because no stochastic moments of material properties are given in [27].

The cumulative distribution function given in Figure 6-19 show that independently from the laminate setup the semi-analytic approach compares well with the Monte Carlo simulations. For the shells Z09, Z10/Z11 and Z12 only one or two experimental results are available and hence, no comparisons of empiric distributions and estimated distributions are possible. However, the results show that results of the probabilistic analysis are reasonable since the estimated distribution and the experimental results have the same order of magnitude.
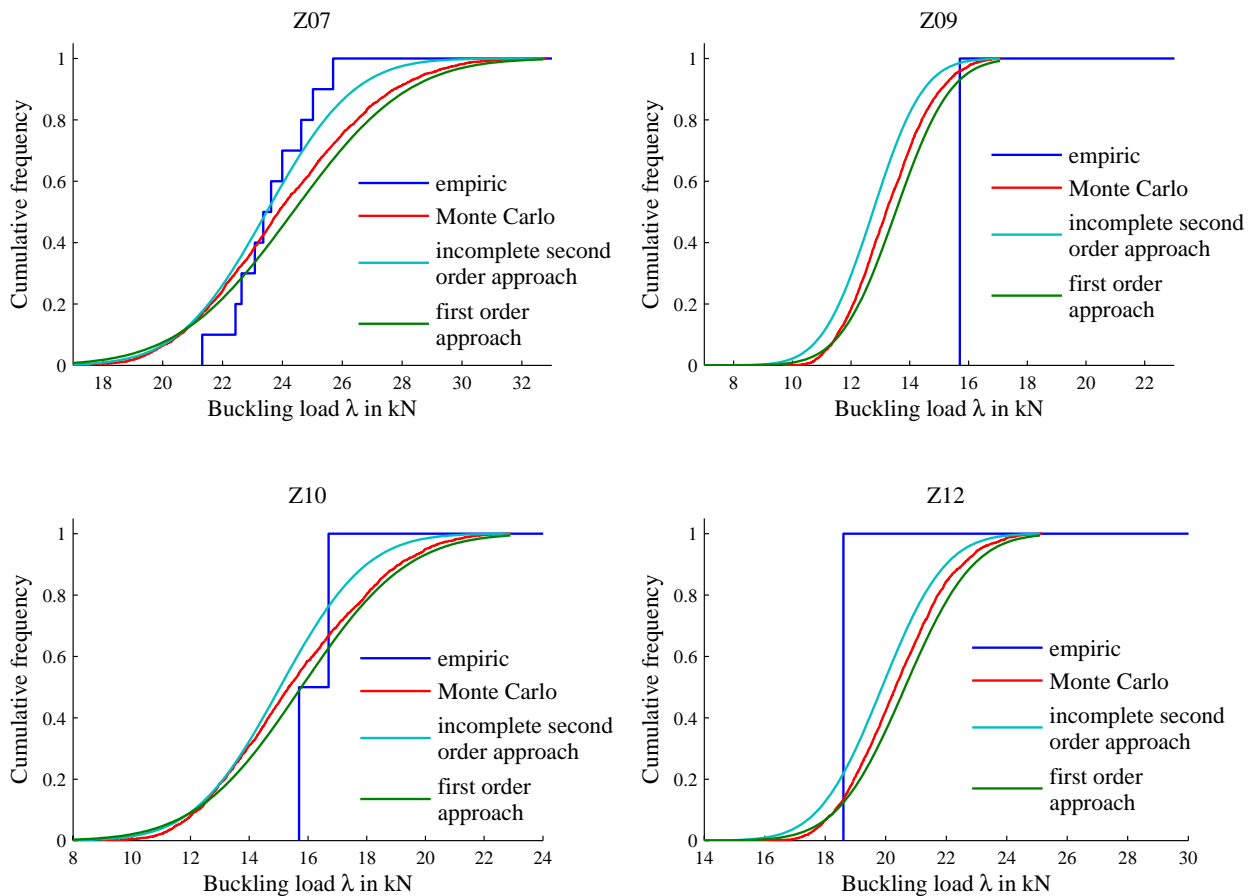
Figure 6-19: Cumulative distribution functions of buckling load for different laminate setups given by experiments, Monte Carlo simulation and incomplete second order approach

The equivalent thickness t^+ determined according to equation (1.6), and the knockdown factor γ given by equation (1.3) are given in Figure 6-7 for the four different laminates considered. By multiplying the KDFs with the buckling load of the perfect shell given by Hühne et al. [27], the design loads according to NASA SP-8007 are obtained (see Table 6-8).

Hühne et al. [27] determined the lower bound given by the single buckle approach for the shells considered, which are given in Table 6-9. Using the convex anti-optimization approach as introduced in section 4.4 delivers the lower bounds given in Table 6-9. For this approach,

the lower bounds given by the first order approach differ significantly from the second order approach. For a details discussion of the results of convex anti-optimization see [53].

Shell	Z07	Z09	Z10	Z12
Equivalent wall thickness t^+ in mm	0.5	0.5	0.48	0.48
Knockdown factor γ	0.322	0.322	0.315	0.315

Table 6-8: Equivalent radius and knockdown factors according to NASA SP-8007 [28]

With the estimated distribution function of buckling load, levels of reliability are determined for the deterministic design procedures. The design loads given by NASA SP-8007 have levels of reliability very close to 100% for all shells. E.g. for Z07 the reliability equals $1 - 4 \cdot 10^{-9}$ and for Z10 the reliability equals 99.97%.

Shell		Z07	Z09	Z10	Z12
Perfect shell analysis, from [27]		31.8kN	17.0kN	23.0kN	22.0kN
Minimal buckling load of experimental tests		21.3kN	15.7kN	15.7kN	18.6kN
Semi-analytic, probabilistic approach*	for R = 99.9 %	15.3kN	8.5kN	7.0kN	14.8kN
	for R = 99 %	17.2kN	9.5kN	9.0kN	16.0kN
Convex anti-optimization (first order approach)		17.1kN	9.8kN	11.7kN	16.7kN
NASA SP-8007		10.2kN	5.5kN	7.2kN	6.9kN
Single buckle approach, from [27]		17.4kN	14.7kN	13.8kN	20.2kN

*Incomplete second order approach, assuming normal distribution

Table 6-9: Design loads for the shells considered given by different design approaches

The SBA delivers design loads with unacceptable reliabilities, except for Z07. For the determination of these reliabilities it is assumed that the calculated distribution functions are exact. For Z07 it has been shown that the variance is overestimated by the probabilistic methods and most probably this is also the case for the other laminate setups. Nevertheless, the design loads given by the SBA for Z09 and Z12 exceed the mean value of buckling load, which means that the reliability of the design load is definitely below 50% for these shells. The lower bounds given by convex anti-optimization have the order of magnitude as the design loads given by the probabilistic approach for a reliability of 99%. Only for Z10 the design load obtained from convex anti-optimization exceeds the probabilistically motivated design load remarkably, while it is still lower than the lowest experimental result.

6.9   Conclusions

Summarized it is stated that the proposed probabilistic design procedure is well suited for an efficient design of composite cylindrical shells by exploiting the knowledge of imperfection data.

Concerning efficiency and computational costs the convex anti-optimization approach is as well suited as the probabilistic approach. The advantage of the probabilistic procedure is that it additionally gives information about the reliability and that it can even be used to evaluate the reliability of other approaches.

The knockdown factor approach leads to overly conservative design load. Furthermore, the safety margin differs for the different shells, which is caused by the fact that the different sensitivities are not captured by the knockdown factor philosophy.

The single buckle approach provides unsatisfying results for two of the shells considered. Still this approach is considered to be very promising, since it does consider the imperfection sensitivity of a shell, but does not require actual imperfection measurements. Probabilistic analyses in which only geometric imperfections are considered as randomly distributed indicate that the SBA indeed covers the effect of geometric imperfections, but not the effect of imperfect boundary conditions [45]. What is lacking is a definition of the application limits of this approach. To underline the applicability of the SBA, a set of composite shells tested at NASA Langley Research Center is considered, for which no imperfection data are available to the author. The measures and laminate setups of these shells are given in section 2.1.

Name	BL_{perf} in kN	Experiment		NASA SP-8007		SBA	
		BL in kN	KD	$\gamma \cdot BL_{perf}$ in kN	KDF γ	N_1 in kN	KDF
AW-Cyl-1-1	184.1	134.2	0.729	83.6	0.454	120	0.652
AW-Cyl-2-1[**]	436.3	329.2	0.755	253.3	0.581	350	0.802
						305	0.699
AW-Cyl-3-1	745.9	657.5	0.881	427.0	0.573	505	0.677
AW-Cyl-4-1	621.4	558.6	0.899	357.6	0.575	465	0.748
AW-Cyl-5-1[*]	672.7	407.9	0.606	390.5	0.581	420	0.624
AW-Cyl-11-1	745.9	676.6	0.907	428.0	0.574	510	0.684
AW-Cyl-92-01	133.1	123.6	0.929	62.1	0.467	115	0.864
AW-Cyl-92-02	170.1	142.0	0.835	79.4	0.467	95	0.558
AW-Cyl-92-03	184.1	152.0	0.826	83.6	0.454	120	0.652

[*]AW-Cyl-5-1 was damaged prior to testing.

[**]AW-Cyl-2-1 has a strong influence of plasticity. Calculations with a simple elastic-plastic material law for the matrix under shear lead to a N_1 load of 305 kN.

Table 6-10: Experimental results from [39] and SBA design loads for composite cylinder tested at NASA Langley Research Center

Table 6-10 summarizes the experimentally determined buckling loads and knockdown factors given in [39], as well as the design loads and corresponding knockdown factors given by the single buckle approach. The design load N_1 is in almost all cases below the experimentally obtained buckling load. In case of cylinder AW-Cyl-5-1 the shell was damage prior to testing, but tested nevertheless. Therefore, it is not critical that the design load exceeds the experimental result for this shell. For shell AW-Cyl-2-1 the initially obtained design load of 350kN exceeds the experimental value. However, this shell showed a significant material nonlinearity in the prebuckling range. Of course, if material nonlinearities occur before buckling, this has to be considered also within the SBA. Using a simple elastic-plastic material model for the unidirectional ply under shear, the SBA provides a design load of 305kN, which is lower than the experimentally obtained buckling load.

Since no measurement data are available for the set of shells tested by NASA, no probabilistic analysis has been performed. Therefore, a determination of the reliability of the design loads given by the SBA is not possible, but it is concluded that the SBA provides satisfying results, since it provides design load below the experimental results and it is less conservative than NASA SP-8007. It is the author's opinion that the single buckle approach is a promising alternative to probabilistic design concept in cases where no imperfection data are available, if its application limits can be determined.

7   Probabilistic Design of Stiffened Composite Panels

In this chapter the probabilistic design procedures proposed in section 4.6.1 and 4.6.2 are applied to a set of stiffened composite panels. In difference to the probabilistic analysis of cylindrical shells, not only one, but three objective values are considered, namely the local buckling load, the global buckling load and the onset of material degradation.

7.1   Properties of the Panels Considered

All panels considered have been manufactured and tested at the German Aerospace Centre in Braunschweig (see Ref. [70], [113] and [61]). Eight panels have been tested in the framework of the POSICOSS project (see e.g. [59]) and one panel tested within the framework of the COCOMAT project (see e.g. [60]) is considered. The nominal dimensions of the panels are summarized in Table 7-1. The POSICOSS panels only differ in radius, number of stringers (and hence stringer distances), and laminate setup of the skin. The COCOMAT panel has the same stringers as the POSICOSS panels and the same skin laminate setup as P12-14, but differs in the arc length and number of stringers, and has stringers at the longitudinal edges.

	POSICOSS, from [70]			COCOMAT, from [62]
	P09-P11	P12-P14	P15-P16	
Panel length L_{tot}		780mm		780mm
Free length L		660mm		660mm
Internal arc length L_a		419mm		560mm
Internal radius R	1000mm	1000mm	400mm	1000mm
Number of stringers n_s	3	4	3	5
Stringer height h		14mm		14mm
Stringer width f		34mm (nominal: 37.9mm)		32mm
Distance stringer to stringer	$L_a/n_s =$ 139.7mm	$L_a/n_s =$ 104.8mm	$L_a/n_s =$ 139.7mm	$L_a/(n_s - 1) - f$ $= 132$mm
Distance stringer to longitudinal edge		$0.5\, L_a/n_s$		$f/2 = 16$mm
Laminate set-up of				
- skin	$[\pm45,0]_s$	$[90, \pm45,0]_s$	$[\pm45,0]_s$	$[90, \pm45,0]_s$
- stringer blade		$[\pm45_3,0_6]_s$		$[\pm45_3,0_6]_s$
- stringer foot	$[\pm45_3,0_6]$ with drop off, see Figure 7-1			$[\pm45_3,0_6]$
Ply thickness t_{ply}		0.125mm		0.125mm

Table 7-1: Characteristics of the panels considered

In order to reduce peel stresses, the stringer feet of the POSICOSS panels have been manufactured with a ply drop off as depicted in Figure 7-3. In the framework of the

COCOMAT project one objective was to predict separation of stringers from skin and hence, the panel was design without ply drop off in order to stimulate skin-stringer debonding.
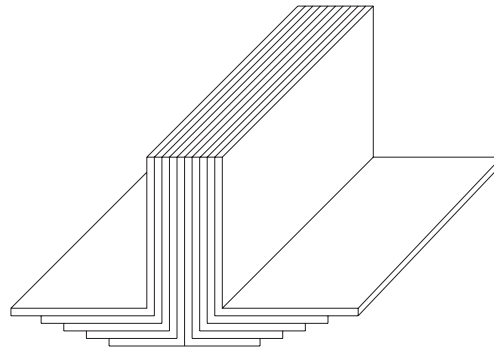
Figure 7-1: Sketch of ply drop off at stringer foot

7.2   Numerical Model

The POSICOSS panels are modeled with an approximate element length of 8mmm where for the stringer foot a element width of 5mm was chosen. This discretization leads to 9602 nodes for the panels P09-11 and P15-16 and to 10902 for the panel P12-14. For the COCOMAT panel an element length of approximately 5mm was chosen for the whole model, which consisted of 26064 nodes.

Four node shell elements with linear shape functions and reduced integrations (S4R elements in ABAQUS) have been chosen to model skin, stringer blade and stringer foot. The stringer foot has not been model in one element with the connected part of the skin. Moreover, the connection of skin and stringer has been model with cohesive elements as depicted in Figure 7-2. The thickness of the cohesive zone is chosen equal to the thickness of the glue layer.
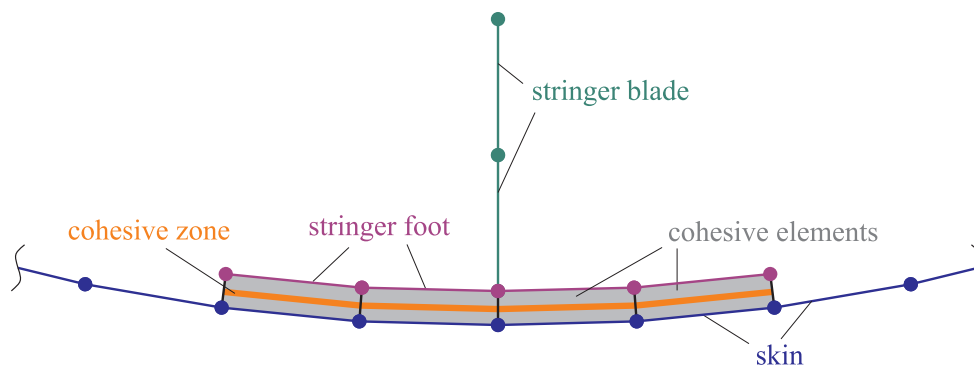
Figure 7-2: Modeling of skin-stringer connection with cohesive elements

In experiments, the clamping of the loaded edges has been realized by potting the ends in epoxy resin. In order to capture the axial load redistribution in this area, the potted region is model (red nodes in Figure 7-3), where only the axial translation is unrestricted for the nodes in this region.

The longitudinal, unloaded edges are free for the COCOMAT panel. The POSICOSS panels were clamped in the experiments, where the longitudinal and radial translation was unrestricted. Zimmermann et al. [70] showed that the rotation about the edge was not rigid enough to assume the rotation about the cylinder axis to be zero. Hence, the longitudinal

edges are modeled with torsional springs as shown in Figure 7-4. The boundary conditions used in the numeric simulations are summarized in Table 7-2.
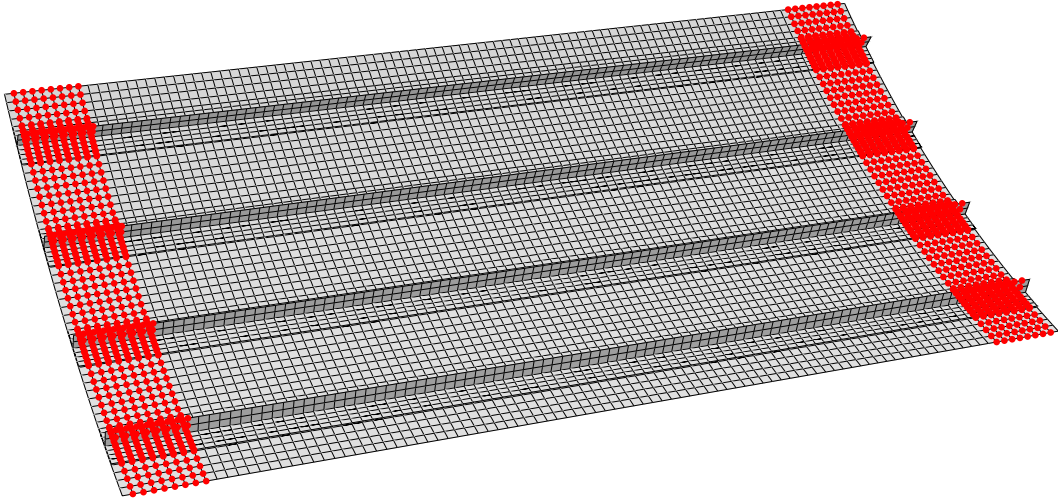
Figure 7-3: Numerical model of the POSICOSS panels P12-14, red spots: potted region

Boundaries	POSICOSS	COCOMAT
Loaded edges	clamped	clamped
Longitudinal edges	$u_r = 0$, u_φ = free, u_z = free, ψ_r = free, $\psi_\varphi = 0$, ψ_z = elastic	free

Table 7-2: Boundary conditions of the panels considered (in cylinder coordinates)

$$u_r = 0, \ u_\varphi = \text{free}, \ u_z = \text{free},$$
$$\psi_r = \text{free}, \ \psi_\varphi = 0, \ \psi_z = \text{elastic}$$
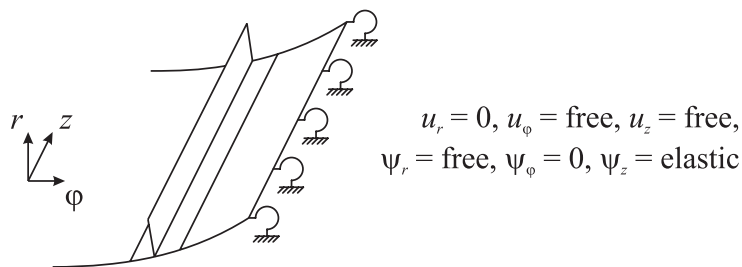
Figure 7-4: Sketch of torsional springs for modelling elastic clamping at longitudinal edges of the POSICOSS panels

For the panels considered, material damage occurs in the postbuckling range. Hence, material degradation has no influence on the local and global buckling loads. Therefore, linear elastic material behavior was assumed in the simulation. For detecting the onset of material degradation, the Hashin [73] criteria as given in section 3.3 is used for skin and stringers. The quadratic nominal stress damage criterion (3.19) are used to detect the onset of skin-stringer separation. In order to detect local buckling, the method described in section 3.2.1 is used. To capture the postbuckling behavior of the stiffened panels, geometrically nonlinear, displacement controlled simulations are performed using artificial damping, as described in

section 3.2.2. Global buckling is detected using the stiffness reduction criterion discussed in section 3.2.6. For the panel considered, the lower bound of axial stiffness that defines global buckling is chosen to be 33% of the initial stiffness, since this value provides comparable results for panel configurations with and without a limit point at global buckling.

7.3   Perfect Shells Analysis

The analysis of the perfect structure shows that all types of material damage, which are captured by the numerical model, occur in the postbuckling range (see Figure 7-5). The first onset of degradation occurs at the skin-stringer connection, which sets in at 1.88mm end shortening and 76.6kN. The global buckling load is 84.1kN and occurs at 1.57mm end shortening. From the linear eigenvalue analysis, the first buckling load is determined to 47.7kN.
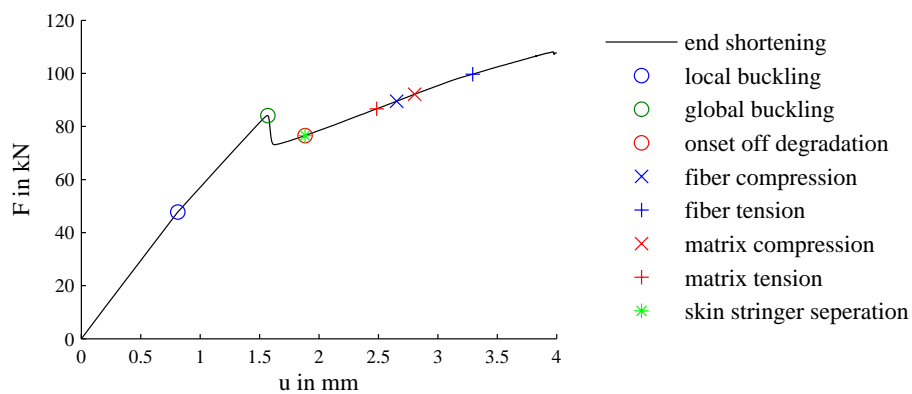
Figure 7-5: Load-displacement curve of perfect panel P12-P14

The first material failure detected is skin-stringer separation, given by the quadratic nominal stress criterion in the cohesive elements. The first intra lamina failure given by Hashin's criterion is matrix cracking due to tension. In order to determine the influence of the chosen failure criterion for intra lamina failure, also the Puck criterion and the invariant based quadratic criterion (IQC) are applied (see also section 3.3). The latter two criteria determine inter fiber failure in exactly the same load increment as the first occurrence of matrix cracking according to Hashin's criterion (see Table 7-3). Also the location of material failure in the panel matches for all three criterions considered (green arrow in Figure 7-6). It is therefore concluded that the Hashin criterion is sufficiently accurate for the investigations presented in the following. In Figure 7-6 the postbuckling pattern of P12-P14 is shown exemplarily, as well as the elements with matrix tension failure in the outermost ply, a few increments after the first intra lamina failure is detected. Since the onset of material degradation occurs after global buckling for the panels considered, no material degradation models are applied. If global buckling occurred after material failure, the material degradation would influence the global buckling behavior and therefore needed to be considered in such cases.

Criterion	Quadratic nominal stress	Hashin	Puck	IQC
Panel end shortening	1.88mm	2.48mm	2.48mm	2.48mm
Failure mode	Cohesive zone	Matrix tension	Mode A	-

Table 7-3: First occurrence of material failure using different failure criterions
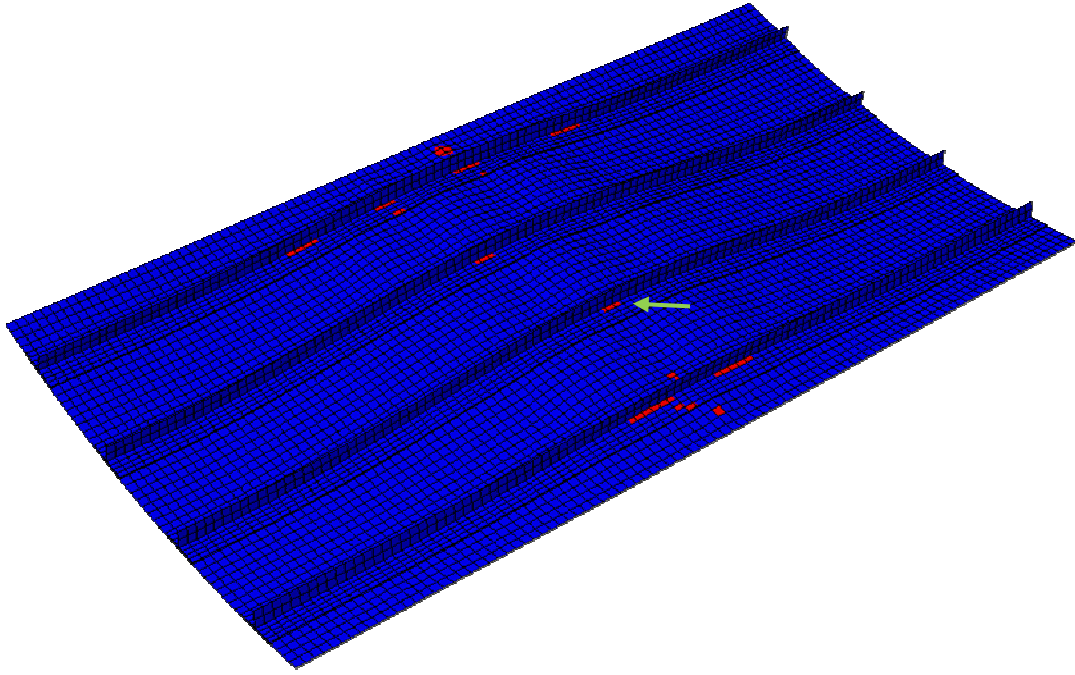
Figure 7-6: Postbuckling pattern of perfect panel P12-P14 with matrix tension failure given by the Hashin criterion in lowest ply (red elements) and location of first intra lamina failure (green arrow)

Following the design rules for stiffened panels that have been derived within the COCOMAT project [60], the design load is obtained by dividing the global buckling load by some safety factor. Ghilai et al. [64] proposed to reduce the global buckling load by 80% in order to account for uncertainties, which corresponds to applying a safety factor of 1.25. For the panel considered, this design approach yields a design load of 67.3kN. It appears that the experimentally observed global buckling load of panel P13 is lower than the design load (see Table 2-4). Obviously, a safety factor of 1.25 is not sufficient in this case. A safety factor of 1.5 yields a design load of 56.1kN, which seems to provide a sufficient safety margin. However, the reliability of this design load is still unknown.
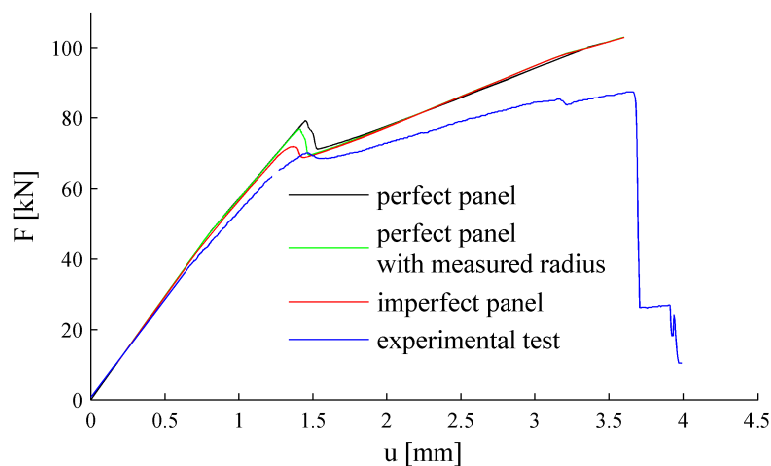
Figure 7-7: Load-displacement curved of panel P12

The load-displacement curve obtained from the perfect shell analysis significantly differs from the experimentally obtained one (see Figure 7-7). Not only the global buckling load, but

also the stiffness after local buckling and global buckling are overestimated. Including the measured radius and the measured geometric imperfections in the numeric model yields a better approximation of the global buckling load, while the stiffness reductions are still underestimated. The reason and the resolution of this issue are discussed in section 7.4.5.

7.4   Imperfection Measurements

For stiffened composites panels no data sets with large sample size are available for one and the same design. Therefore, the eight panels measured at DLR are considered as one data set for the probabilistic analysis. This implicates the assumption that e.g. the geometric imperfections are independent from the design, which is not the case. However, since the variety of the imperfection patterns increases, it is assumed that mixing measurements of different design will leads to a larger scatter of the load carrying capability and can therefore be regarded as a conservative approach.

For the scatter of wall thickness and fiber orientation, tolerance intervals are used to estimate the scatter of these parameters. The size and scatter of a boundary imperfection is determined indirectly.

7.4.1   Geometric Imperfections of the Skin

The geometric imperfections of the skin are given in [70]. The measurements are approximated by double Fourier series, as it is usually done within probabilistic analyses of cylindrical shells. However, using a Fourier series to describe imperfection patterns implicates the assumption that the pattern is periodic and axial as well as in circumferential direction. This leads to inaccuracies of the Fourier approximation at the boundaries of the imperfection pattern, if the full approach is used (see Appendix A). Therefore, a better approximation, especially at the boundaries, is obtained when using the half wave cosine approach in both directions.

$$\overline{w}(x,y) = 4t\sum_{k=0}^{n_x}\sum_{l=0}^{n_y} A_{kl}\cos\frac{k\pi x}{L}\cos\frac{l\pi y}{L_a} \tag{7.1}$$
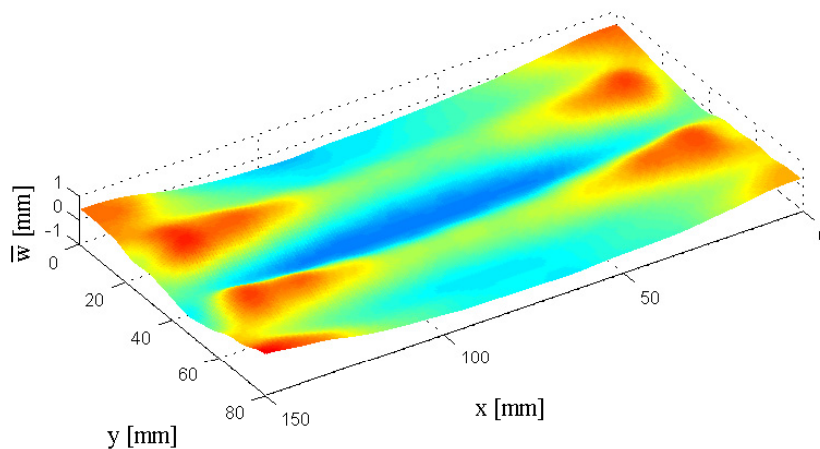
Figure 7-8: Fourier approximation of the imperfection pattern of panel P09

As an example, the Fourier series approximation of the imperfection pattern of the panel P09 is plotted in Figure 7-8. The influence of the three stringers is clearly visible and can also be detected within the Fourier spectrum in Figure 7-9.
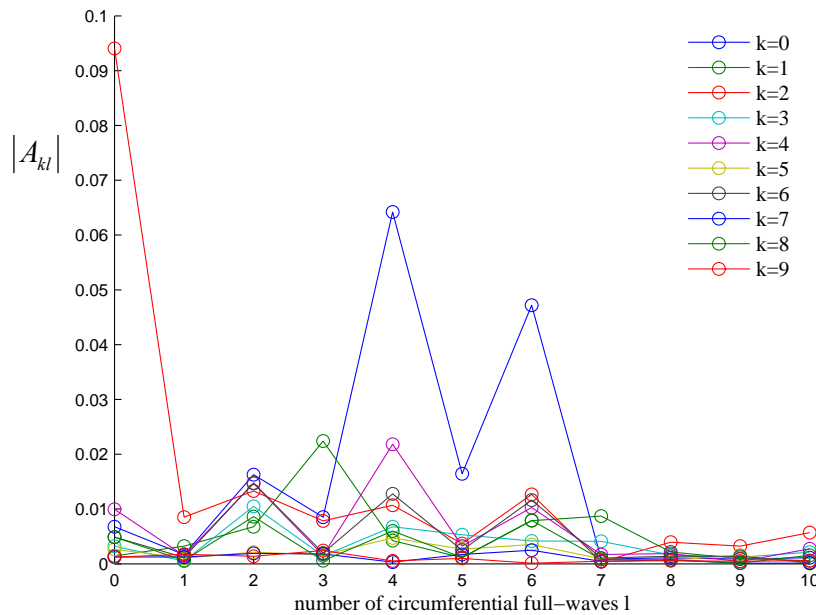
Figure 7-9: Fourier spectrum of the geometric imperfection pattern of panel P09, using the half wave cosine approach
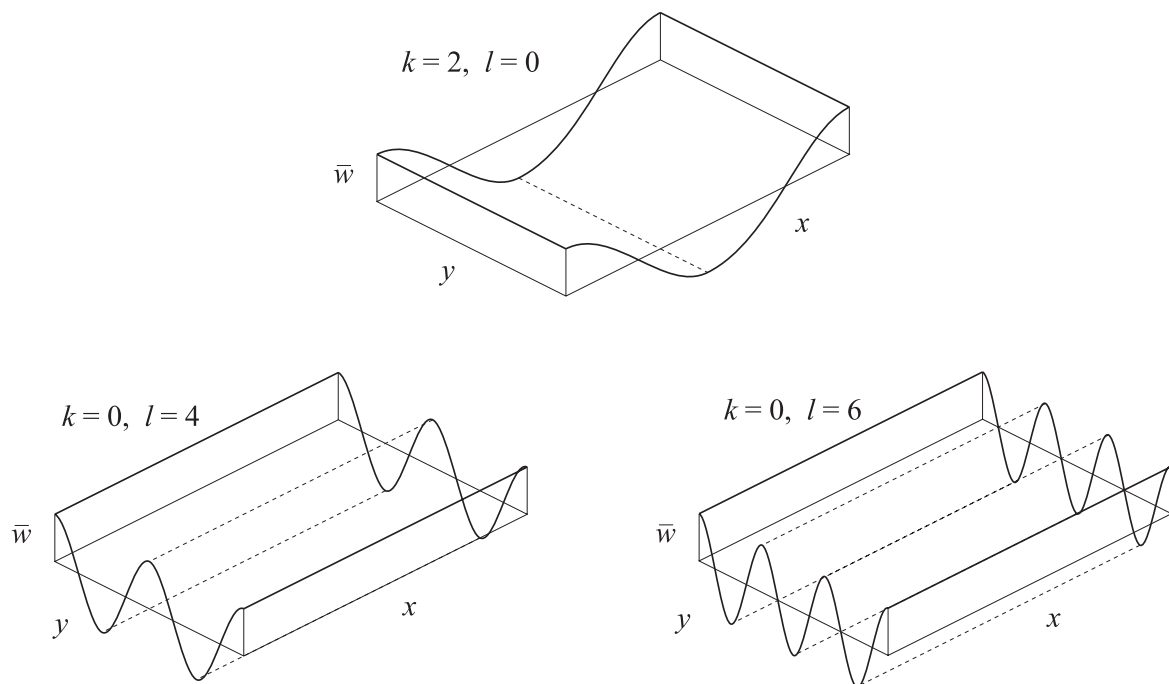
Figure 7-10: Sketch of dominant imperfection modes of panel P09

Three imperfection modes dominate the imperfection pattern of P09. The largest amplitude is detected for a mode with two axial half waves and no circumferential waves (see Figure 7-10, top). The two other modes, which are predominant, have four and six circumferential half waves combined with no axial waves (see Figure 7-10, bottom). These modes represent large imperfections in between the stringers, which shows that the assumption of the independence

of geometric imperfection patterns from the design is not valid within the considered set of panels. However, using the imperfection patterns of P09-P12 and P15-P16 for a probabilistic analysis of P12-14 causes a broader diversity of geometric imperfections, including large deviations at the locations of the stringers of P12-14. Therefore, mixing the measurement data is regarded as a conservative approach.

7.4.2   Radius

The deviations from the nominal radii of the POSICOSS panels are given in [70]. It appears that each radius differs significantly from its nominal value (see Table 7-4). In order to regard all measured radii as one data set, the relative deviation of the measured radii R_{mea} from the nominal radius R_{nom} is regarded as random parameter.

$$r = \frac{R_{mea} - R_{nom}}{R_{nom}} \qquad (7.2)$$

The relative deviations of the radii r are given in the last row of Table 7-4.

Panel	P09	P10	P11	P12	P13	P14	P15	P16
Nominal radius R_{nom} in mm	1000	1000	1000	1000	1000	1000	400	400
Measured radius R_{mea} in mm	1095	1688	1412	1069	1047	947	384	418
Normalized radius r	0.095	0.688	0.412	0.069	0.047	-0.053	-0.041	0.044

Table 7-4: Measured radii of the tested panels in mm, from [70]

The normalized radius r has a mean value of 0.158 and a standard deviation of 0.258. For a nominal radius of $R_{nom} = 1000$mm this equals a mean value of $\mu_R = 1157.6$mm and a standard deviation of $\sigma_R = 258.2$mm. For a nominal radius of $R_{nom} = 400$mm the stochastic moments are $\mu_R = 463.1$mm and $\sigma_R = 103.3$mm.

7.4.3   Wall Thickness

For the wall thickness, no measurement data are given. Hence, the nominal wall thickness is assumed to equal the mean value. In aircraft industry a tolerance interval of ±5% is common practice. Since most types of distribution describe a concentration around the mean value, assuming a uniform distribution within the tolerance interval is regarded as a conservative assumption. The standard deviation σ of a uniform distribution in the interval $[a,b]$ is given by

$$\sigma = \frac{b-a}{\sqrt{12}} \qquad (7.3)$$

Assuming the interval boundaries to be ±5% of the mean value μ leads to a coefficient of variation of 2.89%.

$$\sigma_t = \frac{1.05\,\mu_t - 0.95\,\mu_t}{\sqrt{12}} = 0.0289\,\mu_t \quad \Rightarrow \quad \frac{\sigma_t}{\mu_t} = 2.89\% \qquad (7.4)$$

7.4.4   Material Properties

The panels have been made of the prepreg material IM7/8552. The elastic material properties have been determined by DLR and are given in [70]. Camanho et al. [78] tested the same material and came up with slightly different properties. Since no standard deviation is given in [70], the coefficients of variation given by Camanho et al. are assumed to be the same for the

given material properties. The elastic material properties and their standard deviation used in the following are summarized in Table 7-5. Wilckens et al. [117] also determined the mean values and coefficients of variation of the material properties. However, these investigations have not been published at the time when the following analyses have been performed.

Parameter	Material properties from [70] (assumed mean value)	Coefficient of variation from [78]	Standard deviation
E_{11}	146535MPa	1.39%	2037MPa
E_{22}	9720MPa	1.03%	100MPa
G_{12}	6054MPa	2.53%	153MPa
v_{12}	0.34	6.18%	0.021

Table 7-5: Elastic material properties of the panels considered according to [70] and [78]

The material strength parameters are not given in [70] for the panels considered. Hence, the properties given in [78] and summarized in Table 7-6 are used subsequently.

Parameter	Mean value	Coefficient of variation	Standard deviation
X_t	2326.2MPa	5.8%	134.1MPa
X_c	1200.1MPa	12.1%	145.7MPa
Y_t	62.3MPa	8.5%	5.3MPa
Y_c	199.8MPa	10.2%	20.5MPa
$S_{\perp\parallel}$	92.3MPa	0.7%	0.6MPa

Table 7-6: Material strength according to [78]

For the adhesive film that bonded skin and stringers the values given in [61] and Table 7-7 are used. Due to the lack of data, the material properties of the adhesive are assumed to be deterministic.

$E = 3000MPa$
$v = 0.30$
Maximum shear stress: 38MPa
Maximum normal (tension) stress: 8MPa

Table 7-7: Material properties of the adhesive taken from [61]

7.4.5   Boundary Conditions

For the experiments, the loaded edges of the panels have been potted in epoxy resign in order to realize clamped boundaries. Also the longitudinal edges have been potted, where the axial translation was left free. As shown in Figure 7-11 for panel P12, large discrepancies occur

between simulations and experiments in the postbuckling region. Zimmermann et al. [70] explained this by the imperfect boundary conditions at the longitudinal edges. The potting at the longitudinal edges was not rigid enough in order to keep rotations around the edges negligibly small. In their simulation, Zimmermann et al. [70] applied springs at the longitudinal edges and showed that the experimental behavior in the postbuckling region can be approximated this way
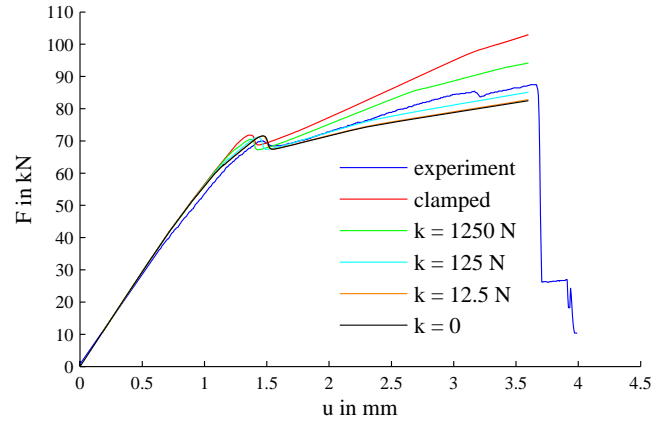
Figure 7-11: Load-displacement curve of panel P12 with different longitudinal edge stiffness

The spring stiffness that leads to the best fitting of the postbuckling behavior has been determined for each panel. Hence, the distribution of the spring constant k is obtained, that delivers a mean value of $\mu_k = 587$N and a standard deviation of $\sigma_k = 595$N. Since k scatters between zero (simply supported edge) and infinity (clamped edge), Weibull distribution is assumed for the Monte Carlo simulation.

7.4.6   Fiber Orientation

No measurement data are available for the fiber orientations of the panels considered and hence, the nominal values are assumed to equal the mean value. For the fiber orientation, a tolerance interval of ±6° is common practice in aircraft industry. According to equation (7.3), assuming uniform distribution within an interval of ±6° leads to a standard deviation of

$$\sigma_\varphi = \frac{\left(\mu_\varphi + 6°\right) - \left(\mu_\varphi - 6°\right)}{\sqrt{12}} = 3.464° \qquad (7.5)$$

The number of plies of 6 or 8 plies in the skin and 24 plies in each stringer leads to a relatively large number of random parameters. For example the panels P12-P14 have $8 + 4 \cdot 24 = 104$ plies with independently scattering fiber orientations. In order to be able to use the reduction technique introduced in section 4.1.3, 8 virtual panel samples are generated using the assumption that each fiber angle is uniformly distributed in an interval ±6° of the nominal value.

7.4.7   Geometric Imperfections of the Stringers

Geometric imperfections of the stringer $\bar{v}$ are deviations from the ideal structure in circumferential direction. Deviations in radial direction are captured by the description of the imperfections of the skin $\bar{w}$.

Depending on the stringer profile, the description of imperfections can be relatively difficult. A simple and general description of the stringer imperfections is to consider only the

deviation of the cross section centroid. This allows representing the imperfections as a one-dimensional function $\overline{v}(x)$. For blade stringers, the imperfections can also easily be described by a two-dimensional function $\overline{v}(x,z)$, which can be approximated by double Fourier series as described in section 4.1.1 (see Figure 7-12). The double half wave cosine approach is then given by

$$\overline{v}(x,z) = 4t\sum_{k=0}^{n_x}\sum_{l=0}^{n_z} A_{kl}\cos\frac{k\pi x}{L}\cos\frac{l\pi z}{H} \tag{7.6}$$
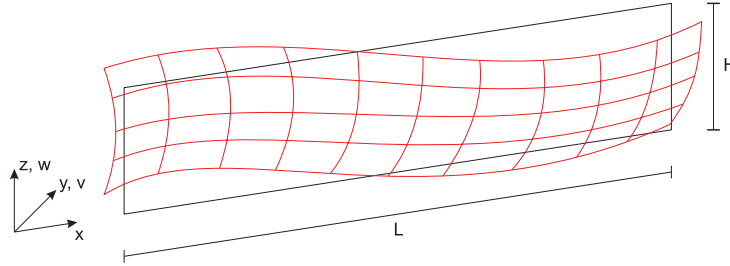
Figure 7-12: Sketch of geometrically imperfect stringer

However, no imperfection measurements are available for stringers. Therefore, a sensitivity study is performed in order to estimate the influence of stringer imperfections on the buckling behavior on the panels considered. All Fourier coefficients are set to zero except A_{01}, which is varied for one stringer. Hence, the pattern of the stringer imperfection is a half wave cosine in axial direction, with the amplitude $4t A_{01}$. Load-displacement curves for different values of A_{01} are shown in Figure 7-13. The largest value considered for A_{01} equals 2.5, at which the imperfection amplitude equals $4 \cdot 2.5 = 8$ times the stringer thickness. Even when applying this very large imperfection amplitude, the structural behavior of the panel hardly differs from the one with perfectly strait stringers. This finding however does not allow concluding that stringer imperfections have no influence on the buckling behavior in general. Moreover, different imperfection patterns had to be scrutinized and in order to investigate the actual influence on the buckling behavior, the scatter of imperfection amplitudes needed to be known.
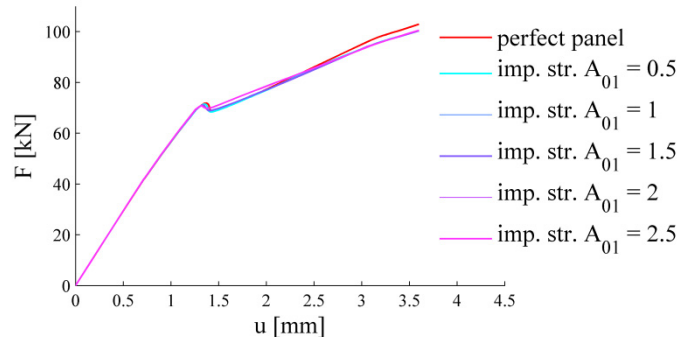
Figure 7-13: Load-displacement curves of panel P12 with imperfect stringer

Since no imperfection measurements are available and the influence on the buckling behavior seems to be small in the considered case, the geometric imperfections of the stringers will not be treated as randomly distributed in the following probabilistic analysis.

7.5   *Probabilistic Analysis of Panel P12-14*

With the assumed and measured scatter of input parameters, probabilistic analyses of the panel P12-14 are performed considering the local buckling load, the global buckling load and the onset of degradation as objective functions.

Using the transformation given in section 4.1.3, the Fourier coefficients describing the geometric imperfections are transformed to seven independent random parameters. The same holds for the fiber orientations. Furthermore, radius, wall thickness, spring stiffness and material properties are regarded as random input parameters for the probabilistic analysis of the panel. Altogether, $7 + 7 + 1 + 1 + 1 + 9 = 26$ uncorrelated random parameters are considered in the probabilistic analysis and hence, $2 \cdot 26 + 1 = 53$ buckling analyses have to be executed for the semi-analytic, probabilistic methods. For a Monte Carlo simulation, 1000 virtual samples have been generated and tested numerically.

In Table 7-8 the estimated stochastic moments given by first-order second-moment (FOSM) method, incomplete second order approach (ISOA) and Monte Carlo simulation are summarized. The moments with the subscript LB refer to the local buckling load, the subscript GB refers to the global buckling load and the subscript OD refers to the onset of material degradation. The correlation of local and global buckling load is denoted as ρ_{LG}, ρ_{LD} is the correlation of local buckling load and onset of degradation and ρ_{GD} is the correlation of global buckling load and onset of degradation.

	Mean values in kN			Standard deviations in kN			Correlations		
	μ_{LB}	μ_{GB}	μ_{OD}	σ_{LB}	σ_{GB}	σ_{OD}	ρ_{LG}	ρ_{LD}	ρ_{GD}
FOSM	37.9	62.9	70.5	3.70	6.30	5.16	0.61	0.75	0.74
ISOA	37.8	66.6	67.1	3.41	5.83	3.80	0.41	0.66	0.65
Monte Carlo	37.8	66.7	69.6	2.83	5.62	2.90	0.48	0.55	0.77

Table 7-8: Mean values, standart deviations and correlations of buckling loads and onset of degradation of panel P12-14

The mean values of local buckling load, global buckling load and onset of degradation, given by the different probabilistic approaches compare very well, where for the standard deviation larger discrepancies occur. Still, for all approaches the global buckling load scatters most and the onset of degradation has a slightly higher standard deviation than the local buckling load, though μ_{OD} is almost twice as high as μ_{LB}. Also concerning the correlations, the three approaches deliver differing results. However, all approaches show that the weakest correlation is between the local and the global buckling load.

Considering the standard deviations and correlations, the ISOA approach compares better with the Monte Carlo simulation than the FOSM method. The biggest discrepancies occur for the onset of degradation, which also become visible from the distribution functions (see Figure 7-14). The Taylor series approximation implicates the assumption of a smooth objective function, which is not necessarily valid for the buckling loads and unlikely for the onset of degradation, because the failure mode may change due to the scatter of input parameters. This may lead to inaccuracies of the Taylor approximation based approaches and the difference to the Monte Carlo simulation results.
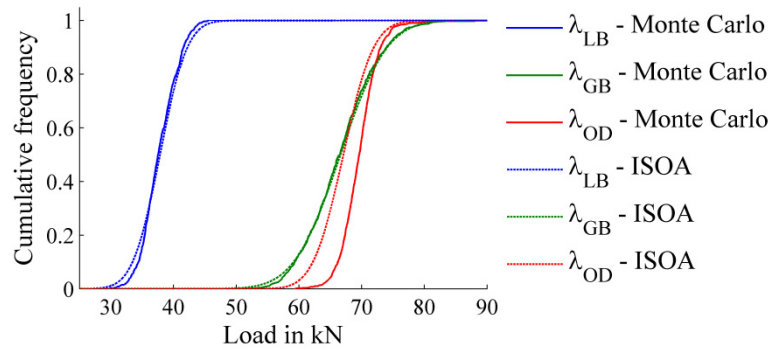
Figure 7-14: Cumulative distribution functions of the buckling loads and onset of degradation for panel P12-14, assuming normal distribution for the ISOA results

By performing the probabilistic analyses under consideration of only a certain set of parameters, the influence of this set on the scatter of the objective values and their correlations is determined. In Table 7-9, the standard deviation and correlation given by the FOSM method, taking into account only a subset of random input parameters, are given.

	Parameter	σ of input	Standard deviations			Correlations		
			σ_{LB}	σ_{GB}	σ_{OD}	ρ_{LG}	ρ_{LD}	ρ_{GD}
FOSM	Geometry		1.40kN	5.12kN	1.94kN	0.54	0.74	0.69
	Radius	258mm	2.26kN	3.25kN	4.47kN	1.0	1.0	1.0
	Wall thickness	2.9%	2.25kN	1.44kN	1.35kN	0.83	0.52	0.91
	Material properties	~2%	1.17kN	0.76kN	0.95kN	0.38	0.49	0.97
	Spring stiffness	595N	0.0kN	0.0kN	0.0kN	-	-	-
	Fiber orientation	3.5°	0.45kN	0.57kN	0.26kN	0.00	-0.20	0.64
	All		3.70kN	6.30kN	5.16kN	0.61	0.75	0.74

Table 7-9: Standart deviations and correlations of buckling loads and onset of degradation of the panels

The sensitivity study shows that the global buckling load is most sensitive to geometric imperfections. The second most influence has the radius, which also has the most significant influence on local buckling load and onset of degradation. The reason for the large influence of the radius is its relatively high standard deviation. For very large radii the panel behaves more like plates, leading to a decrease of the global buckling load and an increase of the postbuckling stiffness, whereas for small radii the panel shows a more cylinder like behavior. Furthermore, the correlations of the three objective values with respect to the radius equal one, meaning that there is a linear relation between local and global buckling load and the onset of degradation. The scattering of material properties and fiber orientations have a small influence on all objective values. The study on the influence of the boundary conditions of the longitudinal edges in section 7.4.5 showed that the spring stiffness of the elastic clamping has no influence on the local and global buckling load. Hence, it is not surprising that also the probabilistic sensitivity study delivers this result, though the scatter of the spring constant

appears to be very large. Surprisingly, the spring stiffness also has not influence on the onset of degradation, despite its strong influence on the postbuckling stiffness.

For determining the probability of failure as proposed in section 4.6.2, the stochastic moments of the displacements at global buckling u_{GB} and onset of degradation u_{OD} are determined (see Table 7-10). While the moments of u_{GB} estimated by the ISOA compare well with the results given by Monte Carlo simulation, the FOSM method provides estimations closer to Monte Carlo results for u_{OD}. Also the correlation of approximately zero is better approximated by the FOSM approach than by ISOA. Obviously, the function of the onset of degradation is approximated better by a liner approach than by a second order approximation. This does not allow concluding that the function of the onset of degradation is linear, since this case is also captured by the second order approach. Moreover, higher order nonlinearities can lead to the effect that a linear approximation is better than a quadratic, which is obviously the case, here.

	Mean value		Standard deviation		Correlation
	μ_{uG}	μ_{uD}	σ_{uG}	σ_{uD}	ρ_{uGD}
FOSM	1.20mm	1.97mm	0.110mm	0.109mm	0.03
ISOA	1.41mm	1.43mm	0.133mm	0.159mm	-0.36
Monte Carlo	1.41mm	1.80mm	0.167mm	0.105mm	0.05

Table 7-10: Statistical measures of the critical displacements

With the results of the Monte Carlo simulation, the integral (4.62) is solved numerically by

$$PoF \simeq \frac{1}{n_{vs}} \sum_{i=1}^{n_{vs}} \begin{cases} 1 & \text{for} \quad u_{GB}^{(i)} < u_d \vee u_{OD}^{(i)} < u_d \\ 0 & \text{for} \quad u_{GB}^{(i)} > u_d \wedge u_{OD}^{(i)} > u_d \end{cases} \tag{7.7}$$

where n_{vs} is the number of virtual samples generated within the Monte Carlo simulation, u_d is the displacement at design load, and $u_{GB}^{(i)}$ and $u_{OD}^{(i)}$ are the displacements at global buckling and onset of degradation of the i-th virtual sample. Note that the approximation (7.7) becomes inaccurate for small probabilities of failure, because then only few samples deliver critical displacements below the design displacement u_d. For a more accurate and efficient prediction of PoF with Monte Carlo simulations, advanced techniques like importance sampling could be used [90], as discussed in section 1.2.9.

For determining the PoF from (4.62) using the semi-analytic analyses results, normal distribution is assumed. In Table 7-11 the PoF is given for different safety factors determined by the different probabilistic approaches. Ghilai et al. [64] proposed to reduce the global buckling load by 80% to 90% for deriving the design load. This corresponds to a safety factor of 1.11 to 1.25. The commonly used safety factor in aerospace industry is 1.5. Furthermore, the safety factors are determined that, according the ISOA approach, lead to probabilities of failure of 1% and 0.1%, respectively. The relation of design load and associated displacement is derived from the perfect shell analysis, since this analysis is the basis for design in practice.

The probabilities of failure given by the ISOA compare much better with the Monte Carlo simulation than the results of the FOSM method. This is not surprising, since the stochastic moments given by ISOA and Monte Carlo compare well for global buckling (see Table 7-10) and for the panel considered, failure is driven more by global buckling than by material failure. For small probabilities of failure, the deviation of Monte Carlo and ISOA is relatively

large, since the standard Monte Carlo approach given by (7.7) becomes inaccurate for small PoFs.

Safety factor γ	1.11	1.25	1.5	1.43	1.57
Design load λ_d	75.7kN	67.3kN	56.1kN	58.9kN	53.4kN
Displacement at design load u_d	1.37mm	1.21mm	0.98mm	1.04mm	0.93mm
PoF – FOSM	95.0%	55.1%	2.2%	6.4%	0.66%
PoF – ISOA	67.5%	14.7%	0.3%	1.0%	0.1%
PoF – Monte Carlo	60.1%	15.6%	0.0%	0.1%	0.0%

Table 7-11: Probability of failure of panel P12-14 for different safety factors

Additionally to the presented analyses, probabilistic analyses of the panel P12-14 have been performed considering only the global buckling load as objective function, similar to the analysis of the cylindrical shells presented in chapter 6. The resulting PoFs are approximately the same as considering both, global buckling and onset of degradation. This is always the case, if the onset of degradation occurs in the deep postbuckling range and/or there is a strong correlation between global buckling and OoD. If the OoD occurs before global buckling and/or the correlation of global buckling and OoD is weak, it is essential to consider the OoD in the probabilistic analysis. This phenomenon is depicted in Figure 7-15. Consider two panel designs that lead to the same load-displacement curves and global buckling loads, but for which the onsets of material degradation occur differently. For one panel, the OoD occurs way beyond global buckling (see Figure 7-15, right). The joint probability density function of GB and OoD of this panel is plotted as green contour lines in central diagram in Figure 7-15. The ellipsoidal shape of the PDF indicates a strong correlation of GB and OoD. For this panel, the probability that the OoD occurs before GB is very small. Hence, deriving the ultimate load only from the distribution of GB will be sufficient. This is implicitly proposed by the COCOMAT design guideline, since it proposes to multiply the global buckling load with some safety factor to account for uncertainties, and then check whether the OoD occurs beyond the so derived design load. However, the following case is not captured by this design approach. Consider the second panel, for which the OoD occurs before GB (see Figure 7-15, top). The correlation of OoD and GB is very small and hence, the joint PDF, given by red contour lines in central diagram in Figure 7-15, is almost circular. Defining the ultimate load based on the GB leads to the same design load as for the first panel considered. However, the probability that the OoD is below that design load, indicated by the blue region in Figure 7-15, is relatively high. Therefore, it would make more sense to define the ultimate load based on the OoD, as depicted by the red dashed line and the red dot in Figure 7-15. However, deriving a lower bound from the PoF determined based on the joint PDF always leads to a safe design.

It must be stated that if material degradation initiates before GB, this can, of course, influence the global buckling load significantly, depending on the type of material failure. For an even more refined analysis of the reliability of stiffened panels, a deterministic model that captures progressive damage evolution should be used. Furthermore, it could be considered to differ between acceptable material damage (e.g. matrix cracking) and unacceptable material failure

(e.g. fiber cracking and skin-stringer debonding), and to define different allowable probabilities for these failures to occur.
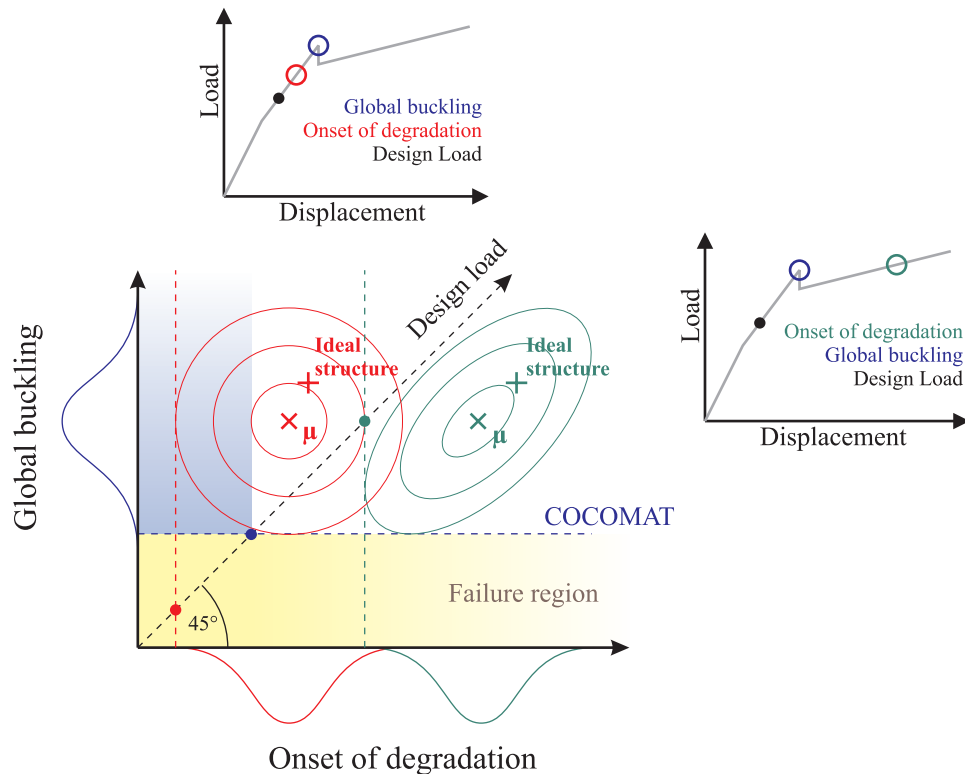
Figure 7-15: Relevance of the failure region given by material degradation depending on the panel design

7.6   *Probabilistic Analyses of Different Designs*

The semi-analytic analysis as performed for panel P12-14 is applied to the P09-11 panel design and to the COCOMAT panel. The load-displacement curves of the perfect and imperfect structures are summarized in Appendix H for all panels considered. The stochastic moments of local buckling load, global buckling load and onset of degradation given by the incomplete second order approach are summarized in Table 7-12.

Panel	Perfect shell results in kN			Mean values in kN			Correlations		
	LB	GB	OoD	μ_{LB}	μ_{GB}	μ_{OD}	ρ_{LG}	ρ_{LD}	ρ_{GD}
P09-11	15.7	48.9	58.8	13.3	41.2	49.8	0.72	0.70	0.84
P12-14	47.7	84.1	76.6	37.8	66.6	67.1	0.41	0.66	0.65
COCOMAT	42.5	82.7	96.2	37.5	76.7	89.1	0.08	-0.05	0.25

Table 7-12: Mean values, standard deviations and correlations of buckling loads and onset of degradation given by incomplete second order approach for all panels considered

The perfect panel analysis results are unsurprisingly smaller for P09-11 than for P12-14 and the COCOMAT panel. Local and global buckling load have the same order of magnitude for P12-14 and the COCOMAT panel. While panel P12-14 has closer spaced stringers, the

COCOMAT panel has more stringers in total, which seems to compensate the stringer distance. Panel P12-14 is the only panel for which the global buckling load is higher than the load at the onset of degradation. The reason is that for the COCOMAT panel and P09-11, no drop occurs in the load-displacement curve of the perfect shell analysis. For panel P12-14 the drop decreases or even vanishes as imperfections are introduced.

The coefficients of correlation are the highest for P09-11, which means that if one of the load levels considered increases due to the scatter of input parameters, most probably also the other load levels will increase. The smallest coefficients of correlation are obtained for the COCOMAT panel. This indicates that the probability that one load level increases while another one decreases is highest for this panel type. This can even lead to a change of the order in which the three different phenomena occur. However, the differences of the local and global buckling load and the onset of degradation are the biggest for the COCOMAT panel.

For all panels the mean values of all load levels are smaller than the perfect shell analysis results. It is noticed that the relative deviation of the mean values is smallest for the COCOMAT panel, which indicates lower imperfection sensitivity. A better measure for the imperfection sensitivity is the standard deviation and the coefficient of variation, respectively. Hence, in order to compare the stochastic scatter of LB, GL and OoD with respect to the mean value, the coefficient of variation (CoV), which is given by

$$CoV = \frac{\sigma}{\mu} \tag{7.8}$$

is regarded. From the CoV given in Table 7-13 it is seen that the relative variability of the local buckling load is higher for P09-11 compared to P12-14. It is interesting to note that the variability of the GB is the smallest for the COCOMAT panel. Due to the free longitudinal edges, the influence of the skin on the GB is smaller and hence, the scatter of geometric imperfections has a minor influence. The CoV of the OoD however is the largest for the COCOMAT panel.

Panel	Standard deviations in kN			Coefficient of variation		
	σ_{LB}	σ_{GB}	σ_{OD}	CoV_{LB}	CoV_{GB}	CoV_{OD}
P09-11	1.68	2.90	2.07	12.6%	7.0%	4.2%
P12-14	3.41	5.83	3.80	9.0%	8.8%	5.7%
COCOMAT	4.47	3.92	6.36	11.9%	5.1%	7.1%

Table 7-13: Coefficient of variation of buckling loads and onset of degradation given by incomplete second order approach for all panels considered

Using the incomplete second order approach, probabilistic analyses of the displacements at GB and OoD are preformed for all panels considered. With the results, the probability of failure is determined as described in section 4.6.2 for design loads given by different safety factors.

Regarding the design loads given by the safety factor considered in Table 7-14 indicated that only a safety factor of 1.5 provides a satisfying probability of failure. For the POSICOSS panels (P09-14), one out of three panels globally buckled at the design load obtained when using a safety factor of 1.25, which underlines that a higher safety factor is necessary, here. For the COCOMAT panel a safety factor between 1.25 and 1.5 might be sufficient, since the

associated PoF is between 1.8% and 0.03%. Hence, if a certain reliability or probability of failure is desired, the COCOMAT panel allows less conservative design. In order to demonstrate this, the design loads obtained for a PoF of 1% and 0.1% as well as the corresponding safety factors are determined.

Safety factor		1.11	1.25	1.5	GB of perfect shell	Min. GB in experiment
P09-11	λ_d	44.0kN	39.1kN	32.6kN	49.8kN	40kN (P09)
	PoF	36.4 %	8.1 %	0.2%		
P12-14	λ_d	75.7kN	67.3kN	56.1kN	84.1kN	67kN (P13)
	PoF	67.5%	14.7%	0.3%		
COCOMAT	λ_d	74.4kN	66.2kN	55.1kN	82.7kN	74kN
	PoF	13.7%	1.8%	0.03		

Table 7-14: Probability of failure given by incomplete second order approach of all panels considered for different safety factors

		PoF = 1.0%	PoF = 0.1%	GB of perfect shell	Min. GB in experiment
P09-11	λ_d	34.8kN	31.8kN	49.8kN	40kN (P09)
	γ	1.40	1.54		
P12-14	λ_d	58.9kN	53.4kN	84.1kN	67kN (P13)
	γ	1.41	1.55		
COCOMAT	λ_d	64.2kN	57.9kN	82.7kN	74kN
	γ	1.29	1.43		

Table 7-15: Probabilistically motivated design laods of all panels considered for different given probabilities of failure

The results in Table 7-15 show that depending on the sensitivity, different safety factors are necessary for different design in order to obtain the same, desired level of reliability (or probability of failure, respectively). The knockdown factor based design yields almost the same design loads for P12-14 and the COCOMAT panel (see Table 7-14). Using the probabilistic design approach, the design load of the COCOMAT panel is significantly higher. This also fits to the experimental observations, since the experimentally determined global buckling load of the COCOMAT panel exceeds the global buckling load of P12-14, which ranges from 65kN (P13) to 72kN (P14) in the experiments. The onset of material failure has not be detected in the experimental tests.

7.7   Comparison of Design Approaches and Conclusions

In industrial practice, two load levels are considered for design, the limit load (LL) and the ultimate load (UL). Limit load is a load level that the aircraft must be able to sustain under normal flight conditions, where the structure must be able to carry UL only once for three seconds. From the load exposure point of view, LL is a load level that occurs once in a lifetime of an aircraft. This statement is already of probabilistic nature, since the LL value of course does not occur exactly once in a lifetime of an aircraft. Moreover, it is a load level that is exceeded with a certain (small) probability. The ultimate load is obtained by multiplying the limit load by some factor of for instance 1.5 in order to provide safety margin. In general, local skin buckling is allowed under flight conditions. While for metallic panels the skin may buckling in the deep postbuckling region, only a small exceedance of the local buckling load (e.g. 10%) is allowed for composite panels. The exact factors depend on the company policy. For the following comparison it is assumed that the limit load equals 110%-120% of the local buckling load (LB).

Since LL is the load level that represents some reduced load carrying capability by including safety margins, it is the load level that corresponds to what is called design load in the context of the probabilistic approach presented in this thesis. For reasons of consistency, the expression limit load is replaced by design load in the following.

Within the COCOMAT project it has been proposed to determine ultimate load to be the global buckling load (GB) and to derive the limit load by dividing by some safety factor (see section 1.2.7). In the previous section it has been shown that a safety factor of about 1.5 is appropriate to obtain a robust design load. Alternatively, the limit load or design load can be derived from probabilistic analysis by determining the load level that e.g. 99.9% of the panels sustain.

Panel	Industrial design		COCOMAT	Probabilistic	Min. GB in experiment
	1.1 LB	1.2 LB	GB/1.5	PoF = 0.1%	
P09-11	17.3kN	18.8kN	32.6kN	31.8kN	40kN (P09)
P12-14	52.5kN	57.2kN	56.1kN	53.4kN	67kN (P13)
COCOMAT	46.8kN	51.0kN	55.1kN	57.9kN	74kN

Table 7-16: Limit loads or design loads, respectively, given by industrial design rules, COCOMAT design guideline and probabilistic design approach

In Table 7-16 the design loads or limit loads, respectively, given by the different approaches are summarized for the panels considered. The safety margins obtained by defining the design load based on the local buckling load extremely differ for the panels considered. Panel P09-11 has the smallest local buckling load relative to the global buckling load. Therefore, exploiting the larger postbuckling range unsurprisingly yields a significantly higher design load. For the COCOMAT panels and P12-14, the design load given by industrial design has the same order of magnitude as the COCOMAT design approach and the probabilistically motivated design load.

It cannot be stated that one design approach yields a lower design load than the other approaches in general. Moreover, the different approaches will lead to different optimal designs. Using industrial design rules, skin and stringer spacing is chosen such that high local

buckling load is obtained. The stringers then must be design such that the panel sustains ultimate load. The ratio of local and global buckling load will always be the same. Following COCOMAT design rules, local buckling is not considered and therefore, the whole panel is designed such that the interacting skin and stringers yields a high global buckling load. This provides additional design freedom and therefore weight saving potential. The probabilistic approach provides even more weight saving potential, since it allows reducing the safety margin. This will be demonstrated in an optimization example in section 9.

However, the reason for the very restricted design of composites in industrial practice is the relatively unexplored skin postbuckling behavior of panels with impact damages that can cause delaminations and delamination growths under repeated buckling, for which reliably analysis techniques are still lacking. These concerns of course must be dispelled before the skin postbuckling range is fully exploited in industrial practice.

8   Design Optimization of Composite Cylindrical Shells under Uncertainty

In this chapter it is discussed whether and how the design procedure influences the optimal design configuration. In practice, the objective of design optimization is often to reduce the weight of the structure, while the load carrying capability must exceed a certain load level. Zimmermann [25] stated that maximizing the buckling load of a cylindrical shell is equivalent to minimizing the weight, while keeping the buckling load constant. Therefore, the objective of the following design optimization is the maximization of the buckling load, where the ply angles of the composite layers are regarded as design variables. As Hühne [47] pointed out, not only the buckling load, but also the sensitivity to imperfections strongly depends on the lay-up, which needs to be taken into account in order to obtained the optimal design for a real shell.

For reasons of simplicity, visualization and comparison, the layup of four layers is restricted to be [±α, ±β] (see Figure 8-1). In order to get the response surface of this optimization problem, the two design parameters are varied in steps of 11.25° in the interval [0°,90°] and for each combination the design load is determined. Besides the layup, all properties of the cylinders considered in the following equal the properties of the cylinders of set #2 in chapter 6.
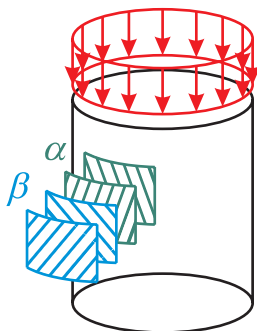
Figure 8-1: Maximization of buckling load by optimization of laminate setup [±α, ±β]
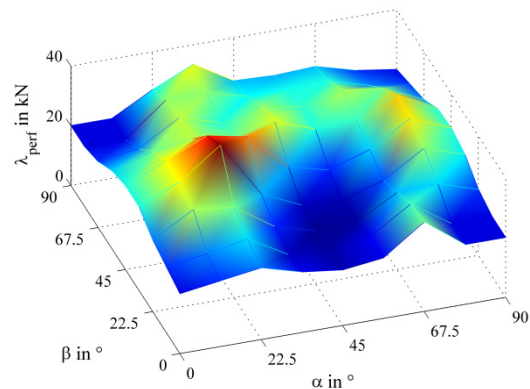
Figure 8-2: Buckling load of the perfect shell for different laminate setups [±α, ±β]

When using the classical knockdown factor philosophy, optimizing the design load is equivalent to maximizing the buckling load of the perfect shell, since the KDF only scales the response surface. Even when applying the KDF given by NASA SP-8007 for orthotropic shells (see (1.3) and (1.5) in section 1.2.4), the KDF is independent from the values of α and β, which is derived in Appendix H. The buckling loads of the perfect shell for different combinations [±α, ±β] are given in Figure 8-2.

8.1   Maximization of the Probabilistic Design Load

Within the probabilistic approach the design load depends on the chosen level of reliability and the assumed type of distribution. Both are represented by the factor b in equation (4.60). Hence, in a first step the mean values and the standard deviations of buckling load are determined for each different ply angle combination (see Figure 8-3 and Figure 8-4). Then, different response surfaces for different values of b are obtained according to equation (4.60),

and plotted in Figure 8-5 and Figure 8-6. Due to the computational cost of the optimization approach, mean values and standard deviations are determined using the first-order second-moment approach in combination with (4.49) for the estimation of derivatives.

Assuming normal distribution, $b = 3$ corresponds to a reliability of 99.87% whereas for $b = 4.5$, which is used within the six sigma concept [116], the level of reliability equals 99.9997% (see Table 4-2). Hence, both values considered can be regarded as realistic for design purposes. In both cases, the optimal design is found for a laminate setup of [±78.75°, ±67.5°].
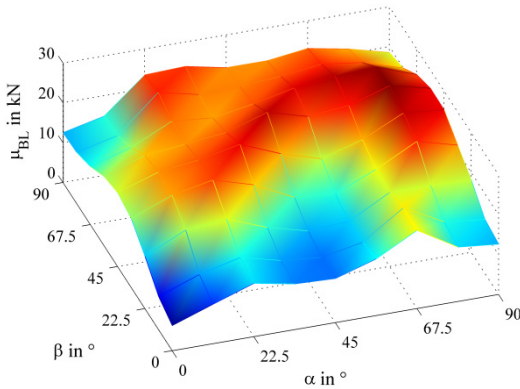
Figure 8-3: Mean value of buckling load for different laminate setups [±α, ±β]
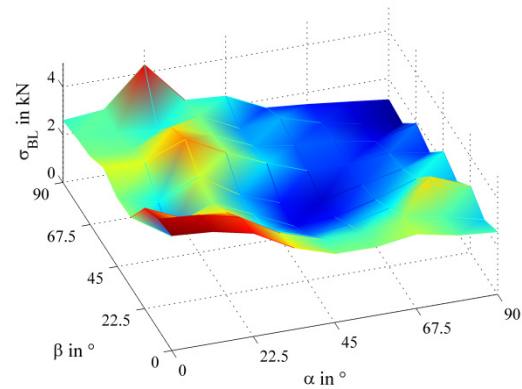
Figure 8-4: Standard deviation of buckling load for different laminate setups [±α, ±β]
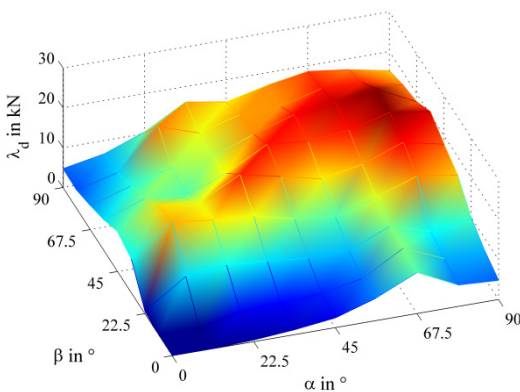
Figure 8-5: Design load λ_d provided by probabilistic analysis with $b = 3$ for different laminate setups [±α, ±β]
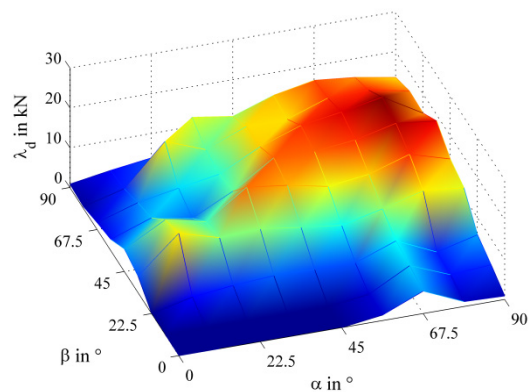
Figure 8-6: Design load λ_d provided by probabilistic analysis with $b = 4.5$ for different laminate setups [±α, ±β]

For axially stiffening layups (α and β close to zero), the probabilistically motivated design load is negative (and set to zero in Figure 8-5 and Figure 8-6). Obviously, the assumption of normal distribution is not valid in these cases, but it is also obvious that the optimal design configuration cannot be found in this region. Hence, scrutinizing this area is unnecessary. It turns out that for realistic values of b the pattern of the response surface does not change significantly and the ply angle combination that leads to the maximum design load does not change either. While it is a non-trivial, societal and political decision, which level of

reliability is acceptable and hence, which value to choose for *b*, the optimal design configuration given by the probabilistic approach is independent from *b*.

8.2   *Maximization of the Convex Pessimum Design Load*

The response surface of optimizing the lower bound given by convex anti-optimization differs significantly from the response surface of the perfect shell optimization (compare Figure 8-7 and Figure 8-2). However, it compares surprisingly well with the mean value of buckling load (see Figure 8-3) and therefore, also with the response surface of the probabilistic design load (Figure 8-5 and Figure 8-6). The optimal design, which is found to be [±78.75°, ±56.25°], is close to the optimal laminate setup given by the probabilistic approach.
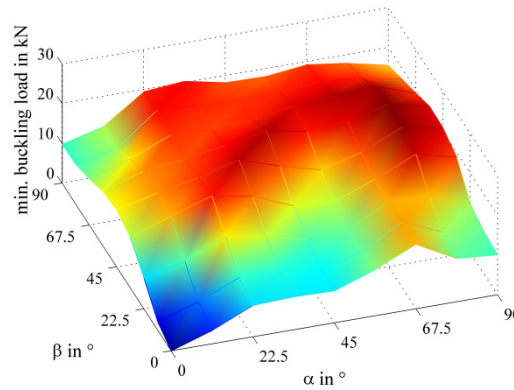
**Figure 8-7: Design load λ_{min} given by convex
anti-optimization for different laminate setups [±α, ±β]**

Though the philosophies of the probabilistic approach and convex anti-optimization are completely different, the good agreement appears not to be surprising. The FOSM approximation of the probabilistic design load can be written as

$$\lambda_d \approx \lambda(\mathbf{\mu}) - \sqrt{\sum_{i=1}^{n}\left[b\,\sigma_{Z_i}\,\frac{\partial\lambda(\mathbf{\mu})}{\partial z_i} \right]^2} \qquad (8.1)$$

When comparing (8.1) with the first order approach of the convex anti-optimum (8.2), the similarities of both approaches become obvious.

$$\lambda_{min} \approx \lambda(\mathbf{x}_c) - \sqrt{\sum_{i=1}^{n}\left[a_i\,\frac{\partial\lambda(\mathbf{x}_c)}{\partial x_i} \right]^2} \qquad (8.2)$$

For both approaches, the buckling load is evaluated and differentiated at some point in the center of the measurement vectors, namely the mean vector $\mathbf{\mu}$ and the center of the MVEE $\mathbf{x}_c$. In both approaches, the derivatives are multiplied by some measure for the scatter of the input parameters, the standard deviation σ_{Z_i} times *b* for the probabilistic approach and the semi axes a_i of the MVEE for the convex anti-optimization.

8.3   *Comparison of Optimal Design Approaches*

The design load N_1 according to the SBA is shown is Figure 8-8 for different layups. The perturbation load P_1, which is an indicator for the imperfection sensitivity of a design, is plotted over the ply angles in Figure 8-9.

Compared to the results of 8.1 and 8.2 the optimization of N_1 load delivers a significantly different optimal design. As mentioned in section 6.9 the SBA does not cover the effect of imperfect boundary conditions, which appears to be significant for the shells considered. Consequently, a different optimal design is obtained. However, the response surfaces of SBA and convex anti-optimization still show similarities, as there are local maxima for [±22.5°, ±78.75°] and a local minimum around [±45°, ±22.5°]. Furthermore, high values of P_1, correlate with a low standard deviation, obtained from the probabilistic approach (compare Figure 8-9 and Figure 8-4).
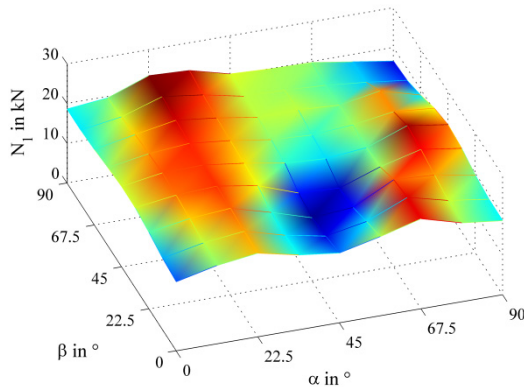
Figure 8-8: Design load N_1 given by single buckle approach for different laminate setups [±α, ±β]
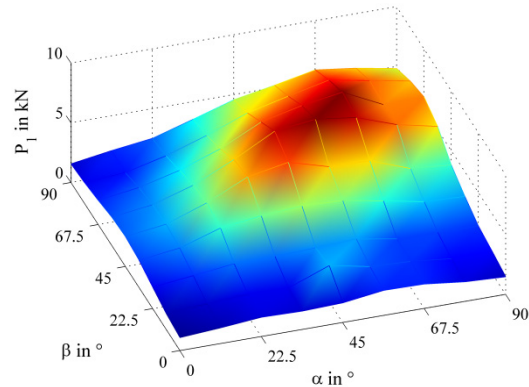
Figure 8-9: Perturbation load P_1 associated to the design load N_1 for different laminate setups [±α, ±β]

The maximal design loads given by SBA and convex anti-optimization compare well with the maximal probabilistically motivated design load for $b = 3$ (see Table 8-1). Optimizing the perfect shell and applying a KDF yields a way more conservative design load. Furthermore, the perfect shell optimization provides an optimal design, which is, according to the probabilistic approach, very sensitive to imperfections.

	Maximum design load	Optimal design
Perfect shell	43.9kN	[±22.5°, ±33.75°]
NASA SP-8007 ($\gamma = 0.322$)	14.1kN	[±22.5°, ±33.75°]
Single buckle approach	23.5kN	[±22.5°, ±78.75°]
Convex anti-optimization	23.3kN	[±78.75°, ±56.25°]
Probabilistic design with $b = 3$ [*]	23.0kN	[±78.75°, ±67.5°]
Probabilistic design with $b = 4.5$ [**]	20.9kN	[±78.75°, ±67.5°]

[*] equivalent to a reliability of 99.87%, assuming normal distribution
[**] equivalent to a reliability of 99.9997%, assuming normal distribution

Table 8-1: Results of the optimization of cylindrical shells

Summarized, it is concluded that especially for optimization purposes of cylindrical shells it is essential to consider imperfection sensitivity and the uncertainty of input parameters. It is interesting to note that when using the probabilistic approach, the choice of the factor b,

which implicates the assumed type of distribution and the chosen level of reliability, does not influence the optimal design configuration.

8.4   Gradient Based Design Optimization

In section 8.1 and 8.2, a multitude of combinations of the two design variables are evaluated, which provides the response surface of the optimization problem considered. This approach of course is too computationally costly to be applied for design optimization, especially as the number of design variables increases. Moreover, efficient gradient based methods are preferable to be used for this purpose.

In section 4.8.2 and section 4.8.3 the gradients of the probabilistically motivated design load and of the lower bound given by convex anti-optimization are given. These allow applying one of the gradient based optimization techniques given in section 4.8.1. Because of the shapes of the response surfaces and because of the computational cost per iteration step (see section 4.8.4), the simple gradient algorithm is used. As start vectors, the optimal design found by stepwise varying the ply angles are used.

In order to show the potential applying gradient based optimization, the design optimization is not only performed for a $[\pm\alpha, \pm\beta]$ laminate, but also regarding all four ply angles as independent design variables. For the optimization of the probabilistically based design load, $b = 3$ is chosen.

	Maximum design load	Optimal design
Convex anti-optimization		
with 2 design variables	23.74kN	$[\pm79.4°, \pm56.8°]$
with 4 design variables	23.78kN	$[84.1°, -75.2°, 57.5°, -55.5°]$
Probabilistic design with $b = 3$		
and 2 design variables	22.16kN	$[\pm78.1°, \pm66.9°]$
and 4 design variables	23.00kN	$[78.4°, -78.1°, 66.2°, -67.6°]$

Table 8-2: Results of the gradient based optimization of cylindrical shells

The results of the gradient based optimization given in Table 8-2 show only a slight change of the optimal design compared to the initial configuration given by the optimization in section 8.1 and 8.2. The maximum design load obtained by the probabilistic approach is even smaller than the one found in section 8.1. The reason is that in the current chapter the ISOA is used, for which the gradient of the design load has been derived in section 4.8.2. In difference to that, the FOSM approach has been used in the previous section to determine the design load for each ply angle combination, in order to keep the computational cost of this costly procedure reasonable.

The response surfaces shown in Figure 8-5 and Figure 8-7 indicate that there is a high risk of finding only local minima. Most probably, this also holds for the optimization in the four dimensional design space. This explains why the located maxima are close to the initial design. Optimization runs using other start vectors did not yield a higher maximum.

It is concluded that optimization techniques that combines genetic algorithms and gradient based methods, as discussed in section 4.8.1, should be consulted for an efficient optimization of cylindrical shells under uncertainty.

9   Design Optimization of Stiffened Composite Panels under Uncertainty

In order to show the weight saving potential of using the probabilistic design approach, an optimized design of a stiffened panel under axial compression is derived in this chapter. As initial design, the POSICOSS panel P12-14 is regarded. The objective of the design optimization is to reduce the panel weight, while the probabilistically motivated lower bound is higher or at least the same as for the initial design.

9.1   Restrictions and Objectives

In order to perform an optimization close to industrial practice, the following constraints are introduced for the optimization. The length, the arc length and the radius of the panel are fixed. The thickness of a single ply is kept constant, the fiber orientations are restricted to 0°, -45°, 45° or 90° and the laminate setup must be symmetric. All stringers are equal and equally spaced over the panel. T-stringers with a ply drop off in the foot are used. Design restrictions are summarized in Table 9-1.

Parameter	Constraint
Panel length L_{tot}	780mm
Free length L	660mm
Internal arc length L_a	419mm
Internal radius R	1000mm
Distance stringer to stringer	L_a/n_s
Distance stringer to longitudinal edge	$0.5\ L_a/n_s$
Ply thickness t_{ply}	0.125mm
Fiber orientations φ_i	$\varphi_i \in \left\{0°, -45°, 45°, 90°\right\}$

Table 9-1: Restrictions of the panel optimization

For optimizing the design performance, the following design parameters are considered as optimization variables. The number of stringers, the stringer height and the stringer width are varied. The numbers of plies in the stringers as well as the number of plies in the skin are considered as free variables, while both values are restricted to even numbers. Furthermore, the fiber orientations in the stringer and the skin are modified with the mentioned restriction. The design parameters and their initial values are given in Table 9-2.

9.2   Optimization Strategy

Since most of the design variables are discrete, applying gradient based methods appears to be difficult. While fiber orientations could be considered as continuous variables and then later be shifted to their discrete values, this appears to be impossible for the number of plies and stringers. Hence, a genetic algorithm is used for the optimization of the panel. However, evaluating the probabilistically motivated design load for a panel appears to be very time

consuming. Therefore, to avoid that each generated panel is analyzed probalistically, the optimization strategy depicted in Figure 9-1 is used.

Parameter		Initial value
Number of stringers	n_s	4
Number of plies in	Skin	8
	stringers	24
Stringer	height	14mm
	width	34mm
Fiber orientations in	Skin	$[90, \pm45,0]_s$
	stringers	$[\pm45_3,0_6]_s$

Table 9-2: Design parameters and their initial values of the panel optimization
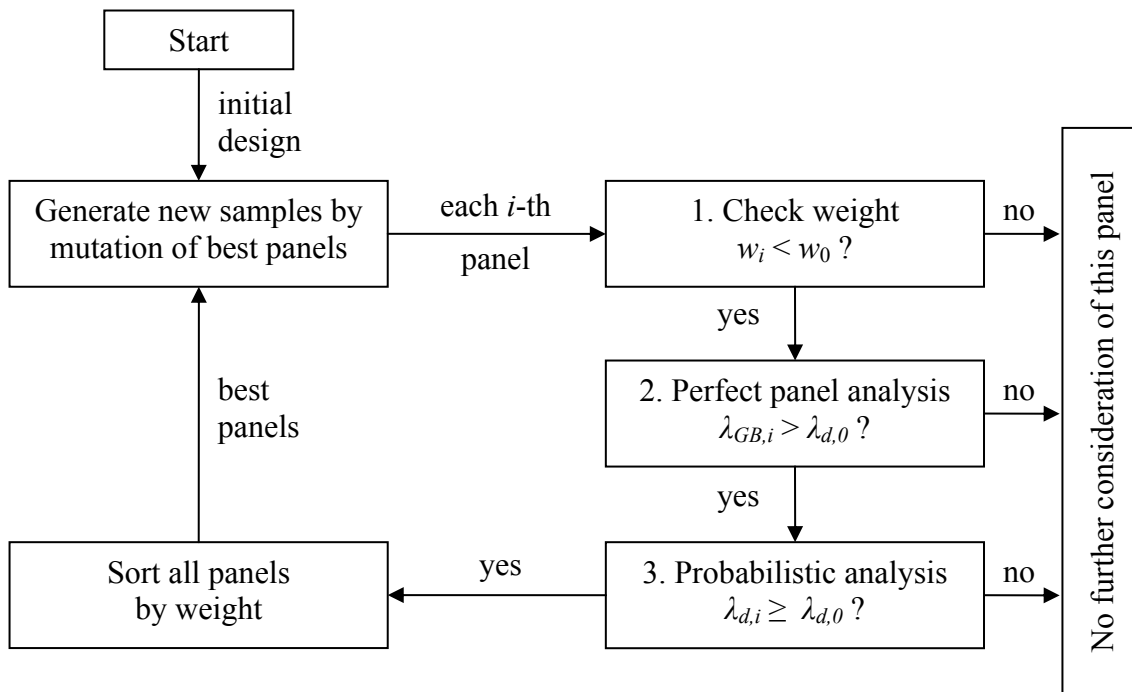
Figure 9-1: Panel optimization strategy based on a genetic algorithm

The design of P12-14 is regarded as initial design and the first population is generated by mutation of this design. For each generated panel it is checked, if the weight w_i of the panel is lower than the weight of the initial design w_0. Only panels that are more lightweight than the initial design are further analyzed. In a second step, a buckling analysis of the perfect virtual panel is executed. If the global buckling load of the perfect panel $\lambda_{GB,i}$ is lower than the design load of the initial design $\lambda_{d,0}$, the panel is not further considered. Otherwise, the panel is probabilistically analyzed and the design load $\lambda_{d,i}$ is determined for a probability of failure of 0.1%. If the design load of the virtual panel is at least as high as the design load of the initial design $\lambda_{d,0}$, the panel is further taken into account.

After one generation of virtual panel samples has run through this process, the remaining panels are sorted by weight and the best panels are used as basis for the generation of the next generation.

One disadvantage of genetic algorithms is that convergence is hard to define. The only indicator that the optimization procedure has converged is that no better sample is found in a certain amount of generation. A big advantage is that the same buckling analyses can be used to find the optimal design considering the perfect panel analysis. The only difference to the procedure shown in Figure 9-1 is that instead of step 2 and 3 it is checked if the global buckling load of the virtual panel sample $\lambda_{GB,i}$ is at least as high as the global buckling load of the initial design $\lambda_{GB,0}$.

9.3   Improved Design Configuration

Since for a genetic algorithm it is difficult to judge whether an optimization run has converged, the determined improved design is not necessarily an optimum, especially if a relatively small number of realizations has been checked. Due to the computational costly evaluation of the performance of a generated panel, the number of virtual samples tested is indeed comparatively small. Nevertheless, improved designs are found and the best of these designs is regarded as preliminary optimum.

After evaluating 404 virtual samples that passed the weight check (see 1. in Figure 9-1), the best designs obtained from the genetic algorithm are given in Table 9-3.

			Best panel designs	
		Initial design	Probabilistic approach	Perfect shell analysis
Number of stringers	n_s	4	4	5
Number of plies in	skin	8	6	6
	stringers	24	22	24
Stringer	height	14mm	16mm	13mm
	width	34mm	33mm	34mm
Fiber orientations in	skin	$[90,\pm45,0]_s$	$[\pm45,0]_s$	$[\pm45,-45]_s$
	stringers	$[\pm45_3,0_6]_s$	$[0,-45_2,45,90,0,$ $-45,0,45,0,-45]_s$	$[-45_2,0_3,-45,0,$ $-45_3,90,-45]$
Weight, relative to w_0		100%	83.5%	90.3%
λ_d for PoF = 0.1%		53.4kN	63.5kN	38.0kN
$GB_{perf}/1.5$		56.1kN	45.3kN	56.9kN

Table 9-3: Design variables, weights and design loads of the initial panel and the best designs located by genetic optimization

For comparison of the obtained weight savings, the design load should be kept constant during optimization and hence, the same design loads should be obtained for the optimal design configurations given by the probabilistic approach and the perfect shell analysis approach. However, since the determination of the design load is a noninvertible process, the

restriction that the design load is equal to *or greater than* the initial design load was defined in the optimization procedure (see Figure 9-1, 3.). The optimization using the probabilistic design approach provides a weight reduction of 16.5%, where the probabilistically motivated design load even exceeds the one of the initial design by about 10kN. At the same time, the COCOMAT based design load is reduced by about 10kN, which shows that the safety margin is reduced significantly without reducing reliability, and a less imperfection sensitive design is obtained. In contrast to that, optimizing the design under consideration of the buckling load of the perfect panel yields only 9.7% weight saving. Thereby, the design load is only slightly above the one of the initial design and the probabilistically motivated design load undercuts the one of the initial design by about 10kN. Note that the probabilistic design approach used here also accounts for material failure, which is neglected within the perfect panel optimization.

From the results of the optimization procedures it is concluded, that taking into account the influence of imperfections in design optimization leads to a more robust design and provides more weight saving potential than optimizing the perfect structure.

10 Summary and Conclusion

The derived methods and obtained results are summarized in this chapter. The main conclusions are given, and open issues and suggestions for further investigations are derived.

10.1 Summary

Estimators for stochastic moments of an objective function are given based on the second order Taylor expansions of the objective function. It has been shown that for reasons of efficiency the complete second order approach should be reduced and the modified approach has been given. Furthermore, the second order Taylor approximation based estimator for the covariance of two objective functions has been given for the first time. A modified version of the Mahalanobis transformation has been derived, which has similarities to the principal component analysis. It has been shown that combining this reduction technique with the stochastic moment approximation provides a probabilistic analysis method, which requires only as many evaluations of an objective function, as measurement data are available. Furthermore, a method to account for the sample size within the probabilistic approach has been provided.

The influence of the numerical derivatives of an objective function on the computational cost as well as on the accuracy of the probabilistic method has been quantified. Furthermore, it has been shown that the step size for the numerical derivatives should equal 1.5 times the standard deviation of an input parameter.

Based on the stochastic moment approximations, a fast, semi-analytic, probabilistic design procedure has been derived and applied to a set of composite cylindrical shells. The results of the semi-analytic procedure compares well with Monte Carlo simulations and empiric distributions. The probabilistic design procedure has been used to determine probabilistically motivated design loads, which are smaller than experimental test results in all cases considered, and at the same time less conservative than the design loads given by NASA SP-8007. The results of the probabilistic analyses have been used to evaluate the reliability of alternative deterministic design approaches.

The design load of composite cylinders has been maximized by optimizing the laminate setup. The influence of the design procedure on the optimization response surface, on the optimal design and the maximal design load has been investigated.

A new concept has been derived for determining the probability of failure for stiffened panels, taking into account global buckling and onset of material degradation. The concept has been applied to a set of composite stiffened panels. With the results, the reliability of different safety factors for stiffened panels has been evaluated. The design of a stiffened composite panel has been enhanced using a genetic algorithm, under consideration of scattering input parameters. It has been shown that using probabilistically based design in optimization provides great weight saving potential.

10.2 Conclusions

The proposed semi-analytic, probabilistic procedure approximates the real distribution of load carrying capability not exact, but sufficiently well. Furthermore, Monte Carlo simulations do not provide more accurate results, which shows that inaccuracies are not caused by the probabilistic method itself, but by uncertainties in the data basis. Therefore, it is not worthwhile to consult advanced and more costly probabilistic procedures in such cases.

The proposed semi-analytic, probabilistic method is an efficient procedure for designing shells prone to buckling by exploiting the knowledge of manufacturing characteristics. Especially if only a small data basis is available, the procedure is well suited. The conservative modification of the new approach, which allows the provision for the sample size, showed that the relatively small sample size of ten cylindrical shells is a sufficiently large sample size to obtained reliably results from the semi-analytic approach.

The evaluation of the reliability of design loads given by deterministic design approaches showed that the design load given by NASA SP-8007 is overly conservative in most cases and cannot be recommended for further use. For the single buckle approach it was found that the provided design loads do not have an acceptable level of reliability in all cases considered. Therefore, it is recommended to investigate the application limits of this promising approach. The convex anti-optimization delivers almost the same results as the probabilistic approach, while the computational cost are the same. However, the inherent assumptions are difficult to verify and no statement about the reliability is possible.

Optimizing the perfect structures leads to a significantly different design than optimizing under consideration of imperfections. When optimizing the design of cylindrical shells by maximizing the design load given by probabilistic analysis, the assumed type of distribution and the chosen level of reliability have no influence on the optimal design configuration.

The design load given by the COCOMAT design guidelines leads to a reliable lower bound, if a safety factor of about 1.5 is applied. This finding is only valid for the panels considered and should be further investigated by future probabilistic analyses of stiffened panels.

Optimizing stiffened panels with respect to the probabilistically based design load provides significant weight saving potentials, because the imperfections sensitivity of the optimized design is decreased significantly. Therefore, the scatter of load carrying capability decreases, which yields a higher design load at less weight for the optimized design.

10.3 Outlook

For the stiffened panels considered the onset of material degradation occurred beyond global buckling. In order to be able to probabilistically analyze panels for which this is not the case, advanced numerical models have to be consulted in order to capture the influence of material degradation on the buckling behavior. With currently available methods this significantly increases the computational cost. Due to the amount of required simulations, this is critical in combination with probabilistic methods, and even more critical when combining optimization and probabilistic analyses. Therefore, a coupled multi scale analysis is proposed for these purposes. A multi scale approach in which the local model consists of solid continuum elements not only provides a more accurate prediction of in plane material failure, but furthermore allows the detection of delaminations.

In the presented probabilistic design approach for stiffened panels, the stochastic distribution of the onset of degradation was considered as the first occurrence of any material failure. However, multiple, very different types of material damage can occur, which have significantly different impacts on the structural performance of a panel and are differently associated to the global panel behavior. Skin-stringer separation for instance has a significant influence on the global panel stiffness, but usually does not occur before globally buckling. In difference to that, matrix cracks potentially can occur at any stage, but do hardly influence the global behavior. Within a probabilistic design concept, the dependencies of different failure modes could be taken into account and their different impacts could be considered by e.g. allowing a higher probability for matrix cracking than for skin-stringer separation. This can lead to a less conservative approach and therefore, provide additional weight saving potential.

The proposed investigations of course require the enhancements suggested in the previous paragraph.

In industrial design practice of stiffened composite panels, local skin buckling may only be exceeded slightly, which restricts the design freedom. The reason is a lack of reliable analysis techniques that enable accounting for the influence of impact damages or other operational induced defects on the buckling behavior. Further research effort should be spent on this field in order to fully exploit the load carrying capability of stiffened composite panels.

The design optimization under uncertainty applied to cylindrical shells showed that using gradient based algorithms yields a high risk of finding local optima only. Genetic algorithms however are extremely costly. Therefore, it is proposed to use hybrid optimization techniques that combine genetic algorithms with gradient based methods for future design optimizations under uncertainty.

The main reason for the fact that probabilistic methods did not find their way to broad application in industrial practice is on the one hand the computational cost, which this dissertation contributes to reduce significantly. On the other hand, there is often a lack of data concerning the considered structure. If this is resolved by arbitrarily assuming stochastic distributions of input data, the information obtained from probabilistic analyses are valueless and no alternative to safety factors based on expert opinions. The solution cannot be of course to always build several samples of a structure. This is only an option in mass production. In order to probabilistically analyze structures, which have not been built, yet, process simulation should be utilized. If the stochastic distributions of the decisive parameters of the manufacturing process are known, a probabilistic process simulation can provide the input for probabilistic analyses of the structural performance. This type of approach is applicable to large scale structures like panels as well as to smaller scale specimens, like Coupon samples. Therefore, the two step probabilistic approach can be performed on multiple scales and the probabilistic analysis results of the smaller scale serve as input parameters for the next higher scale. Such a multi step and multi scale analysis approach would have to be investigated in the framework of a large research project.

Appendix

A   Fourier Series

Fourier series are appropriateto represent continuous, periodic functions. The Fourier series f_F of a function $f : \mathbb{R} \rightarrow \mathbb{R}$ is in the interval [0, a] is given by

$$f_F(x) = \sum_{k=0}^{n_x} a_k \cos \frac{k \pi x}{a} + b_k \sin \frac{k \pi x}{a} \tag{A.1}$$

If f is approximated by f_F it is implicitly assumed that f is periodic and continuous. This can lead to inaccuracies at the boundaries of the interval, as shown in Figure A-1, where the actual function is given by the black line and the Fourier series is given by the red line.
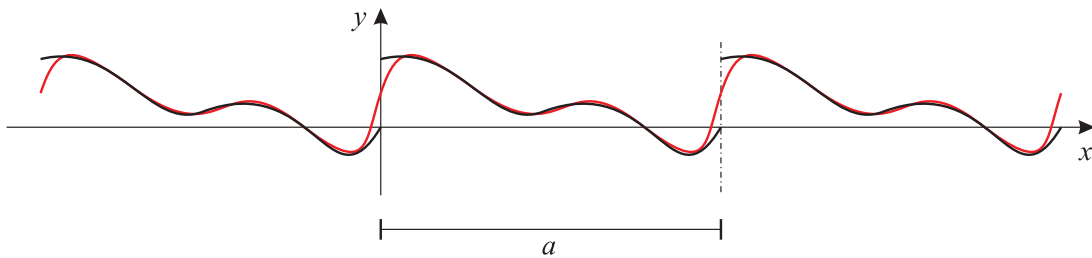
Figure A-1: Example of a non-periodic function approximated by a Fourier series

One possibility to solve this problem is to assume that the function is symmetric with the period $2a$ (see Figure A-2). Eq. (A.1) then simplifies to

$$f_F(x) = 2\sum_{k=0}^{n_x} a_k \cos \frac{k \pi x}{a} \tag{A.2}$$

This approach includes the assumption that the first derivative is zero at the boundaries.
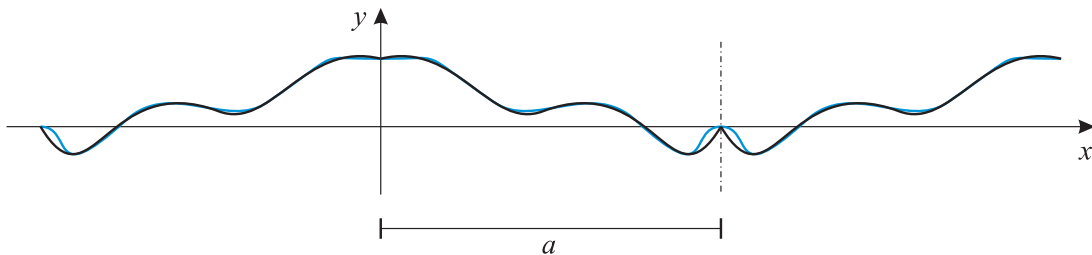
Figure A-2: Example of a non-periodic function approximated by a Fourier series assuming symmetry

Alternatively, it can be assumed that the function is point symmetric, which leads to

$$f_F(x) = 2\sum_{k=0}^{n_x} a_k \cos \frac{k \pi x}{a} \tag{A.3}$$

As depicted in Figure A-3, this approach includes the assumption that the function is zero at the boundaries.

Which series represents the original function best depends on the shape of the original function at the boundaries.
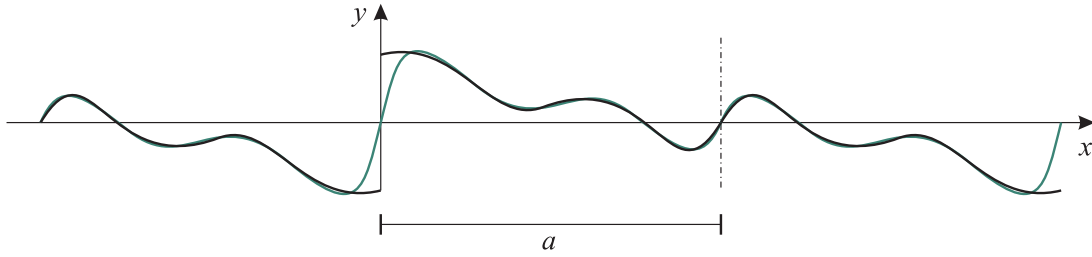
Figure A-3: Example of a non-periodic function approximated by a Fourier series assuming rotational symmetry

In order to represent a function $f : \mathbb{R}^2 \to \mathbb{R}$ by a Fourier series f_F, the approaches for the one-dimensional case are multiplied.

$$
\begin{aligned}
f_F(x,y) &= \left(\sum_{k=0}^{n_x} a_k \cos\frac{k\pi x}{a} + b_k \sin\frac{k\pi x}{a} \right) \cdot \left(\sum_{l=0}^{n_y} c_l \cos\frac{l\pi y}{b} + d_l \sin\frac{l\pi y}{b} \right) \\
&= \sum_{k=0}^{n_x}\sum_{l=0}^{n_y} \left(a_k c_l \cos\frac{k\pi x}{a}\cos\frac{l\pi y}{b} + b_k c_l \sin\frac{k\pi x}{a}\cos\frac{l\pi y}{b} \right. \\
&\qquad\qquad \left. + a_k d_l \cos\frac{k\pi x}{a}\sin\frac{l\pi y}{b} + b_k d_l \sin\frac{k\pi x}{a}\sin\frac{l\pi y}{b} \right)
\end{aligned}
\tag{A.4}
$$

By introducing

$$
a_k c_l = A_{kl} \quad a_k d_l = B_{kl} \quad b_k c_l = C_{kl} \quad b_k d_l = D_{kl}
\tag{A.5}
$$

f_F can be written as

$$
\begin{aligned}
f_F(x,y) &= \sum_{k=0}^{n_x}\sum_{l=0}^{n_y} \left(A_{kl}\cos\frac{k\pi x}{a}\cos\frac{l\pi y}{b} + B_{kl}\cos\frac{k\pi x}{a}\sin\frac{l\pi y}{b} \right. \\
&\qquad\qquad \left. + C_{kl}\sin\frac{k\pi x}{a}\cos\frac{l\pi y}{b} + D_{kl}\sin\frac{k\pi x}{a}\sin\frac{l\pi y}{b} \right) \\
&= \sum_{k=0}^{n_x}\sum_{l=0}^{n_y}\cos\frac{k\pi x}{a}\cdot\left(A_{kl}\cos\frac{l\pi y}{b} + B_{kl}\sin\frac{l\pi y}{b} \right) \\
&\quad + \sum_{k=1}^{n_x}\sum_{l=0}^{n_y}\sin\frac{k\pi x}{a}\cdot\left(C_{kl}\cos\frac{l\pi y}{b} + D_{kl}\sin\frac{l\pi y}{b} \right)
\end{aligned}
\tag{A.6}
$$

In the two-dimensional case, the Fourier coefficients are determined by

$$
A_{kl} = \frac{\alpha}{ab}\int_0^a\int_0^b f(x,y)\cos\frac{k\pi x}{a}\cos\frac{l\pi y}{b}\,dy\,dx
\tag{A.7}
$$

$$
B_{kl} = \frac{\alpha}{ab}\int_0^a\int_0^b f(x,y)\cos\frac{k\pi x}{a}\sin\frac{l\pi y}{b}\,dy\,dx
\tag{A.8}
$$

$$
C_{kl} = \frac{\alpha}{ab}\int_0^a\int_0^b f(x,y)\sin\frac{k\pi x}{a}\cos\frac{l\pi y}{b}\,dy\,dx
\tag{A.9}
$$

$$D_{kl} = \frac{\alpha}{ab} \int\limits_0^a \int\limits_0^b f(x,y) \sin\frac{k\pi x}{a} \sin\frac{l\pi y}{b} \, dy \, dx \tag{A.10}$$

With $\alpha = \frac{1}{4}$ for $k = 0$ and $l = 0$, $\alpha = 1$ for $k > 0$ and $l > 0$ and $\alpha = \frac{1}{2}$ otherwise.

If the function is assumed to be symmetric in x- or y-direction, the remaining coefficients have to be multiplied with two. If e.g. symmetry in x-direction is assumed, the Fourier series is given by

$$f_F(x,y) = 2 \sum_{k=0}^{n_x} \sum_{l=0}^{n_y} A_{kl} \cos\frac{k\pi x}{a} \cos\frac{l\pi y}{b} + B_{kl} \cos\frac{k\pi x}{a} \sin\frac{l\pi y}{b} \tag{A.11}$$

If point symmetry is assumed in y-direction, the Fourier approximation is given by

$$f_F(x,y) = 2 \sum_{k=0}^{n_x} \sum_{l=0}^{n_y} B_{kl} \cos\frac{k\pi x}{a} \sin\frac{l\pi y}{b} + D_{kl} \sin\frac{k\pi x}{a} \sin\frac{l\pi y}{b} \tag{A.12}$$

If, for instance, point symmetry is assumed for the x-direction and symmetry in the y-direction, the Fourier series is given by

$$f_F(x,y) = 4 \sum_{k=0}^{n_x} \sum_{l=0}^{n_y} C_{kl} \sin\frac{k\pi x}{a} \cos\frac{l\pi y}{b} \tag{A.13}$$

B Mahalanobis Transformation

In general, the Mahalanobis transformation is given by

$$\mathbf{x} = \mathbf{\Sigma}^{\frac{1}{2}} \mathbf{z} + \mathbf{\mu} \quad \text{and} \quad \mathbf{z} = \mathbf{\Sigma}^{-\frac{1}{2}} (\mathbf{x} - \mathbf{\mu}) \tag{B.1}$$

The random vector $\mathbf{X}$ has the covariance matrix $\mathbf{\Sigma}$ and the mean vector $\mathbf{\mu}$. The entries of the random vector $\mathbf{Z}$ are uncorrelated, with the standard deviation of one and the mean value of zero. The covariance matrix of $\mathbf{Z}$ is therefore the identity matrix.

B.1 Mahalanobis Transformation is Independent of Type of Distribution

Though often shown in the context of multi-normal distribution, the Mahalanobis transformation is not restricted to any type of distribution. To show this, the proof that the mean vector of $\mathbf{Z}$ is the zero vector and that the covariance matrix of $\mathbf{Z}$ is the identity matrix is given in the following.

Firstly, it is shown that the mean vector of $\mathbf{Z}$ is zero.

$$E(\mathbf{z}) = E\left[\mathbf{\Sigma}^{-\frac{1}{2}}(\mathbf{x}-\mathbf{\mu})\right] = E\left(\mathbf{\Sigma}^{-\frac{1}{2}}\mathbf{x}\right) - E\left(\mathbf{\Sigma}^{-\frac{1}{2}}\mathbf{\mu}\right) = \mathbf{\Sigma}^{-\frac{1}{2}}E(\mathbf{x}) - \mathbf{\Sigma}^{-\frac{1}{2}}\mathbf{\mu} = \mathbf{0} \tag{B.2}$$

Now, the covariance matrix of $\mathbf{Z}$ is determined.

$$\mathbf{\Sigma} = Cov(\mathbf{x}) = Cov\left(\mathbf{\Sigma}^{\frac{1}{2}}\mathbf{z} + \mathbf{\mu}\right) \tag{B.3}$$

With $Cov(\mathbf{A}\mathbf{x}) = \mathbf{A}\,Cov(\mathbf{x})\,\mathbf{A}^T$ and $Cov(\mathbf{x}+\mathbf{b}) = Cov(\mathbf{x})$

$$\mathbf{\Sigma} = Cov\left(\mathbf{\Sigma}^{\frac{1}{2}}\mathbf{z}\right) = \mathbf{\Sigma}^{\frac{1}{2}}\,Cov(\mathbf{z})\,\mathbf{\Sigma}^{\frac{T}{2}} \quad \Leftrightarrow \quad \mathbf{\Sigma}^{-\frac{1}{2}}\mathbf{\Sigma}\,\mathbf{\Sigma}^{-\frac{T}{2}} = Cov(\mathbf{z}) \tag{B.4}$$

With $\mathbf{A} = \mathbf{A}^{\frac{1}{2}}\mathbf{A}^{\frac{T}{2}} \quad \Leftrightarrow \quad \mathbf{A}^{-\frac{1}{2}}\mathbf{A} = \mathbf{A}^{\frac{T}{2}}$

$$\mathbf{\Sigma}^{\frac{T}{2}}\mathbf{\Sigma}^{-\frac{T}{2}} = Cov(\mathbf{z}) = \mathbf{1} \tag{B.5}$$

B.2 The Rank of the Covariance Matrix is Smaller Than or Equal to the Number of Measurements

The covariance of two random parameters is estimated from measurements by

$$\text{cov}\left(X_i, X_j\right) = \Sigma_{ij} = \frac{1}{m-1} \sum_{k=1}^{m} \left(x_i^{(k)} - \mu_i\right)\left(x_j^{(k)} - \mu_j\right) \tag{B.6}$$

Here, m is the number of measurements, $x_i^{(k)}$ is the k-th measurement of i-th random variable. Considering a random vector $\mathbf{X}$ of the length n, the covariance matrix is estimated by

$$\Sigma \simeq \frac{1}{m-1} \sum_{k=1}^{m} \left(\mathbf{x}^{(k)} - \boldsymbol{\mu}\right)\left(\mathbf{x}^{(k)} - \boldsymbol{\mu}\right)^T \tag{B.7}$$

where $\mathbf{x}^{(k)}, \boldsymbol{\mu} \in \mathbb{R}^n$ and $\Sigma \in \mathbb{R}^{n \times n}$. By defining

$$\tilde{\mathbf{X}} = \left(\mathbf{x}^{(1)} - \boldsymbol{\mu}, \ldots, \mathbf{x}^{(k)} - \boldsymbol{\mu}, \ldots, \mathbf{x}^{(m)} - \boldsymbol{\mu}\right) \quad , \qquad \tilde{\mathbf{X}} \in \mathbb{R}^{n \times m} \tag{B.8}$$

the estimator (B.7) can be written as

$$\Sigma = \frac{1}{m-1} \tilde{\mathbf{X}} \, \tilde{\mathbf{X}}^T \tag{B.9}$$

Since

$$rank\left(\tilde{\mathbf{X}}\right) \leq \min\{n, m\} \tag{B.10}$$

and

$$rank\left(\tilde{\mathbf{X}}\right) = rank\left(\tilde{\mathbf{X}} \, \tilde{\mathbf{X}}^T\right) = rank\left(\Sigma\right) \tag{B.11}$$

it follows

$$rank\left(\Sigma\right) \leq \min\{n, m\} \tag{B.12}$$

Since $\Sigma \in \mathbb{R}^{n \times n}$, Σ is singular if $m \leq n$.

B.3 The Matrix B is a Root of the Covariance Matrix

The matrix $\mathbf{B}$ is defined as

$$\mathbf{B} = \mathbf{Q} \, \mathbf{D}^{\frac{1}{2}} = \left(\mathbf{q}_1, \ldots, \mathbf{q}_r\right) diag\left(\sigma_1, \ldots, \sigma_r\right) \tag{B.13}$$

$\mathbf{Q} = (\mathbf{q}_1, \ldots, \mathbf{q}_r)$ is the matrix with eigenvectors of Σ, $\mathbf{D} = diag\left(\sigma_1^2, \ldots, \sigma_r^2\right)$ is a diagonal matrix with the eigenvalues of Σ and r is the rank of Σ. $\mathbf{B}$ is a square root of Σ, because

$$\mathbf{B} \, \mathbf{B}^T = \mathbf{Q} \, \mathbf{D}^{\frac{1}{2}} \left(\mathbf{Q} \, \mathbf{D}^{\frac{1}{2}}\right)^T = \mathbf{Q} \, \mathbf{D}^{\frac{1}{2}} \, \mathbf{D}^{\frac{1}{2}} \, \mathbf{Q}^T = \mathbf{Q} \, \mathbf{D} \, \mathbf{Q}^T = \Sigma \tag{B.14}$$

The inverse of $\mathbf{B}$ is given by

$$\mathbf{B}^{-1} = \Sigma^{-\frac{1}{2}} = \mathbf{D}^{-\frac{1}{2}} \, \mathbf{Q}^T \tag{B.15}$$

since

$$\mathbf{B} \, \mathbf{B}^{-1} = \mathbf{D}^{\frac{1}{2}} \, \mathbf{Q}^T \left(\mathbf{D}^{\frac{1}{2}} \, \mathbf{Q}^T\right)^{-1} = \mathbf{D}^{\frac{1}{2}} \, \mathbf{Q}^T \, \mathbf{Q}^{-T} \, \mathbf{D}^{-\frac{1}{2}} = \mathbf{D}^{\frac{1}{2}} \, \mathbf{D}^{-\frac{1}{2}} = \mathbf{I} \tag{B.16}$$

B.4   Relation to Principal Component Analysis

According to the consideration of section B.3, the Mahalanobis transformation is written as

$$\mathbf{x} = \mathbf{B}\,\mathbf{z} + \boldsymbol{\mu} = \mathbf{Q}\,\mathbf{D}^{\frac{1}{2}}\,\mathbf{z} + \boldsymbol{\mu} \qquad (\text{B.17})$$

In this form, the transformation is similar to the principal component analysis [118], which is given by

$$\mathbf{x} = \mathbf{Q}\,\mathbf{y} + \boldsymbol{\mu} \qquad (\text{B.18})$$

and which is also known as Karhunen-Loève transformation. The entries of the vector $\mathbf{Y}$ are uncorrelated, but their standard deviation is not normalized to one, as it is for the vector $\mathbf{Z}$ given by the Mahalanobis transformation. The idea of the principle component analysis is to find the direction of the largest variance, second largest variance and so on (see Figure B-1, left). The random vector $\mathbf{X}$ is transformed to the random vector $\mathbf{Y}$, whose mean vector equals the zero vector and whose entries are sorted by the variance. This also depicts why $\mathbf{Y}$ must have less entries than the number of measurements. As shown in Figure B-1, right, there is one direction with zero variance, if the number of measurement point equals the dimension of the random vector. Hence, the random vector can be transformed to a vector with one entry less.
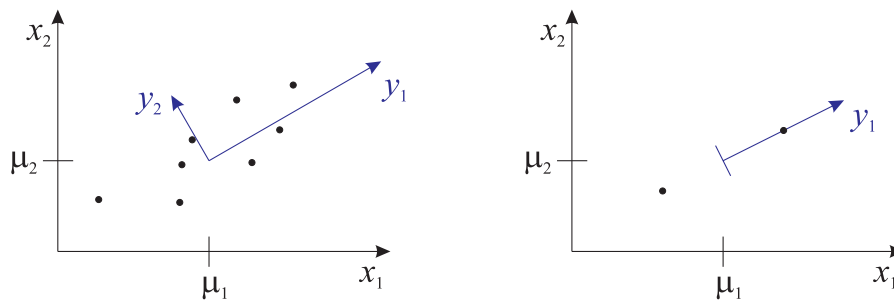
Figure B-1: Idea of principle component analysis

In difference to the PCA, the Mahalanobis transformation additionally scales the coordinates in each direction as shown in Figure B-2, which yields a standard deviation of one in each direction.
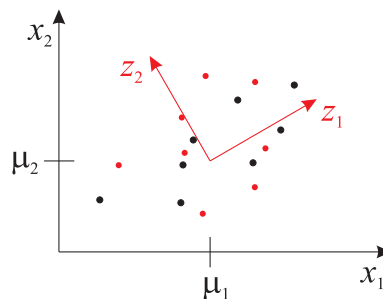
Figure B-2: Geometric interpretation of the Mahalonobis transformation

C   Kolmogorov-Smirnov Test

Within Monte Carlo simulations, realizations of a random number a generated based on an assumed type of distribution. In order to evaluate which type of distribution describes a set a measured data best, the Kolmogorov-Smirnov test (K-S test) [88] can be used. For each

realization x_i the empiric distribution function F_E is compared with the assumed cumulative distribution function F_0. The two distributions are assumed to be different, if the maximal difference between the distributions d_{max} exceeds an allowed value $d_{allowed}$, which depends on the level of significance. Tables for $d_{allowed}$ are for instance given in [88].

$$d_{o,i} = \left| F_E(x_i) - F_0(x_i) \right| \qquad d_{u,i} = \left| F_E(x_{i-1}) - F_0(x_i) \right|$$
$$d_i = \max(d_{o,i}, d_{u,i}) \qquad d_{max} = \max(d_1, \ldots, d_{nm})$$

(C.1)

For the probabilistic analysis of composite cylindrical shells in chapter 6, ten measurement vectors $\mathbf{x}^{(i)}$ with the length 462 are transformed to ten vectors $\mathbf{z}^{(i)}$ with the length nine. The entries of $\mathbf{z}^{(i)}$ are statistically analyzed. Furthermore, the bending angle θ and the average wall thickness t are analyzed. The material properties E_{11}, E_{22} and G_{12} are assumed to be normal distributed, the circumferential variation angle ω is assumed to be uniformly distributed in the interval [0°,360°]. For the K-S test a level of significance of 5 % is chosen, which leads to an allowed difference of $d_{allowed} = 0.41$.

Distribution	Random variables										
	z_1	z_2	z_3	z_4	z_5	z_6	z_7	z_8	z_9	θ	t
Uniform	0.287	0.161	0.342	0.268	0.360	0.280	0.202	0.321	0.217	0.366	0.202
Beta	**0.156**	0.191	0.170	**0.126**	0.201	**0.158**	0.209	0.207	0.179	**0.207**	**0.192**
Normal	0.167	**0.155**	0.144	0.176	0.201	0.192	0.204	0.252	0.128	0.247	0.193
Gumbel	0.161	0.177	0.166	0.209	**0.131**	0.221	**0.183**	**0.204**	0.193	0.307	0.263
Laplace	0.229	0.203	0.157	0.229	0.202	0.242	0.256	0.312	0.140	0.306	0.188
Logistic	0.186	0.172	**0.132**	0.199	0.201	0.214	0.217	0.270	**0.127**	0.264	0.192

Table C-1: d_{max} of the K-S test for the random variables of cylindrical composite shells

In Table C-1 the results of the K-S test for the considered random parameters is shown, where the minimum d_{max} is bold for each random parameter. For the listed types of distribution d_{max} never exceeds $d_{allowed}$, which is caused by the small sample size of the empiric distribution. Distributions that have a domain $[x_0,\infty]$, where x_0 is the lower bound, like the Weibull distribution of the logarithmic normal distribution mostly did not satisfy the K-S test.

Distribution	Random variables							
	z_1	z_2	z_3	z_4	z_5	z_6	z_7	r
Uniform	0.277	0.227	0.538	0.530	0.231	0.334	0.339	0.550
Beta	0.199	0.178	0.292	0.287	0.226	0.225	**0.177**	0.272
Normal	**0.150**	0.166	0.295	0.338	0.179	0.236	0.196	0.346
Gumbel	0.216	**0.163**	0.361	**0.268**	0.172	**0.169**	0.231	0.285
Laplace	0.189	0.215	0.306	0.325	**0.117**	0.252	0.250	0.395
Logistic	0.157	0.178	**0.287**	0.336	0.159	0.239	0.218	0.358
Weibull								**0.250**

Table C-2: d_{max} of the K-S test for the random variables of stiffened composite panels

For the Monte Carlo simulation of stiffened composite panels (see chapter 7) eight measurements of geometry and radius are available. The results of the K-S test of the seven uncorrelated random parameters that describe the scatter of geometry and the K-S test of the normalized radius are given in Table C-2. Choosing a level of significance of 5%, the upper bound for d_{max} is $d_{allowed} = 0.486$.

D   Stochastic Moment Approximation

For the approximation of the stochastic moments of the objective function, the objective function $g(\mathbf{x})$ is approximated at the mean vector of input parameters $\boldsymbol{\mu}$.

$$g(\mathbf{x}) = g(\boldsymbol{\mu}) + \sum_{i=1}^{n} \frac{\partial g(\boldsymbol{\mu})}{\partial x_i}(x_i - \mu_i) + \frac{1}{2}\sum_{i=1}^{n}\sum_{j=1}^{n}\frac{\partial^2 g(\boldsymbol{\mu})}{\partial x_i \, \partial x_j}(x_i - \mu_i)(x_j - \mu_j) + \dots \qquad (D.1)$$

The following abbreviations are used in the following.

$$g_{\boldsymbol{\mu}} = g(\boldsymbol{\mu}) \qquad g_{,i} = \frac{\partial g(\boldsymbol{\mu})}{\partial x_i} \qquad g_{,ij} = \frac{\partial^2 g(\boldsymbol{\mu})}{\partial x_i \, \partial x_j} \qquad (D.2)$$

For the derivation of the stochastic moment approximations, the following introducing remarks are helpful.

The first moment of a random parameter X_i is given by

$$\mu_i = \int_{-\infty}^{\infty} x_i \, f_X(x_i) \, dx_i \qquad (D.3)$$

The k-th central moment of the random parameters X_i is referred to as

$$\mu_{i,k} = \int_{-\infty}^{\infty} (x_i - \mu_i)^k \, f_X(x_i) \, dx_i \qquad (D.4)$$

Note that the first central moment is always equal to one.

$$\mu_{i,1} = \int_{-\infty}^{\infty} (x_i - \mu_X) f_X(x_i) \, dx_i = 0 \qquad (D.5)$$

The joint central moment of the random parameters X_i and X_j is denoted as

$$\mu_{ij} = \int_{-\infty}^{\infty}\int_{-\infty}^{\infty} (x_i - \mu_i)(x_j - \mu_j) f_X(x_i, x_j) \, dx_i \, dx_j \qquad (D.6)$$

If the random parameters X_i are independent, the joint probability density function $f_{\mathbf{X}}(\mathbf{x})$ can be written as product of the PDFs of the random parameters.

$$f_{\mathbf{X}}(\mathbf{x}) = f_1(x_1) \cdot \dots \cdot f_n(x_n) \qquad (D.7)$$

D.1   Mean Value Approximation

The second order approximation of the mean value of the objective function g is give by

$$\mu_g = E\left[g(\mathbf{x})\right] = \int\limits_{-\infty}^{\infty} g(\mathbf{x}) f_{\mathbf{X}}(\mathbf{x}) \, d\mathbf{x}$$

$$\approx \int\limits_{-\infty}^{\infty} \left[g_{\boldsymbol{\mu}} + \sum_{i=1}^{n} g_{,i}\left(x_i - \mu_i\right) + \frac{1}{2}\sum_{i=1}^{n}\sum_{j=1}^{n} g_{,ij}\left(x_i - \mu_i\right)\left(x_j - \mu_j\right) \right] f_{\mathbf{X}}(\mathbf{x}) \, d\mathbf{x} \qquad \text{(D.8)}$$

$$\mu_g \approx \int\limits_{-\infty}^{\infty} g_{\boldsymbol{\mu}} \, f(\mathbf{x}) \, d\mathbf{x} + \int\limits_{-\infty}^{\infty} \sum_{i=1}^{n} \frac{\partial g(\boldsymbol{\mu})}{\partial x_i}\left(x_i - \mu_i\right) f_{\mathbf{X}}(\mathbf{x}) \, d\mathbf{x}$$

$$+ \int\limits_{-\infty}^{\infty} \frac{1}{2}\sum_{i=1}^{n}\sum_{j=1}^{n} g_{,ij}\left(x_i - \mu_i\right)\left(x_j - \mu_j\right) f_{\mathbf{X}}(\mathbf{x}) \, d\mathbf{x}$$

$$\approx g_{\boldsymbol{\mu}} \underbrace{\int\limits_{-\infty}^{\infty} f_{\mathbf{X}}(\mathbf{x}) \, d\mathbf{x}}_{1} + \sum_{i=1}^{n} g_{,i} \underbrace{\int\limits_{-\infty}^{\infty} \left(x_i - \mu_i\right) f_{\mathbf{X}}(\mathbf{x}) \, d\mathbf{x}}_{0} \qquad \text{(D.9)}$$

$$+ \frac{1}{2}\sum_{i=1}^{n}\sum_{j=1}^{n} g_{,ij} \underbrace{\int\limits_{-\infty}^{\infty} \left(x_i - \mu_i\right)\left(x_j - \mu_j\right) f_{\mathbf{X}}(\mathbf{x}) \, d\mathbf{x}}_{\mu_{ij}}$$

$$\mu_g \approx g_{\boldsymbol{\mu}} + \frac{1}{2}\sum_{i=1}^{n}\sum_{j=1}^{n} g_{,ij}\, \mu_{ij} \qquad \text{(D.10)}$$

Assuming independence for the random parameters yields

$$\mu_g \approx g_{\boldsymbol{\mu}} + \frac{1}{2}\sum_{i=1}^{n} g_{,ii}\, \mu_{i,2} \qquad \text{(D.11)}$$

and the first order approximation equals

$$\mu_g \approx g_{\boldsymbol{\mu}} \qquad \text{(D.12)}$$

D.2 *Variance Approximation*

Inserting the second order Taylor series into the definition of the variance of *g* yields

$$\sigma_g^2 = E\left(\left[g(\mathbf{x}) - \mu_g\right]^2\right) \overset{\text{Computational formula for the variance}}{=} E\left(g^2(\mathbf{x})\right) - \mu_g^2$$

$$= \int\limits_{-\infty}^{\infty} g^2(\mathbf{x}) f_{\mathbf{X}}(\mathbf{x}) \, d\mathbf{x} - \mu_g^2 \qquad \text{(D.13)}$$

$$\approx \int\limits_{-\infty}^{\infty} \left[g_{\boldsymbol{\mu}} + \sum_{i=1}^{n} g_{,i}\left(x_i - \mu_i\right) + \frac{1}{2}\sum_{i=1}^{n}\sum_{j=1}^{n} g_{,ij}\left(x_i - \mu_i\right)\left(x_j - \mu_j\right) \right]^2 f_{\mathbf{X}}(\mathbf{x}) \, d\mathbf{x} - \mu_g^2$$

The squared Taylor series is

$$\left[g_{\boldsymbol{\mu}} + \sum_{i=1}^{n} g_{,i} \left(x_i - \mu_i \right) + \frac{1}{2} \sum_{i=1}^{n} \sum_{j=1}^{n} g_{,ij} \left(x_i - \mu_i \right) \left(x_j - \mu_j \right) \right]^2$$

$$= \underbrace{g_{\boldsymbol{\mu}}^2}_{I} + \underbrace{\left[\sum_{i=1}^{n} g_{,i} \left(x_i - \mu_i \right) \right]^2}_{II} + \underbrace{\frac{1}{4} \left[\sum_{i=1}^{n} \sum_{j=1}^{n} g_{,ij} \left(x_i - \mu_i \right) \left(x_j - \mu_j \right) \right]^2}_{III} + \underbrace{2 g_{\boldsymbol{\mu}} \sum_{i=1}^{n} g_{,i} \left(x_i - \mu_i \right)}_{IV} \quad \text{(D.14)}$$

$$+ \underbrace{g_{\boldsymbol{\mu}} \sum_{i=1}^{n} \sum_{j=1}^{n} g_{,ij} \left(x_i - \mu_i \right) \left(x_j - \mu_j \right)}_{V} + \underbrace{\left[\sum_{i=1}^{n} g_{,i} \left(x_i - \mu_i \right) \right] \left[\sum_{i=1}^{n} \sum_{j=1}^{n} g_{,ij} \left(x_i - \mu_i \right) \left(x_j - \mu_j \right) \right]}_{VI}$$

The summands in (D.14) can be integrated individually.

I:
$$\int_{-\infty}^{\infty} g_{\boldsymbol{\mu}}^2 \, f_{\mathbf{X}} \left(\mathbf{x} \right) d\mathbf{x} = g_{\boldsymbol{\mu}}^2 \underbrace{\int_{-\infty}^{\infty} f_{\mathbf{X}} \left(\mathbf{x} \right) d\mathbf{x}}_{1} = g_{\boldsymbol{\mu}}^2 \quad \text{(D.15)}$$

II:
$$\left[\sum_{i=1}^{n} g_{,i} \left(x_i - \mu_i \right) \right]^2 = \sum_{i=1}^{n} \sum_{j=1}^{n} g_{,i} \, g_{,j} \left(x_i - \mu_i \right) \left(x_j - \mu_j \right) \quad \text{(D.16)}$$

$$\int_{-\infty}^{\infty} \sum_{i=1}^{n} \sum_{j=1}^{n} g_{,i} \, g_{,j} \left(x_i - \mu_i \right) \left(x_j - \mu_j \right) f \left(\mathbf{x} \right) d\mathbf{x} = \sum_{i=1}^{n} \sum_{j=1}^{n} g_{,i} \, g_{,j} \underbrace{\int_{-\infty}^{\infty} \left(x_i - \mu_i \right) \left(x_j - \mu_j \right) f \left(\mathbf{x} \right) d\mathbf{x}}_{\mu_{ij}} \quad \text{(D.17)}$$

III:
$$\left[\sum_{i=1}^{n} \sum_{j=1}^{n} g_{,ij} \left(x_i - \mu_i \right) \left(x_j - \mu_j \right) \right]^2$$
$$= \sum_{i=1}^{n} \sum_{j=1}^{n} \sum_{k=1}^{n} \sum_{l=1}^{n} g_{,ij} \, g_{,kl} \left(x_i - \mu_i \right) \left(x_j - \mu_j \right) \left(x_k - \mu_k \right) \left(x_l - \mu_l \right) \quad \text{(D.18)}$$

$$\int_{-\infty}^{\infty} \frac{1}{4} \left[\sum_{i=1}^{n} \sum_{j=1}^{n} g_{,ij} \left(x_i - \mu_i \right) \left(x_j - \mu_j \right) \right]^2 f_{\mathbf{X}} \left(\mathbf{x} \right) d\mathbf{x}$$
$$= \frac{1}{4} \int_{-\infty}^{\infty} \sum_{i=1}^{n} \sum_{j=1}^{n} \sum_{k=1}^{n} \sum_{l=1}^{n} g_{,ij} \, g_{,kl} \left(x_i - \mu_i \right) \left(x_j - \mu_j \right) \left(x_k - \mu_k \right) \left(x_l - \mu_l \right) f_{\mathbf{X}} \left(\mathbf{x} \right) d\mathbf{x} \quad \text{(D.19)}$$
$$= \frac{1}{4} \sum_{i=1}^{n} \sum_{j=1}^{n} \sum_{k=1}^{n} \sum_{l=1}^{n} g_{,ij} \, g_{,kl} \underbrace{\int_{-\infty}^{\infty} \left(x_i - \mu_i \right) \left(x_j - \mu_j \right) \left(x_k - \mu_k \right) \left(x_l - \mu_l \right) f_{\mathbf{X}} \left(\mathbf{x} \right) d\mathbf{x}}_{\mu_{ijkl}}$$

IV:
$$\int_{-\infty}^{\infty} 2 g_{\boldsymbol{\mu}} \sum_{i=1}^{n} g_{,i} \left(x_i - \mu_i \right) f_{\mathbf{X}} \left(\mathbf{x} \right) d\mathbf{x} = 2 g_{\boldsymbol{\mu}} \sum_{i=1}^{n} g_{,i} \underbrace{\int_{-\infty}^{\infty} \left(x_i - \mu_i \right) f_{\mathbf{X}} \left(\mathbf{x} \right) d\mathbf{x}}_{0} = 0 \quad \text{(D.20)}$$

V:
$$\int_{-\infty}^{\infty} g_{\boldsymbol{\mu}} \sum_{i=1}^{n} \sum_{j=1}^{n} g_{,ij} \left(x_i - \mu_i \right) \left(x_j - \mu_j \right) f_{\mathbf{X}} \left(\mathbf{x} \right) d\mathbf{x}$$
$$= g_{\boldsymbol{\mu}} \sum_{i=1}^{n} \sum_{j=1}^{n} g_{,ij} \underbrace{\int_{-\infty}^{\infty} \left(x_i - \mu_i \right) \left(x_j - \mu_j \right) f_{\mathbf{X}} \left(\mathbf{x} \right) d\mathbf{x}}_{\mu_{ij}} \quad \text{(D.21)}$$

$$\int_{-\infty}^{\infty} \left[\sum_{i=1}^{n} g_{,i} \left(x_i - \mu_i \right) \right] \left[\sum_{i=1}^{n} \sum_{j=1}^{n} g_{,ij} \left(x_i - \mu_i \right) \left(x_j - \mu_j \right) \right] f_{\mathbf{X}} \left(\mathbf{x} \right) d\mathbf{x}$$

$$VI: \quad = \int_{-\infty}^{\infty} \sum_{i=1}^{n} \sum_{j=1}^{n} \sum_{k=1}^{n} g_{,i} \, g_{,jk} \left(x_i - \mu_i \right) \left(x_j - \mu_j \right) \left(x_k - \mu_k \right) f_{\mathbf{X}} \left(\mathbf{x} \right) d\mathbf{x} \qquad (D.22)$$

$$= \sum_{i=1}^{n} \sum_{j=1}^{n} \sum_{k=1}^{n} g_{,i} \, g_{,jk} \underbrace{\int_{-\infty}^{\infty} \left(x_i - \mu_i \right) \left(x_j - \mu_j \right) \left(x_k - \mu_k \right) f_{\mathbf{X}} \left(\mathbf{x} \right) d\mathbf{x}}_{\mu_{ijk}}$$

Summarized (D.13) can be written as

$$\sigma_g^2 \approx \underbrace{g_{\boldsymbol{\mu}}^2}_{I} + \underbrace{\sum_{i=1}^{n} \sum_{j=1}^{n} g_{,i} \, g_{,j} \, \mu_{ij}}_{II} + \underbrace{\frac{1}{4} \sum_{i=1}^{n} \sum_{j=1}^{n} \sum_{k=1}^{n} \sum_{l=1}^{n} g_{,ij} \, g_{,kl} \, \mu_{ijkl}}_{III}$$

$$+ \underbrace{g_{\boldsymbol{\mu}} \sum_{i=1}^{n} \sum_{j=1}^{n} g_{,ij} \, \mu_{ij}}_{V} + \underbrace{\sum_{i=1}^{n} \sum_{j=1}^{n} \sum_{k=1}^{n} g_{,i} \, g_{,jk} \, \mu_{ijk}}_{VI} - \mu_g^2 \qquad (D.23)$$

Assuming independence, the summands can be simplified further

$$\frac{1}{4} \sum_{i=1}^{n} \sum_{j=1}^{n} \sum_{k=1}^{n} \sum_{l=1}^{n} g_{,ij} \, g_{,kl} \, \mu_{ijkl} = \underbrace{\frac{1}{4} \sum_{i=1}^{n} \sum_{k=1}^{n} g_{,ii} \, g_{,kk} \, \mu_{i,2} \, \mu_{k,2}}_{i=j \neq k=l} + \underbrace{\frac{1}{4} \sum_{i=1}^{n} \sum_{j=1}^{n} g_{,ij}^2 \, \mu_{i,2} \, \mu_{j,2}}_{i=k \neq j=l}$$

$$III: \qquad + \underbrace{\frac{1}{4} \sum_{i=1}^{n} \sum_{j=1}^{n} g_{,ij}^2 \, \mu_{i,2} \, \mu_{j,2}}_{i=l \neq j=k} + \underbrace{\frac{1}{4} \sum_{i=1}^{n} g_{,ii}^2 \, \mu_{i,4}}_{i=j=k=l} \qquad (D.24)$$

$$= \frac{1}{4} \sum_{i=1}^{n} \sum_{\substack{j=1 \\ j \neq i}}^{n} g_{,ii} \, g_{,jj} \, \mu_{i,2} \, \mu_{j,2} + \frac{1}{2} \sum_{i=1}^{n} \sum_{\substack{j=1 \\ j \neq i}}^{n} g_{,ij}^2 \, \mu_{i,2} \, \mu_{j,2} + \frac{1}{4} \sum_{i=1}^{n} g_{,ii}^2 \, \mu_{i,4}$$

and the approximation of the variance is given by

$$\sigma_g^2 \approx g_{\boldsymbol{\mu}}^2 + \sum_{i=1}^{n} g_{,i}^2 \, \mu_{i,2} + \frac{1}{4} \sum_{i=1}^{n} g_{,ii}^2 \, \mu_{i,4} + g_{\boldsymbol{\mu}} \sum_{i=1}^{n} g_{,ii} \, \mu_{i,2} + \sum_{i=1}^{n} g_{,i} \, g_{,ii} \, \mu_{i,3}$$

$$+ \frac{1}{2} \sum_{i=1}^{n} \sum_{j=1}^{n} g_{,ii} \, g_{,jj} \, \mu_{i,2} \, \mu_{j,2} + \sum_{i=1}^{n} \sum_{j=i+1}^{n} g_{,ij}^2 \, \mu_{i,2} \, \mu_{j,2} - \mu_g^2 \qquad (D.25)$$

Sorted by approximations, the second order approximation of the variance of g equals

$$\sigma_g^2 \approx \underbrace{\sum_{i=1}^{n} g_{,i}^2 \, \mu_{i,2}}_{FOSM} + \underbrace{g_{\boldsymbol{\mu}}^2 - \mu_g^2 + g_{\boldsymbol{\mu}} \sum_{i=1}^{n} g_{,ii} \, \mu_{i,2} + \sum_{i=1}^{n} g_{,i} \, g_{,ii} \, \mu_{i,3}}_{SOTM}$$

$$+ \underbrace{\frac{1}{4} \sum_{i=1}^{n} g_{,ii}^2 \, \mu_{i,4} + \frac{1}{2} \sum_{i=1}^{n} \sum_{j=i+1}^{n} g_{,ii} \, g_{,jj} \, \mu_{i,2} \, \mu_{j,2}}_{incomplete\ second\ order} + \underbrace{\sum_{i=1}^{n} \sum_{j=i+1}^{n} g_{,ij}^2 \, \mu_{i,2} \, \mu_{j,2}}_{full\ approach} \qquad (D.26)$$

and the first order is given by

$$\sigma_g^2 \approx \sum_{i=1}^{n} g_{,i}^2 \, \mu_{i,2} \qquad (D.27)$$

D.3 Covariance Approximation

Two objective functions, $g(\mathbf{x})$ and $h(\mathbf{x})$, are considered, which are both approximated by Taylor series at the mean vector $\boldsymbol{\mu}$. Their covariance is given by

$$\Sigma_{gh} = E\left(\left[g(\mathbf{x}) - \mu_g\right]\left[h(\mathbf{x}) - \mu_h\right]\right) = \int_{-\infty}^{\infty}\left[g(\mathbf{x}) - \mu_g\right]\left[h(\mathbf{x}) - \mu_h\right]f_{\mathbf{X}}(\mathbf{x})\,d\mathbf{x}$$

$$\approx \int_{-\infty}^{\infty}\left[g_{\boldsymbol{\mu}} + \sum_{i=1}^{n}g_{,i}(x_i - \mu_i) + \frac{1}{2}\sum_{i=1}^{n}\sum_{j=1}^{n}g_{,ij}(x_i - \mu_i)(x_j - \mu_j) - \mu_g\right] \quad\text{(D.28)}$$

$$\cdot\left[h_{\boldsymbol{\mu}} + \sum_{i=1}^{n}h_{,i}(x_i - \mu_i) + \frac{1}{2}\sum_{i=1}^{n}\sum_{j=1}^{n}h_{,ij}(x_i - \mu_i)(x_j - \mu_j) - \mu_h\right]f_{\mathbf{X}}(\mathbf{x})\,d\mathbf{x}$$

Expanding the product yields

$$\Sigma_{gh} \approx \int_{-\infty}^{\infty}\Bigg[g_{\boldsymbol{\mu}}\,h_{\boldsymbol{\mu}} + g_{\boldsymbol{\mu}}\sum_{i=1}^{n}h_{,i}(x_i - \mu_i) + \frac{1}{2}g_{\boldsymbol{\mu}}\sum_{i=1}^{n}\sum_{j=1}^{n}h_{,ij}(x_i - \mu_i)(x_j - \mu_j) - g_{\boldsymbol{\mu}}\,\mu_h$$

$$+ h_{\boldsymbol{\mu}}\sum_{i=1}^{n}g_{,i}(x_i - \mu_i) + \sum_{i=1}^{n}\sum_{j=1}^{n}g_{,i}\,h_{,j}(x_i - \mu_i)(x_j - \mu_j)$$

$$+ \frac{1}{2}\sum_{i=1}^{n}\sum_{j=1}^{n}\sum_{k=1}^{n}g_{,i}\,h_{jk}(x_i - \mu_i)(x_j - \mu_j)(x_k - \mu_k) - \mu_h\sum_{i=1}^{n}g_{,i}(x_i - \mu_i)$$

$$+ h_{\boldsymbol{\mu}}\frac{1}{2}\sum_{i=1}^{n}\sum_{j=1}^{n}g_{,ij}(x_i - \mu_i)(x_j - \mu_j)$$

$$+ \frac{1}{2}\sum_{i=1}^{n}\sum_{j=1}^{n}\sum_{k=1}^{n}g_{,ij}\,h_{,k}(x_i - \mu_i)(x_j - \mu_j)(x_k - \mu_k)$$

$$+ \frac{1}{4}\sum_{i=1}^{n}\sum_{j=1}^{n}\sum_{k=1}^{n}\sum_{l=1}^{n}g_{,ij}\,h_{,kl}(x_i - \mu_i)(x_j - \mu_j)(x_k - \mu_k)(x_l - \mu_l)$$

$$- \mu_h\frac{1}{2}\sum_{i=1}^{n}\sum_{j=1}^{n}g_{,ij}(x_i - \mu_i)(x_j - \mu_j) - \mu_g\,h_{\boldsymbol{\mu}} - \mu_g\sum_{i=1}^{n}h_{,i}(x_i - \mu_i)$$

$$- \mu_g\frac{1}{2}\sum_{i=1}^{n}\sum_{j=1}^{n}h_{,ij}(x_i - \mu_i)(x_j - \mu_j) + \mu_g\,\mu_h\Bigg]f_{\mathbf{X}}(\mathbf{x})\,d\mathbf{x} \quad\text{(D.29)}$$

Taking the integral into the sum and introducing the stochastic moments yields

$$\Sigma_{gh} \approx g_{\boldsymbol{\mu}} \, h_{\boldsymbol{\mu}} - g_{\boldsymbol{\mu}} \, \mu_h - \mu_g \, h_{\boldsymbol{\mu}} + \mu_g \, \mu_h$$

$$+ g_{\boldsymbol{\mu}} \sum_{i=1}^{n} h_{,i} \underbrace{\int_{-\infty}^{\infty} (x_i - \mu_i) \, f_{\mathbf{X}}(\mathbf{x}) \, d\mathbf{x}}_{0} - \mu_h \sum_{i=1}^{n} g_{,i} \underbrace{\int_{-\infty}^{\infty} (x_i - \mu_i) \, f_{\mathbf{X}}(\mathbf{x}) \, d\mathbf{x}}_{0}$$

$$+ h_{\boldsymbol{\mu}} \sum_{i=1}^{n} g_{,i} \underbrace{\int_{-\infty}^{\infty} (x_i - \mu_i) \, f_{\mathbf{X}}(\mathbf{x}) \, d\mathbf{x}}_{0} - \mu_g \sum_{i=1}^{n} h_{,i} \underbrace{\int_{-\infty}^{\infty} (x_i - \mu_i) \, f_{\mathbf{X}}(\mathbf{x}) \, d\mathbf{x}}_{0}$$

$$+ \sum_{i=1}^{n} \sum_{j=1}^{n} g_{,i} \, h_{,j} \underbrace{\int_{-\infty}^{\infty} (x_i - \mu_i)(x_j - \mu_j) \, f_{\mathbf{X}}(\mathbf{x}) \, d\mathbf{x}}_{\mu_{ij}}$$

$$+ \frac{1}{2} g_{\boldsymbol{\mu}} \sum_{i=1}^{n} \sum_{j=1}^{n} h_{,ij} \underbrace{\int_{-\infty}^{\infty} (x_i - \mu_i)(x_j - \mu_j) \, f_{\mathbf{X}}(\mathbf{x}) \, d\mathbf{x}}_{\mu_{ij}}$$

$$+ \frac{1}{2} h_{\boldsymbol{\mu}} \sum_{i=1}^{n} \sum_{j=1}^{n} g_{,ij} \underbrace{\int_{-\infty}^{\infty} (x_i - \mu_i)(x_j - \mu_j) \, f_{\mathbf{X}}(\mathbf{x}) \, d\mathbf{x}}_{\mu_{ij}}$$

$$- \frac{1}{2} \mu_h \sum_{i=1}^{n} \sum_{j=1}^{n} g_{,ij} \underbrace{\int_{-\infty}^{\infty} (x_i - \mu_i)(x_j - \mu_j) \, f_{\mathbf{X}}(\mathbf{x}) \, d\mathbf{x}}_{\mu_{ij}}$$

$$- \frac{1}{2} \mu_g \sum_{i=1}^{n} \sum_{j=1}^{n} h_{,ij} \underbrace{\int_{-\infty}^{\infty} (x_i - \mu_i)(x_j - \mu_j) \, f_{\mathbf{X}}(\mathbf{x}) \, d\mathbf{x}}_{\mu_{ij}}$$

$$+ \frac{1}{2} \sum_{i=1}^{n} \sum_{j=1}^{n} \sum_{k=1}^{n} g_{,i} \, h_{jk} \underbrace{\int_{-\infty}^{\infty} (x_i - \mu_i)(x_j - \mu_j)(x_k - \mu_k) \, f_{\mathbf{X}}(\mathbf{x}) \, d\mathbf{x}}_{\mu_{ij}}$$

$$+ \frac{1}{2} \sum_{i=1}^{n} \sum_{j=1}^{n} \sum_{k=1}^{n} g_{,ij} \, h_{,k} \underbrace{\int_{-\infty}^{\infty} (x_i - \mu_i)(x_j - \mu_j)(x_k - \mu_k) \, f_{\mathbf{X}}(\mathbf{x}) \, d\mathbf{x}}_{\mu_{ij}}$$

$$+ \frac{1}{4} \sum_{i=1}^{n} \sum_{j=1}^{n} \sum_{k=1}^{n} \sum_{l=1}^{n} g_{,ij} \, h_{,kl} \underbrace{\int_{-\infty}^{\infty} (x_i - \mu_i)(x_j - \mu_j)(x_k - \mu_k)(x_l - \mu_l) \, f_{\mathbf{X}}(\mathbf{x}) \, d\mathbf{x}}_{\mu_{ijkl}} \tag{D.30}$$

which can be simplified to

$$\Sigma_{gh} \approx g_{\boldsymbol{\mu}} \, h_{\boldsymbol{\mu}} - \mu_g \, h_{\boldsymbol{\mu}} - g_{\boldsymbol{\mu}} \, \mu_h + \mu_g \, \mu_h + \sum_{i=1}^{n} \sum_{j=1}^{n} g_{,i} \, h_{,j} \, \mu_{ij}$$

$$+ \frac{1}{2} \left(g_{\boldsymbol{\mu}} - \mu_g \right) \sum_{i=1}^{n} \sum_{j=1}^{n} h_{,ij} \, \mu_{ij} + \frac{1}{2} \left(h_{\boldsymbol{\mu}} - \mu_h \right) \sum_{i=1}^{n} \sum_{j=1}^{n} g_{,ij} \, \mu_{ij} \tag{D.31}$$

$$+ \frac{1}{2} \sum_{i=1}^{n} \sum_{j=1}^{n} \sum_{k=1}^{n} g_{,i} \, h_{jk} \, \mu_{ijk} + \frac{1}{2} \sum_{i=1}^{n} \sum_{j=1}^{n} \sum_{k=1}^{n} g_{,ij} \, h_{,k} \, \mu_{ijk} + \frac{1}{4} \sum_{i=1}^{n} \sum_{j=1}^{n} \sum_{k=1}^{n} \sum_{l=1}^{n} g_{,ij} \, h_{,kl} \, \mu_{ijkl}$$

Assuming independence for the entries of $\mathbf{X}$ yields

$$\Sigma_{gh} \approx g_\mu h_\mu - \mu_g h_\mu - g_\mu \mu_h + \mu_g \mu_h + \sum_{i=1}^{n} g_{,i} h_{,i} \mu_{i,2}$$
$$+ \frac{1}{2}\left(g_\mu - \mu_g\right)\sum_{i=1}^{n} h_{,ii} \mu_{i,2} + \frac{1}{2}\left(h_\mu - \mu_h\right)\sum_{i=1}^{n} g_{,ii} \mu_{i,2}$$
$$+ \frac{1}{2}\sum_{i=1}^{n} g_{,i} h_{,ii} \mu_{i,3} + \frac{1}{2}\sum_{i=1}^{n} g_{,ii} h_{,i} \mu_{i,3} \tag{D.32}$$
$$+ \frac{1}{4}\sum_{i=1}^{n}\sum_{\substack{j=1 \\ j\neq i}}^{n} g_{,ii} h_{,jj} \mu_{i,2} \mu_{j,2} + \frac{1}{2}\sum_{i=1}^{n}\sum_{\substack{j=1 \\ j\neq i}}^{n} g_{,ij} h_{,ij} \mu_{i,2} \mu_{j,2} + \frac{1}{4}\sum_{i=1}^{n} g_{,ii} h_{,ii} \mu_{i,4}$$

Sorted by approximations, the covariance of g and h is given by

$$\Sigma_{gh} \approx \sum_{i=1}^{n} g_{,i} h_{,i} \mu_{i,2} \Bigg\} \text{first order approach}$$

$$+ g_\mu h_\mu - \mu_g h_\mu - g_\mu \mu_h + \mu_g \mu_h + \frac{1}{2}\left(g_\mu - \mu_g\right)\sum_{i=1}^{n} h_{,ii} \mu_{i,2}$$
$$+ \frac{1}{2}\left(h_\mu - \mu_h\right)\sum_{i=1}^{n} g_{,ii} \mu_{i,2} + \frac{1}{2}\sum_{i=1}^{n} g_{,i} h_{,ii} \mu_{i,3} + \frac{1}{2}\sum_{i=1}^{n} g_{,ii} h_{,i} \mu_{i,3} \Bigg\} \text{ISOA} \tag{D.33}$$
$$+ \frac{1}{4}\sum_{i=1}^{n}\sum_{\substack{j=1 \\ j\neq i}}^{n} g_{,ii} h_{,jj} \mu_{i,2} \mu_{j,2} + \frac{1}{4}\sum_{i=1}^{n} g_{,ii} h_{,ii} \mu_{i,4}$$

$$+ \frac{1}{2}\sum_{i=1}^{n}\sum_{\substack{j=1 \\ j\neq i}}^{n} g_{,ij} h_{,ij} \mu_{i,2} \mu_{j,2} \Bigg\} \text{full second order approach}$$

and the first order approach is given by

$$\Sigma_{gh} \approx \sum_{i=1}^{n} g_{,i} h_{,i} \mu_{i,2} \tag{D.34}$$

D.4 Skewness Approximation

The skewness of the objective function g is given by

$$v_g = \frac{\mu_{g,3}}{\sigma_g^3} \tag{D.35}$$

and can hence be determined from the variance and third central moment of g, which is given by

$$\mu_{g,3} = E\left(\left[g(\mathbf{x}) - \mu_g\right]^3\right) = \int_{-\infty}^{\infty} \left[g(\mathbf{x}) - \mu_g\right]^3 f_{\mathbf{X}}(\mathbf{x}) \, d\mathbf{x}$$

$$= \int_{-\infty}^{\infty} \left[g^3(\mathbf{x}) - 3g^2(\mathbf{x})\mu_g + 3g(\mathbf{x})\mu_g^2 - \mu_g^3\right] f_{\mathbf{X}}(\mathbf{x}) \, d\mathbf{x}$$

$$= \int_{-\infty}^{\infty} g^3(\mathbf{x}) f_{\mathbf{X}}(\mathbf{x}) \, d\mathbf{x} - 3\mu_g \int_{-\infty}^{\infty} g^2(\mathbf{x}) f_{\mathbf{X}}(\mathbf{x}) \, d\mathbf{x} \qquad \text{(D.36)}$$

$$+ 3\mu_g^2 \underbrace{\int_{-\infty}^{\infty} g(\mathbf{x}) f_{\mathbf{X}}(\mathbf{x}) \, d\mathbf{x}}_{\mu_g} - \mu_g^3 \underbrace{\int_{-\infty}^{\infty} f_{\mathbf{X}}(\mathbf{x}) \, d\mathbf{x}}_{1}$$

$$= \int_{-\infty}^{\infty} g^3(\mathbf{x}) f_{\mathbf{X}}(\mathbf{x}) \, d\mathbf{x} - 3\mu_g \int_{-\infty}^{\infty} g^2(\mathbf{x}) f_{\mathbf{X}}(\mathbf{x}) \, d\mathbf{x} + 2\mu_g^3$$

With

$$\sigma_g^2 = \int_{-\infty}^{\infty} g^2(\mathbf{x}) f(\mathbf{x}) \, d\mathbf{x} - \mu_g^2 \Leftrightarrow \int_{-\infty}^{\infty} g^2(\mathbf{x}) f(\mathbf{x}) \, d\mathbf{x} = \sigma_g^2 + \mu_g^2 \qquad \text{(D.37)}$$

inserted into (D.36), the third central moment is given by

$$\mu_{g,3} = \int_{-\infty}^{\infty} g^3(\mathbf{x}) f_{\mathbf{X}}(\mathbf{x}) \, d\mathbf{x} - 3\mu_g \left(\sigma_g^2 + \mu_g^2\right) + 2\mu_g^3$$

$$= \int_{-\infty}^{\infty} g^3(\mathbf{x}) f_{\mathbf{X}}(\mathbf{x}) \, d\mathbf{x} - 3\mu_g \sigma_g^2 - \mu_g^3 \qquad \text{(D.38)}$$

Inserting the Taylor series (D.1) into the first term of (D.38) yields

$$\int_{-\infty}^{\infty} g^3(\mathbf{x}) f_{\mathbf{X}}(\mathbf{x}) \, d\mathbf{x} \approx \int_{-\infty}^{\infty} \left[\underbrace{g_{\boldsymbol{\mu}}}_{a} + \underbrace{\sum_{i=1}^{n} g_{,i}(x_i - \mu_i)}_{b}\right.$$

$$\left. + \underbrace{\frac{1}{2} \sum_{i=1}^{n} \sum_{j=1}^{n} g_{,ij}(x_i - \mu_i)(x_j - \mu_j)}_{c}\right]^3 f_{\mathbf{X}}(\mathbf{x}) \, d\mathbf{x} \qquad \text{(D.39)}$$

With the introduced abbreviations a, b and c, the sum that has to be integrated reads

$$[a + b + c]^3 = a^3 + b^3 + c^3 + 3a^2b + 3a^2c + 3b^2a + 3b^2c + 3c^2a + 3c^2b + 6abc \qquad \text{(D.40)}$$

Each term of the sum is multiplied with $f_{\mathbf{X}}(\mathbf{x})$ and integrated individually in the following. Furthermore, the assumption of independence of the entries of $\mathbf{X}$ is introduced from the beginning.

a^3:
$$\int_{-\infty}^{\infty} g_{\boldsymbol{\mu}}^3 f_{\mathbf{X}}(\mathbf{x}) \, d\mathbf{x} = g_{\boldsymbol{\mu}}^3 \qquad \text{(D.41)}$$

$$\int_{-\infty}^{\infty}\left[\sum_{i=1}^{n}g_{,i}\left(x_i-\mu_i\right)\right]^3 f_{\mathbf{X}}\left(\mathbf{x}\right)d\mathbf{x}$$

b^3:
$$=\sum_{i=1}^{n}\sum_{j=1}^{n}\sum_{k=1}^{n}g_{,i}\,g_{,j}\,g_{,k}\int_{-\infty}^{\infty}\left(x_i-\mu_i\right)\left(x_j-\mu_j\right)\left(x_k-\mu_k\right)f_{\mathbf{X}}\left(\mathbf{x}\right)d\mathbf{x} \tag{D.42}$$

$$\underset{\text{independence}}{=}\sum_{i=1}^{n}g_{,i}^3\,\mu_{i,3}$$

$$\int_{-\infty}^{\infty}\left[\frac{1}{2}\sum_{i=1}^{n}\sum_{j=1}^{n}g_{,ij}\left(x_i-\mu_i\right)\left(x_j-\mu_j\right)\right]^3 f_{\mathbf{X}}\left(\mathbf{x}\right)d\mathbf{x}$$

$$=\frac{1}{8}\sum_{i=1}^{n}\sum_{j=1}^{n}\sum_{k=1}^{n}\sum_{l=1}^{n}\sum_{m=1}^{n}\sum_{p=1}^{n}g_{,ij}\,g_{,kl}\,g_{,mp}\int_{-\infty}^{\infty}\left(x_i-\mu_i\right)\left(x_j-\mu_j\right)$$
$$\cdot\left(x_k-\mu_k\right)\left(x_l-\mu_l\right)\left(x_m-\mu_m\right)\left(x_p-\mu_p\right)f_{\mathbf{X}}\left(\mathbf{x}\right)d\mathbf{x}$$

$$=\frac{1}{8}\sum_{i=1}^{n}\sum_{j=1}^{n}\sum_{k=1}^{n}\sum_{l=1}^{n}\sum_{m=1}^{n}\sum_{p=1}^{n}g_{,ij}\,g_{,kl}\,g_{,mp}\,\mu_{ijklmp}$$

$$\underset{\text{independence}}{=}\frac{1}{8}\left[\underbrace{\sum_{i=1}^{n}\sum_{k=1}^{n}\sum_{m=1}^{n}g_{,ii}\,g_{,kk}\,g_{,mm}\,\mu_{i,2}\,\mu_{k,2}\,\mu_{m,2}}_{\text{for }i=j\neq k=l\neq m=p}+6\underbrace{\sum_{i=1}^{n}\sum_{k=1}^{n}\sum_{l=1}^{n}g_{,ii}\,g_{,kl}^2\,\mu_{i,2}\,\mu_{k,2}\,\mu_{l,2}}_{\text{for }i=j\neq k=m\neq l=p}\right.$$

$$+3\underbrace{\sum_{i=1}^{n}\sum_{j=1}^{n}\sum_{l=1}^{n}g_{,ij}\,g_{,il}\,g_{,jl}\,\mu_{i,2}\,\mu_{j,2}\,\mu_{l,2}}_{\text{for }i=k\neq j=m\neq l=p}+6\underbrace{\sum_{i=1}^{n}\sum_{l=1}^{n}g_{,ii}\,g_{,il}\,g_{,ll}\,\mu_{i,3}\,\mu_{l,3}}_{\text{for }i=j=k\neq l=m=p}$$

$$+4\underbrace{\sum_{i=1}^{n}\sum_{j=1}^{n}g_{,ij}^3\,\mu_{i,3}\,\mu_{j,3}}_{\text{for }i=k=m\neq j=l=p}+3\underbrace{\sum_{i=1}^{n}\sum_{k=1}^{n}g_{,ii}\,g_{,kk}^2\,\mu_{i,2}\,\mu_{k,4}}_{\text{for }i=j\neq k=l=m=p}$$

$$\left.+12\underbrace{\sum_{i=1}^{n}\sum_{j=1}^{n}g_{,ij}^2\,g_{,jj}\,\mu_{i,2}\,\mu_{j,4}}_{\text{for }i=k\neq j=l=m=p}+\underbrace{\sum_{i=1}^{n}g_{,ii}^2\,\mu_{i,6}}_{\text{for }i=j=k=l=m=p}\right]$$

c^3:
$$=\frac{1}{8}\left[6\sum_{i=1}^{n-2}\sum_{j=i+1}^{n-1}\sum_{k=j+1}^{n}g_{,ii}\,g_{,jj}\,g_{,kk}\,\mu_{i,2}\,\mu_{j,2}\,\mu_{k,2}+12\sum_{i=1}^{n}\sum_{\substack{j=1\\j\neq i}}^{n-1}\sum_{\substack{k=j+1\\k\neq i}}^{n}g_{,ii}\,g_{,jk}^2\,\mu_{i,2}\,\mu_{j,2}\,\mu_{k,2}\right.$$

$$+18\sum_{i=1}^{n-2}\sum_{j=i+1}^{n-1}\sum_{k=j+1}^{n}g_{,ij}\,g_{,ik}\,g_{,jk}\,\mu_{i,2}\,\mu_{j,2}\,\mu_{k,2}+12\sum_{i=1}^{n-1}\sum_{j=i+1}^{n}g_{,ii}\,g_{,ij}\,g_{,jj}\,\mu_{i,3}\,\mu_{j,3} \tag{D.43}$$

$$+8\sum_{i=1}^{n-1}\sum_{j=i+1}^{n}g_{,ij}^3\,\mu_{i,3}\,\mu_{j,3}+3\sum_{i=1}^{n}\sum_{\substack{j=1\\j\neq i}}^{n}g_{,ii}\,g_{,jj}^2\,\mu_{i,2}\,\mu_{j,4}$$

$$\left.+12\sum_{i=1}^{n}\sum_{\substack{j=1\\j\neq i}}^{n}g_{,ij}^2\,g_{,jj}\,\mu_{i,2}\,\mu_{j,4}+\sum_{i=1}^{n}g_{,ii}^2\,\mu_{i,6}\right]$$

a^2b:
$$\int_{-\infty}^{\infty}g_{\boldsymbol{\mu}}^2\left[\sum_{i=1}^{n}g_{,ii}\left(x_i-\mu_i\right)\right]f_{\mathbf{X}}\left(\mathbf{x}\right)d\mathbf{x}=g_{\boldsymbol{\mu}}^2\sum_{i=1}^{n}g_{,ii}\underbrace{\int_{-\infty}^{\infty}\left(x_i-\mu_i\right)f_{\mathbf{X}}\left(\mathbf{x}\right)d\mathbf{x}}_{=0}=0 \tag{D.44}$$

$$a^2 c: \qquad \int\limits_{-\infty}^{\infty} g_\mu^2 \left[\frac{1}{2} \sum_{i=1}^n \sum_{j=1}^n g_{,ij} \left(x_i - \mu_i \right) \left(x_j - \mu_j \right) \right] f_{\mathbf{X}} \left(\mathbf{x} \right) d\mathbf{x}$$

$$= \frac{1}{2} g_\mu^2 \sum_{i=1}^n \sum_{j=1}^n g_{,ij} \int\limits_{-\infty}^{\infty} \left(x_i - \mu_i \right) \left(x_j - \mu_j \right) f_{\mathbf{X}} \left(\mathbf{x} \right) d\mathbf{x} \underset{\text{independence}}{=} \frac{1}{2} g_\mu^2 \sum_{i=1}^n g_{,ii} \, \mu_{i,2} \tag{D.45}$$

$$b^2 a: \qquad \int\limits_{-\infty}^{\infty} g_\mu \left[\sum_{i=1}^n g_{,i} \left(x_i - \mu_i \right) \right]^2 f_{\mathbf{X}} \left(\mathbf{x} \right) d\mathbf{x}$$

$$= g_\mu \sum_{i=1}^n \sum_{j=1}^n g_{,i} \, g_{,j} \int\limits_{-\infty}^{\infty} \left(x_i - \mu_i \right) \left(x_j - \mu_j \right) f_{\mathbf{X}} \left(\mathbf{x} \right) d\mathbf{x} \underset{\text{independence}}{=} g_\mu \sum_{i=1}^n g_{,i}^2 \, \mu_{i,2} \tag{D.46}$$

$$\int\limits_{-\infty}^{\infty} \left[\sum_{i=1}^n g_{,i} \left(x_i - \mu_i \right) \right]^2 \left[\frac{1}{2} \sum_{i=1}^n \sum_{j=1}^n g_{,ij} \left(x_i - \mu_i \right) \left(x_j - \mu_j \right) \right] f_{\mathbf{X}} \left(\mathbf{x} \right) d\mathbf{x}$$

$$= \frac{1}{2} \sum_{i=1}^n \sum_{j=1}^n \sum_{k=1}^n \sum_{l=1}^n g_{,i} \, g_{,j} \, g_{,kl} \int\limits_{-\infty}^{\infty} \left(x_i - \mu_i \right) \left(x_j - \mu_j \right) \left(x_k - \mu_k \right) \left(x_l - \mu_l \right) f_{\mathbf{X}} \left(\mathbf{x} \right) d\mathbf{x}$$

$$b^2 c: \qquad = \frac{1}{2} \sum_{i=1}^n \sum_{j=1}^n \sum_{k=1}^n \sum_{l=1}^n g_{,i} \, g_{,j} \, g_{,kl} \, \mu_{ijkl} \tag{D.47}$$

$$\underset{\text{independence}}{=} \underbrace{\frac{1}{2} \sum_{i=1}^n \sum_{k=1}^n g_{,i}^2 \, g_{,kk} \, \mu_{i,2} \, \mu_{k,2}}_{\text{for } i=j \neq k=l} + \underbrace{\sum_{i=1}^n \sum_{j=1}^n g_{,i} \, g_{,j} \, g_{,ij} \, \mu_{i,2} \, \mu_{j,2}}_{\text{for } i=k \neq j=l} + \underbrace{\frac{1}{2} \sum_{i=1}^n g_{,i}^2 \, g_{,ii} \, \mu_{i,4}}_{\text{for } i=j=k=l}$$

$$= \frac{1}{2} \sum_{i=1}^n \sum_{\substack{j=1 \\ j \neq i}}^n g_{,i}^2 \, g_{,jj} \, \mu_{i,2} \, \mu_{j,2} + 2 \sum_{i=1}^{n-1} \sum_{j=i+1}^n g_{,i} \, g_{,j} \, g_{,ij} \, \mu_{i,2} \, \mu_{j,2} + \frac{1}{2} \sum_{i=1}^n g_{,i}^2 \, g_{,ii} \, \mu_{i,4}$$

$$\int\limits_{-\infty}^{\infty} g_\mu \left[\frac{1}{2} \sum_{i=1}^n \sum_{j=1}^n g_{,ij} \left(x_i - \mu_i \right) \left(x_j - \mu_j \right) \right]^2 f_{\mathbf{X}} \left(\mathbf{x} \right) d\mathbf{x}$$

$$= \frac{1}{4} g_\mu \sum_{i=1}^n \sum_{j=1}^n \sum_{k=1}^n \sum_{l=1}^n g_{,ij} \, g_{,kl} \int\limits_{-\infty}^{\infty} \left(x_i - \mu_i \right) \left(x_j - \mu_j \right) \left(x_{ii} - \mu_{ii} \right) \left(x_{jj} - \mu_{jj} \right) f_{\mathbf{X}} \left(\mathbf{x} \right) d\mathbf{x}$$

$$c^2 a: \qquad = \frac{1}{4} g_\mu \sum_{i=1}^n \sum_{j=1}^n \sum_{k=1}^n \sum_{l=1}^n g_{,ij} \, g_{,kl} \, \mu_{ijkl} \tag{D.48}$$

$$\underset{\text{independence}}{=} \frac{1}{4} g_\mu \underbrace{\sum_{i=1}^n \sum_{k=1}^n g_{,ii} \, g_{,kk} \, \mu_{i,2} \, \mu_{k,2}}_{\text{for } i=j \neq k=l} + \frac{1}{2} g_\mu \underbrace{\sum_{i=1}^n \sum_{j=1}^n g_{,ij}^2 \, \mu_{i,2} \, \mu_{j,2}}_{\text{for } i=k \neq j=l} + \frac{1}{4} g_\mu \underbrace{\sum_{i=1}^n g_{,ii}^2 \, \mu_{i,4}}_{\text{for } i=j=k=l}$$

$$= \frac{1}{2} g_\mu \sum_{i=1}^{n-1} \sum_{j=i+1}^n g_{,ii} \, g_{,jj} \, \mu_{i,2} \, \mu_{j,2} + g_\mu \sum_{i=1}^{n-1} \sum_{j=i+1}^n g_{,ij}^2 \, \mu_{i,2} \, \mu_{j,2} + \frac{1}{4} g_\mu \sum_{i=1}^n g_{,ii}^2 \, \mu_{i,4}$$

$$\int\limits_{-\infty}^{\infty}\left[\sum_{i=1}^{n}g_{,i}\left(x_i-\mu_i\right)\right]\left[\frac{1}{2}\sum_{i=1}^{n}\sum_{j=1}^{n}g_{,ij}\left(x_i-\mu_i\right)\left(x_j-\mu_j\right)\right]^2 f_{\mathbf{X}}\left(\mathbf{x}\right)d\mathbf{x}$$

$$=\frac{1}{4}\sum_{i=1}^{n}\sum_{k=1}^{n}\sum_{l=1}^{n}\sum_{m=1}^{n}\sum_{p=1}^{n}g_{,i}\,g_{,kl}\,g_{,mp}\int\limits_{-\infty}^{\infty}\left(x_i-\mu_i\right)\left(x_k-\mu_k\right)$$
$$\cdot\left(x_l-\mu_l\right)\left(x_m-\mu_m\right)\left(x_p-\mu_p\right)f_{\mathbf{X}}\left(\mathbf{x}\right)d\mathbf{x}$$

$$=\frac{1}{4}\sum_{i=1}^{n}\sum_{k=1}^{n}\sum_{l=1}^{n}\sum_{m=1}^{n}\sum_{p=1}^{n}g_{,i}\,g_{,kl}\,g_{,mp}\,\mu_{iklmp}$$

$$\underset{\text{independence}}{=}\underbrace{\sum_{i=1}^{n}\sum_{l=1}^{n}g_{,i}\,g_{,il}\,g_{,ll}\,\mu_{i,2}\,\mu_{l,3}}_{\text{for }i=k\neq l=m=p}+\frac{1}{2}\underbrace{\sum_{i=1}^{n}\sum_{m=1}^{n}g_{,i}\,g_{,ii}\,g_{,mm}\,\mu_{i,3}\,\mu_{m,2}}_{\text{for }i=k=l\neq m=p}$$

$$+\underbrace{\sum_{i=1}^{n}\sum_{l=1}^{n}g_{,i}\,g_{,il}^2\,\mu_{i,3}\,\mu_{l,2}}_{\text{for }i=k=m\neq l=p}+\frac{1}{4}\underbrace{\sum_{i=1}^{n}g_{,i}\,g_{,ii}^2\,\mu_{i,5}}_{\text{for }i=k=l=m=p}$$

$$=\sum_{i=1}^{n}\sum_{\substack{j=1\\j\neq i}}^{n}g_{,i}\,g_{,ij}\,g_{,jj}\,\mu_{i,2}\,\mu_{j,3}+\frac{1}{2}\sum_{i=1}^{n}\sum_{\substack{j=1\\j\neq i}}^{n}g_{,i}\,g_{,ii}\,g_{,jj}\,\mu_{i,3}\,\mu_{j,2}$$

$c^2b:$
$$+\sum_{i=1}^{n}\sum_{\substack{j=1\\j\neq i}}^{n}g_{,i}\,g_{,ij}^2\,\mu_{i,3}\,\mu_{j,2}+\frac{1}{4}\sum_{i=1}^{n}g_{,i}\,g_{,ii}^2\,\mu_{i,5}$$
(D.49)

$$\int\limits_{-\infty}^{\infty}g_{\boldsymbol{\mu}}\left[\sum_{i=1}^{n}g_{,i}\left(x_i-\mu_i\right)\right]\left[\frac{1}{2}\sum_{i=1}^{n}\sum_{j=1}^{n}g_{,ij}\left(x_i-\mu_i\right)\left(x_j-\mu_j\right)\right]f_{\mathbf{X}}\left(\mathbf{x}\right)d\mathbf{x}$$

$a\,b\,c:$
$$=g_{\boldsymbol{\mu}}\frac{1}{2}\sum_{i=1}^{n}\sum_{j=1}^{n}\sum_{k=1}^{n}g_{,i}\,g_{,jk}\int\limits_{-\infty}^{\infty}\left(x_i-\mu_i\right)\left(x_j-\mu_j\right)\left(x_k-\mu_k\right)f_{\mathbf{X}}\left(\mathbf{x}\right)d\mathbf{x}$$
(D.50)

$$\underset{\text{independence}}{=}\frac{1}{2}g_{\boldsymbol{\mu}}\sum_{i=1}^{n}g_{,i}\,g_{,ii}\,\mu_{i,3}$$

Inserting (D.41) to (D.50) into (D.40) and again into (D.39) yields

$$\int_{-\infty}^{\infty} g^3(\mathbf{x}) f_{\mathbf{X}}(\mathbf{x})\, d\mathbf{x}$$

$$\approx \underbrace{g_{\boldsymbol{\mu}}^3}_{a^3} + \underbrace{\sum_{i=1}^{n} g_{,i}^3 \mu_{i,3}}_{b^3} + \underbrace{\frac{3}{4} \sum_{i=1}^{n-2} \sum_{j=i+1}^{n-1} \sum_{k=j+1}^{n} g_{,ii}\, g_{,jj}\, g_{,kk}\, \mu_{i,2}\, \mu_{j,2}\, \mu_{k,2}}_{c^3}$$

$$+ \underbrace{\frac{3}{2} \sum_{i=1}^{n} \sum_{\substack{j=1 \\ j\neq i}}^{n-1} \sum_{\substack{k=j+1 \\ k\neq i}}^{n} g_{,ii}\, g_{,jk}^2\, \mu_{i,2}\, \mu_{j,2}\, \mu_{k,2} + \frac{9}{4} \sum_{i=1}^{n-2} \sum_{j=i+1}^{n-1} \sum_{k=j+1}^{n} g_{,ij}\, g_{,ik}\, g_{,jk}\, \mu_{i,2}\, \mu_{j,2}\, \mu_{k,2}}_{c^3}$$

$$+ \underbrace{\frac{3}{2} \sum_{i=1}^{n-1} \sum_{j=i+1}^{n} g_{,ii}\, g_{,ij}\, g_{,jj}\, \mu_{i,3}\, \mu_{j,3} + \sum_{i=1}^{n-1} \sum_{j=i+1}^{n} g_{,ij}^3\, \mu_{i,3}\, \mu_{j,3} + \frac{3}{8} \sum_{i=1}^{n} \sum_{\substack{j=1 \\ j\neq i}}^{n} g_{,ii}\, g_{,jj}^2\, \mu_{i,2}\, \mu_{j,4}}_{c^3}$$

$$+ \underbrace{\frac{3}{2} \sum_{i=1}^{n} \sum_{\substack{j=1 \\ j\neq i}}^{n} g_{,ij}^2\, g_{,jj}\, \mu_{i,2}\, \mu_{j,4} + \frac{1}{8} \sum_{i=1}^{n} g_{,ii}^2\, \mu_{i,6}}_{c^3} + \underbrace{\frac{3}{2} g_{\boldsymbol{\mu}}^2 \sum_{i=1}^{n} g_{,ii}\, \mu_{i,2}}_{3a^2 c} + \underbrace{3 g_{\boldsymbol{\mu}} \sum_{i=1}^{n} g_{,i}^2\, \mu_{i,2}}_{3b^2 a}$$

$$+ \underbrace{\frac{3}{2} \sum_{i=1}^{n} \sum_{\substack{j=1 \\ j\neq i}}^{n} g_{,i}^2\, g_{,jj}\, \mu_{i,2}\, \mu_{j,2} + 6 \sum_{i=1}^{n-1} \sum_{j=i+1}^{n} g_{,i}\, g_{,j}\, g_{,ij}\, \mu_{i,2}\, \mu_{j,2} + \frac{3}{2} \sum_{i=1}^{n} g_{,i}^2\, g_{,ii}\, \mu_{i,4}}_{3b^2 c}$$

$$+ \underbrace{\frac{3}{2} g_{\boldsymbol{\mu}} \sum_{i=1}^{n-1} \sum_{j=i+1}^{n} g_{,ii}\, g_{,jj}\, \mu_{i,2}\, \mu_{j,2} + 3 g_{\boldsymbol{\mu}} \sum_{i=1}^{n-1} \sum_{j=i+1}^{n} g_{,ij}^2\, \mu_{i,2}\, \mu_{j,2} + \frac{3}{4} g_{\boldsymbol{\mu}} \sum_{i=1}^{n} g_{,ii}^2\, \mu_{i,4}}_{3c^2 a}$$

$$+ \underbrace{3 \sum_{i=1}^{n} \sum_{\substack{j=1 \\ j\neq i}}^{n} g_{,i}\, g_{,ij}\, g_{,jj}\, \mu_{i,2}\, \mu_{j,3} + \frac{3}{2} \sum_{i=1}^{n} \sum_{\substack{j=1 \\ j\neq i}}^{n} g_{,i}\, g_{,ii}\, g_{,jj}\, \mu_{i,3}\, \mu_{j,2}}_{3c^2 b}$$

$$+ \underbrace{3 \sum_{i=1}^{n} \sum_{\substack{j=1 \\ j\neq i}}^{n} g_{,i}\, g_{,ij}^2\, \mu_{i,3}\, \mu_{j,2} + \frac{3}{4} \sum_{i=1}^{n} g_{,i}\, g_{,ii}^2\, \mu_{i,5}}_{3c^2 b} + \underbrace{3 g_{\boldsymbol{\mu}} \sum_{i=1}^{n} g_{,i}\, g_{,ii}\, \mu_{i,3}}_{6abc}$$

$$\tag{D.51}$$

Inserting (D.51) into (D.38) leads to the second order approximation of the third central moment of g given by

$$\mu_{g,3} \approx \sum_{i=1}^{n} g_{,i}^{3} \, \mu_{i,3} \left.\right\} \text{first order approach}$$

$$+ g_{\mu}^{3} + \frac{3}{2} g_{\mu}^{2} \sum_{i=1}^{n} g_{,ii} \, \mu_{i,2} + 3 g_{\mu} \sum_{i=1}^{n} g_{,i}^{2} \, \mu_{i,2}$$

$$+ 3 g_{\mu} \sum_{i=1}^{n} g_{,i} \, g_{,ii} \, \mu_{i,3} - 3 \, \mu_{g} \, \sigma_{g}^{2} - \mu_{g}^{3} \left.\right\} \text{SOTM}$$

$$+ \frac{3}{4} \sum_{i=1}^{n-2} \sum_{j=i+1}^{n-1} \sum_{k=j+1}^{n} g_{,ii} \, g_{,jj} \, g_{,kk} \, \mu_{i,2} \, \mu_{j,2} \, \mu_{k,2} + \frac{3}{2} \sum_{i=1}^{n-1} \sum_{j=i+1}^{n} g_{,ii} \, g_{,ij} \, g_{,jj} \, \mu_{i,3} \, \mu_{j,3}$$

$$+ \frac{3}{8} \sum_{i=1}^{n} \sum_{\substack{j=1 \\ j \neq i}}^{n} g_{,ii} \, g_{,jj}^{2} \, \mu_{i,2} \, \mu_{j,4} + \frac{1}{8} \sum_{i=1}^{n} g_{,ii}^{2} \, \mu_{i,6} + \frac{3}{2} \sum_{i=1}^{n} \sum_{\substack{j=1 \\ j \neq i}}^{n} g_{,i}^{2} \, g_{,jj} \, \mu_{i,2} \, \mu_{j,2}$$

$$+ \frac{3}{2} \sum_{i=1}^{n} g_{,i}^{2} \, g_{,ii} \, \mu_{i,4} + \frac{3}{2} g_{\mu} \sum_{i=1}^{n-1} \sum_{j=i+1}^{n} g_{,ii} \, g_{,jj} \, \mu_{i,2} \, \mu_{j,2} + \frac{3}{4} g_{\mu} \sum_{i=1}^{n} g_{,ii}^{2} \, \mu_{i,4}$$

$$+ \frac{3}{2} \sum_{i=1}^{n} \sum_{\substack{j=1 \\ j \neq i}}^{n} g_{,i} \, g_{,ii} \, g_{,jj} \, \mu_{i,3} \, \mu_{j,2} + \frac{3}{4} \sum_{i=1}^{n} g_{,i} \, g_{,ii}^{2} \, \mu_{i,5}$$

$\left.\vphantom{\begin{array}{c} 1 \\ 1 \\ 1 \\ 1 \end{array}}\right\}$ incomplete second order approach

$$+ \frac{3}{2} \sum_{i=1}^{n} \sum_{\substack{j=1 \\ j \neq i}}^{n-1} \sum_{\substack{k=j+1 \\ k \neq i}}^{n} g_{,ii} \, g_{,jk}^{2} \, \mu_{i,2} \, \mu_{j,2} \, \mu_{k,2} + \frac{9}{4} \sum_{i=1}^{n-2} \sum_{j=i+1}^{n-1} \sum_{k=j+1}^{n} g_{,ij} \, g_{,ik} \, g_{,jk} \, \mu_{i,2} \, \mu_{j,2} \, \mu_{k,2}$$

$$+ \sum_{i=1}^{n-1} \sum_{j=i+1}^{n} g_{,ij}^{3} \, \mu_{i,3} \, \mu_{j,3} + \frac{3}{2} \sum_{i=1}^{n} \sum_{\substack{j=1 \\ j \neq i}}^{n} g_{,ij}^{2} \, g_{,jj} \, \mu_{i,2} \, \mu_{j,4} + 6 \sum_{i=1}^{n-1} \sum_{j=i+1}^{n} g_{,i} \, g_{,j} \, g_{,ij} \, \mu_{i,2} \, \mu_{j,2}$$

$$+ 3 g_{\mu} \sum_{i=1}^{n-1} \sum_{j=i+1}^{n} g_{,ij}^{2} \, \mu_{i,2} \, \mu_{j,2} + 3 \sum_{i=1}^{n} \sum_{\substack{j=1 \\ j \neq i}}^{n} g_{,i} \, g_{,ij} \, g_{,jj} \, \mu_{i,2} \, \mu_{j,3} + 3 \sum_{i=1}^{n} \sum_{\substack{j=1 \\ j \neq i}}^{n} g_{,i} \, g_{,ij}^{2} \, \mu_{i,3} \, \mu_{j,2}$$

$\left.\vphantom{\begin{array}{c} 1 \\ 1 \\ 1 \end{array}}\right\}$ full approach   (D.52)

The first order approach hence equals

$$\mu_{g,3} \approx \sum_{i=1}^{n} g_{,i}^{3} \, \mu_{i,3} \tag{D.53}$$

E   Derivatives of the Moment Approximations

For the optimization of the probabilistically motivated design load with gradient based optimization algorithms, the gradients of the mean value and variance approximation are derived in the following.

Assuming the objective function $g(\mathbf{x},\mathbf{y})$ to be function of random variables, subsumed in the vector $\mathbf{x}$, and design variables, subsumed in the vector $\mathbf{y}$. The stochastic moments of the objective function are functions of the design variable vector $\mathbf{y}$. E.g. the mean value of the objective function is given by

$$\mu_{g}(\mathbf{y}) \approx g(\boldsymbol{\mu},\mathbf{y}) + \frac{1}{2} \sum_{i=1}^{n} \frac{\partial^{2} g(\boldsymbol{\mu},\mathbf{y})}{\partial x_{i}^{2}} \, \mathrm{var}(X_{i}) \tag{E.1}$$

For optimization purposes the derivatives of the objective function with respect to the design variables are required. The partial derivative of μ_{g} with respect to the design variable y_{k} is given by

$$\frac{\partial \mu_g(\mathbf{y})}{\partial y_k} \approx \frac{\partial g(\boldsymbol{\mu}, \mathbf{y})}{\partial y_k} + \frac{1}{2} \sum_{i=1}^{n} \underbrace{\frac{\partial^3 g(\boldsymbol{\mu}, \mathbf{y})}{\partial x_i^2 \, \partial y_k}}_{\approx 0} \text{var}(X_i) \tag{E.2}$$

Since the moment approximations are derived based on a second order Taylor series, derivatives of higher order than two are neglected.

The abbreviations $g_{\boldsymbol{\mu}} = g(\boldsymbol{\mu}, \mathbf{y})$ is used subsequently.

The variance σ_g^2 of the objective function is given by

$$\sigma_g^2(\mathbf{y}) \approx g_{\boldsymbol{\mu}}^2 + \sum_{i=1}^{n} \left(\frac{\partial g}{\partial x_i}\right)^2 \mu_{i,2} + \frac{1}{4} \sum_{i=1}^{n} \left(\frac{\partial^2 g}{\partial x_i^2}\right)^2 \mu_{i,4} + g_{\boldsymbol{\mu}} \sum_{i=1}^{n} \frac{\partial^2 g}{\partial x_i^2} \mu_{i,2} + \sum_{i=1}^{n} \frac{\partial g}{\partial x_i} \frac{\partial^2 g}{\partial x_i^2} \mu_{i,3}$$
$$+ \frac{1}{2} \sum_{i=1}^{n} \sum_{j=i+1}^{n} \frac{\partial^2 g}{\partial x_i^2} \frac{\partial^2 g}{\partial x_j^2} \mu_{i,2}\, \mu_{j,2} + \sum_{i=1}^{n} \sum_{j=i+1}^{n} \left(\frac{\partial^2 g}{\partial x_i \, \partial x_j}\right)^2 \mu_{i,2}\, \mu_{j,2} - \mu_g^2 \tag{E.3}$$

The partial derivative of σ_g^2 with respect to the design variable y_k is given by

$$\frac{\partial \sigma_g^2(\mathbf{y})}{\partial y_k} \approx \underbrace{\frac{\partial g_{\boldsymbol{\mu}}^2}{\partial y_k}}_{I} + \underbrace{\sum_{i=1}^{n} \frac{\partial \left(\frac{\partial g}{\partial x_i}\right)^2}{\partial y_k} \mu_{i,2}}_{II} + \frac{1}{4} \underbrace{\sum_{i=1}^{n} \frac{\partial \left(\frac{\partial^2 g}{\partial x_i^2}\right)^2}{\partial y_k} \mu_{i,4}}_{III} + \underbrace{\frac{\partial \left[g_{\boldsymbol{\mu}} \sum_{i=1}^{n} \frac{\partial^2 g}{\partial x_i^2} \mu_{i,2}\right]}{\partial y_k}}_{IV}$$

$$+ \underbrace{\sum_{i=1}^{n} \frac{\partial \left[\frac{\partial g}{\partial x_i} \frac{\partial^2 g}{\partial x_i^2}\right]}{\partial y_k} \mu_{i,3}}_{V} + \frac{1}{2} \underbrace{\sum_{i=1}^{n} \sum_{j=i+1}^{n} \frac{\partial \left[\frac{\partial^2 g}{\partial x_i^2} \frac{\partial^2 g}{\partial x_j^2}\right]}{\partial y_k} \mu_{i,2}\, \mu_{j,2}}_{VI} \tag{E.4}$$

$$+ \underbrace{\sum_{i=1}^{n} \sum_{j=i+1}^{n} \frac{\partial \left(\frac{\partial^2 g}{\partial x_i \, \partial x_j}\right)^2}{\partial y_k} \mu_{i,2}\, \mu_{j,2}}_{VII} - \underbrace{\frac{\partial \mu_g^2}{\partial y_k}}_{VIII}$$

The derivatives of the summands are given in the following.

I:
$$\frac{\partial \left[g_{\boldsymbol{\mu}}\right]^2}{\partial y_k} = 2 g_{\boldsymbol{\mu}} \frac{\partial g}{\partial y_k} \tag{E.5}$$

II:
$$\sum_{i=1}^{n} \frac{\partial \left(\frac{\partial g}{\partial x_i}\right)^2}{\partial y_k} \mu_{i,2} = \sum_{i=1}^{n} \left(2 \frac{\partial g}{\partial x_i} \frac{\partial^2 g}{\partial x_i \, \partial y_k}\right) \mu_{i,2} \tag{E.6}$$

III:
$$\sum_{i=1}^{n} \frac{\partial \left(\frac{\partial^2 g}{\partial x_i^2}\right)^2}{\partial y_k} \mu_{i,4} = \sum_{i=1}^{n} \left[2 \frac{\partial^2 g}{\partial x_i^2} \underbrace{\frac{\partial^3 g}{\partial x_i^2 \, \partial y_k}}_{=0}\right] \mu_{i,4} = 0 \tag{E.7}$$

IV:

$$\frac{\partial\left[g_\mu \sum_{i=1}^{n}\frac{\partial^2 g}{\partial x_i^2}\mu_{i,2}\right]}{\partial y_k} = \frac{\partial g_\mu}{\partial y_k}\sum_{i=1}^{n}\frac{\partial^2 g}{\partial x_i^2}\mu_{i,2} + g_\mu\frac{\partial\left[\sum_{i=1}^{n}\frac{\partial^2 g}{\partial x_i^2}\mu_{i,2}\right]}{\partial y_k}$$

$$= \frac{\partial g}{\partial y_k}\sum_{i=1}^{n}\frac{\partial^2 g}{\partial x_i^2}\mu_{i,2} + g_\mu\sum_{i=1}^{n}\underbrace{\frac{\partial^3 g}{\partial x_i^2 \partial y_k}}_{=0}\mu_{i,2} = \frac{\partial g}{\partial y_k}\sum_{i=1}^{n}\frac{\partial^2 g}{\partial x_i^2}\mu_{i,2}$$

(E.8)

V:

$$\sum_{i=1}^{n}\frac{\partial\left[\frac{\partial g}{\partial x_i}\frac{\partial^2 g}{\partial x_i^2}\right]}{\partial y_k}\mu_{i,3} = \sum_{i=1}^{n}\left[\frac{\partial^2 g}{\partial x_i \partial y_k}\frac{\partial^2 g}{\partial x_i^2} + \frac{\partial g}{\partial x_i}\underbrace{\frac{\partial^3 g}{\partial x_i^2 \partial y_k}}_{=0}\right]\mu_{i,3} = \sum_{i=1}^{n}\frac{\partial^2 g}{\partial x_i \partial y_k}\frac{\partial^2 g}{\partial x_i^2}\mu_{i,3}$$

(E.9)

VI:

$$\sum_{i=1}^{n}\sum_{j=i+1}^{n}\frac{\partial\left(\frac{\partial^2 g}{\partial x_i^2}\frac{\partial^2 g}{\partial x_j^2}\right)}{\partial y_k}\mu_{i,2}\,\mu_{j,2} = \sum_{i=1}^{n}\sum_{j=i+1}^{n}\left[\underbrace{\frac{\partial^3 g}{\partial x_i^2 \partial y_k}}_{=0}\frac{\partial^2 g}{\partial x_j^2} + \frac{\partial^2 g}{\partial x_i^2}\underbrace{\frac{\partial^3 g}{\partial x_j^2 \partial y_k}}_{=0}\right]\mu_{i,2}\,\mu_{j,2} = 0$$

(E.10)

VII:

$$\sum_{i=1}^{n}\sum_{j=i+1}^{n}\frac{\partial\left(\frac{\partial^2 g}{\partial x_i \partial x_j}\right)^2}{\partial y_k}\mu_{i,2}\,\mu_{j,2} = \sum_{i=1}^{n}\sum_{j=i+1}^{n}\left[2\frac{\partial^2 g}{\partial x_i \partial x_j}\underbrace{\frac{\partial^3 g}{\partial x_i \partial x_j \partial y_k}}_{=0}\right]\mu_{i,2}\,\mu_{j,2} = 0$$

(E.11)

$VIII$:

$$\frac{\partial\mu_g^2}{\partial y_k} = 2\,\mu_g\frac{\partial\mu_g}{\partial y_k} = 2\,\mu_g\frac{\partial g}{\partial y_k}$$

(E.12)

Summarized

$$\frac{\partial\sigma_g^2(\mathbf{y})}{\partial y_k} \approx \underbrace{2\,g_\mu\frac{\partial g}{\partial y_k}}_{I} + \underbrace{\sum_{i=1}^{n}\left(2\frac{\partial g}{\partial x_i}\frac{\partial^2 g}{\partial x_i \partial y_k}\right)\mu_{i,2}}_{II} + \underbrace{\frac{\partial g}{\partial y_k}\sum_{i=1}^{n}\frac{\partial^2 g}{\partial x_i^2}\mu_{i,2}}_{IV}$$

$$+ \underbrace{\sum_{i=1}^{n}\frac{\partial^2 g}{\partial x_i \partial y_k}\frac{\partial^2 g}{\partial x_i^2}\mu_{i,3}}_{V} - \underbrace{2\,\mu_g\frac{g}{\partial y_k}}_{VIII}$$

(E.13)

$$\frac{\partial\sigma_g^2(\mathbf{y})}{\partial y_k} \approx 2\left(g_\mu - \mu_g\right)\frac{\partial g}{\partial y_k} + 2\sum_{i=1}^{n}\frac{\partial g}{\partial x_i}\frac{\partial^2 g}{\partial x_i \partial y_k}\mu_{i,2} + \frac{\partial g}{\partial y_k}\sum_{i=1}^{n}\frac{\partial^2 g}{\partial x_i^2}\mu_{i,2} + \sum_{i=1}^{n}\frac{\partial^2 g}{\partial x_i \partial y_k}\frac{\partial^2 g}{\partial x_i^2}\mu_{i,3}$$

(E.14)

Hence, the following derivatives of the objective function are required.

$$\frac{\partial g}{\partial x_i},\ \frac{\partial^2 g}{\partial x_i^2},\ \frac{\partial^2 g}{\partial x_i \partial y_k}\ \text{and}\ \frac{\partial g}{\partial y_k}\ \text{for } i = 1,\ldots,n\ \text{and } j = 1,\ldots,p$$

(E.15)

F   Derivatives of the Convex Anti-Optimum

For the optimization of the design load given by convex anti-optimization with gradient based optimization algorithms, the gradients of minimum given by convex anti-optimization are derived in the following.

The first order approximation of the minimum of the objective function is given by

$$g_{\min}(\mathbf{y}) = g(\mathbf{x}_c, \mathbf{y}) - \sqrt{\varphi(\mathbf{y})^T \mathbf{G}\, \varphi(\mathbf{y})} \tag{F.1}$$

The derivative with respect to one design variable y_j is given by

$$\frac{\partial g_{\min}(\mathbf{y})}{\partial y_j} = \frac{\partial g(\mathbf{x}_c, \mathbf{y})}{\partial y_j} - \frac{\partial \sqrt{\varphi(\mathbf{y})^T \mathbf{G}\, \varphi(\mathbf{y})}}{\partial y_j} \tag{F.2}$$

The derivative of the second summand is

$$\frac{\partial \sqrt{\varphi^T \mathbf{G}\, \varphi}}{\partial y_j} = \frac{1}{2\sqrt{\varphi^T \mathbf{G}\, \varphi}} \cdot \frac{\partial\left[\varphi^T \mathbf{G}\, \varphi\right]}{\partial y_j} \tag{F.3}$$

with

$$\frac{\partial\left[\varphi^T \mathbf{G}\, \varphi\right]}{\partial y_j} = \left(\frac{\partial \varphi}{\partial y_j}\right)^T \mathbf{G}\, \varphi + \varphi^T \mathbf{G}\, \frac{\partial \varphi}{\partial y_j} \tag{F.4}$$

Since $\mathbf{G}$ is symmetric,

$$\left(\frac{\partial \varphi}{\partial \beta_j}\right)^T \mathbf{G}\, \varphi = \left(\frac{\partial \varphi}{\partial \beta_j}\right)^T \left[\varphi^T \mathbf{G}^T\right]^T = \left[\varphi^T \mathbf{G}^T\right]\frac{\partial \varphi}{\partial \beta_j} = \varphi^T \mathbf{G}\, \frac{\partial \varphi}{\partial \beta_j} \tag{F.5}$$

Hence, (F.4) can be expressed by

$$\frac{\partial\left[\varphi^T \mathbf{G}\, \varphi\right]}{\partial \beta_j} = 2\, \varphi^T \mathbf{G}\, \frac{\partial \varphi}{\partial \beta_j} \tag{F.6}$$

This leads to the first derivative of the minimum of the objective function.

$$\frac{\partial g_{\min}}{\partial y_j} = \frac{\partial g}{\partial y_j} - \frac{1}{\sqrt{\varphi^T \mathbf{G}\, \varphi}}\, \varphi^T \mathbf{G}\, \frac{\partial \varphi}{\partial y_j} \tag{F.7}$$

with

$$\frac{\partial \varphi}{\partial y_j} = \left(\frac{\partial^2 \lambda}{\partial x_1\, \partial y_j}, \ldots, \frac{\partial^2 \lambda}{\partial x_d\, \partial y_j}\right)^T \tag{F.8}$$

Note that

$$\varphi = (\varphi_1, \ldots, \varphi_d)^T = \left(\frac{\partial g}{\partial x_1}, \ldots, \frac{\partial g}{\partial x_d}\right)^T \quad \text{and} \quad \frac{\partial \varphi_i}{\partial y_j} = \frac{\partial^2 g}{\partial x_i\, \partial y_j} \tag{F.9}$$

Hence, the following derivatives of the objective function are required.

$$\frac{\partial^2 g}{\partial x_i\, \partial y_j},\ \frac{\partial g}{\partial x_i}\ \text{and}\ \frac{\partial g}{\partial y_j}\ \text{for } i = 1, \ldots, d \text{ and } j = 1, \ldots, p \tag{F.10}$$

G   Results of Probabilistic Analyses Using Different Imperfection Models

The results of the investigations described in section 6.4 are summarized for all shells considered in Figure G-1.
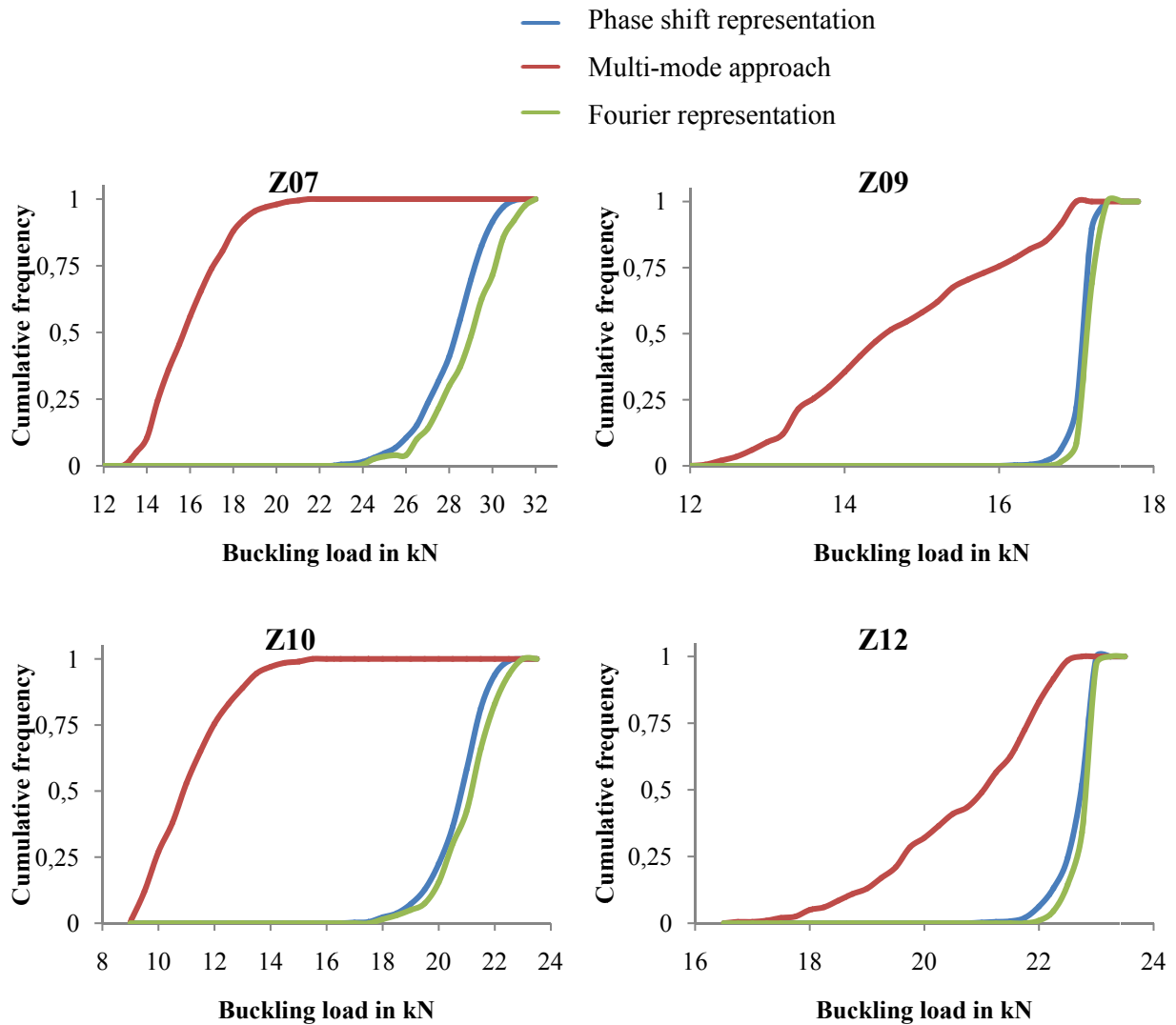
Figure G-1: Cumulative frequency of Monte Carlo simulations with different representations of imperfection patterns for shell Z07, Z09, Z10 and Z12

H   Load-Displacement Curves of the Panels Considered

In the following section, the load-displacement curves are given for the panels considered. The properties of these panels are summarized in section 7.1.

The intra lamina failures indicated in the load-displacement curves in Figure H-1, the Hashin criterion was used, while skin-stringer debonding has been detected using the quadratic nominal stress damage criterion and cohesive elements. The failure criteria have only been used to detect the onset of degradation and no actual stiffness degradation was implemented in the models.
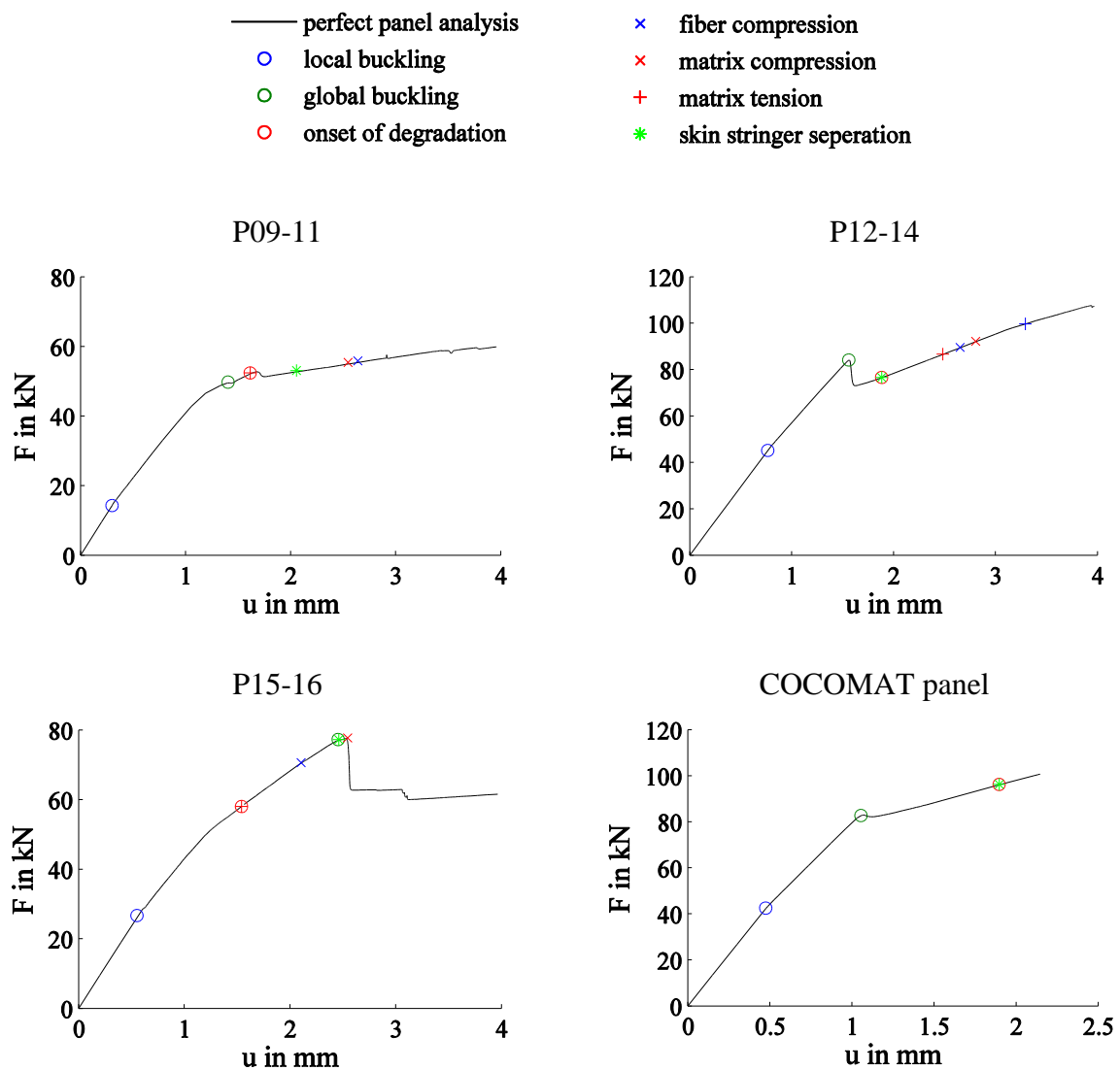
Figure H-1: Load-displacement curves of the perfect panels

In the analyses of imperfect panels, measured geometric imperfections and the measured radius have been included in the model. Furthermore, non-rigid longitudinal edges have been realized by applying rotational spring as shown in Figure 7-4 and discussed in section 7.4.5. For material properties, wall thickness and fiber orientation and the nominal values have been used.

For the COCOMAT panel no measurement data are published. Panel P15-16 showed a less typical behavior compared to panels P09-11 and P12-14 and is therefore not analyzed any further. The load-displacement curves of the imperfect panels P09-P14 and the associated experimental results are given in Figure H-2.
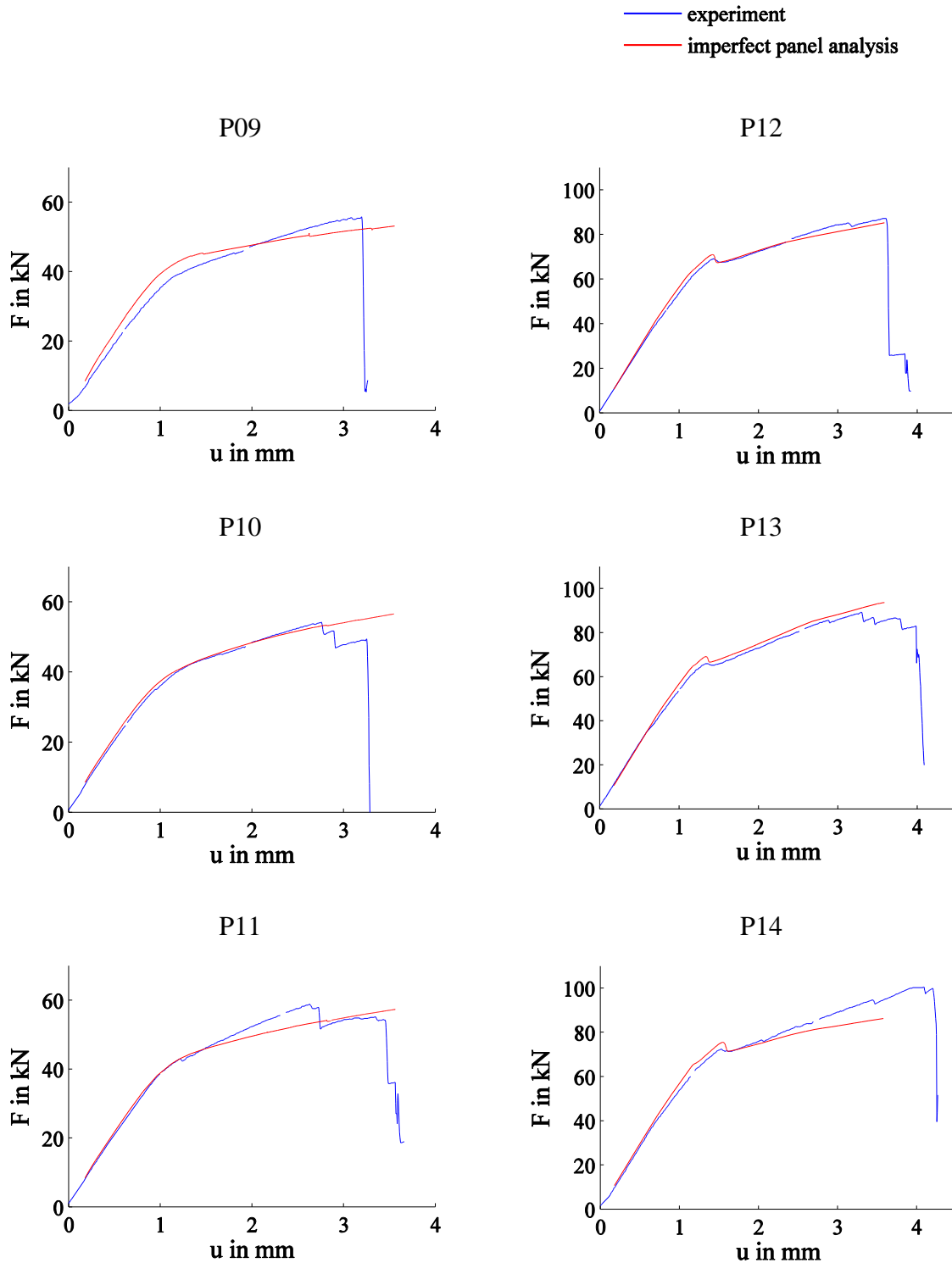
Figure H-2: Load-displacement curves of the imperfect POSICOSS panels

I   Knockdown Factor given by NASA SP-8007 for [±*α*, ±*β*] Laminates

For orthotropic shells, NASA SP-8007 [28] proposes determining the equivalent wall thickness t^* according to (1.4). When applying this approach to composite shells and using the unified formulation (1.6), the equivalent wall thickness t^+ is given by

$$t^+ = \sqrt{12} \ \sqrt[4]{\frac{D_{11} \, D_{22}}{A_{11} \, A_{22}}} \tag{I.1}$$

According to [119] the entries of the ABD matrix of fiber composites made of unidirectional plies are given by

$$A_{ij} = \sum_{k=1}^{n} t_k \, Q_{ij}^{(k)} \tag{I.2}$$

and

$$D_{ij} = \sum_{k=1}^{n} t_k \, Q_{ij}^{(k)} \left(\frac{t_k^2}{12} + \frac{z_k^2}{4} \right) \tag{I.3}$$

Here, A_{ij} and D_{ij} are entries of the ABD matrix. $Q_{ij}^{(k)}$ is the entry of stiffness matrix of the k-th ply, t_k is the wall thickness and z_k is the center of gravity of the k-th ply. For a laminate with the layup $[\pm\alpha, \pm\beta]$ and a ply thickness of $t_{ply} = \frac{1}{4} t$, where t is the thickness of the whole laminate, the entries A_{11} and D_{11} of ABD matrix are given by

$$A_{11} = t_{ply} \left[Q_{11}^{(1)} + Q_{11}^{(2)} + Q_{11}^{(3)} + Q_{11}^{(4)} \right] \tag{I.4}$$

and

$$\begin{aligned} D_{11} = t_{ply} &\left[Q_{11}^{(1)} \left(\frac{t_{ply}^2}{12} + \left[\frac{3}{2} t_{ply} \right]^2 \right) + Q_{11}^{(2)} \left(\frac{t_{ply}^2}{12} + \left[\frac{1}{2} t_{ply} \right]^2 \right) \right. \\ &\left. + Q_{11}^{(3)} \left(\frac{t_{ply}^2}{12} + \left[\frac{1}{2} t_{ply} \right]^2 \right) + Q_{11}^{(4)} \left(\frac{t_{ply}^2}{12} + \left[\frac{3}{2} t_{ply} \right]^2 \right) \right] \\ = t_{ply}^3 &\left[\tfrac{7}{3} Q_{11}^{(1)} + \tfrac{1}{3} Q_{11}^{(2)} + \tfrac{1}{3} Q_{11}^{(3)} + \tfrac{7}{3} Q_{11}^{(4)} \right] \end{aligned} \tag{I.5}$$

Due to the restriction of the laminate setup, the entries of the first two plies and the third and fourth ply are equal.

$$Q_{11}^{(1)} = Q_{11}^{(2)} \quad \text{and} \quad Q_{11}^{(3)} = Q_{11}^{(4)} \tag{I.6}$$

Hence, (I.4) and (I.5) can be written as

$$A_{11} = 2t_{ply} \left[Q_{11}^{(1)} + Q_{11}^{(3)} \right] = \tfrac{1}{2} t \left[Q_{11}^{(1)} + Q_{11}^{(3)} \right] \tag{I.7}$$

and

$$D_{11} = t_{ply}^3 \left[\tfrac{8}{3} Q_{11}^{(1)} + \tfrac{8}{3} Q_{11}^{(3)} \right] = \tfrac{8}{3} t_{ply}^3 \left[Q_{11}^{(1)} + Q_{11}^{(3)} \right] = \tfrac{1}{24} t^3 \left[Q_{11}^{(1)} + Q_{11}^{(3)} \right] \tag{I.8}$$

The same holds for the entries A_{22} and D_{22}, which are consequently given by

$$A_{22} = \tfrac{1}{2} t \left[Q_{22}^{(1)} + Q_{22}^{(3)} \right] \tag{I.9}$$

and

$$D_{22} = \tfrac{1}{24} t^3 \left[Q_{22}^{(1)} + Q_{22}^{(3)} \right] \tag{I.10}$$

Inserting (I.7)–(I.10) into the quotient in (I.1) yields

$$\frac{D_{11} D_{22}}{A_{11} A_{22}} = \frac{\frac{1}{24}t^3 \left[Q_{11}^{(1)} + Q_{11}^{(3)} \right] \frac{1}{24}t^3 \left[Q_{22}^{(1)} + Q_{22}^{(3)} \right]}{\frac{1}{2}t \left[Q_{11}^{(1)} + Q_{11}^{(3)} \right] \frac{1}{2}t \left[Q_{22}^{(1)} + Q_{22}^{(3)} \right]} = \frac{1}{144}t^4 \tag{I.11}$$

Hence, the equivalent wall-thickness t^+ equals

$$t^+ = \sqrt{12} \ \sqrt[4]{\frac{D_{11} D_{22}}{A_{11} A_{22}}} = \sqrt{12} \ \sqrt[4]{\frac{1}{144}t^4} = t \tag{I.12}$$

Summarized, for any laminate with a layup [±α, ±β], for which all ply thicknesses are equal, the equivalent wall thickness t^+ equals the real wall thickness t. Consequently, the KDF for such laminates is independent from the actual values of α and β.

List of Figures

List of Tables

References

[1] J. Arbocz, C. Bisagni, A. Calvi, E. Carrera, R. Cuntze, R. Degenhardt, N. Gualtieri, H. Haller, N. Impollonia, M. Jacquesson, E. Jansen, H.-R. Meyer-Piening, H. Oery, A. Rittweger, R. Rolfes, G. Schullerer, G. Turzo, T. Weller, and J. Wijker, "Buckling of Structures," ECSS-E-HB-32-24A, Mar. 2010, ESA Requirements and Standards Division.

[2] J. Singer, T. Weller, and J. Arbocz, *Buckling Experiments: Experimental Methods in Buckling of Thin-Walled Structures*, **1**. Wiley, New York, 1997.

[3] R. Lorenz, "Achsensymmetrische Verzerrungen in dünnwandigen Hohlzylindern," *Zeitschrift Verein Deutscher Ingenieure*, **52**(43), 1706–1713, 1908.

[4] S. P. Timoshenko, "Einige Stabilitätsprobleme der Elastizitätstheorie," *Zeitschrift für Mathematik und Physik*, **58**(4), 378–385, 1910.

[5] R. V. Southwell, "On the General Theory of Elastic Stability," *Philosophical Transactions of the Royal Society of London. Series A, Containing Papers of a Mathematical or Physical Character*, **213**, 187–244, 1914.

[6] E. E. Lundquist, "Strength Tests of Thin-Walled Duralumin Cylinders in Compression," NACA Report 473, 1934, National Advisory Committee for Aeronautics.

[7] L. H. Donnell, "A New Theory for the Buckling of Thin Cylinders Under Axial Compression and Bending," *Trans. ASME*, **56**(11), 795–806, 1934.

[8] V. I. Weingarten, E. J. Morgan, and P. Seide, "Elastic Stability of Thin-Walled Cylindrical and Conical Shells Under Axial Compression," *AIAA Journal*, **3**(3), 500–505, 1965.

[9] W. T. Koiter, "On the Stability of Elastic Equilibrium," NASA-TT-F-10833, 1967, NASA-TT-F-10833.

[10] L. H. Donnell and C. C. Wang, "Effects of Imperfections of Thin Cylinders and Columns Under Axial Compression," *Journal of Applied Mechanics*, **17**, 73–83, 1950.

[11] J. Arbocz, "The Effect of Initial Imperfections on Shell Stability," *Thin-shell structures: Theory, experiment, and design*, 205–245, 1974.

[12] H. Ohira, "Local Buckling Theory of Axially Compressed Cylinders," in *Proceedings of the Eleventh Japan National Congress for Applied Mechanics*, 1961, 37–41.

[13] B. O. Almroth, "Influence of Edge Conditions on the Stability of Axially Compressed Cylindrical Shells," NASA CR-161, 1965.

[14] T. von Kármán and H. S. Tsien, "The Buckling of Thin Cylindrical Shells Under Axial Compression," *Journal of Aeronautical Sciences*, **8**, 302–335, 1941.

[15] N. J. Hoff, W. A. Madsen, and J. Mayers, "Postbuckling equilibrium of axially compressed circular cylindrical shells," *AIAA Journal*, **4**, 126–133, 1966.

[16] W. F. Thielemann and M. Esslinger, "On the Postbuckling Behavior Thin-Walled Axially Compressed Circular Cylindrical Shells of Finite Length," in *Proceedings: Symposium on the Theory of Shells, to honor Lloyd Hamilton Donnell*, 1967, 431.

[17] B. O. Almroth, A. M. C. Holmes, and D. O. Brush, "An Experimental Study of the Bucking of Cylinders Under Axial Compression," *Experimental Mechanics*, **4**(9), 263–270, Sep. 1964.

[18] M. Eßlinger, "Hochgeschwindigkeitsaufnahmen vom Beulvorgang dünnwandiger, axialbelasteter Zylinder," *Der Stahlbau*, **39**, 73–76, 1970.

[19] M. Baruch and J. Singer, "Effect of Eccentricity of Stiffeners on the General Instability of Stiffened Cylindrical Shells Under Hydrostatic Pressure," *Journal of Mechanical Engineering Science*, **5**(1), 23–27, 1963.

[20] J. W. Hutchinson and J. C. Amazigo, "Imperfection-Sensitivity of Eccentrically Stiffened Cylindrical Shells," *AIAA Journal*, **5**(3), 392–401, 1967.

[21] T. Weller, "Combined Stiffening and in-Plane Boundary Conditions Effects on the Buckling of Circular Cylindrical Stiffened-Shells," *Computers & Structures*, **9**(1), 1–16, Jul. 1978.

[22] E. Byskov and J. W. Hutchinson, "Mode Interaction in Axially Stiffened Cylindrical Shells," *AIAA Journal*, **15**(7), 941–948, 1977.

[23] T. Weller and J. Singer, "Experimental Studies on the Buckling Under Axial Compression of Integrally Stringer-Stiffened Circular Cylindrical Shells," *Journal of Applied Mechanics*, **44**(4), 721–730, Dec. 1977.

[24] M. W. Hilburger and J. H. Starnes Jr, "Effects of Imperfections on the Buckling Response of Compression-Loaded Composite Shells," *International Journal of Non-Linear Mechanics*, **37**(4-5), 623–643, 2002.

[25] R. Zimmermann, "Optimierung axial gedrückter CFK-Zylinderschalen," Fortschritt-Berichte VDI 207, 1992, VDI Verlag, Fortschritt-Berichte VDI, Reihe 1.

[26] B. Geier, H.-R. Meyer-Piening, and R. Zimmermann, "On the Influence of Laminate Stacking on Buckling of Composite Cylindrical Shells Subjected to Axial Compression," *Composite Structures*, **55**(4), 467–474, Mar. 2002.

[27] C. Hühne, R. Rolfes, E. Breitbach, and J. Teßmer, "Robust Design of Composite Cylindrical Shells Under Axial Compression – Simulation and Validation," *Thin-Walled Structures*, **46**(7-9), 947–962, 2008.

[28] "Buckling of Thin-Walled Circular Cylinders," NASA SP-8007, 1968, NASA.

[29] J. de Vries, "The Imperfection Data Bank and its Applications," TU Delft, Delft, 2009.

[30] "Buckling of Steel Shells: European recommendations," ECCS 56, 1988, Brussels, Belgium.

[31] "General Rules: Strength and Stability of Shell Structures," Eurocode 3 Part 1.6, 2002, Brussels, Belgium.

[32] "Stahlbauten – Stabilitätsfälle, Schalenbeulen," DIN 18800 Teil 4, 1990, Berlin.

[33] V. V. Bolotin, "Statistical Aspects in the Theory of Structural Stability," in *Dynamic Stability of Structures (G. Herrmann, ed.)*, Oxford: Pergamon Press, 1967, 67–81.

[34] I. Elishakoff and J. Arbocz, "Reliability of Axially Compressed Cylindrical Shells With General Nonsymmetric Imperfections," *Transactions of the ASME*, **52**, 122–128, 1985.

[35] I. Elishakoff, S. van Manen, P. G. Vermeulen, and J. Arbocz, "First-Order Second-Moment Analysis of the Buckling of Shells with Random Imperfections," *AIAA journal*, **25**(8), 1113–1117, 1987.

[36] J. Arbocz and H. Abramovich, "The Initial Imperfection Data Bank at the Delft University of Technology: Part I," LR-290, 1979, TU Delft, LR-290.

[37]   R. Dancy and D. Jacobs, "The Initial Imperfection Data Bank at the Delft University of Technology: Part II," LR-559, 1988, Delft University of Technology, Faculty of Aerospace Engineering.

[38]   M. K. Chryssanthopoulos, M. J. Baker, and P. J. Dowing, "Imperfection Modeling for Buckling Analysis of Stiffened Cylinders," *Journal of Structural Engineering*, **117**(7), 1998–2017, 1991.

[39]   J. Arbocz and M. W. Hilburger, "Toward a Probabilistic Preliminary Design Criterion for Buckling Critical Composite Shells," *AIAA Journal*, **43**(8), 1823–1827, 2005.

[40]   B. Kriegesmann, "Probabilistic Design Method for Cylindrical Shells made of Composite Material," Diplomarbeit, 2007, Leibniz Universität Hannover, Institut für Statik und Dynamik.

[41]   M. Biagi and F. Del Medico, "Reliability-Based Knockdown Factors for Composite Cylindrical Shells Under Axial Compression," *Thin-Walled Structures*, **46**(12), 1351–1358, 2008.

[42]   R. Degenhardt, A. Kling, A. Bethge, J. Orf, L. Kärger, R. Zimmermann, K. Rohwer, and A. Calvi, "Investigations on Imperfection Sensitivity and Deduction of Improved Knock-down Factors for Unstiffened CFRP Cylindrical Shells," *Composite Structures*, **92**(8), 1939–1946, 2010.

[43]   C. C. Chamis and G. H. Abumeri, "Probabilistic Dynamic Buckling of Composite Shell Structures," *Composites Part A: Applied Science and Manufacturing*, **36**(10), 1368–1380, Oct. 2005.

[44]   M. Broggi, A. Calvi, and G. I. Schuëller, "Reliability Assessment of Axially Compressed Composite Cylindrical Shells with Random Imperfections," *International Journal of Structural Stability and Dynamics*, **11**(02), 215, 2011.

[45]   B. Kriegesmann, R. Rolfes, C. Hühne, J. Teßmer, and J. Arbocz, "Probabilistic Design of Axially Compressed Composite Cylinders with Geometric and Loading Imperfections," *International Journal of Structural Stability and Dynamics*, **10**(4), 623–644, 2010.

[46]   B. Kriegesmann, R. Rolfes, C. Hühne, and A. Kling, "Fast Probabilistic Design Procedure for Axially Compressed Composite Cylinders," *Composites Structures*, **93**, 3140–3149, 2011.

[47]   C. Hühne, "Robuster Entwurf beulgefährdeter, unversteifter Kreiszylinderschalen aus Faserverbundwerkstoff," PhD Thesis at Technischen Universität Carolo-Wilhelmina zu Braunschweig, 2006, published as DLR report FB2006-17, also published as Mitteilungen des Instituts für Statik und Dynamik der Leibniz Universität Hannover 04/2006, ISSN 1862-4650.

[48]   B. Kröplin, D. Dinkler, and J. Hillmann, "An Energy Perturbation Applied to Nonlinear Structural Analysis," *Computer Methods in Applied Mechanics and Engineering*, **52**(1-3), 885–897, Sep. 1985.

[49]   M. Deml and W. Wunderlich, "Direct Evaluation of the 'worst' Imperfection Shape in Shell Buckling," *Computer Methods in Applied Mechanics and Engineering*, **149**(1-4), 201–222, Oct. 1997.

[50]   P. Steinmüller, R. Degenhardt, and K. Rohwer, "Investigations of Axially Loaded Unstiffened CFRP Cylindrical Shells Subject to Single Perturbation Loads," presented at the 2nd International Conference on Buckling and Postbuckling Behaviour of

Composite Laminated Shell Structures with COCOMAT Workshop, Braunschweig, Germany, 2008.

[51] Y. Ben-Haim and I. Elishakoff, "Non-Probabilistic Models of Uncertainty in the Nonlinear Buckling of Shells with General Imperfections: Theoretical Estimates of the Knockdown Factor," *Journal of Applied Mechanics*, **56**(2), 403–410, Jun. 1989.

[52] H. L. van den Nieuwendijk, "Preliminary Study of a New Design Criterion for Shells Under Axial Compression," Memorandum M-805, 1997, Delft University of Technology, Faculty of Aerospace Engineering.

[53] I. Elishakoff, B. Kriegesmann, R. Rolfes, C. Hühne, and A. Kling, "Optimization and Anti-Optimization of Buckling Load for Composite Cylindrical Shells under Uncertainties," *AIAA Journal*, accepted for publication, 2011.

[54] W. T. Koiter and M. Pignataro, "A General Theory for the Interaction Between Local and Overall Buckling of Stiffened Panels," WTHD 83 83, 1976, Delft University of Technology, Delft, The Netherlands.

[55] F. Hashhagen, C. Haack, and M. Wiedemann, "Glare - from Invention to Innovation," in *Fibre Metal Laminates - An Introduction*, A. Vlot and J. W. Gunnik, Eds. Kluwer Academic Publisher, 2001, 299–307.

[56] W. Wohlers, H.-G. Reimerdes, D. Fitzsimmons, J. Wilhelmi, and S. Dieker, "Untersuchung des Stabilitätsverhaltens von Flugzeugrümpfen mittels einer modifizierten Balkentheorie und der Berücksichtigung der elastischen Bettung durch die Haut," presented at the Deutscher Luft- und Raumfahrtkongress, 2002, DGLR–JT2002–163.

[57] M. Wiedemann, "CFRP Status of Application and Future Development Process," presented at the NAFEMS World Congress, Crete, Greece, 2009.

[58] C. Meeks, E. Greenhalgh, and B. G. Falzon, "Stiffener Debonding Mechanisms in Post-Buckled CFRP Aerospace Panels," *Composites Part A: Applied Science and Manufacturing*, **36**(7), 934–946, Jul. 2005.

[59] R. Zimmermann and R. Rolfes, "POSICOSS — Improved Postbuckling Simulation for Design of Fibre Composite Stiffened Fuselage Structures," *Composite Structures*, **73**(2), 171–174, May 2006.

[60] R. Degenhardt, R. Rolfes, R. Zimmermann, and K. Rohwer, "COCOMAT — Improved Material Exploitation of Composite Airframe Structures by Accurate Simulation of Postbuckling and Collapse," *Composite Structures*, **73**(2), 175–178, May 2006.

[61] A. C. Orifici, R. S. Thomson, R. Degenhardt, A. Kling, K. Rohwer, and J. Bayandor, "Degradation Investigation in a Postbuckling Composite Stiffened Fuselage Panel," *Composite Structures*, **82**(2), 217–224, Jan. 2008.

[62] R. Degenhardt, A. Kling, K. Rohwer, A. C. Orifici, and R. S. Thomson, "Design and Analysis of Stiffened Composite Panels Including Post-Buckling and Collapse," *Computers & Structures*, **86**(9), 919–929, May 2008.

[63] J. W. H. Yap, M. L. Scott, R. S. Thomson, and D. Hachenberg, "The Analysis of Skin-to-Stiffener Debonding in Composite Aerospace Structures," *Composite Structures*, **57**(1-4), 425–435, Jul. 2002.

[64] G. Ghilai, E. Feldman, and A. David, "COCOMAT Design and Analysis Guidelines for CFRP-Stiffened Panels in Buckling and Postbuckling," *International Journal of Structural Stability and Dynamics*, **10**(04), 917–926, 2010.

[65] M. C. W. Lee, Z. Mikulik, D. W. Kelly, and R. S. Thomson, "An Assessment of Stiffened Composite Fuselage Panels Based on the Robustness Parameter," *International Journal of Structural Stability and Dynamics*, **10**(04), 717736, 2010.

[66] M. C. W. Lee, D. W. Kelly, R. Degenhardt, and R. S. Thomson, "A Study on the Robustness of Two Stiffened Composite Fuselage Panels," *Composite Structures*, **92**, 223–232, 2010.

[67] D. W. Kelly, M. C. W. Lee, A. C. Orifici, R. S. Thomson, and R. Degenhardt, "Collapse Analysis, Defect Sensitivity and Load Paths in Stiffened Shell Composite Structures," *Computers, Materials & Continua (CMC)*, **10**(2), 163, 2009.

[68] M. Seibel, B. Geier, R. Zimmermann, and H. Eschenauer, "Optimization and Experimental Investigations of Stiffened, Axially Compressed CFRP-Panels," *Structural Optimization*, **15**(2), 124–131, Apr. 1998.

[69] E. Pietropaoli and A. Riccio, "A Global/Local Finite Element Approach for Predicting Interlaminar and Intralaminar Damage Evolution in Composite Stiffened Panels Under Compressive Load," *Applied Composite Materials*, **18**(2), 113–125, Apr. 2010.

[70] R. Zimmermann, H. Klein, and A. Kling, "Buckling and Postbuckling of Stringer Stiffened Fibre Composite Curved Panels-Tests and Computations," *Composite Structures*, **73**(2), 150–161, 2006.

[71] S. W. Tsai and E. M. Wu, "A General Theory of Strength for Anisotropic Materials," *Journal of Composite Materials*, **5**(1), 58 −80, Jan. 1971.

[72] A. Puck and W. Schneider, "On Failure Mechanisms and Failure Criteria of Filament-Wound Glass-Fibre/Resin Composites," *Plastics and Polymers*, **37**(127), 33–43, 1969.

[73] Z. Hashin, "Failure Criteria for Unidirectional Fiber Composites," *Journal of Applied Mechanics*, **47**(2), 329–334, Jun. 1980.

[74] A. Puck and H. Schürmann, "Failure Analysis of FRP Laminates by Means of Physically Based Phenomenological Models," *Composites Science and Technology*, **62**(12-13), 1633–1662, 2002.

[75] M. J. Hinton, A. S. Kaddour, and P. D. Soden, *Failure Criteria in Fibre Reinforced Polymer Composites: The World-Wide Failure Exercise*. Elsevier Science, 2004.

[76] M. Vogler, G. Ernst, and R. Rolfes, "Invariant Based Transversely-Isotropic Material and Failure Model for Fiber-Reinforced Polymers," *Computers, Materials and Continua*, **16**(1), 25–49, 2010.

[77] G. Ernst, M. Vogler, C. Hühne, and R. Rolfes, "Multiscale Progressive Failure Analysis of Textile Composites," *Composites Science and Technology*, **70**(1), 61–72, Jan. 2010.

[78] P. P. Camanho, P. Maimí, and C. G. Dávila, "Prediction of Size Effects in Notched Laminates Using Continuum Damage Mechanics," *Composites Science and Technology*, **67**(13), 2715–2727, Oct. 2007.

[79] S. P. Engelstad and J. N. Reddy, "Probabilistic Methods for the Analysis of Metal-Matrix Composites," *Composites Science and Technology*, **50**(1), 91–107, 1994.

[80] M. R. Gurvich and R. B. Pipes, "Probabilistic Analysis of Multi-Step Failure Process of a Laminated Composite in Bending," *Composites Science and Technology*, **55**(4), 413–421, 1995.

[81]   M. R. Gurvich and R. B. Pipes, "Probabilistic Strength Analysis of Four-Directional Laminated Composites," *Composites Science and Technology*, **56**(6), 649–656, 1996.

[82]   T. P. Philippidis and D. J. Lekou, "Probabilistic Failure Prediction for FRP Composites," *Composites Science and Technology*, **58**(12), 1973–1982, Dec. 1998.

[83]   E. M. Wu and C. S. Robinson, "Computational Micro-Mechanics for Probabilistic Failure of Fiber Composites in Tension," *Composites Science and Technology*, **58**(9), 1421–1432, Sep. 1997.

[84]   G. Ernst, "Multiscale Analysis of Textile Composites - Stiffness and Strength -," Mitteilungen des Instituts für Statik und Dynamik der Leibniz Universität Hannover 10/2009, ISSN 1862-4650, Gottfried Wilhelm Leibniz Universität Hannover, Hannover, Germany, 2009.

[85]   C. C. Chamis, "Probabilistic Simulation of Multi-Scale Composite Behavior," *Theoretical and Applied Fracture Mechanics*, **41**(1-3), 51–61, Apr. 2004.

[86]   A. Shaw, S. Sriramula, P. D. Gosling, and M. K. Chryssanthopoulos, "A Critical Reliability Evaluation of Fibre Reinforced Composite Materials Based on Probabilistic Micro and Macro-Mechanical Analysis," *Composites Part B: Engineering*, **41**(6), 446–453, Sep. 2010.

[87]   S. Czichon, D. Jürgens, W. V. Liebig, R. Rolfes, R. Niekamp, and K. Schulte, "Progressive Failure Analysis of Carbon Fiber Reinforced Polymers with Porosity Defects using a Continuum Damage Approach," in *Proceedings of the 3rd ECCOMAS Thematic Conference on the Mechanical Response of Composites*, R. Rolfes and E. L. Jansen, Eds., 2011, 611–618.

[88]   A. Haldar and S. Mahadevan, *Probability, Reliability, and Statistical Methods in Engineering Design*. John Wiley & Sons New York/Chichester, UK, 2000.

[89]   I. Elishakoff, *Safety Factors and Reliability: Friends or Foes?* Springer, 2004.

[90]   C. P. Robert and G. Casella, *Monte Carlo Statistical Methods*. Springer, 2004.

[91]   B. Kriegesmann, R. Rolfes, C. Hühne, and A. Kling, "Probabilistic Second-Order Third-Moment Approach for Design of Axially Compressed Composite Shells," in *Proceedings of the 51st AIAA/ASME/ASCE/AHS/ASC Structures, Structural Dynamics, and Materials Conference*, Orlando, Florida, USA, 2010, AIAA–2010–2534.

[92]   M. Eßlinger, "Eine Erklärung des Beulmechanismus von dünnwandigen Kreiszylinderschalen," *Der Stahlbau*, **12**, 366–371, 1967.

[93]   R. Degenhardt, A. Kling, W. Hillger, H. C. Goetting, R. Zimmermann, K. Rohwer, and A. Gleiter, "Experiments on Buckling and Postbuckling of Thin-Walled CFRP Structures using Advanced Measurement Systems," *International Journal of Structural Stability and Dynamics*, **7**(2), 337–358.

[94]   W. A. Waters, "Effects Initial Geometric Imperfections on the Behavior of Graphite-Epoxy Cylinders Loaded in Compression," Master thesis, 1996, Old Dominion University, Norfolk, Virginia, USA.

[95]   M. S. El Naschie, *Stress, stability, and chaos in structural engineering: An energy approach*. McGraw-Hill London, 1990.

[96]   P. Wriggers, *Nichtlineare Finite-Element-Methoden*. Birkhäuser, 2001.

[97]   *ABAQUS v6.10 Manual*.

[98]   E. Riks, "Bifurcation and stability, a numerical approach," NLR MP 84078 U, Dec. 1984, Presented at the WAM Symposium on Innovative Methods for Nonlinear Problems, New Orleans, USA.

[99]   C. Hühne and R. Rolfes, "Stabilitätsanalyse perfekter und imperfekter Kreiszylinderschalen aus Faserverbundwerkstoff," in *14. deutschsprachiges ABAQUS Anwendertreffen*, Wiesbaden, Germany, 2002, 1–10.

[100] D. Chrupalla, S. Berg, L. Kärger, M. Doreille, T. Ludwig, E. L. Jansen, R. Rolfes, and A. Kling, "A Homogenization-Based Two-Way Multiscale Approach for Composite Structures," in *Proceedings of the 3rd ECCOMAS Thematic Conference on the Mechanical Response of Composites*, Hannover, Germany, R. Rolfes and E. L. Jansen, Eds., 2011, 263–270.

[101] A. Puck, J. Kopp, and M. Knops, "Guidelines for the Determination of the Parameters in Puck's Action Plane Strength Criterion," *Composites Science and Technology*, **62**(3), 371–378, 2002.

[102] R. Rolfes, M. Vogler, S. Czichon, and G. Ernst, "Exploiting the structural reserve of textile composite structures by progressive failure analysis using a new orthotropic failure criterion," *Computers & Structures*, **89**(11-12), 1214–1223, 2011.

[103] S. Czichon, K. Zimmermann, P. Middendorf, M. Vogler, and R. Rolfes, "Three-Dimensional Stress and Progressive Failure Analysis of Ultra Thick Laminates and Experimental Validation," *Composite Structures*, **93**(5), 1394–1403, Apr. 2011.

[104] J. Arbocz and J. H. Starnes Jr, "Future Directions and Challenges in Shell Stability Analysis," *Thin-Walled Structures*, **40**(9), 729–754, 2002.

[105] W. Härdle and L. Simar, *Applied Multivariate Statistical Analysis*. Berlin: Springer Verlag, 2007.

[106] J. Orf, "Einfluss von Imperfektionen auf das Beulverhalten unversteifter CFK-Zylinder," Diplomarbeit, 2008, Bauhaus-Universität Weimar, Institut für Strukturmechanik.

[107] I. Elishakoff, "Simulation of Space-Random Fields for Solution of Stochastic Boundary-Value Problems," *The Journal of the Acoustical Society of America*, **65**(2), 399–403, Feb. 1979.

[108] Y. J. Hong, J. Xing, and J. B. Wang, "A Second-Order Third-Moment Method for Calculating the Reliability of Fatigue," *International Journal of Pressure Vessels and Piping*, **76**(8), 567–570, 1999.

[109] L. P. Zhu, I. Elishakoff, and J. H. Starnes, "Derivation of Multi-Dimensional Ellipsoidal Convex Model for Experimental Data," *Mathematical and Computer Modelling*, **24**(2), 103–114, Jul. 1996.

[110] S. S. Wilks, *Mathematical statistics*. Wiley, 1962.

[111] B. Kriegesmann, R. Rolfes, E. L. Jansen, I. Elishakoff, C. Hühne, and A. Kling, "Design Optimization of Composite Cylindrical Shells Under Uncertainty," in *Proceedings of the 3rd ECCOMAS Thematic Conference on the Mechanical Response of Composites*, Hannover, Germany, R. Rolfes and E. Jansen, Eds., 2011, 431–438.

[112] F. Jarre and J. Stoer, *Optimierung*. Springer, 2004.

[113] J. E. Herencia, R. T. Haftka, P. M. Weaver, and M. I. Friswell, "Lay-Up Optimization of Composite Stiffened Panels Using Linear Approximations in Lamination Space," *AIAA JOURNAL*, **46**(9), 2008.

[114] P. Knabner and L. Angermann, *Numerik partieller Differentialgleichungen: eine anwendungsorientierte Einführung*. Springer, 2000.

[115] "3D Coordinate Measuring: GOM." [Online]. Available: http://www.gom.com/metrology-systems/3d-coordinate-measuring.html. [Accessed: 10-May-2011].

[116] G. Tennant, *Six Sigma: SPC and TQM in manufacturing and services*. Gower Publishing, Ltd., 2001.

[117] D. Wilckens, R. Degenhardt, K. Rohwer, R. Zimmermann, M. Kepke, B. Hildebrandt, and A. Zipfel, "Cyclic Buckling Tests of Pre-Damaged CFRP Stringer-Stiffened Panels," *International Journal of Structural Stability and Dynamics*, **10**(04), 827, 2010.

[118] I. T. Jolliffe, *Principal Component Analysis*. Springer, New York, 1986.

[119] R. M. Jones, *Mechanics of Composite Materials*. Hemisphere Pub., 1999.